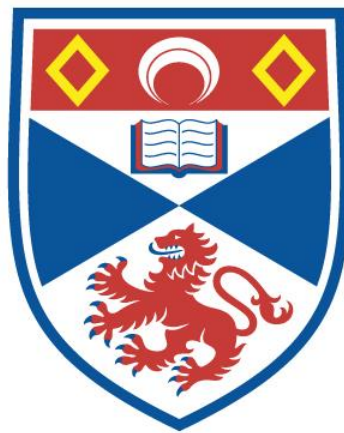


# THE DEVELOPMENT OF ALTERNATIVE CATHODES FOR HIGH TEMPERATURE SOLID OXIDE ELECTROLYSIS CELLS

Xiangling Yue

A Thesis Submitted for the Degree of PhD  
at the  
University of St Andrews



2013

Full metadata for this item is available in  
Research@StAndrews:FullText  
at:  
<http://research-repository.st-andrews.ac.uk/>

Please use this identifier to cite or link to this item:  
<http://hdl.handle.net/10023/6531>

This item is protected by original copyright

This item is licensed under a  
Creative Commons Licence

# **The Development of Alternative Cathodes for High Temperature Solid Oxide Electrolysis Cells**

**This thesis is submitted in partial fulfilment for the degree of PhD  
at the  
University of St Andrews**

**By**

**Xiangling Yue**



**University  
of  
St Andrews**

**Supervised by Prof. John T S Irvine**

**Submitted 15 Jul 2013**







The Development of Alternative Cathodes for High  
Temperature Solid Oxide Electrolysis Cells

Xiangling Yue, PhD thesis

15<sup>th</sup> Jul 2013







## **Declarations**

### **1. Candidate's declarations**

I, Xiangling Yue, hereby certify that this thesis, which is approximately 55,000 words in length, has been written by me, that it is the record of work carried out by me and that it has not been submitted in any previous application for a higher degree.

I was admitted as a research student in Oct, 2008 and as a candidate for the degree of PhD in Oct, 2009; the higher study for which this is a record was carried out in the University of St Andrews between 2008 and 2013.

Date ..... Signature of candidate.....

### **2. Supervisor's declarations**

I hereby certify that the candidate has fulfilled the conditions of the Resolution and Regulations appropriate for the degree of PhD in the University of St Andrews and that the candidate is qualified to submit this thesis in application for that degree.

Date..... Signature of supervisor.....

### **3. Permission for electronic publication:**

In submitting this thesis to the University of St Andrews I understand that I am giving permission for it to be made available for use in accordance with the regulations of the University Library for the time being in force, subject to any copyright vested in the work not being affected thereby. I also understand that the title and the abstract will be published, and that a copy of the work may be made and supplied to any bona fide library or research worker, that my thesis will be electronically accessible for personal or research use unless exempt by award of an embargo as requested below, and that the library has the right to migrate my thesis into new electronic forms as required to ensure continued access to the thesis. I have obtained any third-party copyright permissions that may be required in order to allow such access and migration, or have requested the appropriate embargo below.

The following is an agreed request by candidate and supervisor regarding the electronic publication of this thesis:

(i) Access to printed copy and electronic publication of thesis through the University of St Andrews.

Date .....

Signature of candidate .....

Signature of supervisor .....

## Acknowledgements

This thesis is dedicated to my husband, Liang Wei. Pursuing a PhD requires hard work, intense focus and long hours, without his understanding and support all these years when I was far away from home, I would not make it. Not mention his willingness to come to the UK to join me and spend a lot time looking after our baby boy, so that I could focus on writing.

I would like to express my gratefulness to my supervisor, Prof. John Irvine, for giving me the opportunity to carry out this work, and for providing me with a lot of helpful suggestions, discussion and expert advice. Without his guidance, this work would not be possible.

I wish to thank the following members in Prof. John Irvine's group: Cristian Savaniu and Mark Cassidy for their help and discussion in cell fabrication; Paul Connor for advice and suggestions on software utilization and impedance fitting; David Miller and Gael Corre for help in solving testing-related problems; Julie Nairn for help in chemical/gas purchase and many lab-related matters. I also wish to thank Ross Blackley and Zixue Su (who has left St Andrew) for giving me trainings and help on SEM measurement, James Rennie for designing and building up the vacuum impregnation equipment for me and George Anthony for fixing up all the broken pieces I brought to his workshop.

I also wish to thank all the other members in our research group for useful discussions and advice. And I would like to thank Xuedi Yang and Xiaoxiang Xu for a lot of help in getting me familiar with the surroundings when I first arrived at St Andrews, and all my other friends who made my life in St Andrews enjoyable.

My sincere thanks go to my parents, my brothers and my sister for their spiritual support from thousands miles away. And my special thanks go to my 10-month baby boy, Jeromy Chuyan Wei, who has brought me a lot of happiness and joy ever since his birth.

Finally, I would like to acknowledge the funding support from the ORS University of St Andrews and the EPSRC for my PhD study.

## Abstract

This study mainly explores the development of alternative cathode materials for the electrochemical reduction of CO<sub>2</sub> by high temperature solid oxide electrolysis cells (HTSOECs), which operate in the reverse manner of solid oxide fuel cells (SOFCs). The conventional Ni-yttria stabilized zirconia (YSZ) cermet cathode suffered from coke formation, whereas the perovskite-type (La, Sr)(Cr, Mn)O<sub>3</sub> (LSCM) oxide material displayed excellent carbon resistance. Initial CO<sub>2</sub> electrolysis performance tests from different cathode materials prepared by screen-printing showed that LSCM based cathode performed poorer than Ni-YSZ cermets, due to non-optimized microstructure. Efforts were made on microstructure modification of LSCM based cathodes by means of various fabrication methods. Among the LSCM/YSZ graded cathode, extra catalyst (including Pd, Ni, CeO<sub>2</sub>, and Pt) aided LSCM/GDC (Gd<sub>0.1</sub>Ce<sub>0.9</sub>O<sub>1.95</sub>) cathode, LSCM impregnated YSZ cathode, and GDC impregnated LSCM cathode, the GDC impregnated LSCM cathode, with porous LSCM as backbone for finely dispersed GDC nanoparticles, was found to possess the desired microstructure for CO<sub>2</sub> splitting reaction via SOEC. Incorporating of 0.5wt% Pd into GDC impregnated LSCM cathode gave rise to an R<sub>p</sub> of 0.24 Ω cm<sup>2</sup> at open circuit voltage (OCV) at 900°C in CO<sub>2</sub>-CO 70-30 mixture, comparable with the Ni/YSZ cermet cathode operated in the identical conditions.

Meanwhile, the cathode kinetics and possible mechanisms of the electrochemical reduction of CO<sub>2</sub> were studied, and factors including CO<sub>2</sub>/CO composition, operation temperature and potential were taken into account. The current-to-chemical efficiency of CO<sub>2</sub> electrolysis was evaluated with gas chromatography (GC). The high performance Pd and GDC co-impregnated LSCM cathode was also applied for CO<sub>2</sub> electrolysis without protective CO gas in feed. This cathode also displayed superb performance towards CO<sub>2</sub> electrochemical reduction under SOEC operation condition in CO<sub>2</sub>/N<sub>2</sub> mixtures, though it had OCV as low as 0.12V at 900°C.

The LSCM/GDC set of SOEC cathode materials were investigated in the application of steam electrolysis and H<sub>2</sub>O-CO<sub>2</sub> co-electrolysis as well. For the former, adequate supply of steam was essential to avoid the appearance of S-shaped I-V curves and limited steam transport. The 0.5wt% Pd and GDC co-infiltrated LSCM material has been found to be a versatile cathode with high performance and good durability in SOEC operations.

## Table of contents

<b>Declarations</b> .....	I
<b>Acknowledgements</b> .....	II
<b>Abstract</b> .....	III
<b>Table of contents</b> .....	V

### Chapter 1: Literature review

1.1 Introduction.....	2
1.2 Solid oxide electrolysis cells (SOECs).....	6
1.2.1 Principle of solid oxide electrolysis cells.....	7
1.2.2 Thermodynamics of SOEC.....	9
1.2.3 Characteristics of solid oxide electrolysis cells.....	12
1.3 High temperature CO <sub>2</sub> electrolysis via SOEC.....	15
1.4 Materials for high temperature SOECs used for CO <sub>2</sub> electrolysis.....	16
1.4.1 Electrolyte.....	16
1.4.2 Cathode.....	19
1.4.2.1 Ni-cermet cathodes.....	20
1.4.2.2 LSCM perovskite cathodes.....	21
1.4.2.3 Doped ceria cathodes.....	24
1.4.2.4 (La <sub>1-x</sub> Sr <sub>x</sub> )TiO <sub>3</sub> perovskite cathodes.....	25
1.4.3 Anode.....	26
1.5 Triple phase boundaries (TPBs).....	27
1.6 Aims of study.....	28
References.....	29

### Chapter 2: Methods and techniques

Introduction.....	35
2.1 General recipe for screen-printing ink preparation.....	35
2.2 General steps for single cell preparation.....	37
2.2.1 Single cells with fuel electrode made from screen-printing.....	39
2.2.2 Single cells with a gradient cathode structure.....	41
2.2.3 Single cells with fuel electrode on an impregnated architecture .....	42
2.3 Cell testing set-up and gas flows.....	45
2.3.1 Single cell testing set-up .....	45
2.3.2 Gas supply.....	47
2.4 Material characterization.....	48
2.4.1 Thermal gravimetric analysis (TGA).....	48
2.4.2 X-ray diffraction (XRD) pattern .....	49
2.5 Single solid oxide cell characterization.....	51
2.5.1 Single cell electrochemical characterization.....	51
2.5.2 Single cell microstructure characterization.....	56
2.6 Single cell electrolysis efficiency analysis.....	59
2.6.1 Gas chromatography (GC).....	59
2.6.2 Calculation of electrolysis efficiency.....	60
References.....	60

### **Chapter 3: Carbon sensitivity study on different potential cathode materials**

Introduction.....	64
3.1 Carbon sensitivity on Ni-YSZ cathode.....	65
3.1.1 Ni/YSZ pellets preparation, treatment and post-characterization.....	65
3.1.2 Microstructure of Ni/YSZ pellets treated in CO <sub>2</sub> /CO atmospheres.....	67
3.1.3 TGA analysis on Ni/YSZ pellets treated in CO <sub>2</sub> /CO atmospheres.....	69
3.1.4 XRD inspection on Ni/YSZ pellets treated in CO <sub>2</sub> /CO atmospheres.....	76
3.2 Carbon sensitivity on LSCM-YSZ composite.....	78
3.2.1 LSCM/YSZ treatment in CO <sub>2</sub> -CO mixture and post-analysis on LSCM/YSZ pellet.....	78
3.2.2 SEM test on LSCM/YSZ pellets treated in CO <sub>2</sub> /CO 50/50 atmosphere.....	79

3.2.3 Thermo gravimetric analysis on LSCM/YSZ samples pre-treated in CO <sub>2</sub> /CO 50/50 mixture.....	81
3.2.4 XRD measurement on LSCM/YSZ pellets after treatment in CO <sub>2</sub> /CO 50/50 atmosphere.....	82
3.3 Summary.....	83
References.....	83

## **Chapter 4: Initial performance from different cathode materials for high temperature CO<sub>2</sub> electrolysis**

Introduction.....	86
4.1 Cell fabrication and characterization.....	87
4.2 Ni-YSZ cermet cathode performance towards CO <sub>2</sub> electrolysis.....	89
4.3 LSCM-YSZ composite.....	95
4.3.1 Choice of current collector for LSCM/YSZ cathode.....	95
4.3.2 Performance from LSCM/YSZ composite cathode for CO <sub>2</sub> electrolysis.....	97
4.4 LSCM-GDC composite cathode.....	102
4.5 Comparisons between Ni-cermet and LSCM based cathode.....	109
4.5.1 Microstructure comparisons.....	109
4.5.2 Performance comparisons for CO <sub>2</sub> electrolysis by SOEC.....	111
4.5.3 Cathode activation energy for CO <sub>2</sub> reduction via a SOEC.....	114
4.6 Stability test on LSCM/GDC cathode in CO <sub>2</sub> -CO mixture.....	116
4.7 Summary.....	118
References.....	119

## **Chapter 5: Modification of LSCM based cathode to enhance performance for high temperature CO<sub>2</sub> electrolysis**

Introduction.....	123
5.1 Cathode with a graded structure.....	124
5.1.1 Preparation of the graded LSCM/YSZ cathode cell.....	124
5.1.2 Performance of the graded LSCM/YSZ cathode cell.....	125
5.1.3 Microstructure of the LSCM/YSZ gradient cathode.....	128

5.2 LSCM/GDC composite cathode with additional catalyst.....	129
5.2.1 Fabrication and characterization of LSCM/GDC cathode with extra catalyst. .....	129
5.2.2 Performance from LSCM/GDC composite impregnated with different catalyst... .....	130
5.2.3 Performance from LSCM/GDC composite cathode with different level of catalyst loading.....	136
5.2.4 Microstructure analysis on LSCM/GDC composite impregnated with extra catalyst.....	138
5.3 LSCM based cathode with impregnated architecture.....	140
5.3.1 Single cell fabrication and characterization.....	140
5.3.1.1 Fabrication and characterization of LSCM impregnated YSZ cathode cell .....	140
5.3.1.2 Preparation and characterization of GDC impregnated LSCM cathode cell.....	141
5.3.2 LSCM impregnated YSZ cathode.....	143
5.3.3 GDC impregnated LSCM cathode.....	149
5.3.3.1 Microstructure of the GDC impregnated LSCM cathode.....	149
5.3.3.2 Performance of the GDC impregnated LSCM cathode for CO <sub>2</sub> electrolysis .....	151
5.3.3.3 Effect of introducing H <sub>2</sub> on the performance of the GDC impregnated LSCM cathode for CO <sub>2</sub> electrolysis.....	158
5.4 Pd and GDC co-impregnated LSCM cathode.....	162
5.4.1 Manufacture and characterization of Pd and GDC co-impregnated LSCM cathode cell.....	162
5.4.2 Performance from Pd and GDC co-impregnated cathode in various CO <sub>2</sub> -CO atmospheres.....	163
5.4.3 Microstructure analysis of the Pd-GDC co-impregnated cathode material.....	167
5.4.4 Stability of the Pd and GDC co-impregnated LSCM cathode for CO <sub>2</sub> electrolysis.....	168
5.5 Conclusions.....	169
References.....	170

## **Chapter 6: Efficiency analysis on CO<sub>2</sub> electrolysis by SOEC and CO<sub>2</sub> electrolysis without protective gas**

Introduction.....	174
6.1 Gas chromatography analysis and Faraday efficiency calculation.....	175
6.2 Faraday efficiency analysis for CO <sub>2</sub> electrolysis on different cathode materials for SOEC.....	177
6.2.1 CO <sub>2</sub> electrolysis efficiency analysis on screen-printed LSCM/GDC cathode with extra Pt catalyst.....	177
6.2.2 CO <sub>2</sub> electrolysis efficiency on the GDC impregnated LSCM cathode for SOEC.....	183
6.2.3 CO <sub>2</sub> electrolysis efficiency on the Pd-GDC co-impregnated LSCM cathode for SOEC.....	188
6.3 CO <sub>2</sub> electrolysis without protective gas and corresponding efficiency evaluation.....	190
6.3.1 Performance and efficiency of CO <sub>2</sub> electrolysis in CO <sub>2</sub> -N <sub>2</sub> feed into SOEC cathode.....	190
6.3.2 Impact of 5%H <sub>2</sub> /Ar on the SOEC cathode performance and efficiency of CO <sub>2</sub> electrolysis in CO <sub>2</sub> -N <sub>2</sub> feed.....	197
6.4 Summary.....	201
References.....	202

## **Chapter 7: High temperature steam electrolysis and steam-carbon dioxide co-electrolysis**

Introduction.....	204
7.1 Steam delivery and single cell characterization.....	205
7.2 Steam electrolysis on LSCM/GDC cathode SOEC.....	207
7.2.1 Steam electrolysis on screen-printed LSCM/GDC cathode SOEC.....	207
7.2.2 Steam electrolysis on the GDC impregnated LSCM cathode SOEC.....	213
7.2.3 Comparisons between high temperature steam electrolysis and CO <sub>2</sub> electrolysis.....	218
7.3 Steam and CO <sub>2</sub> co-electrolysis on LSCM/GDC cathode cell.....	219
7.3.1 Co-electrolysis study on screen-printed LSCM/GDC cathode SOEC.....	219

7.3.2 Co-electrolysis study on the GDC impregnated LSCM cathode SOEC.....	223
7.3.3 Co-electrolysis in different ratio of H <sub>2</sub> O-H <sub>2</sub> -CO <sub>2</sub> -CO mixture .....	226
7.3.4 Co-electrolysis stability test in H <sub>2</sub> O-H <sub>2</sub> -CO <sub>2</sub> -CO mixtures .....	228
7.4 Conclusions.....	230
References.....	231
<b>General conclusions.....</b>	<b>233</b>
<b>Publications.....</b>	<b>235</b>

## Chapter 1: Literature review

### Table of Contents

1.1 Introduction .....	2
1.2 Solid oxide electrolysis cells (SOECs).....	6
1.2.1 Principle of solid oxide electrolysis cells .....	7
1.2.2 Thermodynamics of SOEC .....	9
1.2.3 Characteristics of solid oxide electrolysis cells .....	12
1.3 High temperature CO <sub>2</sub> electrolysis via SOEC .....	15
1.4 Materials for high temperature SOECs used for CO <sub>2</sub> electrolysis .....	16
1.4.1 Electrolyte .....	16
1.4.2 Cathode .....	19
1.4.2.1 Ni-cermet cathodes.....	20
1.4.2.2 LSCM perovskite cathodes .....	21
1.4.2.3 Doped ceria cathodes .....	24
1.4.2.4 (La <sub>1-x</sub> Sr <sub>x</sub> )TiO <sub>3</sub> perovskite cathodes .....	25
1.4.3 Anode.....	26
1.5 Triple phase boundaries (TPBs) .....	27
1.6 Aims of study .....	28
References .....	29

## Chapter 1: Literature review

### 1.1 Introduction

Global atmospheric concentration of greenhouse gas has remarkably increased due to human activities since the industrial revolution in the 18<sup>th</sup> century. Carbon dioxide (CO<sub>2</sub>) is the primary constituent of anthropogenic greenhouse gas. Fig. 1.1 shows the atmospheric concentration of CO<sub>2</sub> over the last 10,000 years from ice cores and modern time since 1750 to 2005. The CO<sub>2</sub> concentration in atmosphere was about 280 ppm in pre-industrial period and it had increased quickly to around 379 ppm by 2005 [1]. The use of fossil fuels plays a dominant role in the increasingly vast emissions of CO<sub>2</sub> into the atmosphere, and it has been reported that the potential emissions from remaining fossil resources could lead to greenhouse gas concentration levels far above 600 ppm by 2100 [2]. This undoubtedly will aggravate the global warming if the CO<sub>2</sub> emissions are not controlled.

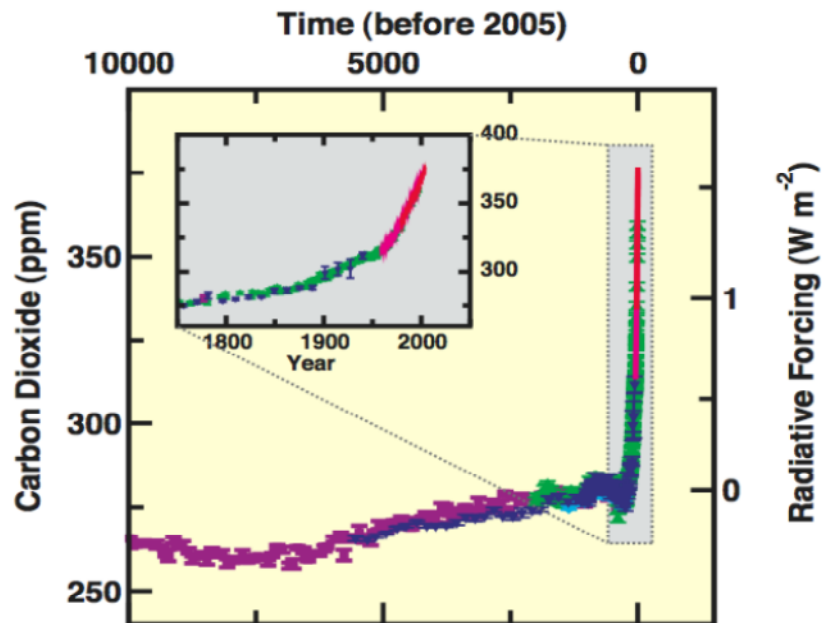


**Fig. 1.1** Atmospheric concentration of carbon dioxide over the last 10, 000 years (large panels) from ice cores and modern times since 1750 to 2005 (inset panels). The term “radiative forcing” was used to compare the range of human and natural factors drive warming influences on global climate and its values were much higher for CO<sub>2</sub> than for methane and nitrous oxide [1]

The majority of CO<sub>2</sub> emissions are as a result of the heavy dependence of human activities on fossil fuels as an energy source. Shown in Fig. 1.2 is the share of energy sources in total global primary energy supply in 2008. Fossil fuels, including crude oil, coal, etc., constitute the majority sources of energy consumption in current energy system, while the renewable sources, for instance, nuclear, wind, solar, tidal, geothermal and so on, share only ca. 15% of the total energy sources, though the renewable energies have attracted increasing interest in recent years. The fossil fuels are non-renewable in nature, and their supplies are decreasing. Yet, the energy demand for human activities is still increasing. Therefore, the global issue of climate change due to the great amount of CO<sub>2</sub> emissions and of sustainable energy production due to the depleting supply of fossil fuels is an urgent question to be addressed.

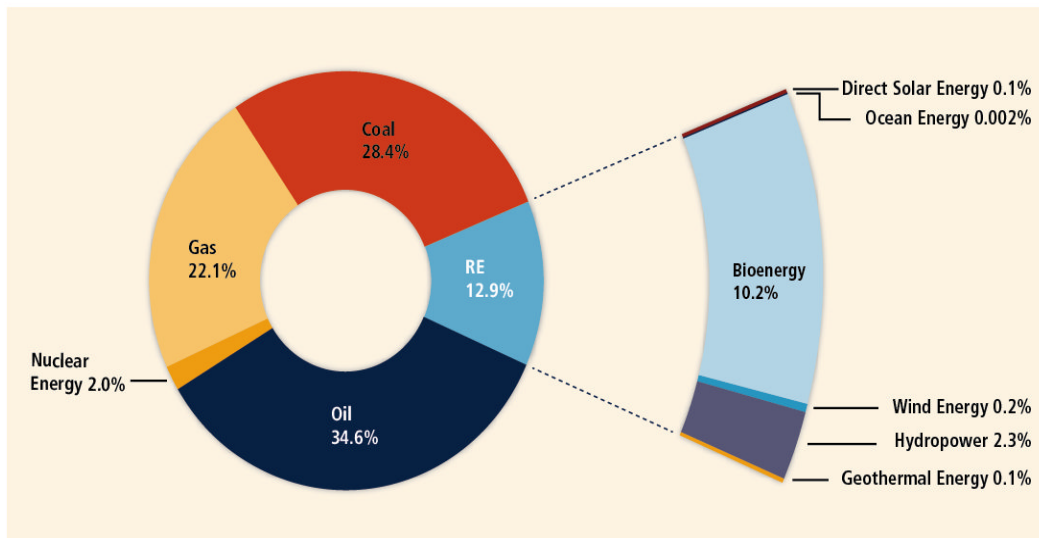


**Fig. 1.2** Shares of energy sources in total global primary energy supply in 2008 [2]

Carbon sequestration and storage (CSS) has been proposed, to minimize the accumulation of CO<sub>2</sub> in the atmosphere and the resulting climate changes [3]. Approaches including geological storage, ocean storage, and mineral carbonation have been put forward for CSS strategy. However, the CSS may not be a long term solution due to reasons of costs for regulation and remediation of CO<sub>2</sub> leakages if they occur and of cost for re-use/disposal. In this sense, CO<sub>2</sub> is considered more likely as a waste with cost of disposal, thus, the CSS may be regarded as a bridging technology to a

sustainable and efficient energy supply associated with utilization/recycling of CO<sub>2</sub> in the system.

Carbon neutral sources and/or fuels were raised and defined as those whose utilization would not lead to a net increase in the concentration of atmospheric CO<sub>2</sub> [4]. An alternative to storing CO<sub>2</sub> in geological reservoirs or biosphere, captured CO<sub>2</sub> from atmosphere or from large emission sources such as power plants can be used to produce carbon neutral fuels, for instance, hydrocarbons. This has been exploited as an active R&D research topic, especially when low carbon emission sources, such as nuclear and renewable energies are incorporated as energy input.

Whipple and Kenis compared the primary energy consumption by source and sector in the U.S. for 2008 with a hypothetical energy distribution scenario, as displayed in Fig. 1.3. This energy consumption by sector and source in current economy could also be representative for the rest of the developed countries though the exact percentage may vary. The hypothetical situation for future energy sources distribution scenario was depicted with lower level of CO<sub>2</sub> emissions accomplished by increasing carbon-neutral sources (renewable and nuclear energy) utilization, while decreasing fossil fuels consumption.

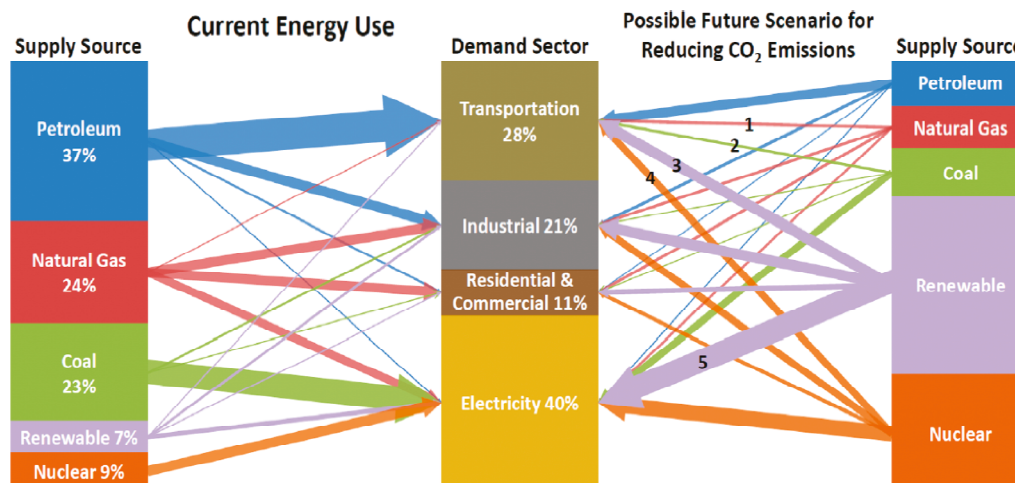


**Fig. 1.3** Comparison between our current energy consumption divided by source and sector (based on data of the primary energy consumption in the U.S. for 2008) and a hypothetical energy sources distributions with the level of CO<sub>2</sub> emissions reduced significantly by increasing the utilization portion from renewable and nuclear while decreasing fossil fuels consumption [5]

The electrochemical conversion of CO<sub>2</sub> to chemicals and fuels was highlighted in the comparison in Fig. 1.3, and it could play an important role in enabling the hypothetical scenario of energy make up, most significantly in reducing the fossil fuels consumption on transportation and electricity sectors. Synthetic fuels produced from cycling of CO<sub>2</sub> could be supplied to transportation sector using electricity from renewables and nuclear energy. Meanwhile, nuclear and the intermittent renewable sources can be an alternative means for electricity generation by storing them in chemicals including H<sub>2</sub> and carbonaceous fuels from the electrochemical conversion of CO<sub>2</sub>, with the latter being more versatile due to its wide usage in transportation fuels, electricity generation, and feedstock in industrial. These routes for reducing human dependence on fossil fuels would not increase the atmospheric concentration of CO<sub>2</sub> ascribed to that carbon neutral sources are incorporated.

The electrochemical conversion of CO<sub>2</sub> for chemicals and fuels production, rather storage is more attractive, not only because of its possibility of reducing greenhouse gas emissions but also the opportunities it offers of reducing human dependence on non-

renewable fossil fuels consumptions, thus, it will direct us to a more sustainable economy also a more friendly environment. What is more, carbonaceous fuels from CO<sub>2</sub> conversion are compatible with the existing petroleum infrastructure, which avoids the need to build an entirely new infrastructure as H<sub>2</sub> fuel encounters. Actually, these fuels can be regarded as a form of H<sub>2</sub> and carbon storage, which offer a better way to store H<sub>2</sub>. When renewable energy is utilized for CO<sub>2</sub> electrochemical reduction, the resulting fuels can be viewed as energy carriers with higher energy density, in comparison with H<sub>2</sub>, an energy carrier but with a lower volumetric energy density [6].

There are several pathways for the electrochemical conversion of CO<sub>2</sub>, including electrolytic reduction in aqueous solution [7-9], high temperature electrolysis [10, 11], and photo electrochemical/catalytic reduction [12, 13]. Of all these, the electrochemical reduction of CO<sub>2</sub> via high temperature solid oxide electrolysis cells (SOECs) has been identified as one of the most promising approaches [11].

The electrochemical reduction of CO<sub>2</sub> has been extensively studied in aqueous alkaline solution utilizing various metal electrodes [7-9, 14, 15]. This low temperature process underwent several crucial problems, such as low reaction kinetics due to the low CO<sub>2</sub> solubility in aqueous electrolyte which required high pressure to get more CO<sub>2</sub> available for reaction [8, 12], catalyst deactivation from graphite and/or hydroxide poisons [7, 14], and requirement of PH control for desirable product selectivity etc [7]. Compared with the low temperature electrolysis in aqueous solutions, the high temperature CO<sub>2</sub> electrolysis by SOECs has several positive traits. It employs an all solid state device, thereby avoids the problems associated with utilizing of aqueous electrolyte, e.g. leakage and corrosion. It works in the temperature range of 700-1000°C, such high temperature operation not only decreases the electricity demand, but also guarantees fast electrode kinetics and thus low resistance. These positive traits of high temperature CO<sub>2</sub> electrolysis by SOECs have motivated research into the materials development and mechanisms investigation.

### **1.2 Solid oxide electrolysis cells (SOECs)**

The utilization of SOECs as a means for energy conversion was proposed by Isenberg during the 1980s [16]. It was suggested to use SOECs to split H<sub>2</sub>O/CO<sub>2</sub> to generate

H<sub>2</sub>/CO and O<sub>2</sub>. The former could act as the basis for chemical production via Fischer-Tropsch synthesis, and the latter was considered as propellant and important life support consumables for Mars missions [17-19]. The SOEC techniques were also carried out within the HotElly project for H<sub>2</sub> production, and high efficiencies (40-50%) from high temperature steam electrolysis were demonstrated [20, 21]. However, the SOEC study for CO<sub>2</sub> electrolysis was soon stopped and efforts were turned to the reverse reaction, i.e. solid oxide fuel cells (SOFC) for electricity generation due to the low price of crude oils at 1990s.

In recent years, SOEC applications in electrochemical reduction of CO<sub>2</sub> and green H<sub>2</sub> production have retrieved increasing interest due to its potential rewards both in energy and environmental aspects. SOECs provide an efficient and environmental friendly means of H<sub>2</sub> production compared to steam reforming, which is presently the approach of massive H<sub>2</sub> production [22]. As for CO<sub>2</sub> dissociation, SOEC offers a way to recycle CO<sub>2</sub> into chemicals and fuels, which helps to reduce the accumulation of atmospheric CO<sub>2</sub> and relieve the pressure from shrinking supply of fossil fuels [11]. Combined with CO<sub>2</sub> capture and CO<sub>2</sub> gas separation technologies, SOEC can present a promising way to realize the carbon neutral cycling of fuels.

Furthermore, vigorous development of SOFC has taken place during the last two decades [23]. The developed materials and techniques in SOFC facilitate SOEC expansion as they work in reverse manner. The same device can work as an energy convertor to generate electricity in SOFC direction and to produce chemicals to store excess electricity in SOEC direction and use these chemicals when necessary. Most attractively, when the excess electricity is from the intermittent renewable energy sources (wind, tidal etc.), the process in SOEC direction thus offers a means to store the renewable energy in the form of H<sub>2</sub>/CO, with the added possibility of using this H<sub>2</sub>/CO as a transportation fuel or a feedstock for the production of transportation fuels.

### **1.2.1 Principle of solid oxide electrolysis cells**

Working in reverse manner, SOEC and SOFC share a lot in common. In fact, a solid oxide cell can be fabricated, with the abilities of working for both the oxidation of H<sub>2</sub>/CO and the dissociation of H<sub>2</sub>O/CO<sub>2</sub>. A schematic graph of a solid oxide cell that

can work both as SOFC and SOEC is shown in Fig. 1.4, with the working principles for both operations sketched in the graph. In SOFC,  $O_2$  is dissociated to oxide ions which diffuse to the other side of electrolyte, where  $H_2/CO$  is oxidized by these oxide ions. Electricity is produced during this whole process. While in SOEC, the reverse reaction happens. That is electricity is supplied to drive the  $H_2O/CO_2$  splitting to oxide ions, which transport through electrolyte and combine with each other to form  $O_2$  on the other side.

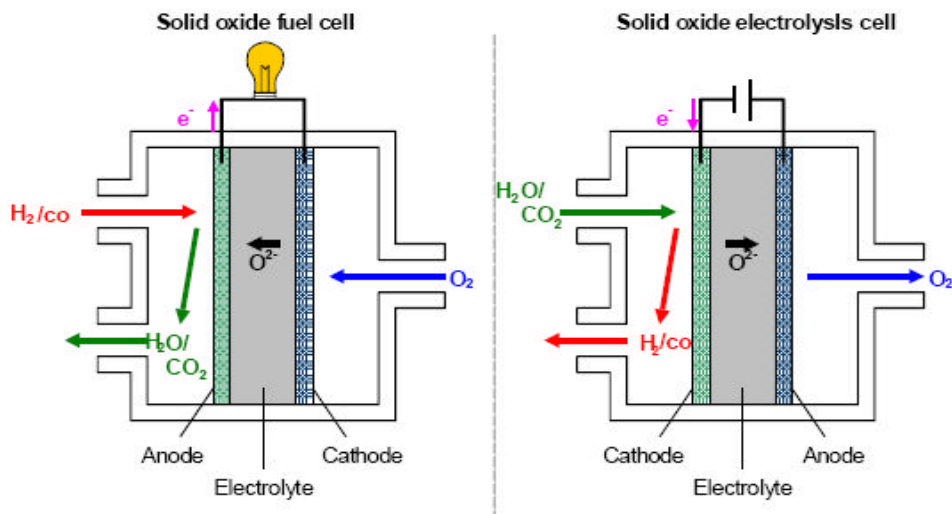
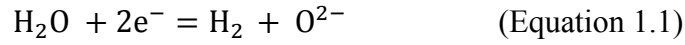


**Fig. 1.4** Schematic graph of a SOFC and a SOEC and their working principles

Both SOFC and SOEC consist of a dense, gas tight, and ion-conducting electrolyte (the grey layer in Fig. 1.4) sandwiched between two porous electrodes. The conventional material for electrolyte is zirconia ( $ZrO_2$ ) ceramic, with trivalent cations (e.g.  $Y^{3+}$ ,  $Sc^{3+}$ ) as dopant to stabilize a cubic structure and introduce oxygen vacancy defects [24]. The green layer is the negative electrode or fuel electrode (cathode in SOEC and anode in SOFC mode), and the blue layer is the positive electrode or air electrode (anode in SOEC while cathode in SOFC mode).

Currently, there are many reports that deal with high temperature solid oxide electrolysis of steam [24, 25-31]. During this process, the electrochemical dissociation

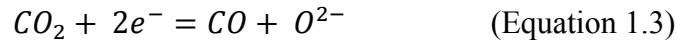
of steam to H<sub>2</sub> and oxygen anions, as shown in Equation 1.1, occurs on the cathode side of an SOEC.



The produced oxygen anions then diffuse to the anode side through electrolyte by vacancy mechanism. While the combination of oxygen anions to O<sub>2</sub>, as shown in Equation 1.2, takes place on the anode side of an SOEC.



Similar to water electrolysis, the CO<sub>2</sub> electrolysis involves the reduction of CO<sub>2</sub> to carbon monoxide and oxygen ions on the cathode side, as shown in Equation 1.3,



the transport of oxygen ions through the electrolyte membrane and the recombination of oxygen ions at the anode (Equation 1.2). The whole process of H<sub>2</sub>O/CO<sub>2</sub> electrolysis embraces not only the above steps, but also others including the diffusion of reactant gas from bulk gas to the surface of cathode, the surface diffusion of reactant gas or intermediate species to the active reaction sites, and the products from the interface of electrode/electrolyte to the surface of electrode etc. In summary, the heterogeneous electrochemical reduction of H<sub>2</sub>O/CO<sub>2</sub> by SOEC is a complicated process and its fundamental mechanisms need to be investigated in details.

### 1.2.2 Thermodynamics of SOEC

In SOEC operation, for example, for CO<sub>2</sub> electrolysis which involves the reaction  $\text{CO}_2(g) = \text{CO}(g) + \frac{1}{2}\text{O}_2(g)$ , a cell voltage is established between the electrodes with different oxygen partial pressure, according the Nernst equation, listed below as Equation 1.4.

$$E = -\frac{\Delta G^o}{2F} - \frac{RT}{2F} \ln \left( \frac{\left(\frac{P_{\text{CO}}}{P^o}\right) \left(\frac{P_{\text{O}_2}}{P^o}\right)^{\frac{1}{2}}}{\frac{P_{\text{CO}_2}}{P^o}} \right) = E^o - \frac{RT}{4F} \ln \left( \frac{\left(\frac{P_{\text{CO}}}{P^o}\right)^2 \left(\frac{P_{\text{O}_2}}{P^o}\right)}{\left(\frac{P_{\text{CO}_2}}{P^o}\right)^2} \right) \quad (\text{Equation 1.4})$$

In Equation 1.4, R is the universal gas constant, which is 8.314J K<sup>-1</sup> mol<sup>-1</sup>, T is the cell operation temperature in Kelvin, and F is Faraday constant 96485C mol<sup>-1</sup>. P<sub>CO</sub>, P<sub>O<sub>2</sub></sub> and

$P_{CO_2}$  stand for the partial pressure of CO, O<sub>2</sub> products and CO<sub>2</sub> reactant, respectively.  $\Delta G^o$  and  $E^o$  is the standard free energy and cell potential for CO<sub>2</sub> electrolysis reaction respectively. The Nernst equation explains the relationship between the ideal standard potential  $E^o$  and cell potential at other temperatures and partial pressures of products and reactants.

When the cell is operated at open circuit, in other words, no current is flowing through circuit, the cell reaction is in an equilibrium state and the reversible thermodynamic potential, known as Nernst potential or open circuit voltage (OCV), is obtained. When considering the cell reaction as an oxygen transfer process, the Nernst potential can be simplified as:

$$E_{ocv} = -\frac{RT}{nF} \ln \left( \frac{P_1}{P_2} \right) \quad (\text{Equation 1.5})$$

where  $P_1$  and  $P_2$  stand for the oxygen partial pressure at cathode and anode side of a SOEC. For an electrochemical cell, OCV indicates the minimum electric energy required for initiating and maintaining a chemical process in equilibrium state at a constant temperature and pressure. For  $CO_2(g) = CO(g) + \frac{1}{2}O_2(g)$  process, there is:

$$K = \frac{(P_{CO})(P_{O_2})^{\frac{1}{2}}}{(P_{CO_2})} \quad (\text{Equation 1.6})$$

where K is the reaction constant at the corresponding operation temperature. At a certain temperature and at OCV, when air is supplied to the anode chamber ( $P_2=0.21\text{atm}$ ) and CO<sub>2</sub>/CO mixture is provided to the cathode chamber, K can be indexed, and from Equation 1.6,  $P_1$  can be calculated and then OCV will be calculated according to Equation 1.5.

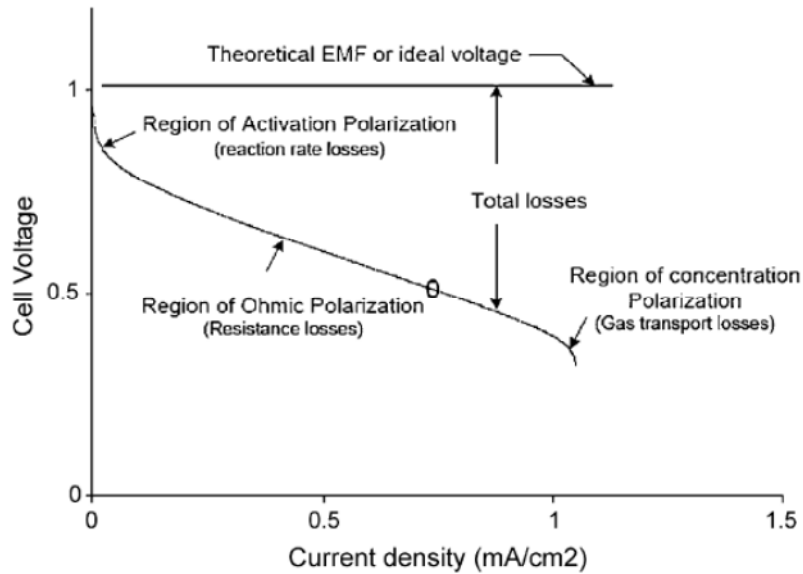


**Fig. 1.5** Schematic plot of I-V curve of a solid oxide cell showing different types of polarisations [32]

When there are current flows in a SOEC, the system becomes irreversible due to polarizations. Polarization is the degree that the actual cell voltage deviated from its thermodynamic open circuit voltage, which can be learned from a schematic plot of the polarization curve, namely, I-V curve, of a solid oxide cell, as displayed in Fig. 1.5. The I-V curve of a specific cell depends significantly on the composition and atmosphere of the cell as well as operational conditions.

On the I-V curve of a fuel cell, a linear region exists. This region suggests the ohmic polarization, which takes into account the IR drops from various components in the cell. In SOFC and SOEC, the ohmic loss in electrolyte is predominant, due to its ionic nature of electrolyte conductivity; therefore, the ohmic loss in electrolyte layer is dependent on the thickness of electrolyte, the electronic conductivity of electrolyte, and cell operation temperature. Because of this, it is important to make the dense, gas-tight electrolyte film as thin as possible to improve cell performance.

The non-linear region at small current on the I-V curve represents the activation polarization, while the region at high current reveals the concentration polarization. The activation polarization is defined as the external energy required overcoming the

activation energy barrier so that the electrode reaction can be maintained at an appreciable rate, and is related to the charge transfer processes taking place on the electrode during the electrochemical reactions [17].

The concentration polarization, occurs in the high current region on the I-V curve, is related with the limiting diffusion of gaseous species through the porous electrodes. It is defined as the external energy required maintaining constant supplies of certain amount of gases that are needed for the electrode reaction. This polarization loss can be reduced by optimizing the microstructure-related porosity, pore sizes, and thickness of electrode and supplying with sufficient fuels for the reduction reaction.

Due to the irreversible polarization losses, the actual cell voltage can also be written as:

$$E = E_o - IR - \eta_c - \eta_a \quad (\text{Equation 1.7})$$

Where I is the current flowing through cell, and  $\eta_c$ ,  $\eta_a$  are the total of activation and concentration polarization losses from cathode and anode respectively.

### **1.2.3 Characteristics of solid oxide electrolysis cells**

The one distinct characteristic of an SOEC is that it is an all solid-state device ideally suited for operation at elevated temperature range of 700-1000°C. This high temperature operation is advantageous for electrode kinetics. The elevated temperature will accelerate the electrode kinetics, which in turn will reduce the cell resistance and thereby, enhance the performance of SOEC. On the other hand, the high temperature operation requires less electrical energy as most part of the total energy demand is provided by thermal energy, for which high quality heat from a nuclear reactor, geothermal, etc. can be utilized to enhance electrolysis efficiency.

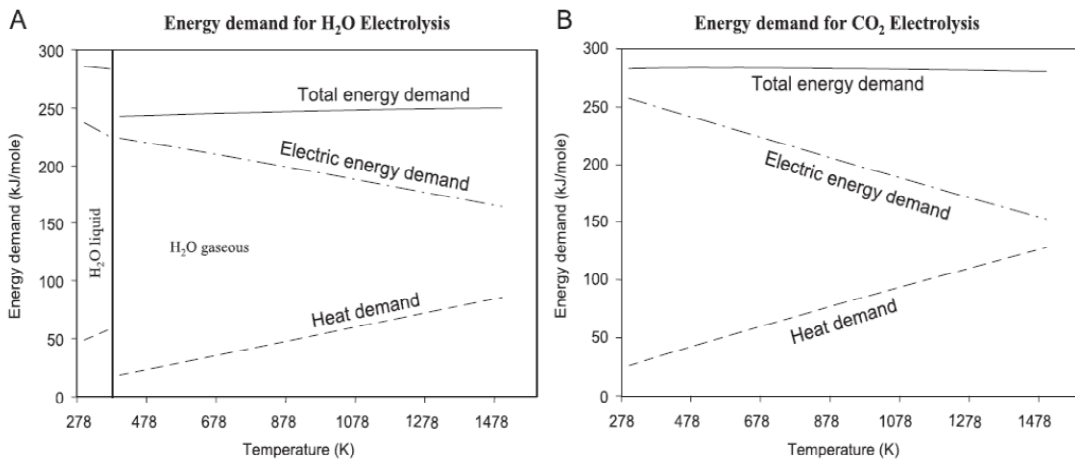


**Fig. 1.6** The energy demand with varying temperature for high temperature steam (A) and CO<sub>2</sub> (B) electrolysis via SOEC [33]

The energy demand as a function of operation temperature for high temperature steam and CO<sub>2</sub> electrolysis is illustrated in Fig. 1.6. The total energy demand ( $\Delta H$ ) for the high temperature SOEC is consisted of electric energy demand ( $\Delta G$ ) and thermal energy demand ( $T\Delta S$ ), as expressed in Equation 1.8.

$$\Delta H = \Delta G + T\Delta S \quad (\text{Equation 1.8})$$

With increasing temperature, the required electric energy for an SOEC decreases and the thermal energy demand increases, while the total energy demand is insensitive to the operation temperature. These trends are more pronounced for an SOEC used as CO<sub>2</sub> electrolyser.

At elevated temperatures, the electric energy demand is reduced in that the unavoidable joule heat from internal resistance is utilized in the steam/CO<sub>2</sub> splitting process occurring on SOEC. If the thermal energy needed is available from solar, geothermal, and nuclear origins or industrial waste heat, then the electricity consumption in steam/CO<sub>2</sub> electrolysis will be further decreased. For steam electrolysis, this characteristic is an advantage of high temperature SOEC over the traditional low temperature electrolyser which obviously needs higher electric energy input as indicated in Fig. 1.6(A) and by Equation 1.8 as well. Besides the possibility to utilize heat from

geothermal, solar and nuclear origins and waste heat from power plants, SOEC offers an opportunity to use the intermittent renewable source as energy input and to store the renewable energies in the form of chemicals which can be easily handled.

The electrochemical reactions taking place in SOEC are endothermic in nature, which requires additional heat to initiate and maintain these reactions. Meanwhile, as long as current flows through SOEC, joule heat ascribed to the internal resistance appears. Consequently, there is a balance between the heat required by the endothermic reaction and the joule heat released from the cell. Depending on the applied electric power to SOEC, there are possibly three operation modes: endothermal mode, exothermal mode, and thermoneutral mode.

At thermoneutral mode, the joule heat generated by internal cell resistance equals to the heat consumed by the endothermic reaction happened on SOEC cathode, and the electrical-to-chemical energy conversion efficiency is 100%. The cell voltage under this mode is consequently called the thermoneutral voltage. At thermoneutral voltage, there is no need to supply/remove extra heat to/from SOEC. Given this, the thermoneutral voltage can be obtained combining Equation 1.8 and Equation 1.9, as shown below in Equation 1.10.

$$\Delta G = -nEF \quad (\text{Equation 1.9})$$

$$E_{NEV} = -\frac{\Delta H}{nF} \quad (\text{Equation 1.10})$$

Where  $E_{NEV}$  stands for the thermoneutral voltage, while  $n$ ,  $F$ , and  $E$  have their usual meanings.

In endothermal mode, the cell voltage is smaller than thermoneutral voltage, Joule heat is less than the heat consumed by the SOEC cathode reaction, yielding electrical-to-chemical efficiency  $> 100\%$ . An extra heat source is required at this mode of operation. At the exothermal mode, the cell voltage is higher than thermoneutral voltage, and the joule heat exceeds the heat consumed in the steam/ $\text{CO}_2$  reduction reaction, thereby, a heating effect of SOEC happens. The electrical-to-chemical efficiency is  $< 100\%$  at this mode.

Other characteristics of SOEC include its good chemical flexibility, as the same basic cell is probably capable of doing the electrolysis of steam as well as  $\text{CO}_2$ . The same device can also be performed in steam-carbon dioxide co-electrolysis which produces  $\text{CO}$  and  $\text{H}_2$ , known as syngas, at one goal, and is also of great interest for carbon-neutral synthetic fuel production [6, 33, and 34]. With same amount of fuels being fed in both directions, SOEC displays lower performance than SOFC, due to the difficulty in mass transport of  $\text{H}_2\text{O}/\text{CO}_2$  which has higher molecular weight than  $\text{H}_2/\text{CO}$  [16, 33, and 35].

### 1.3 High temperature $\text{CO}_2$ electrolysis via SOEC

The high temperature  $\text{CO}_2$  electrolysis concept was initiated by NASA on  $\text{O}_2$  regeneration for Mars missions, most of these work was started from the early 1960s and continued to the 1980s [17-19]. This concerned  $\text{O}_2$  extraction from  $\text{CO}_2$  as propellant and life support needed for the return-trip in human exploitation of Mars missions based on the fact that the atmosphere on Mars contains over 95%  $\text{CO}_2$ .

In recent years, however, interest in this technology has shifted to the product on the cathode side of SOEC due to the issue of global warming caused by high level of  $\text{CO}_2$  emissions and of searching for sustainable energy sources. The  $\text{CO}$ , produced at an SOEC cathode, can be a feedstock for a variety of synthetic fuels production, including formic acid, methanol, hydrocarbons, etc. These fuels can be converted to liquid fuels as alternatives to the electrochemically produced  $\text{H}_2$ , not only because the relative ease in storage and transport of the former, but also because its compatibility with the existing fossil fuel infrastructure of the former, which will lead to a significant savings in building an entirely new  $\text{H}_2$  infrastructure. Further, the volumetric energy densities of synthetic fuels are higher than that of  $\text{H}_2$ ; as a result, fuel storage volume will be lower [6].

In spite of these positive traits, there are more efforts dedicated to high temperature steam electrolysis for  $\text{H}_2$  production, possibly because of the difficulty in achieving high performance in  $\text{CO}_2$  electrolysis due to the high thermal stability of  $\text{CO}_2$  and the higher diffusion resistance from  $\text{CO}_2/\text{CO}$  than from  $\text{H}_2\text{O}/\text{H}_2$ . Therefore, the development of SOEC used for high temperature  $\text{CO}_2$  electrolysis is still at an early stage, and only a few reports covered this field of research. Advances involved materials selection,

structural design, and optimization of operating conditions have to be made. Besides, understanding the mechanisms of CO<sub>2</sub> reduction reaction in SOECs is an objective that needs to be done.

#### **1.4 Materials for high temperature SOECs used for CO<sub>2</sub> electrolysis**

As SOEC and SOFC work in reversible directions and have a lot in common, the general requirements for materials selection for SOEC components are similar to those for SOFC. The current practice is to use the state-of-the-art SOFC component materials as the starting point of SOEC materials development. Identical with SOFC, SOEC is primarily composed of pore-free, ion-conducting electrolyte, porous and electrochemically active anode and cathode. The following parts will describe the general requirements of materials selection for these SOEC components, and the conventional employed materials in SOFC and steam electrolysis via SOEC applications. These materials can be the candidates in high temperature CO<sub>2</sub> electrolysis via SOEC.

##### **1.4.1 Electrolyte**

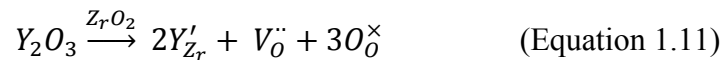
The ionic charge carrier electrolyte is one of the central components and largely determines the operation temperature of solid oxide cells. The electrolyte must be gas-tight and dense in order to separate the fuel and air compartments, must exhibit adequately high ionic conductivity allowing easy migration of oxygen anions, and must be chemical and mechanically compatible with neighbouring electrodes materials, sealants and interconnect material. It is undesirable to have electronic conduction in the electrolyte as that will cause short-circuit inside the cell and thus waste power. Moreover, it is critical for a satisfactory electrolyte maintaining its properties over a wide range of oxygen partial pressure ( $P_{O_2}$ ), as the  $P_{O_2}$  may vary from  $\sim 1$  atm at SOFC cathode side to  $\sim 10^{-20}$  atm or even lower at SOFC anode side [23].

To date, the frequently used electrolyte materials in solid oxide cells include stabilized zirconia, doped ceria and strontium/magnesium doped lanthanum gallate [24, 36].

##### ***Stabilized zirconia***

8 vol% yttria stabilized zirconia (YSZ) is the most common electrolyte material owing to its high purely ionic conductivity, excellent stability in oxidizing and reducing atmospheres, high quality raw material availability and fairly good mechanical strength under high temperature SOFCs working conditions.

The introduction of  $Y_2O_3$  helps to stabilize the high temperature cubic fluorite structure of  $ZrO_2$  and to generate extra oxygen vacancies by charge compensation (see Equation 1.11).



The ionic conductivity of YSZ rises up to about 8 mol% yttria doping, when the cubic phase becomes stable, and then reduces with higher levels of yttria substitution due to defects association [36, 37].

The most important disadvantage of YSZ against commercial utilization is its low ionic conductivity at lower temperature, which induces significant ohmic loss in the solid oxide cells. A promising though less widely used dopant for zirconia is Scandia. Scandium stabilized zirconia (ScSZ) exhibits higher conductivity than YSZ, with the ionic conductivity of the former roughly three fold of the latter at 1000°C [38]. The high conductivity of ScSZ enables the intermediate temperature operation. Scandium and ceria co-doped zirconia was reported to be promising for steam electrolysis via SOEC at 700°C [39]. Nevertheless, the availability and high price of scandium obstructs extensive interest in this type of solid solution.

### ***Doped ceria ceramic***

Ceria based solid electrolytes also have the fluorite structure, and as zirconia, doping is a useful strategy to reinforce the oxide ion transport property. The considered dopants include yttrium, lanthanum, gadolinium and samarium, of which, gadolinium (Gd) and samarium (Sm) doped ceria with a formula of  $M_xCe_{1-x}O_{2-\delta}$  ( $M = Gd$  or  $Sm$ ), denoted as GDC and SDC respectively herein, displays the best conductivities (usually at  $x = 0.1-0.2$ ) resulting from their similar sizes with respect to the host cerium cation and are of wide interest as alternatives to YSZ electrolyte in SOFC [36, 38, 40, 41] and SOEC [42].

Compared with YSZ, GDC and SDC offer significantly higher ionic conductivity, particularly at lower temperature (600-800°C). Besides, GDC is chemically compatible with the state of the art electrode materials.

The major problem with doped ceria originates from the easy reducibility of  $\text{Ce}^{4+}$  to  $\text{Ce}^{3+}$  in reducing environment, typical for SOFC anode conditions. This means that the doped ceria becomes a mixed ionic and electronic conductor at low  $P_{\text{O}_2}$ , which is detrimental for electrolyte because the induced electronic conduction will result in lower open circuit voltage and decreased fuel conversion efficiency.

Meanwhile, the reduction of  $\text{Ce}^{4+}$  poses a threat to the mechanical integrity of cells, as there is volume expansion in doped ceria accompanying  $\text{Ce}^{4+}$  reduction in low  $P_{\text{O}_2}$ , which obviously is harmful for long-term operation.

As a result, it is of interest to utilize doped ceria as electrode components rather electrolyte. Undoubtedly, the high oxygen ion mobility and electronic paths in doped ceria is favourable for charge transfer processes in electrode reactions.

### ***Strontium/magnesium-doped lanthanum gallate***

Perovskite-type  $\text{LaGaO}_3$  can be doped with strontium and magnesium, giving  $\text{La}_{1-x}\text{Sr}_x\text{Ga}_{1-y}\text{Mg}_y\text{O}_3$  (LSGM herein), which is an alternative electrolyte material with higher oxygen-ion conductivity than that of YSZ, especially at lowered temperatures. Therefore, LSGM materials have attracted extensive interest in applications of intermediate temperature solid oxide cells [36, 38, 43, 44].

The conductivity of LSGM is largely dependent on the dopant levels. The highest conductivity was achieved with  $\text{La}_{0.85}\text{Sr}_{0.15}\text{Ga}_{0.8}\text{Mg}_{0.2}\text{O}_{3-\delta}$  or  $\text{La}_{0.8}\text{Sr}_{0.2}\text{Ga}_{0.85}\text{Mg}_{0.15}\text{O}_{3-\delta}$ , which was 0.15 S/cm at 800°C [45]. This value is close to the ionic conductivity of YSZ at 1000°C.

Though possessing very high conductivity, LSGM material is restricted by several challenges for usage as electrolyte for solid oxide cells, including the development of cost-effective processes for fabricating the desired single-phase microstructures and of alternative anode material as LSGM is incompatible with NiO [44].

To summarize, doped ceria and doped lanthanum gallate are regarded as the two widely used alternatives of YSZ electrolyte in SOFCs, particularly those working in intermediate temperature range. As mentioned previously, the SOEC development is current at an early stage, with focus on high temperature operation, for which YSZ turns to be the best option for electrolyte material. The thin film fabrication techniques provide a means to reduce the dominant ohmic loss from YSZ electrolyte [46, 47]. By adopting an anode supported design, the performance of SOFCs with YSZ as electrolyte was markedly enhanced.

Nonetheless, the trend of lowering operation temperature will be necessary in the future, in the purpose to broaden materials selection and to debate costs, just as what happened in SOFCs. Pioneered research in this aspect was carried out by Ishihara et.al using LSGM electrolyte for steam electrolysis through intermediate temperature SOECs [48, 49].

### 1.4.2 Cathode

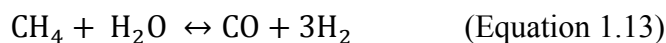
The rationale for SOEC cathode material and structure is that they should have sufficient electronic and ionic conductivities for fast charge transfer in cathode reaction, that they should be porous enough to facilitate gas diffusions to/from electrochemical active sites through bulk cathode but not too porous to maintain the continuous paths for electron and ion conduction, and that most importantly, they should exhibit high electrochemical and catalytic properties towards desirable SOEC cathode reactions. Other requirements that are crucial for selection of SOEC cathode materials include chemical and mechanical (thermal expansion behaviour) compatibility with adjacent SOEC electrolyte and interconnect components, decent thermal cycling capability, and desirable stability over long-term operation. Last but not least, they should be easily fabricated with cost-effective approaches. Currently, materials developed in SOFC anode cover Ni-cermet, perovskite structured  $(\text{La}, \text{Sr})(\text{Cr}_{0.5}\text{Mn}_{0.5})\text{O}_{3\pm\delta}$  (denoted as LSCM herein) material, doped ceria, and  $(\text{La}_{1-x}\text{Sr}_x)\text{TiO}_{3\pm\delta}$  (abbreviated as LST henceforth). These materials have been applied in steam electrolysis and can be candidates of SOEC cathode for  $\text{CO}_2$  electrochemical reduction.

### 1.4.2.1 Ni-cermet cathodes

The state-of-the-art anode materials in SOFC applications are Ni-based cermets, in which Ni provides electronic conductivity and catalytic activity and YSZ acts as the ionic conductor and a support for Ni distribution to prevent Ni sintering. This set of materials possesses high conductivity, good compatibility with electrolyte and excellent catalytic properties towards oxidation of fuels. Based on these positive characteristics, Ni-cermets have also been applied in high temperature steam electrolysis and CO<sub>2</sub> electrolysis by SOECs [10, 25-31]. However, Ni-cermets suffer from several limitations.

According to knowledge has obtained in SOFC, the choice of fuels is restricted to H<sub>2</sub>-containing fuels and to high steam to carbon (S/C) ratio reformates on Ni-cermets to avoid coke deposition in hydrocarbon-fuelled SOFC. This originates from the fact that Ni is also a superior catalyst for hydrocarbon cracking and CO disproportionation reaction (also known as the Boudouard reaction). The occurrence of coke will block pores and electrochemically active sites, and hence leads to Ni catalyst deactivation and eventually performance degradation. It has been reported that a Ni-YSZ anode that was able to obtain a power density of 1.8W/cm<sup>2</sup> in H<sub>2</sub>/H<sub>2</sub>O atmosphere displayed less than 0.3W/cm<sup>2</sup> in 44%CO-56%CO<sub>2</sub> mixture at 800°C [50].

Ni-cermets exhibit slow activity towards direct CO and hydrocarbon oxidation, and limiting current density showed up for the cell working with CO/hydrocarbon fuels, as results of the higher molecular weight of CO/hydrocarbon than H<sub>2</sub> which led to difficulty in mass transportation and most significantly of the poor carbon tolerance [50-52]. This poor tolerance necessitates the introduction of excess steam to realize a reforming route as first step. In this case, the oxidation takes place primarily through water gas shift reaction (Equation 1.12), steam reforming reaction (Equation 1.13) and H<sub>2</sub> oxidation reaction.



The presence of steam is also helpful to remove deposited coke [53], however, the introduction of surplus steam for reformates on Ni-cermets increases the complexity and costs of SOFC design in addition to a fuel diluting effect.

The poor redox stability of Ni-cermets limited its practical application in SOFCs, especially the ones for long-term operation. Formation of NiO would happen during start-up and shut-down cycles, causing volume instability and interfacial deteriorations between anode and electrolyte phases. Further, Ni tends to agglomerate during prolonged operation, which results in decreases in TPB areas and thus performance degradation.

Concerning the limitations of Ni-cermets in SOFC, the stability of Ni-cermets is of great concern as SOEC cathode working in H<sub>2</sub>O-H<sub>2</sub> and CO<sub>2</sub>-CO mixture, especially the latter. The electrolyser operation firstly necessitates the addition of sufficient protective H<sub>2</sub> or CO gas to ensure reducing surroundings over all parts of Ni-cermets electrode, diluting fuels and decreasing efficiencies. Highly volatile Ni carbonyls are readily to form in CO rich mixture at low temperature [53, 54], leading to catalyst losses. In the meantime, Boudouard reaction (expressed in Equation 1.14), which yield solid carbon, is favourable at high CO/CO<sub>2</sub> ratios at low temperatures. These make it crucial to engineer the fuel compositions to avoid these detrimental effects on the performance of Ni-cermets as a SOEC cathode.



#### 1.4.2.2 LSCM perovskite cathodes

A unit cell of the perovskite lattice is shown in Fig. 1.7. Perovskite related materials are diverse series whose formula is ABO<sub>3</sub>, doping and partial substitution can be conducted on either A site or B site or both to tune the material properties, including redox stability, conductivity, catalytic activity, etc., to specific applications.

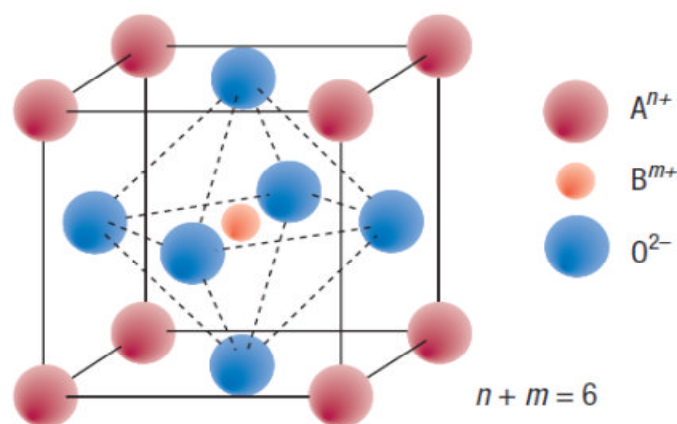


**Fig. 1.7** Unit cell of the  $ABO_3$  perovskite structure

$(La_{0.75}Sr_{0.25})_{1-x}Cr_{0.5}Mn_{0.5}O_{3-\delta}$  ( $0 \leq x \leq 0.1$ ) perovskite-type material was found by Tao and Irvine as alternative anode in SOFC [55]. The doping of Mn at a level higher than percolation limit (e.g., >33%) into the B-site of  $(La,Sr)CrO_3$  perovskite yielded a dramatically improved material with the two B-site elements acting in a complementary fashion.

LSCM forms a single-phase complex perovskite structure at high temperature firing (1100-1400°C), and is chemically compatible with YSZ to at least 1300°C. LSCM is a mixed ionic and electronic conductor (MIEC), and the total conductivity of the one in the formula of  $La_{0.75}Sr_{0.25}Cr_{0.5}Mn_{0.5}O_{3-\delta}$  at 900°C is 38.6 S/cm in air and 1.49 S/cm in 5% $H_2$  ( $P_{O_2} \approx 10^{-21}$  atm) [56]. Most importantly, LSCM possesses good redox stability and resistance to sulphur poisoning and carbon depositions [57, 58], which makes LSCM versatile in high temperature SOFC running with a wide variety of fuels, including hydrocarbons. The redox stability and flexibility in choice of fuels from LSCM overcomes the major two limitations of the Ni-cermets as SOFC anode.

It has been demonstrated by several research groups that LSCM based anode performed fairly well for the oxidation of weakly humidified (3%) methane, but its catalytic property needs to be enhanced to compete with that of Ni-cermets [55-57, 59, 60]. Given that the oxidation of methane could take place by internal reforming followed by oxidation, or direct full oxidation or partial oxidation, catalysis measurements regarding

the methane oxidation mechanism were conducted in a fixed-bed reactor, with an approximation to the anodic conditions in SOFC [61]. A dominantly direct full oxidation route was detected with insignificant selectivity of CO and H<sub>2</sub> on LSCM catalyst at high temperature.

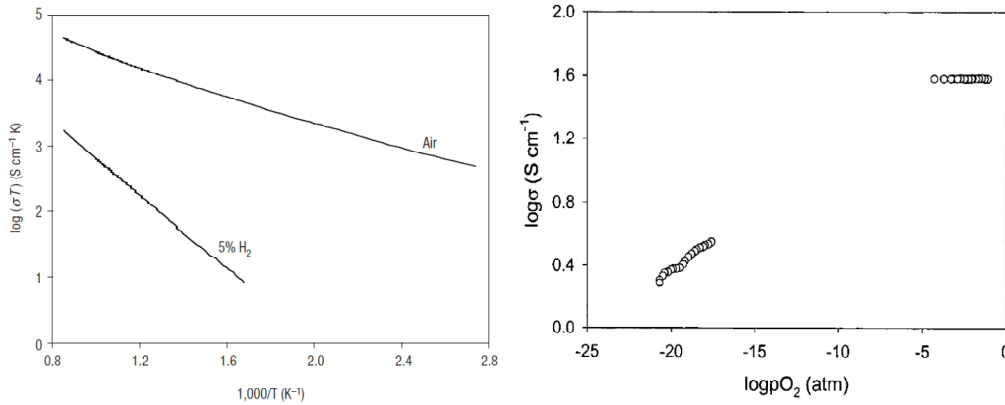
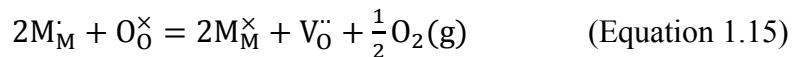


**Fig. 1.8** The total conductivity of LSCM as a function of temperature (a) and oxygen partial pressure ( $P_{O_2}$ ) in different atmospheres [56]

Generally speaking, an electronic conductivity of at least 1 S/cm is required to minimize the electrode ohmic loss. In LSCM, the substitution of Sr into the A-site results in the transition of Cr<sup>3+</sup>/Mn<sup>3+</sup> to Cr<sup>4+</sup>/Mn<sup>4+</sup> as charge compensation. This transition can lead to increase in small polaron concentration and as a result, high electronic conductivity. Being a p-type conductor, the concentration of the charge carriers in LSCM reduces at low  $P_{O_2}$  based on the formation of oxygen vacancies, expressed in Equation 1.15.



Where M= Cr, Mn for LSCM. Therefore, as illustrated in Fig. 1.8, the conductivity of LSCM decreases remarkably in reducing atmosphere whereas it stays constant in oxidizing environment. This suggests that LSCM electrode may undergo inadequate electronic conductivity for current collection in reducing atmosphere, at the absence of an additional component with high electronic conductivity.

Incorporating a doped ceria interfacial layer between LSCM and YSZ electrolyte layers promoted the anode oxidizing activity [56]. And similarly, introducing finely dispersed

GDC nanoparticles onto LSCM by aqueous impregnation effectively improved the electrochemical activity of LSCM for methane oxidation, resulting from promoted current collection and oxide ion transport [62]. The enhancement in electrochemical properties of LSCM towards methane oxidation can also be achieved by adding dopant levels of metal catalyst, such as Pt, Ni, and Pd, which are believed to present good catalytic properties for oxidation reaction [63].

An investigation of Ni-free LSCM/YSZ composite was performed as SOEC cathode for high temperature steam electrolysis by Yang and Irvine. A sigmoidal shaped polarization curve was observed for steam electrolysis and it was found that LSCM material performed better over traditional Ni/YSZ cermets, especially in the fuels without protective H<sub>2</sub> gas [64]. Similar, it is anticipated that LSCM based material can also be considered an alternative SOEC cathode for high temperature CO<sub>2</sub> electrolysis. The ability of LSCM based cathode for CO<sub>2</sub> splitting through SOEC has been proven [65]. However, the report concerning employment of this material in CO<sub>2</sub> electrolysis is still scarce.

### 1.4.2.3 Doped ceria cathodes

As mentioned in section 1.4.1, GDC and SDC exhibit mixed conductivities in low P<sub>O<sub>2</sub></sub>, which is harmful as electrolyte but favourable as electrode materials, thus are considered as potential alternatives to Ni-cermets in the fields of SOFC and SOEC. The high ionic conductivity of GDC/SDC is especially profitable to the oxidation reaction in SOFC anode [66, 67]. What is more, doped ceria have reasonably good catalytic activity towards various hydrocarbon oxidations without the need of adding a reformer or excess steam to avoid the formation of graphite which is highly possible on Ni catalyst. This allows SOFC to work directly with CO and more readily available hydrocarbon fuels.

Barnett et al introduced 0.5µm thin (Y<sub>2</sub>O<sub>3</sub>)<sub>0.15</sub>(CeO<sub>2</sub>)<sub>0.85</sub> (YDC) porous films between YSZ electrolyte and NiO/YSZ anode as well as YSZ electrolyte and lanthanum manganate/YSZ cathode. Such fuel cell design gave power densities up to 0.37 Wcm<sup>-2</sup> at 650°C for methane oxidation with ambient humidity, without the presence of carbon deposition [68]. Gorte et al. replaced Ni-YSZ anode with a Cu-ceria anode for

electrochemical oxidation of various hydrocarbons using SOFC, to suppress carbon formation. It was demonstrated that the final products of oxidation contained only CO<sub>2</sub> and water and that reasonable power densities could be obtained [69, 70]. In Cu-ceria composite, Cu acted as current collector while ceria played an important role in catalyzing the oxidation reactions. Adding dopant level of metal catalyst, such as, Pd, is advantageous to enhance the electro-catalytic properties of the ceria based electrode [66].

In a high temperature steam electrolysis study, the addition of GDC into (La, Sr)MnO<sub>3</sub> (LSM) anode by wet impregnation tremendously promoted the electro-catalytic activities for the oxygen oxidation reaction [71]. It also prevented delamination of LSM anode from YSZ electrolyte. Moreover, CO<sub>2</sub> electrolysis was conducted on pure Gd<sub>0.4</sub>Ce<sub>0.6</sub>O<sub>2</sub> cathode SOEC by Green et al, and it was reported that the vacancy diffusion coefficient and surface exchange rate of GDC electrode increased with decreasing P<sub>O<sub>2</sub></sub>, which were beneficial for the CO<sub>2</sub> electrochemical reduction processes occurring on SOEC cathode [72]. This indicated the potential utilization of GDC as SOEC cathode material for high temperature CO<sub>2</sub> electrolysis.

Current concerns with practical utilization of doped ceria in solid oxide cells are associated with the reactivity of doped ceria with the state of the art YSZ electrolyte and the lattice expansion/contraction of ceria resulting from transitions between Ce<sup>4+</sup> and Ce<sup>3+</sup> in reducing/oxidizing environment. The former will introduce a detrimental inter-diffusion layer with high resistivity for ion transfer between YSZ electrolyte and doped ceria electrode [73, 74]; whereas the latter poses problems for sustainable cells in that it is possible to lead to cracks at the electrode-electrolyte interface and subsequent delamination of the electrode layer from electrolyte. Caution in fabrication method and material compositions options should be taken to avoid the above mentioned concerns [66, 70, and 75].

#### 1.4.2.4 (La<sub>1-x</sub> Sr<sub>x</sub>)TiO<sub>3</sub> perovskite cathodes

La-doped strontium titanates (LST), also showing the ABO<sub>3</sub> perovskite structure, have been investigated as alternative anode materials in SOFCs [76, 77], considering its wide range of defect chemistry that can be controlled and tuned favourable for SOFC anode

property by doping and its resistance to sulphur, which is one of the limitations of Ni-cermets anode using hydrocarbon fuels .

LST exhibits n-type semiconducting behaviour in reducing environment, giving good electronic conductivity due to the occurrence of the  $Ti^{4+}/Ti^{3+}$  redox couple, which is suitable for the reducing atmosphere encountered in cathode of SOECs. Tsekouras and Irvine have employed LST /YSZ composite as SOEC cathode for steam electrolysis and demonstrated the significant role of defect chemistry in LST based electrode on its properties for high temperature steam splitting processes [78]. The steam electrolysis performance was observed to be largely independent of the presence or absence of  $H_2$  in cathode inlet, indicating the superior redox stability of LST materials over the Ni-based cermets cathode.

Following on their work of utilising LST based cathode for high temperature steam electrolysis, Tsekouras et al. investigated B-site doped  $La_{0.4}Sr_{0.4}M_x^{n+}Ti_{1-x}O_{3-\gamma-\delta}$  (where  $M = Fe^{3+}$  or  $Ni^{2+}$ ,  $x = 0.06$ ,  $\gamma = (4-n)x/2$  = inherent oxygen deficiency, and  $\delta$  = oxygen deficiency introduced upon reduction) perovskite cathode materials, in an effort to introduce metallic nanoparticles by B-site exsolution driven by A-site deficiency under reducing SOEC cathode operating conditions [79]. The exsolved electro-catalytically active Fe or Ni nanoparticles on the surface of LST cathode helped to dramatically lower the activation barrier to steam electrolysis compared to LST without B-site doping.

### 1.4.3 Anode

The ideal SOEC anode material should readily recombine the oxide anions to form molecular oxygen, have sufficiently high electronic and ionic conductivities, and have good chemical and thermal expansion compatibility with the neighbouring electrolyte, namely, YSZ. Optimized microstructure for ease of gaseous diffusion as well as for electrons and oxygen ions conduction is also critical for highly performed SOEC anode.

The most frequently used air electrode in SOFCs is (La, Sr)  $MnO_3$  (LSM) perovskite-type material, ascribed to its high electronic conductivity, good catalytic properties at elevated operating temperatures, excellent stability and closely-matched thermal expansion coefficient with YSZ electrolyte. Whereas the ionic conductivity of LSM is

very limited, the combination of YSZ to form LSM/YSZ composite is advantageous for enhancing oxygen ions diffusion and consequently anode performance, as well as for improving anode/electrolyte interfacial attachment. As so, LSM/YSZ has been extensively applied as SOEC anode, and there are a number of reports on utilising LSM/YSZ anode in SOEC used for steam electrolysis [26-29, 31, 34].

Though efforts have been set out to find alternative SOEC anodes that will perform better due to the fact that air electrode gave higher losses in electrolysis mode than in fuel cell [34], LSM is still considered the best choice for high temperature electrolysis operation currently, regarding to its ease in fabrication, excellent long-term stability and relatively good compatibility with the commonly used YSZ electrolyte [30, 35, 80].

It is generally acknowledged that polarization activation of LSM based cathode occurs with applying current passage in SOFC, leading to increased oxygen vacancies in LSM lattice and significant enhance in cathode performance [81-83]. Similarly, a low anodic polarization current treatment was reported to improve the electrochemical properties of a freshly prepared LSM/YSZ electrode or a cathodically polarized one, though deactivation happened quickly when switching back to OCV or to fuel cell mode [31, 71, and 80]. However, high anodic polarization current resulted in separation of the LSM anode from YSZ electrolyte. These phenomena were proposed to be related to microstructural changes in LSM resulting from polarization treatment and oxygen generation/consumption with LSM reduction/oxidation [31, 71]. The mechanisms for activation/deactivation of LSM upon a low level of current polarization and for delamination upon high level of current polarization need to be fully understood.

### **1.5 Triple phase boundaries (TPBs)**

The concept of triple phase boundaries (TPBs) is of great importance in determining the electrochemical performance of electrodes in solid oxide cells. The TPB is defined where the gas phase, electrode phase (or electrons) and electrolyte phase (oxide ions) meet and react, and the electrochemically active sites for electrode reaction are mainly located in the TPBs area.

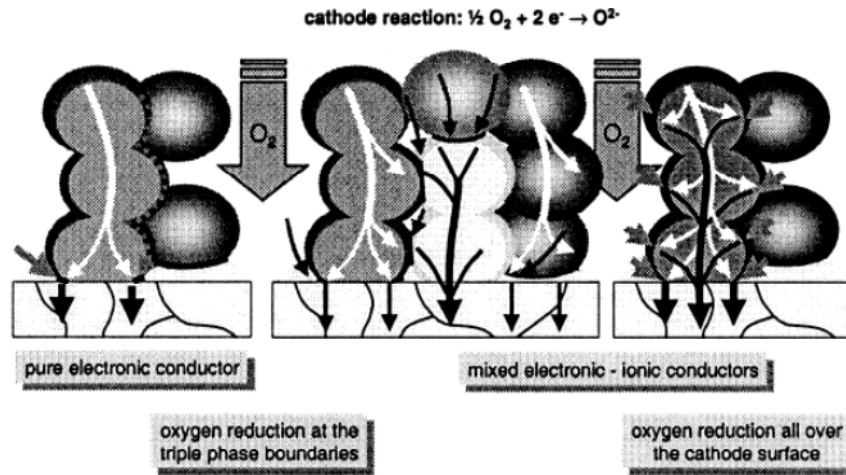


**Fig. 1.9** Oxygen reduction at a pure electronic, composite and mixed ionic electronic conducting cathode in SOFCs [84]

A schematic of oxygen conduction at a pure electronic cathode, a composite cathode, and a mixed ionic and electronic conductor (MIEC) cathode in SOFCs is illustrated in Fig. 1.9. With a pure electronic conduction cathode, the TPBs area is restricted to the planar cathode/electrolyte interface; with a composite cathode that incorporates an ionic conducting phase, the TPBs area is extended to depth of cathode; and with a MIEC cathode, the TPBs area is further extended to volume cathode, so that several possible diffusion pathways exist [85]. The enlargement in TPBs area is undoubtedly beneficial to accelerate the electrode reaction processes and to reinforce electrode performance.

As a result, the TPB area offers important implications for optimization in microstructure and material properties for both cathode and anode in solid oxide cells. In general, oxide electrodes that exhibit mixed conductivities are of particular interest in solid oxide cells.

## 1.6 Aims of study

High temperature SOECs offer a promising means to produce  $\text{H}_2$  and synthetic fuels with the utilization of carbon neutral renewable energies, which helps to address the global issues of reducing  $\text{CO}_2$  emission and production of sustainable energy.

In this study, we will set out to find a high performance, efficient cathode material for high temperature SOECs as an alternative to Ni-YSZ cermets, with focus on CO<sub>2</sub> electrolysis performance and behaviour since it has been scarcely reported. Cathode microstructure modification will be conducted in order to improve cathode performance for the electrochemical reduction of CO<sub>2</sub>, by adopting different cathode fabrication procedures. The mechanisms concerning the CO<sub>2</sub> electrochemical dissociation will be investigated with the aid of impedance spectroscopy, and factors including fuel gas composition, operation temperature, and presence of extra metal catalyst will be taken into account for their impacts on the CO<sub>2</sub> splitting process via SOECs. Faradaic efficiency of CO<sub>2</sub> electrolysis as well as CO formation rate on different cathode SOECs will be assessed.

High temperature steam electrolysis will be studied with different level of steam supply using the identical cathode SOEC device for CO<sub>2</sub> electrolysis, to figure out the reasons underneath the S-shaped polarization curve observed by previous researchers [64]. Finally, the highly performed cathode from CO<sub>2</sub> electrolysis will be applied to steam-carbon dioxide co-electrolysis. Performances from the same SOEC device working for steam electrolysis, CO<sub>2</sub> electrolysis and co-electrolysis will be characterized and compared.

### References

1. S. Solomon, D. Qin, M. Manning, Z. Chen, M. Marquis, K. B. Averyt, M. Tignor and H. L. Miller, Contribution of Work Group I to the Fourth Assessment of the Intergovernmental Panel on Climate Change (IPCC), 2007: The Physical Science Basis: Summary for Policymakers.  
[http://www.ipcc.ch/publications\\_and\\_data/ar4/wg1/en/spmssp-human.html](http://www.ipcc.ch/publications_and_data/ar4/wg1/en/spmssp-human.html)
2. O. Edenhofer, R. P. Madruga, Y. Sokona, K. Seyboth, P. Matschoss, S. Kadner, T. Zwickel, P. Eickemeier, G. Hansen, S. Schlömer, C. Stechow, *Renewable Energy Sources and Climate Change Mitigation: Special Report of the Intergovernmental Panel on Climate Change*, p.10, Cambridge University Press, New York (2012)

3. B. Metz, O. Davidson, H. Coninck, M. Loos, L. Meyer, *IPCC Special Report on Carbon Dioxide Capture and Storage*, Cambridge University Press, New York (2005)
4. F. S. Zeman and D. W. Keith, *Phil. Trans. R. Soc. A*, **366**, 3901 (2008)
5. D. T. Whipple and P. J. A. Kenis, *J. Phys. Chem. Lett.*, **1**, 3451 (2010)
6. Z. Zhan, W. Kobsiriphat, J. R. Wilson, M. Pillai, I. Kim, and S. A. Barnett, *Energy Fuels*, **23**, 3089 (2009)
7. H. Yano, F. Shirai, M. Nakayama, K. Ogura, *J. Electroanal. Chem.*, **533**, 113 (2002)
8. K. Hara, A. Kudo, T. Sakata, *J. Electroanal. Chem.*, **391**, 141-147 (1995)
9. T. Yamamoto, D. A. Tryk, A. Fujishima, H. Ohata, *Electrochem. Acta*, **47**, 3327 (2002)
10. S. D. Ebbesen, M. Mogensen, *J. Power Sources*, **193**, 349 (2009)
11. C. Graves, S. D. Ebbesen, M. Mogensen, K. S. Lackner, *Renew. Sust. Energy Rev.*, **15**, 1 (2011)
12. G. Centi, S. Perathoner, *Catal. Today*, **148**, 191 (2009)
13. N. R. Tacconi, W. Chanmanee, B. H. Dennis, F. M. MacDonnell, D. J. Boston, and K. Rajeshwar, *Electrochem. Solid-State Lett.*, **15** (1), B5 (2012)
14. D. W. DeWulf, T. Jin, and A. J. Bard, *J. Electrochem. Soc.*, **136** (6), 1686 (1989)
15. Y. Hori, H. Wakebe, T. Tsukamoto and O. Koga, *Electrochimica Acta*, **39** (11/12) 1833 (1994)
16. A. O. Isenberg, *Solid State Ionics*, **3/4**, 431 (1981)
17. K. R. Sridhar, B. T. Vaniman, *Solid State Ionics*, **93**, 321 (1997)
18. G. Tao, K. R. Sridhar, C. L. Chan, *Solid State Ionics*, **175**, 615 (2004)
19. G. Tao, K. R. Sridhar, C. L. Chan, *Solid State Ionics*, **175**, 621 (2004)
20. W. Doenitz, R. Schmidberger, E. Steinheil, *Int. J. Hydrogen Energy*, **5** (1), 55 (1980)
21. W. Dönitz, G. Dietrich, E. Erdle, R. Streicher, *Int. J. Hydrogen Energy*, **13** (5), 283 (1988)
22. J. D. Holladay, J. Hu, D. L. King, Y. Wang, *Catal. Today*, **139**, 244 (2009)
23. C. Sun, U. Stimming, *J. Power Sources*, **171**, 247 (2007)
24. M. Ni, M. Leung, D. Leung, *Int. J. Hydrogen Energy*, **33**, 2337 (2008)
25. A. Hauch, S. D. Ebbesen, S. H. Jensen and M. Mogensen, *J. Mater. Chem.*, **18**, 2331 (2008)

26. A. Brisse, J. Schefold, M. Zahid, *Int. J. Hydrogen Energy*, **33**, 5375 (2008)
27. A. Hauch, S. H. Jensen, S. Ramousse, M. Mogensen, *J. Electrochem. Soc.*, **153**, A1741 (2006)
28. A. Hauch, S. Ebbesen, S. Jensen, M. Mogensen, *J. Electrochem. Soc.*, **155**, B1184 (2008)
29. C. Yang, A. Coffin, F. Chen, *Int. J. Hydrogen Energy*, **35**, 3221 (2006)
30. P. Kim-Lohsoon, D. J. L. Brett, N. Laosiripojana, Y-M. Kim, J-M. Bae, *Int. J. Hydrogen Energy*, **35**, 3958 (2010)
31. M. Liang, B. Yu, M. Wen, J. Chen, J. Xu, Y. Zhai, *J. Power Sources*, **190**, 341 (2009)
32. A. Kirubakaran, S. Jain, R. K. Nema, *Renew. Sust. Energy Rev.*, **13**, 2430 (2009)
33. S. H. Jensen, P. H. Larsen, M. Mogensen, *Int. J. Hydrogen Energy*, **32**, 3253 (2007)
34. C. Graves, S. D. Ebbesen, M. Mogensen, *Solid State Ionics*, **192** (1), 398 (2010)
35. O. A. Marina, L. R. Pederson, M. C. Williams, G. W. Coffey, K. D. Meinhardt, C. D. Nguyen, and E. C. Thomsen, *J. Electrochem. Soc.*, **154** (5), B452 (2007)
36. J. W. Fergus, *J. Power Sources*, **162**, 30 (2006)
37. S. P. S. Badwal, *Solid State Ionics*, **143**, 39 (2001)
38. F. M. L. Fifeiredo and F. M. B. Marques, *WIREs Energy Environ.*, **2**, 52 (2013)
39. M. A. Laguna-Bercero, S. J. Skinner, J. A. Kilner, *J. Power Sources*, **192**, 126 (2009)
40. M. Mogensen, N. M. Sammes, G. A. Tompsett, *Solid State Ionics*, **129**, 63 (2000)
41. V. V. Kharton, F. M. Figueiredo, L. Navarro, E. N. Naumovich, A. A. Yaremchenko, A. P. Viskup, A. Carneiro, F. M. B. Marques, J. R. Frade, *J. Mater. Sci.*, **36**, 1105 (2001)
42. B. Zhu, I. Albinsson, C. Andersson, K. Borsand, M. Nilsson, B. Mellander, *Electrochem. Commun.*, **8**, 495 (2006)
43. M. Feng, J. B. Goodenough, K. Huang, C. Milliken, *J. Power Sources*, **63**, 47 (1996)
44. S. Elangovan and J. J. Hartvigsen, L. J. Frost, *Int. J. Appl. Ceram. Technol.*, **4** (2), 109 (2007)
45. N. Liu, M. Shi, C. Wang, Y. P. Yuan, P. Majewski, F. Aldinger, *J. Mater. Sci.*, **41**, 4205 (2006)
46. S. de Souza, S. J. Visco, L. C. De Jonghe, *Solid State Ionics*, **98**, 57 (1997)

47. P. Charpentier, P. Fragnaud, D. M. Schleich, E. Gehain, *Solid State Ionics*, **135**, 373 (2000)
48. T. Ishihara and T. Kanno, *ISI J Int.*, **50** (9), 1291 (2010)
49. T. Ishihara, N. Jirathiwathanakul, and H. Zhong, *Energy Environ. Sci.*, **3**, 665 (2010)
50. Y. Jiang and A. Virkar, *J. Electrochem. Soc.*, **150**, A942 (2003)
51. Y. Matsuzaki and I. Yasuda, *J. Electrochem. Soc.*, **147** (5), 1630 (2000)
52. J. Koh, Y. Yoo, J. Park, H. C. Lim, *Solid State Ionics*, **49**, 157 (2002)
53. P. Holtappels, L. G. J. de Haart, U. Stimming, I. C. Vinke, and M. Mogensen, *J. Appl. Electrochem.*, **29**, 561 (1999)
54. L. Mond, C. Langer, and F. Quincke, *J. Chem. Soc., Trans.*, **57**, 749 (1890)
55. S. Tao and J. T. S. Irvine, *Nat. Mater.*, **2**, 320 (2003)
56. S. Tao and J. T. S. Irvine, *J. Electrochem. Soc.*, **151** (2), A252 (2004)
57. D. M. Bastidas, S. Tao and J. T. S. Irvine, *J. Mater. Chem.*, **16**, 1603 (2006)
58. X. J. Chen, Q. L. Liu, S. H. Chan, N. P. Brandon, and K. A. Khor, *J. Electrochem. Soc.*, **154** (11), B1206 (2007)
59. G. Kim, G. Corre, J. T. S. Irvine, J. M. Vohs, and R. T. Gorte, *Electrochem. Solid-State Lett.*, **11** (2), B16 (2008)
60. S. P. Jiang, X. J. Chen, S. H. Chan, J. T. Kwok, K. A. Khor, *Solid State Ionics*, **177**, 149 (2006)
61. S. Tao, J. T. S. Irvine, and S. M. Plint, *J. Phys. Chem. B*, **110**, 21771 (2006)
62. S. P. Jiang, X. J. Chen, S. H. Chan, and J. T. Kwok, *J. Electrochem. Soc.*, **153** (5), A850 (2006)
63. J. Kim, V. V. Nair, J. M. Vohs and R. G. Gorte, *Scripta Mater.*, **65**, 90 (2011)
64. X. Yang and J. T. S. Irvine, *J. Mater. Chem.*, **18**, 2349 (2008)
65. F. Bidrawn, G. Kim, G. Corre, J. T. S. Irvine, J. M. Vohs, and R. J. Gorte, *Electrochem. Solid-State Lett.*, **11** (9), B167 (2008)
66. M. D. Gross, J. M. Vohs, and R. J. Gorte, *J. Electrochem. Soc.*, **154** (7), B694 (2007)
67. J. B. Goodenough, Y. H. Huang, *J. Power Sources*, **173**, 1 (2007)
68. E. P. Murray, T. Tsai and S. A. Barnett, *Nature*, **400**, 649 (1999)
69. S. Park, J. M. Vohs and R. J. Gorte, *Nature*, **404**, 265 (2000)
70. R. J. Gorte, S. Park, J. M. Vohs, and C. Wang, *Adv. Mater.*, **12**, 1465 (2000)
71. K. Chen, N. Ai, and S. P. Jiang, *J. Electrochem. Soc.*, **157** (11), P89 (2010)

72. R. D. Green, C. Liu, S. B. Adler, *Solid State Ionics*, **179**, 647 (2008)
73. K. Eguchi, N. Akasaka, H. Mitsuyasu, Y. Nonaka, *Solid State Ionics*, **135**, 589 (2000)
74. A. Tsoga, A. Gupta, A. Naoumidis, and P. Nikolopoulos, *Acta Mater.*, **48**, 4709 (2000)
75. O. A. Marina, C. Bagger, S. Primdahl, M. Mogensen, *Solid State Ionics*, **123**, 199 (1999)
76. C. D. Savaniu and J. T. S. Irvine, *J. Mater. Chem.*, **19**, 8119 (2009)
77. A. Atkinson, S. Barnett, R. J. Gorte, J. T. S. Irvine, A. J. McEvoy, M. Mogensen, S. C. Singhal and J. Vohs, *Nat. Mater.*, **3** (1), 17 (2004)
78. G. Tsekouras and J. T. S. Irvine, *J. Mater. Chem.*, **21**, 9367 (2011)
79. G. Tsekouras and J. T. S. Irvine, *Energy Environ. Sci.*, **6**, 256 (2013)
80. W. Wang, Y. Huang, S. Jung, J. M. Vohs, and R. J. Gorte, *J. Electrochem. Soc.*, **153** (11), A2066 (2006)
81. W. Wang, S. P. Jiang, *J. Solid State Electrochem.*, **8**, 914 (2004)
82. S. McIntosh, S. B. Adler, J. M. Vohs, and R. J. Gorte, *Electrochem. Solid-State Lett.*, **7** (5), A111 (2004)
83. S. P. Jiang, *J. Solid State Electrochem.*, **11**, 93 (2007)
84. E. Ivers-Tiffée, A. Weber, D. Herbstritt, *J. Eur. Ceram. Soc.*, **21**, 1805 (2001)
85. S. B. Adler, *Chem. Rev.*, **104**, 4791 (2004)

## Chapter 2: Methods and techniques

### Table of Contents

Introduction .....	35
2.1 General recipe for screen-printing ink preparation.....	35
2.2 General steps for single cell preparation .....	37
2.2.1 Single cells with fuel electrode made from screen-printing .....	39
2.2.2 Single cells with a gradient cathode structure.....	41
2.2.3 Single cells with fuel electrode on an impregnated architecture .....	42
2.3 Cell testing set-up and gas flows .....	45
2.3.1 Single cell testing set-up .....	45
2.3.2 Gas supply.....	47
2.4 Material characterization .....	48
2.4.1 Thermal gravimetric analysis (TGA).....	48
2.4.2 X-ray diffraction (XRD) pattern .....	49
2.5 Single solid oxide cell characterization.....	51
2.5.1 Single cell electrochemical characterization.....	51
2.5.2 Single cell microstructure characterization.....	56
2.6 Single cell electrolysis efficiency analysis .....	59
2.6.1 Gas chromatography (GC).....	59
2.6.2 Calculation of electrolysis efficiency.....	60
References .....	60

## Chapter 2: Methods and techniques

### Introduction

The fabrications and characterization methods/techniques of the solid oxide cells used for high temperature electrolysis will be described in this chapter. Thick YSZ electrolyte supported cells were fabricated in three-electrode geometry, and the fabrication of air electrode (anode in SOECs) was kept identical throughout this thesis. Therefore, the focus was on the cathode materials and processes and SOECs with different cathodes were prepared and tested. General steps for cathode SOEC preparation and testing will be depicted in this Chapter with detailed information mentioned in following chapters.

### 2.1 General recipe for screen-printing ink preparation

Screen-printing is a well-known approach for solid state electrode and/or electrolyte fabrication in solid oxide cells [1-3], and the detailed procedures will be described in single cell preparation in later part.

The principal steps for preparation of screen-printing ink are shown in the flow chart in Fig. 2.1. The ceramic powders for electrode components were weighed out and placed into a bottle, together with KD-1 dispersant (2 wt% of ceramic powders) and zirconia milling balls (1 cm in diameter). Acetone was then poured in the bottle to an amount that can cover the contents inside the bottle. The mixtures were ball milled for overnight (18-24 hrs) at a milling rate of around 160 rpm. This process helped to grind chemicals to a finer consistency thus increase their surface area and make mixtures more homogenous. After ball milling, the resulting slurry was moved to a beaker, and was stirred constantly at room temperature using a magnetic stirrer. The organic vehicles (consisted of 5 wt% butvar in 95 wt% terpineol), with 30/70 weight ratio towards ceramic powders, was weighed out and poured into the stirring slurry. The acetone in the slurry was evaporated slowly at room temperature under stirring by covering the beaker with a pierced “parafilm”. When all the acetone in the above slurry was evaporated, the remaining ink was bottled ready for use.

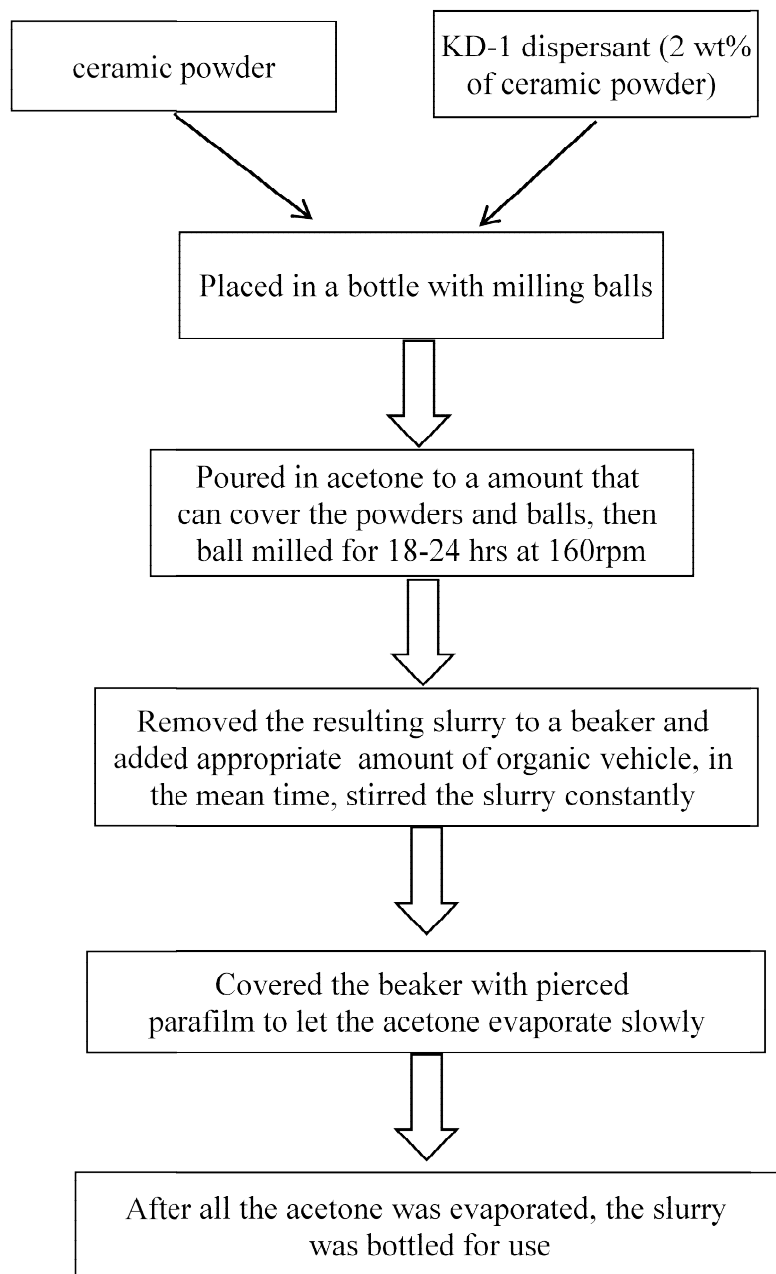


**Fig. 2.1** Flow chart of preparing screen-printing ink

The inks prepared as explained above include NiO/YSZ mixture,  $(\text{La}_{0.75}\text{Sr}_{0.25})_{0.97}(\text{Cr}_{0.5}\text{Mn}_{0.5})\text{O}_{3-\delta}$  / 8 mol.%  $\text{Y}_2\text{O}_3$  stabilized  $\text{ZrO}_2$  (abbreviated as LSCM/YSZ hereinafter) and LSCM /  $(\text{Gd}_{0.1}\text{Ce}_{0.9})\text{O}_{1.95}$  (denoted as GDC hereinafter) composites as cathode materials as well as  $(\text{La}_{0.8}\text{Sr}_{0.2})\text{MnO}_3$  / Sc stabilized zirconia (LSM/ScSZ in short

hereafter). Detailed ratios between ceramics for the above mentioned inks are summarized in Table 2.1, as shown below.

**Table 2.1** List of ceramic ratios for screen-printing inks preparation

	<b>Ceramic</b>	<b>ceramic ratios (wt % / wt %)</b>
	NiO/YSZ	65/35
Fuel electrode	LSCM/YSZ	50/50
	LSCM/GDC	50/50
Air electrode	LSM/ScSZ	50/50

In some cases, extra pore formers were added into the fuel electrode compositions for later introduction of electrode component via a different means, for instance, wet impregnation (see Chapter 5). In such circumstances, glassy carbon and graphite, in a ratio of 20/80 by weight, were added together with ceramic powders in preparing screen-printing inks. The weight of pore formers was 30wt% towards ceramic powders. When extra pore formers were introduced, the ratio between solid content and organic vehicles was 70/30 and 60/40, respectively in preparing YSZ and LSCM screen-printing inks for the construction of porous YSZ and porous LSCM layers as electrode backbone. The other steps for YSZ and LSCM inks preparation were similar as described in Fig. 2.1.

## 2.2 General steps for single cell preparation

All single cells studied in this thesis featured an approximately 2mm thick YSZ electrolyte supporting the 30-40 $\mu$ m thick electrodes. The cells were in three-electrode geometry. The schematic graph of a single cell configuration is shown in Fig. 2.2. The working electrode (WE), i.e. fuel electrode (cathode in SOEC and anode in SOFC) was on one side of YSZ electrolyte, while the counter electrode (CE) and reference electrode (RE) were on the other side of the electrolyte, with RE locating in the centre. The effective area for circular WE and CE was ca. 1cm<sup>2</sup>, and ca. 0.03cm<sup>2</sup> for RE. The thickness of electrodes was in the range of 30-40 $\mu$ m. Other dimensional parameters are

shown in Fig. 2.2. There are different types of cell design regarding the placement of RE [4]. The type of design developed in our lab was believed to be optimal for minimization of the uncompensated resistance in thick solid electrolyte and to be compatible with the testing set-up built in our lab. In our study, the CE and RE were made from the same material, which was screen-printed LSM/ScSZ composite, so that the focus was on the fuel electrode side, specifically, the cathode for SOECs. The single cells with different cathode materials and the same cathode material manufactured via different procedures were studied.

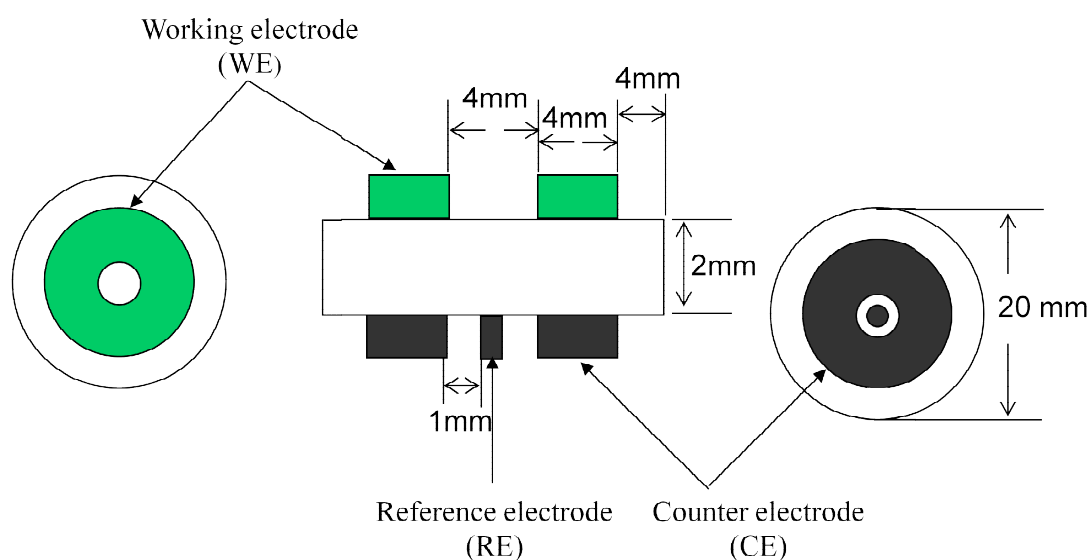


**Fig. 2.2** Schematic graph of the three-electrode geometry

Initially, thick YSZ pellets were prepared as support of electrodes. Commercial YSZ (P<sub>1</sub>-KEM) powder was weighed out (ca. 3.70g) and uniaxially pressed under a pressure of around 2.0 tons/cm<sup>2</sup> using circular stainless steel pellet dies. When placed in dies, the YSZ powders were spread evenly and pressed manually with a stainless steel column prior to high pressure pressing. This was intended to avoid uneven compaction which could lead to cracks and inner fractures in the pellet during later sintering process. The resulting pellet was placed on an alumina plate and fired at 1500°C for 4 hrs right after pressing, at a ramp rate of 2°C/min. The as-prepared YSZ pellet was ca. 20mm in diameter and 2mm in thickness. The YSZ pellet was polished on both sides before introducing electrode materials.

### 2.2.1 Single cells with fuel electrode made from screen-printing

As mentioned before, screen-printing has been frequently used for solid electrode/electrolyte fabrication, due to its simplicity, ease of fabrication, low cost.

Fig. 2.3 displays the schematic of screen-printing fabrication setup. Briefly, a screen-printer consists of a sample holder, an ink blocking screen which has mesh openings defining the image going to be printed, and a movable squeegee (i.e. rubber blade). To start fabricating, electrode ink was placed on top of the screen and applied onto the substrate of YSZ pellet underneath the mesh opening area, by moving the squeegee across the screen. Proper pressure was necessary to pump the ink through the porous mesh open areas when drawing the squeegee. The image and area of electrode was determined by the mesh opening areas because ink was totally blocked at other areas. The screen was cleaned thoroughly before changing materials and after finishing printing, using iso-propanol, in order to avoid cross contamination. Caution should always be taken to centre the sample in sample holder to align the WE and CE on the two sides of YSZ pellet before printing.

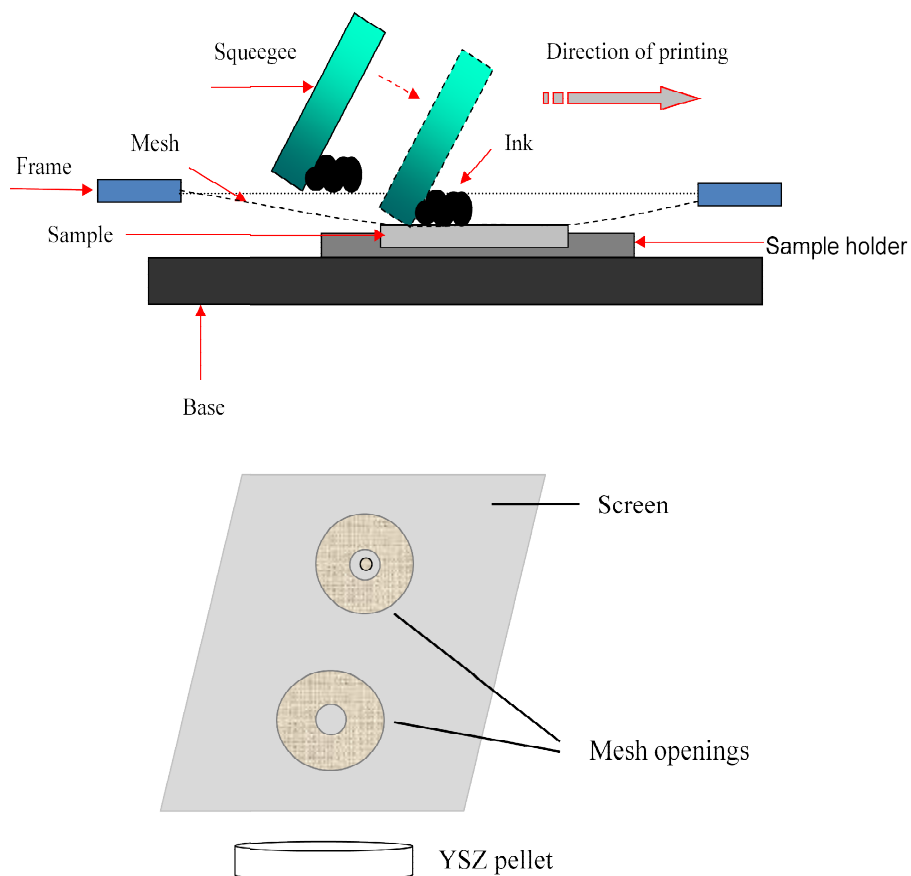


**Fig. 2.3** Schematic picture of screen-printing fabrication (Top: screen-printer; Bottom: screen with mesh openings)

Cathode ink was firstly printed on one side of YSZ pellet, considering that it needed higher sintering temperature. Printing was repeated to get desired thickness for each electrode, with baking the electrode at  $80^{\circ}\text{C}$  in oven in between each printing. Subsequently, cathode was fired in high temperature furnace, and different cathode materials required different sintering conditions. The sintering temperature and dwelling time for different cathodes prepared via screen-printing are listed in Table 2.2.

**Table 2.2** Sintering conditions for different electrodes made from screen-printing

Electrode	Calcination temperature (°C)	Dwelling time (h)
NiO/YSZ	1350	1
LSCM/YSZ	1200	2
LSCM/CGO	1200-1300	2
LSM/ScSZ	1100	2

On the other side of YSZ pellet, LSM/ScSZ anode was screen-printed. Similarly, printing was repeated with drying anode in oven at 80°C in between, followed by sintering at high temperature. The firing conditions for anode are also given in Table 2.2. The procedures for fabrication of anode were kept constant through all of our experiments, and only variations on cathode side were regarded.

### 2.2.2 Single cells with a gradient cathode structure

Concept and advantages of gradient electrode structure have been widely acknowledged in SOFC applications [5-6]. A graded electrode is composed of a thin functional layer close to electrolyte membrane and a thicker conduction layer further from electrolyte. The functional layer is optimized for electrochemical activity towards electrode reaction, whereas the conduction layer manages the gas diffusion and current collection for electrode reaction. Electrode of this design is believed to have several positive characteristics, such as improved electrolyte/electrode interface and extended TPB area in total.

In our experiment, an SOEC with a graded LSCM/YSZ cathode was made based on screen-printing procedures. LSCM/YSZ ink with 30/70 and 60/40 weight ratios of the two components were prepared similarly as described in section 2.1. For the gradient LSCM/YSZ cathode, LSCM/YSZ 30/70 ink was printed on the surface of YSZ pellet, followed by baking it to dry and printing of LSCM/YSZ 60/40 ink on top of it. These two layers were then fired at 1200°C for 2hrs. The as-prepared graded cathode was ca.30-40µm totally in thickness, around 10µm for LSCM/YSZ 30-70 layer and ca. 20µm for LSCM/YSZ 60/40 layer. The following steps related to preparing screen-

printed LSM/ScSZ anode on the other side of YSZ pellet and firing at 1100°C, which were kept identical throughout this thesis.

### **2.2.3 Single cells with fuel electrode on an impregnated architecture**

Screen-printing approach for electrode fabrication is based on the conventional ceramic mixing method. This method usually involves high temperature sintering to improve electrode/electrolyte interfacial adherence and thermal expansion coefficient mismatch between adjacent electrode and electrolyte, however, this requirement would lead to grain growth and solid phase reaction [7]. Wet impregnation technique offers a means to introduce different components separately and fire them at different temperatures accordingly, thus avoid the problems that ceramic mixing method suffers. Besides, wet impregnation provides an effective way to enhance the electro-catalytic activity of electrode, ascribed to the modified microstructure that this approach introduced, that is fine particles highly dispersed on the porous electrode framework [7-9]. As this, wet impregnation has been widely used in the preparation of heterogeneous catalysts; however, the application of it in the SOFC/SOEC field is quite recent.

In our experiment, two kinds of cathode SOEC were prepared by wet impregnation. The first was metal catalyst infiltrated LSCM/GDC composite cathode SOEC, and the second was LSCM infiltrated YSZ cathode SOEC and GDC infiltrated LSCM cathode SOEC. The manufacture of these two kinds SOECs will be described as follows.

Transition metals, for example, Co, Ni, Fe, and so on, and precious metals, such as, Pt, Pd, Rh, etc., have been reported having excellent catalytic activity towards oxidation reactions, thus have been applied as additional catalyst to assist electrode reactions in SOFC/SOECs [8, 10-12]. In our experiment, Pd, Ni, CeO<sub>2</sub>, and Pt were doped into LSCM/GDC composite at a dopant level, which was 0.5 -1 wt%. Regarding the preparation of these SOECs, single cells with 2mm YSZ electrolyte, screen-printed LSCM/GDC composite as cathode and screen-printed LSM/ScSZ composite as anode were initially prepared. Subsequently, nitrate precursor solutions for Pd, Ni, CeO<sub>2</sub> and Pt catalyst were added into the porous LSCM/GDC electrode framework using a syringe, as shown in Fig. 2.4. The amount of solution used was calculated according to the desired metal doping amount. The precursor nitrate solution was dropped on the

surface of LSCM/GDC cathode at atmospheric pressure, with a shield in the centre of the pellet surface so that doping only occurred in cathode area. The nitrate solution diffused into porous LSCM/GDC layer by a capillary force. The following step was to fire the cathode at 500°C to decompose nitrate. The impregnation steps were repeated to obtain desired metal catalyst loading. The metal oxide after firing at 500°C would be reduced in situ at 900°C in 5% H<sub>2</sub>/Ar atmosphere prior to electrochemical characterization.

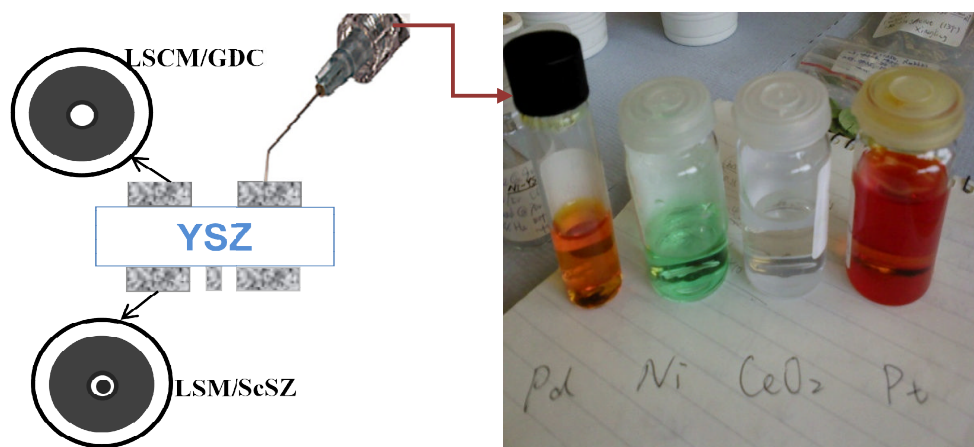


**Fig. 2.4** Picture of preparing metal aided LSCM/GDC cathode SOEC by wet impregnation

Above, metal catalysts were introduced by wet atmospheric impregnation at a dopant level, into an established LSCM/GDC porous electrode. When the amount of infiltrated component are at a high level, wet vacuum impregnation, namely, adding impregnated component under a vacuum pressure, is necessary to introduce catalyst deep into the electrode/electrolyte interface. In addition, the vacuum impregnation is likely to be time and cost saving, compared to the traditional atmospheric impregnation approach. Fig. 2.5 is the schematic of a home-built setup for wet vacuum impregnation. Basically, it is comprised of a tank which has a sample holder inside and a lid with a built-in syringe which incorporates a valve to control the release of nitrate solution. A rubber ring was used to seal the tank when it was covered by the lid with vacuum pressure applied to it during the whole process of impregnation. Before carrying out infiltration, gas inside the tank and inside pores of the sample was firstly pumped out. Vacuum was applied to

the tank with sample inside, then, open the valve at top part of the syringe to place some nitrate solution on top of the surface that was going to be coated. Vacuum was held for a certain time, during which the penetration of nitrate solution into porous substrate took place. After this, vacuum pressure was released, the sample taken out from tank, and the extra solution on the surface wiped off using blue roll, and then the sample was fired at 500°C to decompose nitrate. The amount of component loaded via this vacuum impregnation was obtained by the weight difference before and after impregnation, and the impregnation was repeated until desired amount of component was reached.

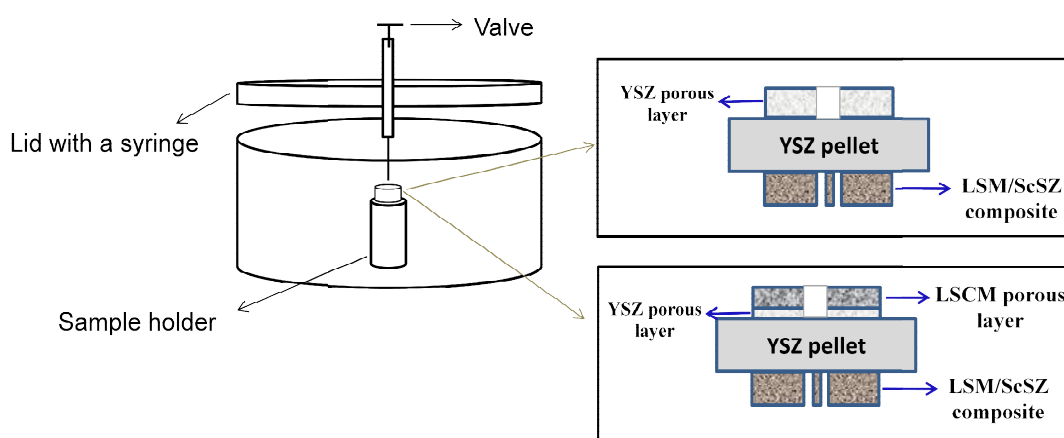


**Fig. 2.5** Schematic representation of a home-made setup for wet vacuum impregnation and sample SOECs prepared in vacuum impregnation

The following is the brief explanation of SOEC cathodes prepared based on an impregnated architecture, i.e. LSCM impregnated YSZ cathode and GDC impregnated LSCM cathode as displayed in Fig. 2.5, by vacuum impregnation. More detailed information on the fabrication of these cathode cells will be included in Chapter 5.

*LSCM impregnated YSZ cathode SOEC*- A porous YSZ layer was applied onto the surface of 2mm YSZ pellet by screen-printing and firing at high temperature. During heating up, the pellet was heated slowly to 800°C, dwelled at this temperature for some time to get rid of carbon, and then heated to the calcinations temperature, 1350°C. This high sintering temperature helped to improve the cathode/YSZ electrolyte interface. LSCM nitrate solution was prepared by dissolving metal nitrate salts, in stoichiometric ratios, into distilled water under stirring. The resulting LSCM nitrate solution was added

into the YSZ porous backbone through vacuum impregnation under 0.22bar. The impregnation steps were repeated until required amount of LSCM, which was 50/50 over the weight of YSZ, was achieved. Sintering of the pellet at 1100°C was then conducted to form LSCM perovskite phase. The next step was introducing LSM/ScSZ anode on the other side of YSZ pellet, as described previously.

*GDC infiltrated LSCM cathode SOEC*- Similar to the preparation of LSCM impregnated YSZ cathode, a porous YSZ layer was firstly screen-printed on top of YSZ pellet, but with a very thin thickness (around 5-10µm). The LSCM porous layer was then introduced on top of YSZ layer by screen-printing, followed by co-firing the LSCM/YSZ layers at 1300°C. The purpose of introducing a thin YSZ layer between YSZ electrolyte and LSCM porous layer was to enhance the cathode/electrolyte interfacial bonding. GDC nitrate solution was made by dissolving and mixing metal nitrate salts in distilled water, according to the formula of  $Gd_{0.1}Ce_{0.9}O_{2-\delta}$ . The infiltration of GDC nitrate solution into LSCM/YSZ porous layer was carried out by vacuum impregnation at 0.22bar, and it was repeated to get the weight ratio of 50/50 for GDC over LSCM/YSZ. After impregnation was done, the calcination of GDC at 1100°C was conducted, and following that was the introduction of LSM/ScSZ anode by screen-printing. For the purpose of comparison, an SOEC with GDC impregnated YSZ cathode was also fabricated by introducing GDC nitrate solution in YSZ porous skeleton under vacuum pressure, similar to the preparation of SOEC with GDC impregnated LSCM cathode. Besides, Pd catalyst was added for some GDC impregnated LSCM cathode SOECs to further improve cathode performance, and it was introduced identically as explained before, by wet atmospheric impregnation after the fabrication of GDC impregnated LSCM cathode SOEC.

### **2.3 Cell testing set-up and gas flows**

#### **2.3.1 Single cell testing set-up**

Current collectors for both fuel electrode and air electrode were applied before electrochemical measurements. The selections for current collector for different electrode materials will be discussed in following chapters (chapter 4-5).

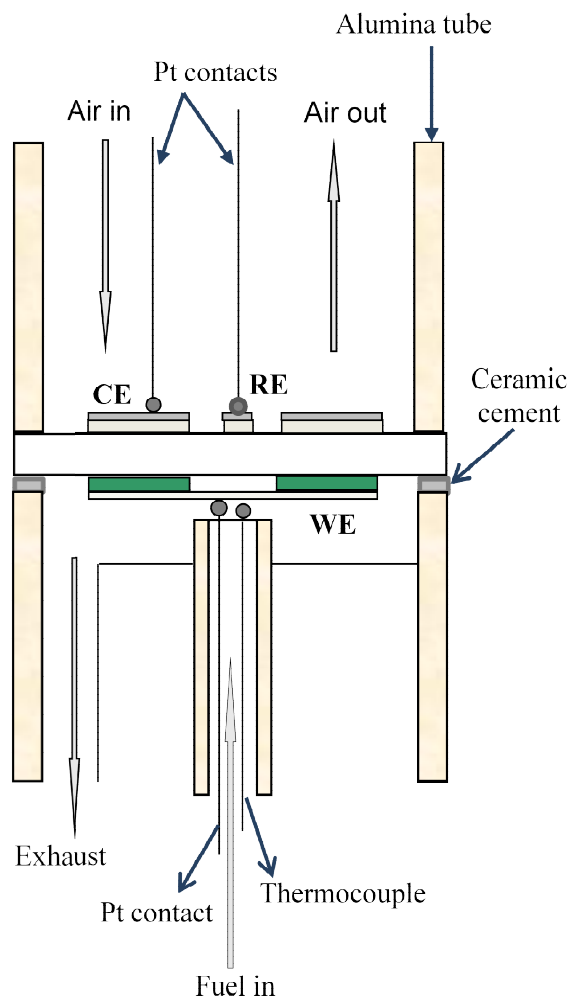


**Fig. 2.6** Schematic graph of sing cell testing set-up

Fig. 2.6 is the schematic picture of the home-built single cell testing set-up. The ready-to-test single cell was mounted to an alumina tube, and it was sealed to the alumina tube on the cathode side using ceramic cement (Aremco 552). Then the whole assembly was placed into a temperature-controlled furnace, with the anode part sitting on top and cathode part at bottom. Pt probes were used to connect the cell to electrochemical instruments. An R-type thermocouple was placed close to the sample, in order to monitor the sample temperature during operation. Before heating the furnace up to operating temperature, the test chamber was heated to 300°C at a very low ramp rate (0.5°C/min), to properly cure the ceramic cement. Subsequently, the test chamber was heated directly to the operating temperature at a ramp rate of 3°C/min.

### 2.3.2 Gas supply

During electrochemical measurement, different fuel gas was fed into cathode chamber at a certain flow rate controlled by mass flow controllers (MFC, CO MFC from AALBORG and CO<sub>2</sub> MFC from Cole-Parmer), and bubble leak test was conducted on the downstream of the cathode to check seals and leakage across electrolyte. With respect to the anode side, air was flushed through at a constant flow rate, 100ml/min during the whole test.

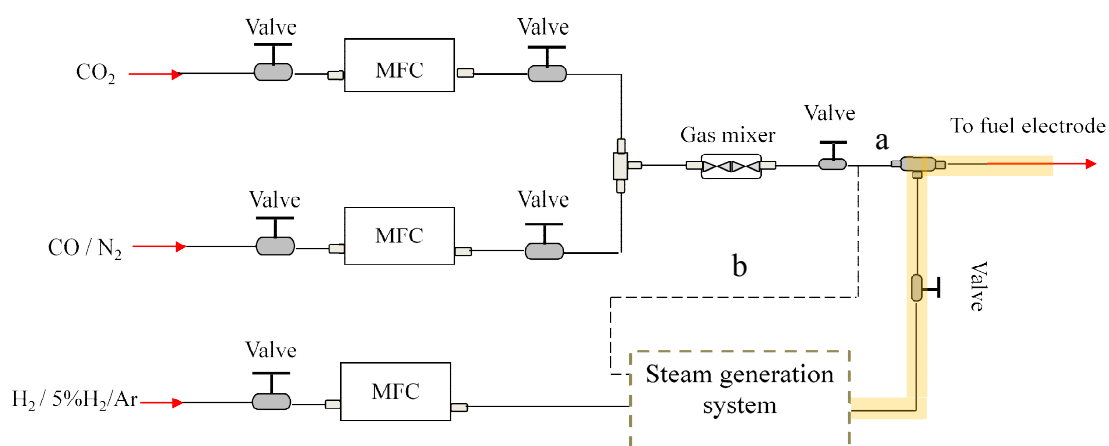


**Fig. 2.7** Gas lines for fuel gas supply with the incorporation of steam generation system for steam electrolysis/steam-carbon dioxide co-electrolysis (the highlighted gas line was wrapped with heating tapes when steam generator was on)

Fig. 2.7 exhibits the cathode gas lines for fuel gases supply. During heating up, both the fuel and air electrode were exposed to ambient air except the Ni/YSZ cathode SOEC for which N<sub>2</sub> rather air was flowed through fuel electrode. At the operation temperature, humidified 5% H<sub>2</sub>/Argon was firstly fed into the cathode chamber to evaluate cell open circuit voltage (OCV) to check if the cell was well sealed, before the introduction of fuel gas. Humidified 5% H<sub>2</sub>/Ar was also used for NiO reduction in the case of Ni/YSZ cermet cathode SOEC. Reduction was performed in the experimental setup in situ until OCV value of the cell stayed constant. Regarding the LSCM based cathode SOEC, 5%H<sub>2</sub>/Ar was run for a certain time to get a steady state before providing fuel gas.

Concerning CO<sub>2</sub> electrolysis, CO<sub>2</sub>/CO gas mixture with various CO<sub>2</sub>/CO ratios, at a total flow rate of 30 ml/min was introduced into the fuel side, i.e. cathode side in SOEC. Prior to entry cathode chamber, CO<sub>2</sub> and CO gas were connected to a gas mixer to get a uniform mixture gas. The initial performance for the cells with different cathode material was characterized in atmospheres with different CO<sub>2</sub>/CO ratios ranging from 90/10 to 30/70 controlled by MFCs. CO<sub>2</sub> electrolysis was also conducted on the GDC impregnated LSCM cathode SOEC in fuels without protective CO gas, at this circumstance, N<sub>2</sub> was used as saturate gas for CO<sub>2</sub>, and cell performance was characterized in different CO<sub>2</sub>/N<sub>2</sub> ratio gas mixtures (see section 6.3). In some cases, 5%H<sub>2</sub>/Ar, at a flow rate of 10ml/min controlled by a separate MFC (from Brooks), was introduced into fuel electrode, along with CO<sub>2</sub>/CO or CO<sub>2</sub>/N<sub>2</sub> mixture, in order to study the effect of presence of H<sub>2</sub> on CO<sub>2</sub> reduction reaction kinetics.

Regarding steam electrolysis and/or steam-carbon dioxide co-electrolysis, a steam generation system was incorporated for fuel gas supply. Steam was generated by heating a saturator (BekkTech BT-512 system) at a certain temperature to obtain the required steam concentration. The generated steam was carried to the fuel compartment by 5%H<sub>2</sub>/Ar or pure H<sub>2</sub> gas in steam electrolysis study, and all the gas line from the exit of saturator to furnace was wrapped with insulated heating tapes (from Omega Engineering), as shown in Fig. 2.7 in yellow colour, which were heated at around 100°C to prevent steam from condensation. The flow rate for steam-containing fuel ranged from 10 to 30 ml/min. In co-electrolysis studies, steam carried by 5% H<sub>2</sub>/Ar or H<sub>2</sub> and CO<sub>2</sub>-CO mixture were joined at some point of gas line (route a in Fig. 2.7) before being co-fed to fuel compartment. Alternatively, steam was carried by CO<sub>2</sub>-CO mixture (route b in Fig. 2.7) as feed gas for co-electrolysis measurement. The total feed flow rate was 30 ml/min for co-electrolysis studies. More detailed information will be found in chapter 7 for fuel gas compositions for steam electrolysis/co-electrolysis studies.

## **2.4 Material characterization**

### **2.4.1 Thermal gravimetric analysis (TGA)**

TGA is a method to analyze the mass changes of materials that are under examination as a function of temperature and time, and it is commonly used to characterize materials

that exhibit weight gain/loss due to decomposition, oxidation/reduction, dehydration, phase transitions, or thermal degradation etc [13]. Basically, TGA measurement records the weight gain/loss of a material during programmed heating/cooling or dwelling in a certain atmosphere. The weight changes can be utilized to analyze the physical/chemical phenomena taking place on the material upon varying temperature/time.

In our experiment, TGA was conducted on a Netzsch TG 209 to measure the thermal behaviour of Ni/YSZ cermet after being treated in CO<sub>2</sub>-CO mixtures at different temperatures. Ni/YSZ pellets after treatment were fractured. A few pieces (around 50mg) were used as sample for TGA examination. The sample was placed in a crucible and heated to 900°C at a ramp rate of 5°C/min in air during which Ni would be re-oxidized and carbon, if there was, would be burnt out. At 900°C, air was switched to Ar, which was flushed for the dwelling and the subsequent cooling down to 800°C, at which 5% H<sub>2</sub>/Ar was introduced and Ar was switched off. The samples were kept at 800°C for 2 hrs till NiO was fully reduced (no more weight loss was observed) after which temperature was lowered down to room temperature. The weight changes for the whole process were recorded as a function of temperature and running time. TGA measurement was also performed on LSCM/YSZ composite after being treated identically to that of the Ni/YSZ cermet. The weight changes in air during heating from room temperature to 900°C and cooling down to room temperature were recorded.

### 2.4.2 X-ray diffraction (XRD) pattern

The XRD technique is one of the primary techniques used for fingerprint characterization of crystalline materials and determining the crystallographic structure of a solid [14].

When the incident X-ray beam encounters a crystal lattice, the atomic planes of the crystal cause the X-rays to interfere with one another as they leave the crystal. Diffraction takes place only when constructive interference happens. That is the two waves, represented by 1' and 2' as shown in Fig. 2.8, are in phase and reflected beam with maximum intensity occurs. The path difference between two waves in phase can be expressed by Bragg's law.

$$n\lambda = 2d\sin\theta \quad (n \text{ is an integral number})$$

Where  $d$  is the interplanar spacing,  $\theta$  is the angle of the incident beam with a certain atomic plane, and  $\lambda$  is the wavelength.

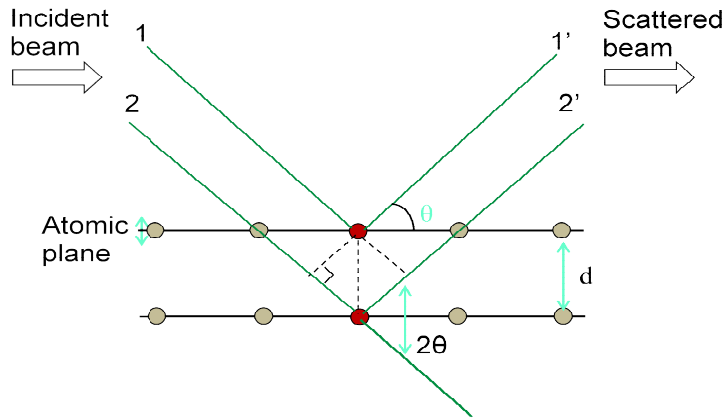


**Fig. 2.8** Reflection of incident X-ray beam on two atomic planes of a solid

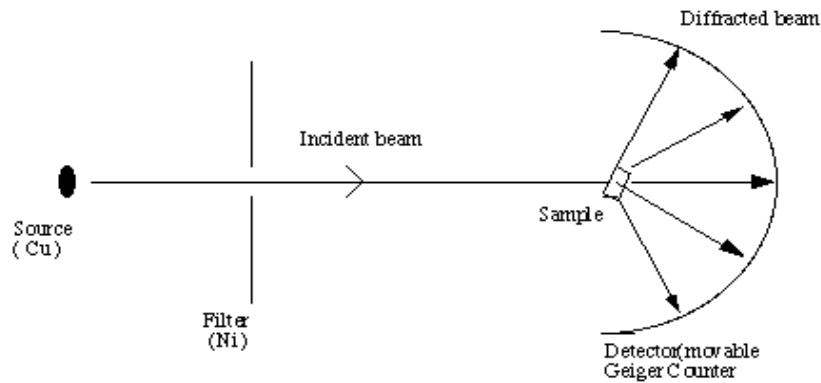


**Fig. 2.9** Schematic diagram of an X-ray powder diffractometer [15]

The X-ray diffraction equipment includes an X-ray source for which copper (Cu) target is commonly used, a sample holder and a detector to collect the diffracted X-rays. As displayed in Fig. 2.9, the X-ray detector locates on the circumference of a graduated circle centred on the sample under examination. The detector and sample holder are mechanically coupled with a goniometer so that the detector and sample holder can rotate during measurement.

In our experiment, the XRD was used for phase identification in SOEC cathode and current collector materials. Room temperature powder XRD was performed on a Stoe Stasi-P powder diffractometer and a Philips diffractometer operating in reflection geometry, both using Cu K $\alpha$ 1 radiation ( $\lambda = 1.54056 \text{ \AA}$ ) over the  $2\theta$  range of 10 to 90 degree.

## **2.5 Single solid oxide cell characterization**

### **2.5.1 Single cell electrochemical characterization**

DC polarization curves, namely, I-V curves as well as electrochemical impedance spectroscopy (EIS herein) were recorded for electrochemical characterization. For some cells, the cell potential as a function of operation time was measured at a constant current density (i.e. galvanostatic mode), in order to investigate the stability of cathode materials.

*I-V curve* – I-V curves describe the trends of the cell voltage with the increase of current density applied in SOEC, in other words, the polarization behaviour upon the current flow through the cell. On the I-V curve, one can get the open circuit voltage (OCV), the resistance of the cell (the slope of the I-V curve) and the limiting current density if there is one. Fig. 2.10 shows the typical I-V curve of a SOEC operated at 900°C in CO<sub>2</sub>-CO mixture. The I-V curve was recorded both in SOEC and SOFC operation. The positive current was in SOFC mode and negative current represented SOEC operation. I-V curves were measured in various atmospheres, for instance, CO<sub>2</sub>-CO mixture, CO<sub>2</sub>-N<sub>2</sub> mixtures, H<sub>2</sub>O-H<sub>2</sub> mixtures and so on. Factors affecting I-V behaviour including fuel gas flow rate and operation temperature were investigated.

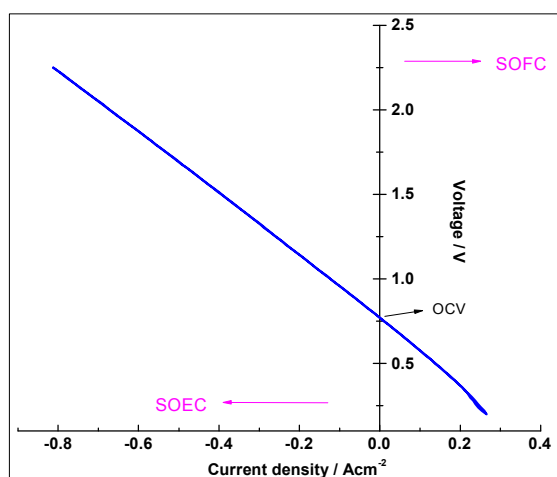


**Fig. 2.10** Typical I-V curve of a SOEC operated at 900°C in CO<sub>2</sub>-CO mixture (the tested cell was consisted of a 2mm YSZ electrolyte, a Ni/YSZ cermet cathode and a LSM/ScSZ anode, and the cathode atmosphere was CO<sub>2</sub>-CO 90-10 mixture. The fairly linear I-V curve indicated the predominant contribution from ohmic resistance of thick YSZ electrolyte to cell performance)

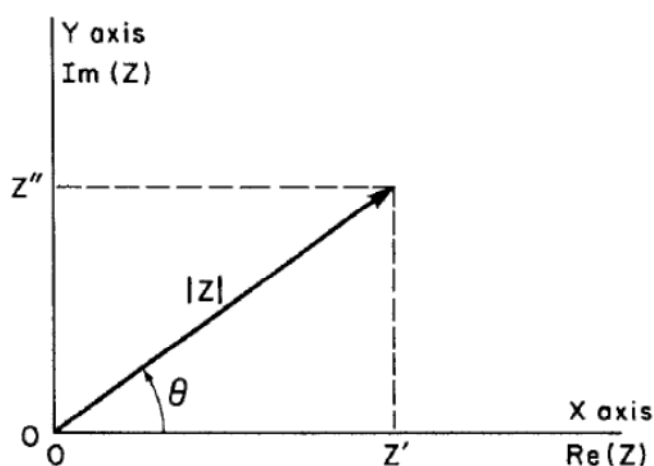


**Fig. 2.11** The impedance Z plotted as a planar vector using rectangular and polar coordinates [16]

*Impedance spectroscopy* – Electrochemical impedance spectroscopy (EIS), also known as Ac-impedance spectroscopy, has been widely used in studies of electrochemical

systems and is regarded as a powerful technique to characterize electrical properties of electrode materials and their interfaces with electrolyte.

The general approach for EIS characterization is to apply a single-frequency voltage or current as stimuli to electrodes/interfaces and measure the resulting variations in magnitude and phase of the cell voltage/current. For example, a monochromatic signal  $v(t) = V_m \sin(\omega t)$ , involving the single frequency  $\nu \equiv \omega/2\pi$ , is applied to a cell and the resulting steady state current  $i(t) = I_m \sin(\omega t + \theta)$ , where  $\theta$  is the phase difference between voltage and current, is measured. Using Fourier transformation, the relation between system properties and response to periodic voltage/current excitation can be simplified as an impedance  $Z(\omega) = Z' + jZ''$  which can be plotted as a planar vector quantity with either rectangular or polar coordinates, as shown in Fig. 2.11. The two rectangular coordinate values can be expressed as

$$\text{Re}(Z) \equiv Z' = |Z| \cos(\theta) \quad \text{and} \quad \text{Im}(Z) \equiv Z'' = |Z| \sin(\theta)$$

Where  $\text{Re}(Z)$  and  $Z'$  stands for the real part of impedance, with  $\text{Im}(Z)$  and  $Z''$  the imaginary part of impedance, and  $\theta$  is the phase angle.

Shown in Fig. 2.12 and Fig. 2.13 are the complex plot, i.e. Nyquist plot of EIS. For an idealized fuel cell, the Nyquist plot is characterized by a semicircular arc, with its intersection at high frequency reflecting electrolyte resistance and the difference between intersections at high frequency and low frequency the polarization resistance  $R_p$ . The EIS of a real electrochemical system is complicated, as displayed in Fig. 2.13, and is more commonly featured with several depressed semicircular arcs and with overlapped semicircular arcs which make it difficult to separate and analyse the contributions.

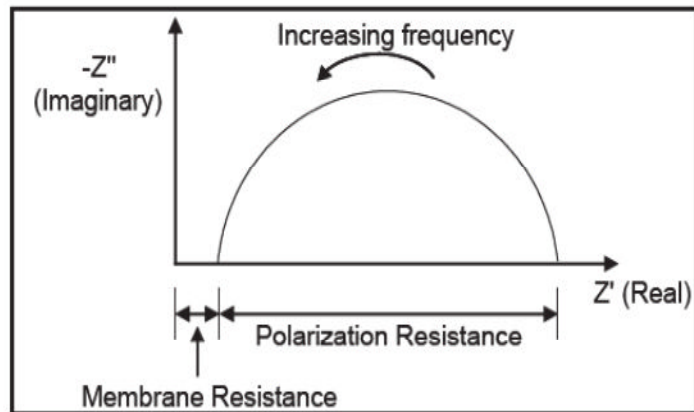


**Fig. 2.12** An idealized Nyquist plot of the EIS of a fuel cell [17]

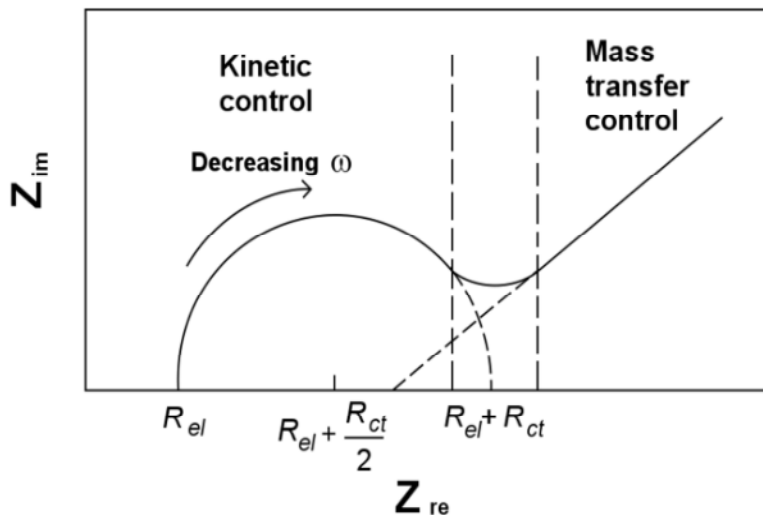


**Fig. 2.13** Nyquist plot of EIS of a real electrochemical system [18]

While the impedance data may be complicated for interpretation of properties/mechanism of the electrochemical system being studied, a data-fitted equivalent circuit model can be established to determine different contributions and suggest valuable chemical processes or mechanisms for the electrochemical system. Such equivalent circuit can produce the same response as the electrochemical system does and should be as simple as possible.

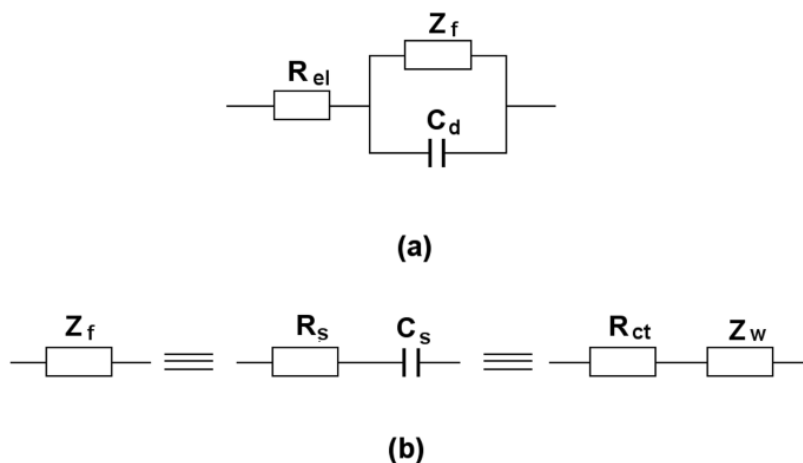


**Fig. 2.14** a. Typical equivalent circuit of an electrochemical cell; b. subdivision elements of  $Z_f$  [18]

Fig. 2.14 displays a typical equivalent circuit of an electrochemical cell.  $R_{el}$ ,  $C_d$ , and  $Z_f$  respectively represent the electrolyte resistance, a pure capacitor associated with the double layer of the electrode/electrolyte interface, and the Faradaic impedance. The impedance  $Z_f$  can be divided in a resistance  $R_s$  in series with a pseudo-capacitance  $C_s$  and a charge transfer resistance  $R_{ct}$  and a Warburg impedance  $Z_w$ . The above only reflects the simplest electrode process happening at the electrode/electrolyte interface. When the electrode process is a complicated one with more steps involved more complex circuits have to be built.

In this study, impedance measurements were performed using three-probe configuration with ZAHNER IM6e Electrochemical Workstation. The frequency in the EIS testing ranged from  $10^5$  to 0.1 or 0.015Hz, and AC voltage amplitude of 10mV or 20mV was used. The EIS were recorded at OCV as well as at different potential being applied to SOEC. For some SOECs, impedance data were fitted using equivalent circuit model for analysis (see section 4.4).

*Stability measurement-* Stability is one of the critical properties considered for the selection of materials applied in solid oxide cells. Stability measurement was thus carried out to study the performance degradation of SOEC cathode material in long-term operation for  $CO_2$  electrolysis and  $H_2O-CO_2$  co-electrolysis.

With respect to CO<sub>2</sub> electrolysis, stability test were performed in CO<sub>2</sub>-CO 70-30 mixture at 900°C, and LSCM/GDC cathode SOEC potential was recorded as a function of operation time at a constant current ( $-0.25\text{Acm}^{-2}$ ) being applied to SOEC (section 4.6). As for H<sub>2</sub>O-CO<sub>2</sub> co-electrolysis, stability measurement was conducted on Pd-GDC co-impregnated LSCM cathode SOEC operated in various H<sub>2</sub>O-H<sub>2</sub>-CO<sub>2</sub>-CO atmospheres, and cell potential at current density of  $-0.15\text{Acm}^{-2}$  was recorded along extended operation time (section 7.3.4).

### 2.5.2 Single cell microstructure characterization

Scanning electron microscopy (SEM) is a widely used technique for the characterization of solid materials, and it has a lot of advantages over traditional optical microscope, for example, high resolution image, a larger depth of field, and wider range of magnifications. Besides, SEM can provide lots of information on sample's microstructure, morphology, and chemical composition/elemental identification that are inaccessible by light microscope. SEM also has modest restrictions on sample preparation and is user friendly. Because of these traits, SEM has actually become a valuable tool in research today.

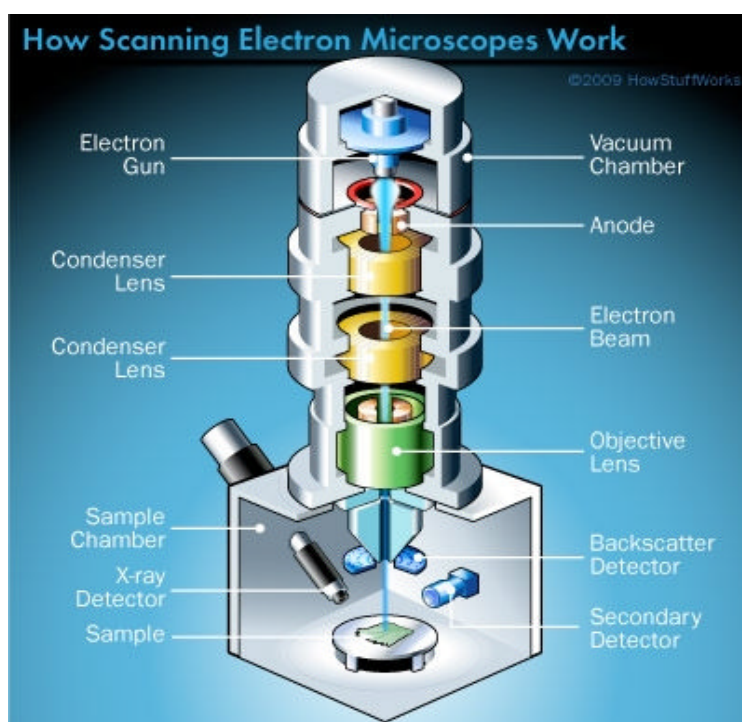


**Fig. 2.15** Diagram of the key components of a scanning electron microscope [19]

A diagram of the key components of a SEM is presented in Fig. 2.15. In principle, SEM utilises electron beam instead of light as probe to scan and produce a largely magnified image of the specimen. A steady stream of incident electrons is created at the top of microscope by electron gun. Following a vertical path in the microscope, the electron beam travels through electromagnetic lenses, which focus the electron beam down towards the specimen sitting in the sample chamber at the base of a microscope. When the highly focused electron beam strikes the surface of specimen, a variety of signals, as shown in Fig. 2.16, will be generated as a result of interaction between the incident electrons and sample. The signals carry a wealth of information about a sample's properties, including morphology, microstructure and composition and will be detected by various detectors and converted into a signal that is sent to a screen to produce the final image. Noticeably, it is necessary for a SEM working in a vacuum column to avoid interference from air particles in the atmosphere which would block the path of electron beam and distort the surface of the specimen.

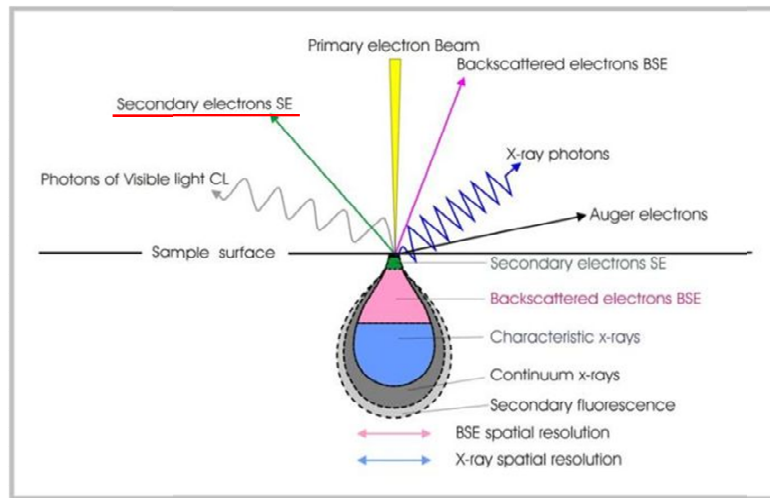


**Fig. 2.16** Different signals emitted as a result of incident electrons interaction with the specimen under observation (the highlighted signal is the one most familiar in SEM) [20]

Of all the signals ejected from the specimen due to the interaction of incident electrons with the specimen under examination, the three signals that provide the greatest amount of information in SEM are the secondary electrons (SE), backscattered electrons (BE), and X-rays. The SE are generated as a result of interaction between the incident

electrons and the electrons of atoms presented in the surface of sample, thus SE provide information on the sample's surface topography and the images SE produced are most familiar. The BE are primary incident electrons that are scattered by sample atoms and reflected from the sample surface. BE provide information on the topographic and contrast of the specimen with the contrast determined by the atomic number of the sample atoms, therefore, the image produced will show chemical composition information of the sample. X-rays are produced by the incident electrons interaction with the inner shell electrons of atoms in the sample. Characteristic X-rays are emitted from the specimen atom after a secondary electron is produced and allow qualitative identification of elements in sample. SEM coupled with energy-dispersive X-rays detector (EDX) offers information not only on topographic microstructure, but also on the chemical composition/element composition maps of materials.

The field-emission gun (FEG) SEM employs a field-emission gun, rather the traditional tungsten-filament, as a source of electrons. The secondary electron image resolution for an ideal sample is about 3.5 nm for a tungsten-filament electron source SEM and 1.5 nm for field emission SEM [21].

Although SEM requires little restrictions on sample preparation as long as the sample stands stable in vacuum environment, it is essential for the sample that is to be observed to be conductive. Otherwise, sputter coating should be carried out to cover a very thin layer of metal or carbon, to make it conductive. Further, the sample should have a clean surface before going into SEM.

In our experiment, SEM measurements were performed to study the microstructure and morphology of SOEC cathode and cathode/electrolyte interfaces. In some cases, EDX was incorporated with SEM to inspect the distribution of elements in cathode materials. The SEM equipments used were JEOL JSM-5600 (with tungsten filament as electron gun) and JEOL JSM-6700F (with field emission gun). An Oxford INCA Energy 200 device was coupled with JSM-5600 instrument for EDX examination. All the samples examined were coated with a thin layer of gold on its surface, in order to obtain clear and informative images.

## 2.6 Single cell electrolysis efficiency analysis

Electricity-to-chemical efficiency, namely, Faradaic efficiency, was evaluated for CO<sub>2</sub>/steam electrolysis using Faraday's law. To realize this, gas chromatography was conducted to analyze the SOEC cathode downstream gas compositions in various conditions.

### 2.6.1 Gas chromatography (GC)

Gas chromatography is a technique to separate chemicals in a complex sample. Fig. 2.17 shows the schematic diagram of a typical gas chromatograph, which consists of an injection port, a flowing mobile phase known as carrier gas, a column containing the stationary phase inside, a column oven, a detector, and a data recording system. The carrier gas serves to carry the molecules of sample through separation column, and is generally inert gases such as helium, argon, or nitrogen. The separation column is usually placed in a thermostat-controlled oven due to the fact that the sample mixture partitioning process is dependent on temperature. The detector and recorder located at the end of column to output the separated results electronically.

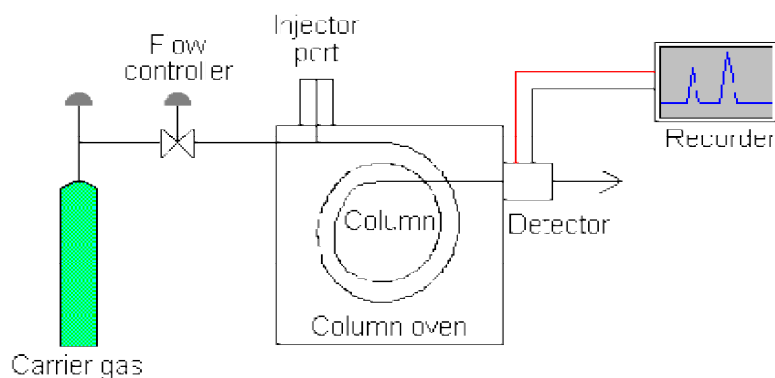


**Fig. 2.17** Schematic graph of a typical gas chromatograph [22]

In a gas chromatograph, fundamentally, a sample mixture is injected and vaporized, if a liquid, at the entrance of column, then the sample mixture is carried through the column by a carrier gas. Adsorption and partitioning of sample mixture occur in the column, and components in the sample mixture exit from the end of column at different time known retention time, depending on their various chemical and physical properties and

their interaction with the column filling, i.e. the stationary phase. Factors influencing the retention time also include the flow rate of carrier gas, column length and temperature.

In our experiment, an Agilent 3000 Micro gas chromatograph (instrument series number: US10713003), which was equipped with an injection port, was employed to analyze the cathode outlet gas compositions. At a certain external load, the cathode downstream gas was connected to GC. Ar and He were respectively used as carrier gas for module A and B in the operation of instrument. Both modules used 1.0 $\mu$ l backflush injector for sample injection, with Mol-sieve 5A and PLOTU, adopted as columns in module A and B respectively. Different gases were detected by thermal conductivity detectors (TCD) and distinguished according to their fingerprint retention time in the chromatography. The concentrations, i.e. the volume percentages of each gas in the cathode outlet gas mixture were proportional to the GC peak areas, which were calibrated regularly using mass flow controllers.

### 2.6.2 Calculation of electrolysis efficiency

Faradaic efficiency was calculated to assess the CO<sub>2</sub>/H<sub>2</sub>O electrolysis efficiency. At a certain current, the Faradaic efficiency  $\eta$  for, e.g. CO yield thus could be described as:

$$\eta = \frac{\text{Actual CO production rate determined by GC analysis}}{\text{theoretical CO yield calculated according to Faraday's law}}$$

The actual CO production rate was calculated from the total flow rate and the variation in volume percentage of CO in the condition between a certain load and OCV, based on GC peak analysis. The theoretical CO yield was calculated using the current at the loading potential, according to Faraday's law. The electric efficiency, i.e. Faradaic efficiency of CO production was evaluated in different conditions, for instance, various CO<sub>2</sub>/CO ratios, operation temperatures, and cathode materials. In some cases, 5% H<sub>2</sub>/Ar was introduced to study its impact on the CO<sub>2</sub> electrochemical reduction process as well as on the Faradaic efficiency of CO<sub>2</sub> electrolysis.

### References

1. C. Xia, F. Chen, and M. Liu, *Electrochem. Solid-State Lett.*, **4** (5), A52 (2001)

2. D. Rotureau, J. –P. Viricelle, C. Pijolat, N. Caillol, M. Pijolat, *J. Eur. Ceram. Soc.*, **25**, 2633 (2005)
3. Y. Zhang, X. Huang, Z. Lu, X. Ge, J. Xu, X. Xin, X. Sha, W. Su, *Solid State Ionics*, **177**, 281 (2006)
4. A. Q. Pham and R. S. Glass, Proceedings of the Symposium on Electrically-Based Microstructural Characterization, Fall meeting of The Materials Research Society (MRS), Boston, MA (1995)
5. N. T. Hart, N. P. Brandon, M. J. Day, N. Lapeña-Rey, *J. Power Sources*, **106**, 42 (2002)
6. A. C. Müller, D. Herbstritt, E. Ivers-Tiffée, *Solid State Ionics*, **152-153**, 537 (2002)
7. S. Jiang, *Mater. Sci. Eng. A*, **418**, 199 (2006)
8. J. Kim, V. V. Nair, J. M. Vohs and R. J. Gorte, *Scripta Mater.*, **65**, 90 (2011)
9. A. Babaei, S. Jiang, and J. Li, *J. Electrochem. Soc.*, **156** (9), B1022 (2009)
10. J. Rossmeisl, W. G. Bessler, *Solid State Ionics*, **178**, 1694 (2008)
11. S. McIntosh, J. M. Vohs, and R. J. Gorte, *Electrochem. Solid-State Lett.*, **6** (11), A240 (2003)
12. G. Tsekouras, D. Neagu and J. T. S. Irvine, *Energy Environ. Sci.*, **6**, 256 (2013)
13. Thermal gravimetric analysis (TGA). Available online:  
[http://en.wikipedia.org/wiki/Thermogravimetric\\_analysis](http://en.wikipedia.org/wiki/Thermogravimetric_analysis)
14. X-ray diffraction (XRD). Available online:  
<http://epswww.unm.edu/xrd/xrdbasics.pdf>
15. XRD. Available online:  
<http://materials.binghamton.edu/labs/xray/xray.html>
16. J. R. Macdonald, W. B. Johnson, *Impedance spectroscopy Theory, Experiment, and Applications*, 2nd Edition, E. Barsoukov, J. R. Macdonald, Editors, p. 6, John Wiley & Sons, New Jersey (2005)
17. M. Smith, K. Cooper, D. Johnson, L. Scribner, *Comparison of Fuel Cell Electrolyte Resistance Measurement Techniques*, Reedited from April/May 2005 issue of Fuel Cell Magazine (2005)
18. X. Yuan, C. Song, H. Wang, J. Zhang, *Electrochemical Impedance Spectroscopy in PEM Fuel Cells Fundamentals and Applications*, p. 117, Springer, London (2010)
19. Scanning electron microscopy (SEM). Available online:

<http://science.howstuffworks.com/scanning-electron-microscope2.htm>

20. SEM. Available online:

<http://www.gla.ac.uk/schools/ges/research/researchfacilities/isaac/services/scanning-electronmicroscopy/>

21. SEM. Available online:

<http://mee-inc.com/sem.html>

22. Gas chromatography (GC). Available online:

<http://teaching.shu.ac.uk/hwb/chemistry/tutorials/chrom/gaschrn.htm>

## Chapter 3: Carbon sensitivity study on different potential cathode materials

### Table of Contents

Introduction .....	64
3.1 Carbon sensitivity on Ni-YSZ cathode.....	65
3.1.1 Ni/YSZ pellets preparation, treatment and post-characterization .....	65
3.1.2 Microstructure of Ni/YSZ pellets treated in CO <sub>2</sub> /CO atmospheres .....	67
3.1.3 TGA analysis on Ni/YSZ pellets treated in CO <sub>2</sub> /CO atmospheres .....	69
3.1.4 XRD inspection on Ni/YSZ pellets treated in CO <sub>2</sub> /CO atmospheres.....	76
3.2 Carbon sensitivity on LSCM-YSZ composite.....	78
3.2.1 LSCM/YSZ treatment in CO <sub>2</sub> -CO mixture and post-analysis on LSCM/YSZ pellet .....	78
3.2.2 SEM test on LSCM/YSZ pellets treated in CO <sub>2</sub> /CO 50/50 atmosphere .....	79
3.2.3 TGA on LSCM/YSZ samples pre-treated in CO <sub>2</sub> /CO 50/50 mixture .....	81
3.2.4 XRD measurement on LSCM/YSZ pellets after treatment in CO <sub>2</sub> /CO 50/50 atmosphere.....	82
3.3 Summary.....	83
References .....	83

## Chapter 3: Carbon sensitivity study on different potential cathode materials

### Introduction

Carbon sensitivity is vital for choice of cathode materials in the application of CO<sub>2</sub> reduction by SOECs, in that carbon formation through Boudouard reaction (Equation 1.14) occurs readily at high CO contents and at lowered temperature, such as 700°C. Coking resistance has been widely considered as one of the criteria to determine anode material that is capable of performing efficiently and durably in methane and/or hydrocarbon SOFCs, due to the obstacles in obtaining hydrogen fuel [1]. Unfortunately, the state-of-the-art anode material in SOFCs, namely, Ni based cermets, suffered from carbon deposition when CO or methane or other hydrocarbon was used as fuel, though Ni cermets showed excellent oxidation activity [2-5]. The introduction of large amount of steam into fuel for reformates could inhibit coke formation, however at a sacrifice of efficiency. Therefore, extensive efforts have been made either to develop alternative anode materials that are carbon resistant and could directly oxidize hydrocarbons or to construct innovative anode structures to protect anode from carbon and sulphur poisoning [2, 6-10]. In regard to the development of new materials to replace Ni cermet, a range of oxide materials including mixed electronic and ionic conducting perovskite ceramics and doped ceria, have been performed [2, 11-13]. (La,Sr)(Cr,Mn)O<sub>3</sub> (LSCM) perovskite is versatile in SOFCs with flexible options for fuels, because of its excellence in resistance of carbon and sulphur poisoning, thus has been considered as a potential alternative anode. In addition, LSCM has also been applied in high temperature steam electrolysis, and was reported to perform better than Ni/YSZ, especially at the absence of protective H<sub>2</sub> gas [14]. According to these studies, interest arises to apply LSCM to CO<sub>2</sub> electrolysis via a SOEC.

On the other hand, not all of the aspects of coke formation processes are completely clear, although Ni-cermets are well-known for its excellent C-C bond breaking activity and coking on an Ni surface is fairly well understood [15, 16]. The mechanisms of coke formation need to be looked into, especially in a complicated system such as SOFC running with a variety of fuels. For instance, carbon formed by CO disproportionation

(i.e. Boudouard reaction) or by methane pyrolysis could be readily removed at the presence of steam via Equation (3.1) [3, 10], which has been widely applied in industrial steam reforming for minimisation of coking [16].



Further, carbon could also be re-oxidized at high oxygen activities. Based on all these possibilities, a ‘modified reconstruction model’ was put forwarded to explain the unstable CO oxidation rate on Ni/YSZ electrode, which basically assumed a reconstruction and rearrangement of the Ni surfaces caused by different degree of carbon coverage on Ni surface [3]. Though the interpretation seemed reasonable from the indirect support of micro structural and chemical changes observed, more research work needs to be done to obtain insight into the processes occurring on Ni/YSZ electrodes in CO<sub>2</sub>-CO atmospheres.

In this chapter, a carbon sensitivity study will be carried out on Ni-cermet and LSCM/YSZ composite, prior to using them as SOEC cathode materials for CO<sub>2</sub> reduction. The experiment is according to Mond process, a technique used to be used commercially to extract and purify nickel [17]. Both materials will be treated in CO<sub>2</sub>-CO mixtures at a range of temperatures, with post-characterizations such as microstructure inspection, thermo gravimetric analysis and so on, followed.

### **3.1 Carbon sensitivity on Ni-YSZ cathode**

#### **3.1.1 Ni/YSZ pellets preparation, treatment and post-characterization**

Commercial NiO (NOVAMET) and 8% YSZ (P1-KEM) powder in a weight ratio of 65:35 was blended with 2 wt% KD-1 dispersant and 10 wt% of glassy carbon, then the powder mixture was ball milled for 24 hours in acetone, similar to that of preparing NiO/YSZ screen-printing ink as described in Chapter 2. The NiO/YSZ powder was obtained after evaporating all the acetone slowly after ball milling, and it was grounded for half an hour using a mortar and pestle. The resulting NiO/YSZ powder was then pressed uniaxially and fired at 1350°C for 4 hours, producing NiO/YSZ pellet with 0.8±0.05 mm in thickness and 19.5±0.5 mm in diameter.

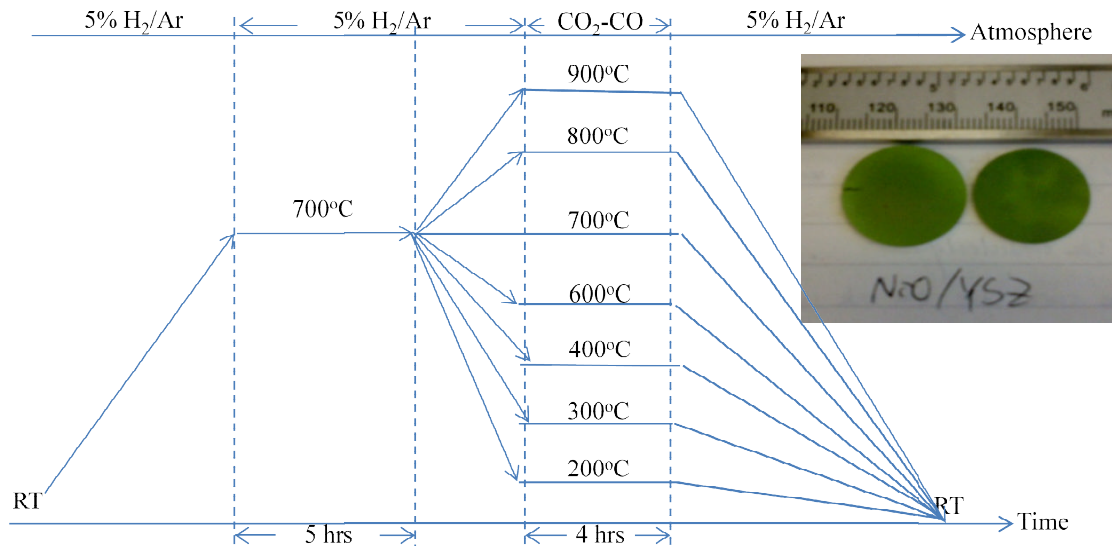


**Fig. 3.1** Schematic chart of Ni/YSZ pellets treatment

The as-prepared NiO/YSZ pellet was placed and sealed (using high vacuum grease) in a quartz tube which would be held in a tube furnace, followed by the CO<sub>2</sub>-CO treatment at different temperatures, as shown in Fig. 3.1. An image of fresh NiO/YSZ pellets is inserted on the top right in Fig. 3.1. The sample was heated 3°/min to 700°C in 5% H<sub>2</sub>/Ar gas, and it was left at 700°C for 5 hrs to reduce NiO to metallic Ni completely. Then, the furnace was heated or cooled 3°/min to different temperatures (900-200°C) at which 5% H<sub>2</sub>/Ar gas was switched off and Ni/YSZ pellets were exposed to various CO<sub>2</sub>-CO mixture for 4 hrs. The CO<sub>2</sub>-CO mixture studied included CO<sub>2</sub>/CO 90/10, CO<sub>2</sub>/CO 70/30, and CO<sub>2</sub>/CO 50/50. The Ni/YSZ pellet treated at 200°C was denoted as Ni/YSZ 200 herein, which was applicable to Ni/YSZ pellets treated at other temperatures. The NiO/YSZ pellet with only the reduction of NiO being conducted was regarded as reference sample, and was denoted as Ni/YSZ<sub>ref</sub> herein, compared to those being treated in CO<sub>2</sub>/CO mixtures at different temperatures after NiO reduction. After the above treatment, the 5% H<sub>2</sub>/Ar was switched back on and the furnace was cooled down to room temperature (RT) to retrieve the treated samples for post analysis.

The post-characterization of Ni/YSZ pellets consisted of SEM inspection, TGA and XRD measurements. For TGA, the thermal behaviours of the above as-treated samples were investigated in air, Ar and in 5% H<sub>2</sub>/Ar. The treated pellets were fractured, and a

few pieces (around 50 mg) were put in a crucible and heated to 900°C at a ramp rate of 5°C/min in air during which Ni would be re-oxidized (corresponding to a weight gain) and carbon, if there was, would be burnt out (corresponding to a weight loss). At 900°C, air was switched to Ar, which was flushed for the dwelling and the subsequent cooling down to 800°C, at which 5% H<sub>2</sub>/Ar was introduced and Ar was switched off. The samples were kept at 800°C for 2 hrs till NiO was fully reduced (no more weight loss was observed) after which temperature was lowered down to room temperature in 5% H<sub>2</sub>/Ar. The weight changes for the whole process were recorded as a function of running time and temperature as shown in Fig. 3.2.

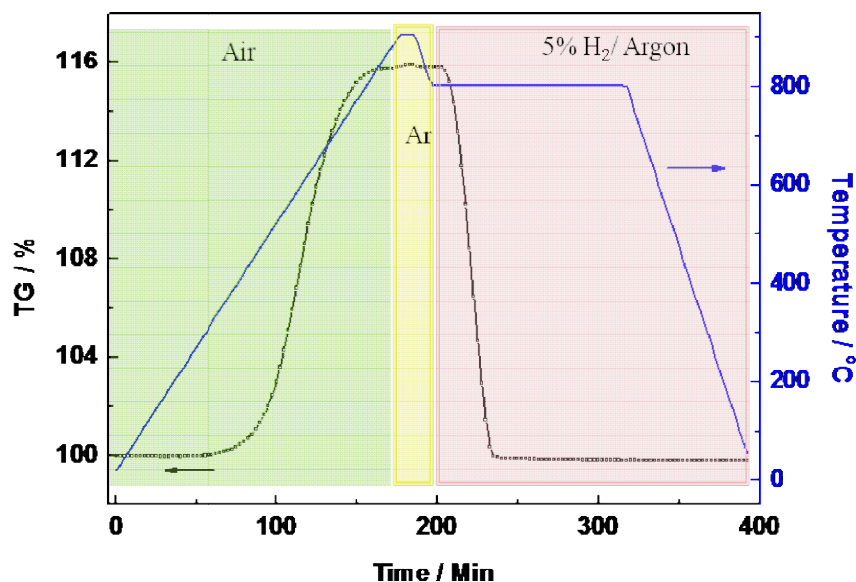


**Fig. 3.2** Typical TGA curve of Ni/YSZ<sub>ref</sub> sample (the green, yellow, and pink zone reflects running in air, Ar, and 5% H<sub>2</sub>/Ar gas, respectively)

The chemical phases present in the Ni/YSZ samples treated at different temperatures and CO<sub>2</sub>/CO mixtures were identified by XRD before and after TGA studies.

### 3.1.2 Microstructure of Ni/YSZ pellets treated in CO<sub>2</sub>/CO atmospheres

The SEM micrographs of Ni/YSZ<sub>ref</sub> and Ni/YSZ samples treated at different temperature in CO<sub>2</sub>/CO 50/50 condition are exhibited in Fig. 3.3. All the Ni/YSZ samples have porous structures, with large pores with dimensions of 5-15 μm from

glassy carbon pore former and small pores in sizes of 1-2  $\mu\text{m}$  from organic vehicles. From their SEM images, there are no evident difference between Ni/YSZ 900, Ni/YSZ 600, Ni/YSZ 400, and Ni/YSZ 300 sample from Ni/YSZ<sub>ref</sub> sample, in particle sizes and pore structures.

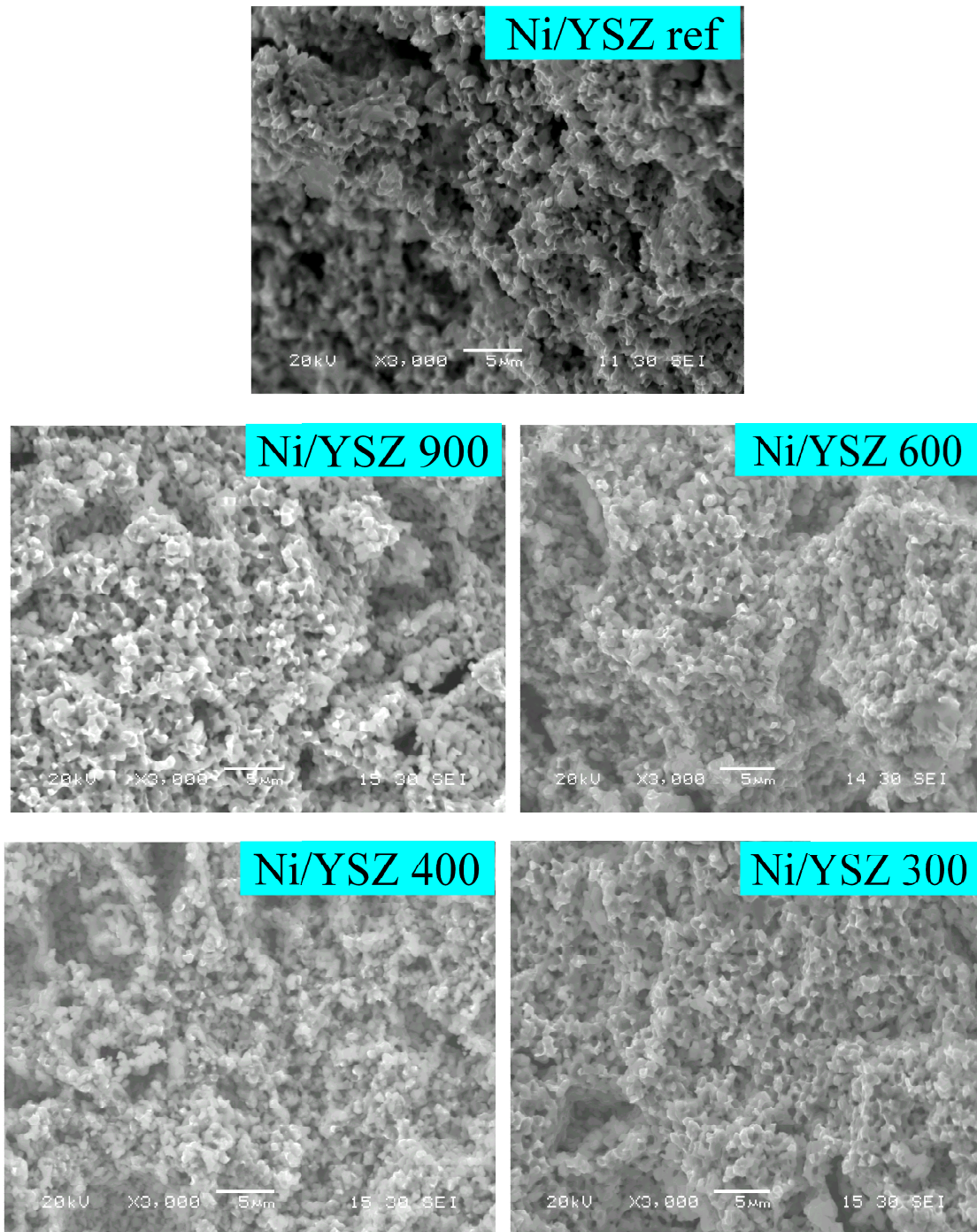


**Fig. 3.3** SEM images of the cross-sectional view of Ni/YSZ<sub>ref</sub> sample and Ni/YSZ pellet treated at 900°C, 600°C, 400°C and 300°C in CO<sub>2</sub>/CO 50/50 atmosphere

Fig. 3.4 is an image of NiO/YSZ fresh sample and fractures of Ni/YSZ pellets after treatment in CO<sub>2</sub>-CO 50-50 gas mixture and at different temperatures. As expected, the fresh NiO/YSZ pellet is green, and after reduction, the colour of the pellet turns to grey as shown by Ni/YSZ<sub>ref</sub> sample. Similar to Ni/YSZ<sub>ref</sub> sample, the Ni/YSZ pellets also become grey after being treated in CO<sub>2</sub>-CO mixture at different temperatures after reduction, with little distinction in colour among them.

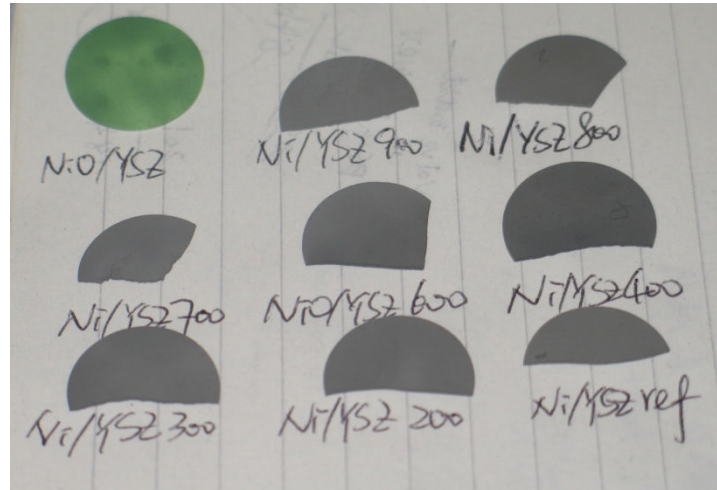


**Fig. 3.4** Graph of NiO/YSZ fresh pellet and Ni/YSZ pellets after treatment in CO<sub>2</sub>-CO 50-50 mixture at different temperatures

### 3.1.3 TGA analysis on Ni/YSZ pellets treated in CO<sub>2</sub>/CO atmospheres

Fig. 3.5 shows the TGA curves of Ni/YSZ samples pre-treated under different conditions. From the TGA curve of Ni/YSZ<sub>ref</sub> sample, the sample weight decreases a little bit from room temperature to around 300°C, due to a loss of moisture on the sample, and the sample weight increases markedly from 400 to 820°C, because of the weight gain from re-oxidation of metallic Ni to NiO, and at temperature higher than 820°C, the sample weight seems to level off. There is no significant weight change on heating in Ar atmosphere. However, when the atmosphere was switched to 5% H<sub>2</sub>/Ar at 800°C, a weight loss originating from reduction of NiO to Ni can be seen, and there is no more decrease in sample weight in 5% H<sub>2</sub>/Ar during the cooling down from 800°C to room temperature, indicating that the reduction of NiO has been completed during dwelling at 800°C.

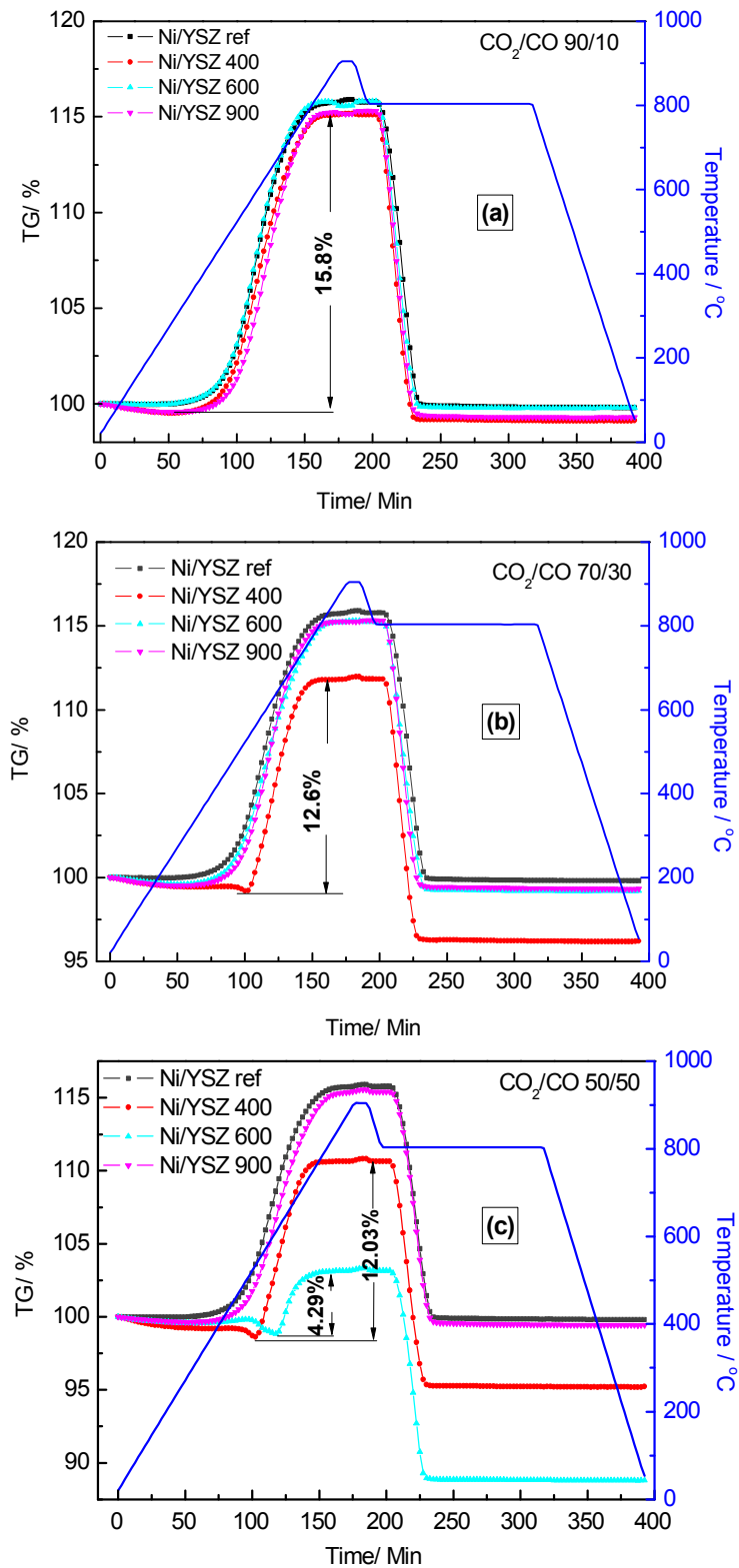


**Fig. 3.5** TGA curves of Ni/YSZ samples (Batch 1) that have been pre-treated at different temperatures in (a) CO<sub>2</sub>/CO 90/10, (b) CO<sub>2</sub>/CO 70/30 and (c) CO<sub>2</sub>/CO 50/50 atmosphere

In CO<sub>2</sub>/CO 90/10 mixture (Fig. 3.5(a)), the TGA curves of Ni/YSZ 400, Ni/YSZ 600, and Ni/YSZ 900 are similar to that of the Ni/YSZ<sub>ref</sub> sample, and there is no significant difference in weight increase from 400°C to 900°C in air for Ni/YSZ 400, Ni/YSZ 600 and Ni/YSZ 900 samples, compared to that of Ni/YSZ<sub>ref</sub> sample. The weight increases in air are around 16%, close to the theoretical value (17.6%) if there was no carbon deposited on Ni surface during the treatment in CO<sub>2</sub>/CO mixtures and thus weight gains were all from the re-oxidation of Ni. Similar results can be obtained from TGA curves in 5% H<sub>2</sub>/Ar gas where weight losses from the reduction of NiO are observed. The weight gain in air and the weight loss in 5% H<sub>2</sub>/Ar are almost identical; therefore, there is no big difference in weight change before and after TGA running for Ni/YSZ samples treated at different temperatures in CO<sub>2</sub>/CO 90/10 atmosphere.

The TGA curves of Ni/YSZ samples treated in CO<sub>2</sub>/CO 70/30 at different temperatures are presented in Fig. 3.5(b). It can be seen that the thermal behaviour of Ni/YSZ 600 and Ni/YSZ 900 in air and in 5% H<sub>2</sub>/Ar is similar to those being pre-treated in CO<sub>2</sub>/CO 90/10 atmosphere, i.e. only the weight variations from baking out moist, the re-oxidation of Ni in air and the reduction of NiO in 5% H<sub>2</sub>/Ar are observed, same with Ni/YSZ<sub>ref</sub> sample. With respect to the thermal response of Ni/YSZ 400 being pre-treated in CO<sub>2</sub>/CO 70/30, the sample weight reduces until temperature rises to around 522°C in air, and after this, sample weight increases remarkably, thus a peak due to weight loss at around 522°C can be observed besides the weight gain from re-oxidation of Ni at higher temperature in air. The weight gain from weight minimum to maximum is 12.6%, less than that of other samples. However, the weight loss from Ni/YSZ 400 sample as a result of re-reduction of NiO in 5% H<sub>2</sub>/Ar is 15.62%, almost identical to the weight loss from other samples in 5% H<sub>2</sub>/Ar.

Fig. 3.5(c) presents the TGA curves of Ni/YSZ samples that have been pre-treated in CO<sub>2</sub>/CO 50/50 mixture at different temperatures. Clearly, there is a peak with a weight minimum located at around 535°C and 610°C for Ni/YSZ 400 and Ni/YSZ 600 sample, respectively. And the subsequent weight gain from re-oxidation of Ni for the above two samples is 12.05% and 4.29%, respectively, smaller than the correspondent weight gain (~15.80%) for Ni/YSZ<sub>ref</sub> and Ni/YSZ 900 sample. Regarding the weight loss due to the

reduction of resultant NiO in 5% H<sub>2</sub>/Ar, the weight losses for Ni/YSZ 400 and Ni/YSZ 600 samples are lower than those for Ni/YSZ<sub>ref</sub> and Ni/YSZ 900 sample.

To obtain a clear idea, the results from TGA tests are summarized in Table 3.1 and Table 3.2. From Table 3.1, it can be learnt that the weight gains from Ni re-oxidation are 12.6% and 12.03% for Ni/YSZ 400 being pre-treated in CO concentration higher than 10% (i. e. CO<sub>2</sub>/CO 70/30 and CO<sub>2</sub>/CO 50/50, respectively) atmospheres, smaller than that on Ni/YSZ<sub>ref</sub> and Ni/YSZ 900 sample pre-treated under identical conditions, and the weight gain is 4.29% for Ni/YSZ 600 sample pre-treated in CO<sub>2</sub>/CO 50/50 mixture, dramatically smaller than Ni/YSZ<sub>ref</sub> and Ni/YSZ 900 sample in the same conditions. As Ni is well-known for its catalytic property for carbon formation via Boudouard reaction (Equation (1.14)), the weight losses at 300-650°C which thus resulted in smaller weight gains on Ni/YSZ 400 and Ni/YSZ 600 samples in air are probably due to the oxidation of carbon deposited on Ni/YSZ surface during pre-treatment in CO<sub>2</sub>/CO mixture. On the other hand, weight loss from oxidation of carbon in air is not present for Ni/YSZ 900 being pe-treated in CO<sub>2</sub>/CO atmospheres in Table 3.1, implying that carbon deposition is not favourable at temperature as high as 900°C. Therefore, from TGA results, the coke formation tended to occur at high CO concentration at 400-600°C.

**Table 3.1** Weight gain in air from Ni/YSZ samples pre-treated in different conditions

Atmosphere	Weight gain from the oxidation of Ni in air (%)			
	Ni/YSZ ref	Ni/YSZ 400	Ni/YSZ 600	Ni/YSZ 900
CO <sub>2</sub> /CO 90/10	15.80	15.59	15.85	15.72
CO <sub>2</sub> /CO 70/30	15.80	12.6	16.03	15.81
CO <sub>2</sub> /CO 50/50	15.80	12.03	4.29	15.78

**Table 3.2** Weight loss in 5% H<sub>2</sub>/Ar from Ni/YSZ samples treated in different conditions

Atmosphere	Weight loss from the reduction of NiO in 5% H <sub>2</sub> /Ar (%)			
	Ni/YSZ ref	Ni/YSZ 400	Ni/YSZ 600	Ni/YSZ 900
CO <sub>2</sub> /CO 90/10	15.98	15.97	16.02	15.99
CO <sub>2</sub> /CO 70/30	15.98	15.62	16.03	15.99
CO <sub>2</sub> /CO 50/50	15.98	15.43	14.36	15.98

Interestingly in Table 3.2, the weight losses in 5% H<sub>2</sub>/Ar are much lower on Ni/YSZ 400 being pre-treated in CO<sub>2</sub>/CO 70/30 and CO<sub>2</sub>/CO 50/50 atmospheres and on Ni/YSZ 600 being pre-treated in CO<sub>2</sub>/CO 50/50 mixture, compared to the weight losses on Ni/YSZ<sub>ref</sub> and on Ni/YSZ 900 sample. The above phenomenon indicates that some nickel compounds, possibly nickel carbide took place during sample pre-treatment and remained after Ni re-oxidation in air. Nickel carbide has been supposed to be an intermediate for whisker coke occurred on Ni surface, and to be unstable above 573 K, nonetheless, some researchers have found traces of nickel carbide in a steam reforming catalyst after using at about 723K [15]. Thereby, the smaller weight loss from reduction on Ni/YSZ 400 and Ni/YSZ 600 sample can be tentatively ascribed to the presence of nickel carbide, which survived after re-oxidation and reduction processes carried out in TGA test. The weight loss from NiO reduction is the smallest for Ni/YSZ 600 being pre-treated in CO<sub>2</sub>/CO 50/50 mixture, corresponding to the smallest weight gain from re-oxidation for this sample which might have the largest amount of carbon dissolution on Ni surface.

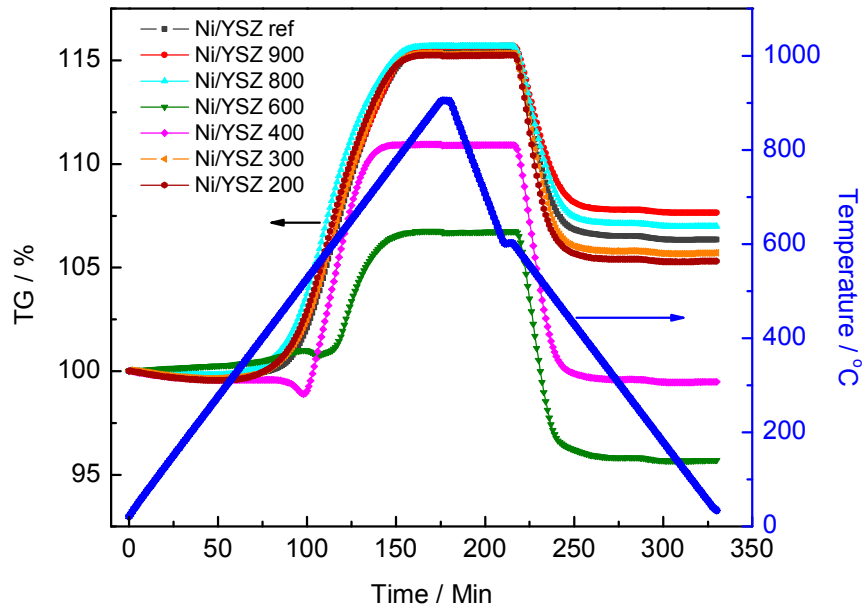


**Fig. 3.6** TGA curves of Ni/YSZ samples (Batch 2) treated at a temperature range of 200-900°C in CO<sub>2</sub>/CO 50/50 mixture (reduction program in 5% H<sub>2</sub>/Ar different from previous, but the oxidation program in air was the same)

The Ni/YSZ sample treatments were conducted in a wider range of temperature in CO<sub>2</sub>/CO 50/50 gas, and the TGA results from Ni/YSZ pre-treated at 200-900°C are shown in Fig. 3.6. The TGA running was the same as previous experiment, except that 5% H<sub>2</sub>/Ar was introduced at 600°C rather than 800°C and dwelling time was very short. It can be observed that only Ni/YSZ 400 and Ni/YSZ 600 sample show weight loss from removal of carbon in air, with other samples only presenting weight gain from re-oxidation of Ni. Note that the weight loss for NiO reduction from Ni/YSZ 200-300, Ni/YSZ 800-900, and Ni/YSZ<sub>ref</sub> are much smaller though little evidence of carbon was found, probably because the re-reduction of NiO to Ni has not been completed yet as the reducing temperature was low and dwelling time was not long enough. The weight losses for NiO reduction are in the sequence of Ni/YSZ 900 < Ni/YSZ 800 < Ni/YSZ<sub>ref</sub> < Ni/YSZ 300 < Ni/YSZ 200, which is reasonable considering the sintering of Ni particles at high temperature may slow reduction rate. As demonstrated in Fig. 3.7, when samples are exposed to 5% H<sub>2</sub>/Ar at a higher temperature (800°C) and a longer

period, the weight loss becomes identical for Ni/YSZ 200, Ni/YSZ 700, and Ni/YSZ<sub>ref</sub> sample where carbon was not found.

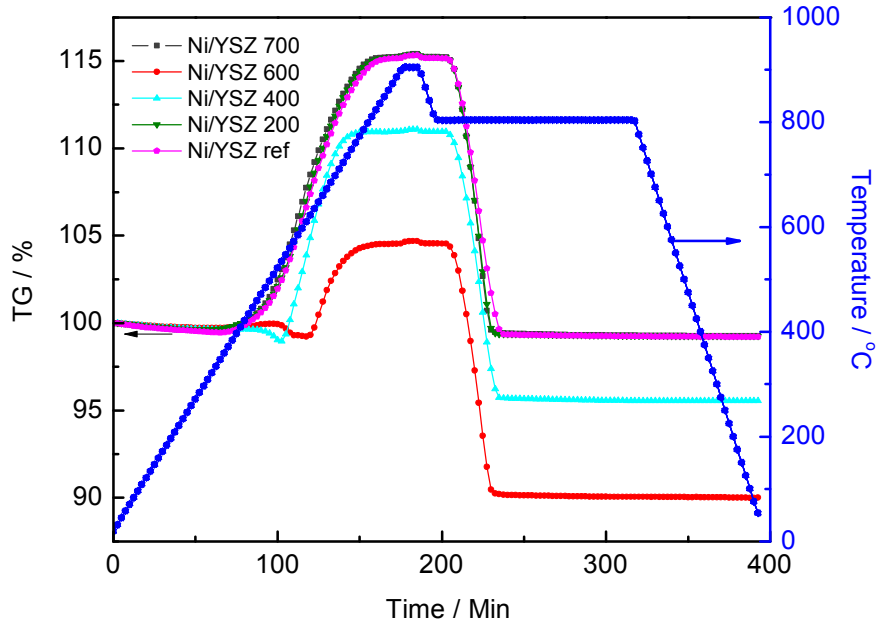


**Fig. 3.7** TGA curves of Ni/YSZ samples (Batch 2) pre-treated in CO<sub>2</sub>/CO 50/50 atmosphere with TGA reduction time extended and reduction temperature increased to 800°C compared to those in Fig. 3.6

Further, Ni/YSZ 200 and Ni/YSZ 300 samples behave similarly to Ni/YSZ<sub>ref</sub> in TGA measurement, and there is little evidence that volatile nickel carbonyl was formed during pre-treatment in CO<sub>2</sub>-CO mixtures. Nickel carbonyl is highly toxic and its formation is favoured when CO is concentrated at temperature lower than 230°C via Equation (3.2) [17, 18].



Nevertheless, the same weight gains in air for Ni/YSZ 200 and Ni/YSZ 300 sample suggest that the possible formation of nickel carbonyl seems not happening on these two samples in CO<sub>2</sub>/CO 50/50 mixture.

### 3.1.4 XRD inspection on Ni/YSZ pellets treated in CO<sub>2</sub>/CO atmospheres

Fig. 3.8 displays the XRD pattern comparison of Ni/YSZ 600 pre-treated in CO<sub>2</sub>/CO 50/50 atmosphere before and after TGA tests. Obviously, the diffraction peaks from Ni/YSZ 600 sample treated in CO<sub>2</sub>/CO 50/50 before TGA running can be assigned to Ni and YSZ phase except the one appears at 26.2° which might correspond to graphite carbon, whereas this peak is not present for Ni/YSZ 600 sample after TGA test, in accordance with the results obtained from TGA tests.

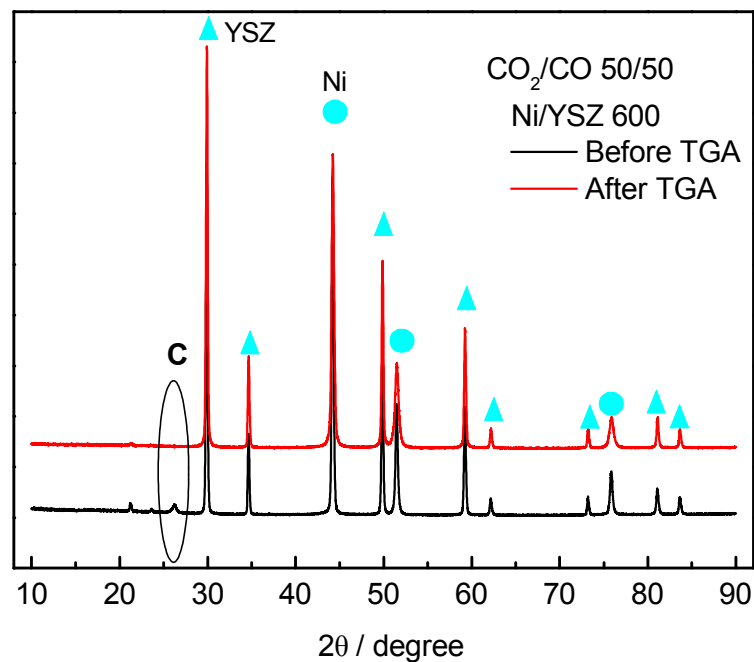


**Fig. 3.8** XRD pattern of Ni/YSZ 600 treated in CO<sub>2</sub>/CO 50/50 before and after TGA measurements

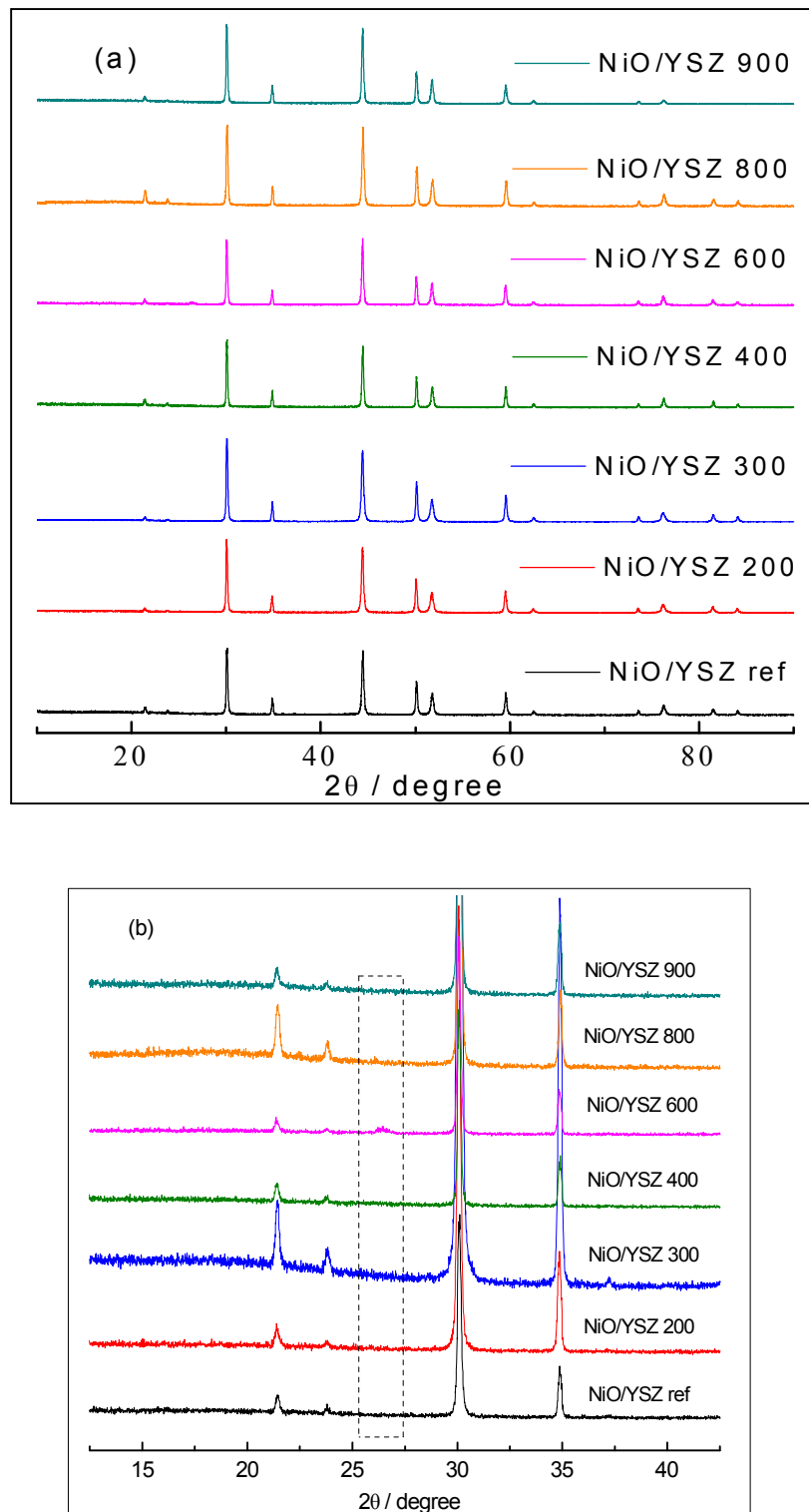


**Fig. 3.9** XRD pattern of (a) Ni/YSZ samples pre-treated at different temperatures in  $\text{CO}_2/\text{CO}$  50/50 mixture before TGA running and (b) its close up in the  $2\theta$  range of 12.5-47.5 degree

Fig. 3.9 is the XRD patterns of Ni/YSZ samples pre-treated at 200-900°C before TGA measurement as well as that of Ni/YSZ<sub>ref</sub> sample. No diffraction peaks originated from carbon can be seen for Ni/YSZ samples treated at temperatures other than 600°C in CO<sub>2</sub>/CO 50/50 mixture, which is in agreement with TGA results. The absence of carbon peaks on Ni/YSZ 400 sample is possibly due to its small amount accumulated on Ni surface which is under the detection limit. It is worth mentioning that coke on Ni catalyst has been found to be an accumulation process [16], therefore, coke has always been suspicious to pose problems to catalyst such as Ni in long term operation, though coke formed only at 400-600°C at high CO concentrations here. Besides, coke may take place at higher temperatures as a result of uneven local gas distribution and long-term operation.

### 3.2 Carbon sensitivity on LSCM-YSZ composite

In this experiment, LSCM/YSZ pellets will be prepared and treated in CO<sub>2</sub>-CO mixture, similar with the treatment of Ni/YSZ cermet pellet, in order to study its carbon resistance.

#### 3.2.1 LSCM/YSZ treatment in CO<sub>2</sub>-CO mixture and post-analysis on LSCM/YSZ pellet

(La<sub>0.75</sub>Sr<sub>0.25</sub>)<sub>0.97</sub>(Cr<sub>0.5</sub>Mn<sub>0.5</sub>)O<sub>3-δ</sub> (LSCM, EMPA) and YSZ (P1-KEM) powders in a weight ratio of 50/50 were mixed and pressed into pellets, with similar procedures with preparation of Ni/YSZ pellets in part 3.1.1. The LSCM/YSZ pellets were obtained after firing at 1300°C for 5 hrs; images of which is presented by Fig. 3.10. The LSCM/YSZ pellets were 23.1±0.1 cm in diameter and 1.2±0.5 mm in thickness. The LSCM/YSZ pellets were then treated in CO<sub>2</sub>/CO 50/50 mixture at different temperatures, similar to what have been done with Ni/YSZ pellets. And in like manner with Ni/YSZ sample, the LSCM/YSZ sample treated at 600°C was expressed as LSCM/YSZ 600, other samples were expressed likewise.

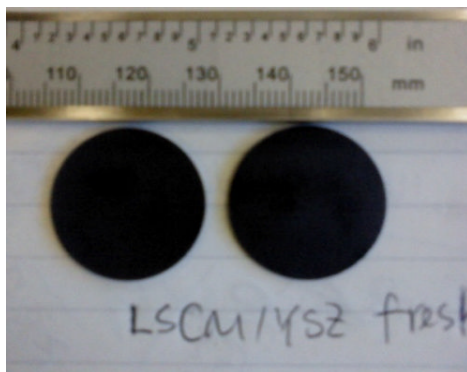


**Fig. 3.10** Image of LSCM/YSZ fresh samples

After being exposed to CO<sub>2</sub>/CO at different temperatures, the LSCM/YSZ pellets were fractured and a few pieces (total weight around 50mg) were picked for TGA measurements. The samples were heated at 5°/min to 900°C in air, held at 900°C for 2 hrs, and then cooled at 10°/min to room temperature. The weight changes during this process were recorded for TGA. The SEM was performed to evaluate the microstructure and morphology of pre-treated LSCM/YSZ pellets. The XRD measurement on LSCM/YSZ pellet was also undertaken at room temperature to inspect the phase purity after treatment in CO<sub>2</sub>-CO mixture.

### 3.2.2 SEM test on LSCM/YSZ pellets treated in CO<sub>2</sub>/CO 50/50 atmosphere

The microstructure of LSCM/YSZ pre-treated samples and LSCM/YSZ reference sample is indicated in Fig. 3.11 by SEM images.

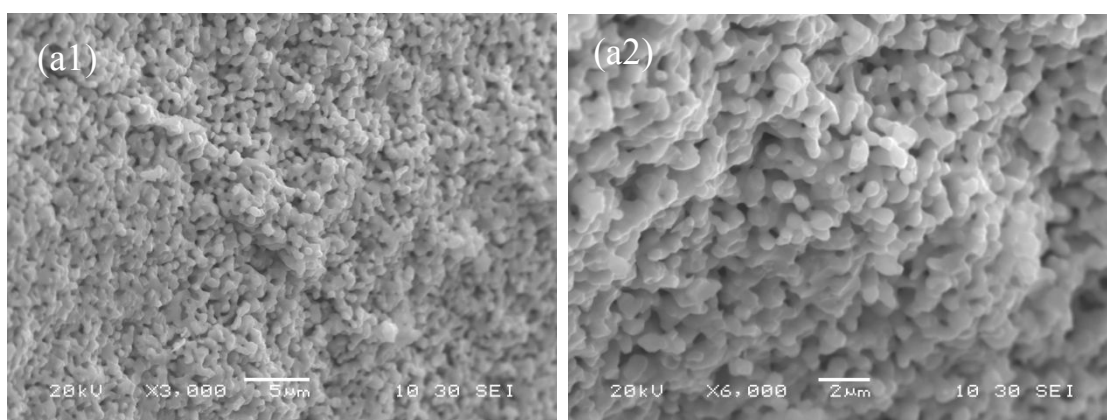


(Figure continued on the following page)

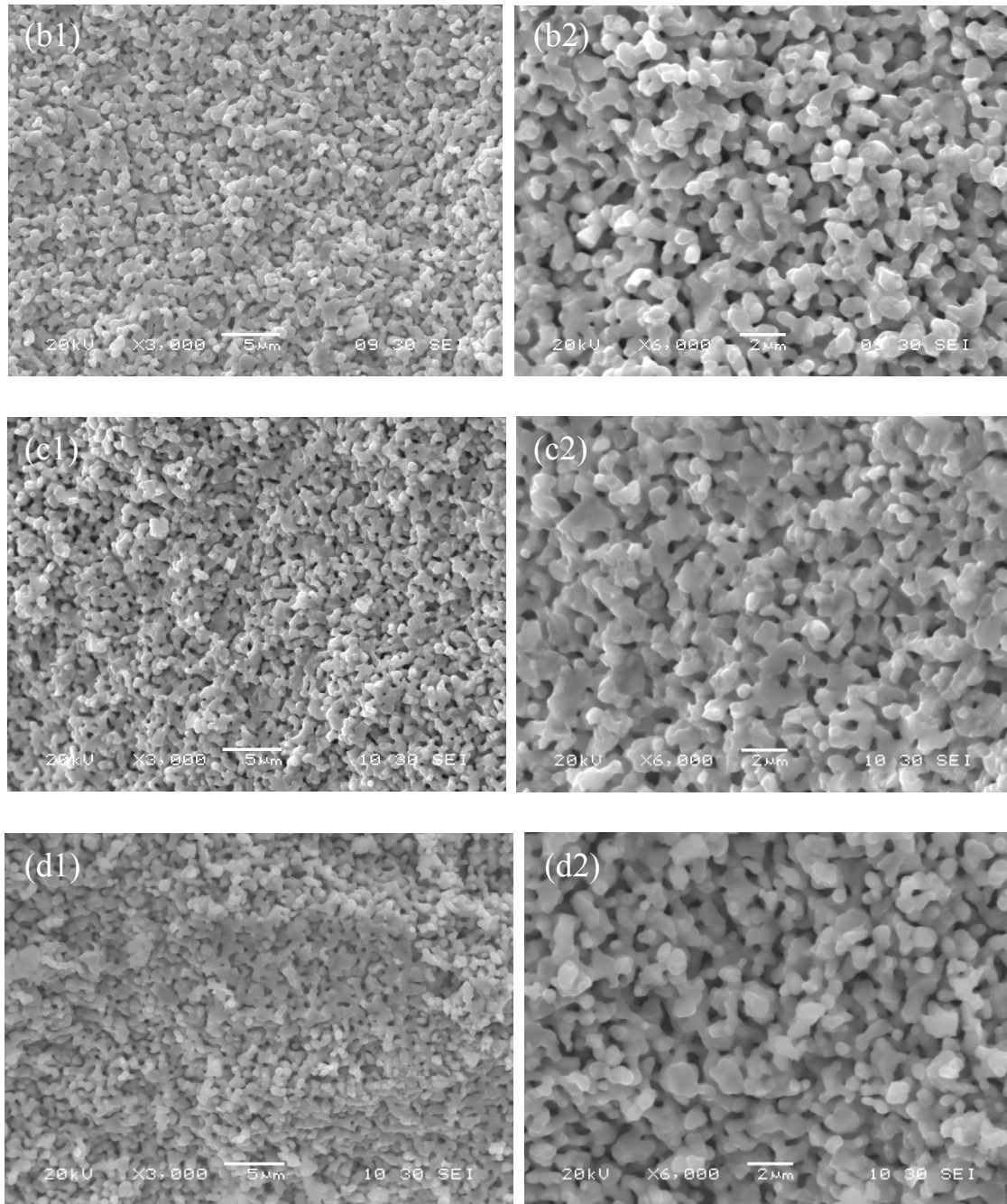


**Fig. 3.11** SEM cross-sectional view of LSCM/YSZ pellet after being treated in CO<sub>2</sub>/CO 50/50 mixture at (a1 and a2) 600°C, (b1 and b2) 700°C and (c1 and c2) 800°C as well as that of (d1 and d2) LSCM/YSZ reference sample

In Fig. 3.11, the LSCM/YSZ samples treated in different conditions all possess porous structure, with most of pore sizes in the range of few microns. In LSCM/YSZ composite,

it seems that YSZ particles weld together and LSCM particles locate on the surface of YSZ. The microstructures of LSCM/YSZ pre-treated at different temperatures appear to be similar, and no significant amount of carbon was detected by EDX on these samples.

### 3.2.3 TGA on LSCM/YSZ samples pre-treated in CO<sub>2</sub>/CO 50/50 mixture

Fig. 3.12 shows the TGA curves of LSCM/YSZ samples in air after the sample treatments at 600-900°C in CO<sub>2</sub>/CO 50/50 mixture. The weight gains of ~0.7-0.85% were obtained for LSCM/YSZ pre-treated samples, with most of the weight gain taking place between room temperature and 600°C. Contrast with pre-treated Ni/YSZ, there are hardly any evidences for weight loss from carbon oxidation, in other words, LSCM possesses rather good tolerance towards coke formation, even at the condition which contains CO content as high as 50 mol%, which is a preferable characteristic over Ni/YSZ cermets.

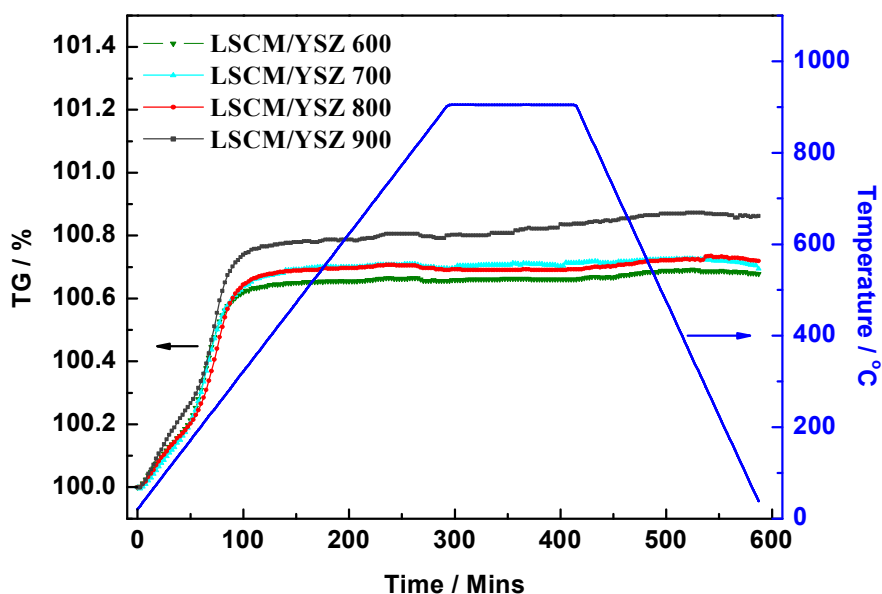


**Fig. 3.12** TGA curves of pre-treated (in CO<sub>2</sub>/CO 50/50) LSCM/YSZ samples in air

The weight gain from LSCM/YSZ sample in air, corresponding to the change of oxygen content in LSCM phase, is around 0.8% for LSCM/YSZ 600-800, and is a little higher, 1.0% for LSCM/YSZ 900 sample. These values are less than 1.8% as reported in

literature [11], which is reasonable considering LSCM was pre-reduced for 120 hrs and may uptake more oxygen in literature [11].

### 3.2.4 XRD measurement on LSCM/YSZ pellets after treatment in CO<sub>2</sub>/CO 50/50 atmosphere

The XRD pattern of LSCM/YSZ samples treated in CO<sub>2</sub>/CO 50/50 prior to TGA measurement is shown in Fig. 3.13. Apparently, no secondary phase is observed from LSCM/YSZ 600 sample and diffraction peaks can only be assigned to either LSCM or YSZ phase, identical with LSCM/YSZ<sub>ref</sub> sample, which was not pre-treated in CO<sub>2</sub>/CO mixture. This phenomenon is in contrast with what was observed from Ni/YSZ 600 sample being pre-treated in similar conditions as LSCM/YSZ counterpart, the latter clearly showed evidence for coke formation during treatment in CO<sub>2</sub>/CO mixture. This is not surprising as LSCM has been demonstrated promising as anode component in methane or hydrocarbon fuelled SOFC and LSCM performed superior over Ni/YSZ cermet in SOFC running with methane or hydrocarbon without using excess steam due to its relatively good carbon and sulphur tolerance [6, 11, 19-21].

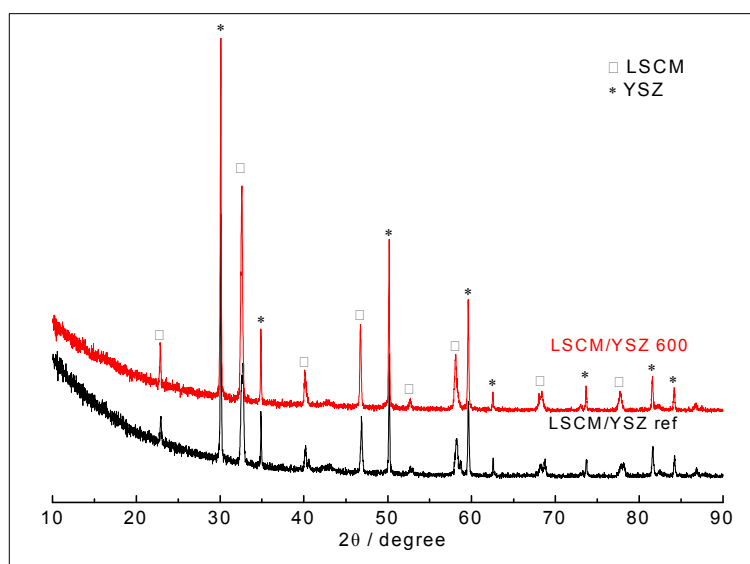


**Fig. 3.13** XRD results of LSCM/YSZ<sub>ref</sub> and LSCM/YSZ 600 samples pre-treated in CO<sub>2</sub>/CO 50/50 mixture

### 3.3 Summary

In this chapter, the carbon tolerance of Ni/YSZ cermet and LSCM/YSZ composite was investigated and compared between these two kinds of cathode that are potential in high temperature CO<sub>2</sub> electrolysis.

Ni/YSZ cermet was subjected to coking, and carbon formation happened in temperature range of 400-600°C when CO content in CO<sub>2</sub>-CO mixture was higher than 10 vol. %. Further, a loss of Ni was observed on Ni/YSZ 400 and Ni/YSZ 600 sample from TGA results, probably due to the occurrence of nickel carbide, however, extra evidence needs to be provided to prove this. Nickel carbonyl was not found from Ni/YSZ 200-300 sample after treatment in various CO<sub>2</sub>-CO mixtures, from TGA measurements, because the weight of Ni was hardly varied compared to that of the sample without treatment. Contrast with Ni/YSZ cermet, LSCM/YSZ composite showed no evidence for carbon formation when being treated in CO<sub>2</sub>-CO 50-50 mixture at 600-900°C, indicating its good carbon tolerance.

### References

1. Y. Huang, R. I. Dass, Z. Xing, J. B. Goodenough, *Science*, **312**, 254 (2006)
2. J. B. Goodenough, Y. Huang, *J. Power Sources*, **173**, 1 (2007)
3. P. Holtappels, L. G. J. De Haart, U. Stimming, I. C. Vinke and M. Mogensen, *J. Appl. Electrochem.*, **29**, 561 (1999)
4. J. Liu, S. A. Barnett, *Solid State Ionics*, **158**, 11 (2003)
5. J. Koh, Y. Yoo, J. Park, H. Lim, *Solid State Ionics*, **149**, 157 (2002)
6. S. Tao and J. T. S. Irvine, *Nature Mater.*, **2**, 320 (2003)
7. A. Atkinson, S. Barnett, R. J. Gorte, J. T. S. Irvine, A. J. Mcevoy, M. Mogensen, S. C. Singhal and J. Vohs, *Nature Mater.*, **3**, 17 (2004)
8. R. J. Gorte, S. Park, J. M. Vohs and C. Wang, *Adv. Mater.*, **12**, 1465 (2000)
9. E. P. Murray, T. Tsai & S. A. Barnett, *Nature*, **400**, 649 (1999)
10. J. Kang, D. Kim, S. Lee, S. Hong, D. Moon, *App. Catal. A: General*, **332**, 153 (2007)
11. S. Tao and J. T. S. Irvine, *J. Electrochem. Soc.*, **151(2)**, A252 (2004)
12. S. Park, J. M. Vohs & R. J. Gorte, *Nature*, **404**, 265 (2000)
13. O. A. Marina, C. Bagger, S. Primdahl, M. Mogensen, *Solid State Ionics*, **123**, 199

(1999)

14. X. Yang and J. T. S. Irvine, *J. Mater. Chem.*, **18**, 2349 (2008)
15. D. L. Trimm, *Catal. Today*, **37**, 233 (1997)
16. D. L. Trimm, *Catal. Today*, **49**, 3 (1999)
17. L. Mond, C. Langer, and F. Quincke, *J. Chem. Soc. Trans.*, **57**, 749 (1890)
18. M. Pastula, J. Smith et. al, U S Patent, US 7892687 B2 (2011)
19. S. P. Jiang, X. L. Chen, S. H. Chan, J. T. Kwok, K. A. Khor, *Solid State Ionics*, **177**, 149 (2006)
20. S. Tao, J. T. S. Irvine, and S. M. Plint, *J. Phys. Chem. B*, **110**, 21771 (2006)
21. X. J. Chen, Q. L. Liu, S. H. Chan, N. P. Brandon, and K. A. Khor, *J. Electrochem. Soc.*, **154** (11), B 1206 (2007)

**Chapter 4: Initial performance from different cathode materials for  
high temperature CO<sub>2</sub> electrolysis**

**Table of Contents**

Introduction .....	86
4.1 Cell fabrication and characterization.....	87
4.2 Ni-YSZ cermet cathode performance towards CO <sub>2</sub> electrolysis.....	89
4.3 LSCM-YSZ composite.....	95
4.3.1 Choice of current collector for LSCM/YSZ cathode.....	95
4.3.2 Performance from LSCM/YSZ composite cathode for CO <sub>2</sub> electrolysis.....	97
4.4 LSCM-GDC composite cathode.....	102
4.5 Comparisons between Ni-cermet and LSCM based cathode .....	109
4.5.1 Microstructure comparisons .....	109
4.5.2 Performance comparisons for CO <sub>2</sub> electrolysis by SOEC.....	111
4.5.3 Cathode activation energy for CO <sub>2</sub> reduction via a SOEC.....	114
4.6 Stability test on LSCM/GDC cathode in CO <sub>2</sub> -CO mixture.....	116
4.7 Summary.....	118
References .....	119

## **Chapter 4: Initial performance from different cathode materials for high temperature CO<sub>2</sub> electrolysis**

### **Introduction**

Since the dissociation of CO<sub>2</sub> to form CO and oxygen anion occurs on the cathode of SOEC, it is of great importance to study the state-of-the-art cathode materials, the kinetics of cathode reaction, and the electrochemical reaction mechanisms of CO<sub>2</sub> electrolysis. Taking the practical application of this technology in the future into account, it is also of great concern to investigate inexpensive materials and cost-effective fabrication techniques, in order to achieve high performing and long-term stable SOECs.

Required by SOEC cathode reaction, the cathode material should have an adequately porous structure to make the gas diffuse easily; in the mean time, it should have sufficiently high ionic and electronic conductivity in which case the electrons and oxide ions would transfer fast from/to the active sites to facilitate cathode reaction. Moreover, to guarantee a long-term operation, the cathode material should be chemically and physically stable in highly oxidizing/reducing environments and compatible with its adjacent components, i.e. electrolyte and interconnect.

Based on the similarity between SOFC and SOEC, it is natural to consider the well-known anode materials used in SOFCs as starting point for development of cathode materials in SOECs. A few reports concerned the reduction of CO<sub>2</sub> in SOECs employing precious metal platinum (Pt) as cathode, and it has been found that Pt has very high activation over-potential thus low electrolysis efficiency [1-2]. In addition, Pt would not be considered as a practical cathode for large-scale CO<sub>2</sub> electrolysis cell because of its high cost. Alternatively, Ni based cermets [3-11] and ceramic materials [12-18] are the most investigated anode materials in SOFCs, which may also be employed as cathode materials in SOECs, and there are already some research efforts on these materials aiming to obtain a high performance SOEC used for CO<sub>2</sub> electrolysis [19-21]. Yet, there are still limited reports on CO<sub>2</sub> electrolysis, and the mechanisms of CO<sub>2</sub> reduction are still not fully understood. In this chapter, a number of SOECs with different cathodes, such as Ni/YSZ, LSCM/YSZ and LSCM/GDC composite will be

fabricated simply by screen printing and firing at different temperatures. The cathode performance will be evaluated in various CO<sub>2</sub>/CO atmospheres, potentials, and operation temperatures and, comparisons will be made among these cathodes performance.

#### 4.1 Cell fabrication and characterization

An YSZ pellet was pressed and fired, as described previously in Chapter 2, producing an YSZ pellet with ca. 20 mm in diameter and ca. 2 mm in thickness. The as-prepared YSZ pellet was polished and cleaned on both sides.

Three-electrode geometry was adopted, and electrodes were introduced by screen-printing. Regarding the working electrode (WE), i.e. cathode in electrolysis cell, NiO/YSZ (65/35 by weight) ink, (La<sub>0.75</sub>Sr<sub>0.25</sub>)<sub>0.97</sub>(Cr<sub>0.5</sub>Mn<sub>0.5</sub>)O<sub>3-δ</sub> (LSCM, EMPA, Switzerland)/YSZ (50/50 by weight) ink or LSCM/(Gd<sub>0.1</sub>Ce<sub>0.9</sub>)O<sub>1.95</sub> (GDC, PRAXAIR, 99.9%, d<sub>50</sub> 1μm) (50/50 by weight) ink was screen-printed on one side of YSZ pellet and fired at different temperatures, 1350°C (1h) for Ni/YSZ cathode, 1200°C (2 hrs) for LSCM/YSZ composite cathode, and 1300°C (2 hrs) for LSCM/GDC composite cathode, respectively. While considering counter electrode (CE) and reference electrode (RE), (La<sub>0.8</sub>Sr<sub>0.2</sub>) MnO<sub>3</sub> / Scandium stabilized YSZ (LSM/ScSZ, 50/50 by weight) ink was screen-printed on the back side of YSZ pellet and sintered at 1100°C (2 hrs).

Prior to electrochemical characterization, current collectors were applied. Pt paste (Gwent, C2000904P3) was painted on CE and RE side and fired at 900°C for 1 h as current collector. With regard to cathode current collector, Ni mesh was adhered to NiO/YSZ surface using dot-painted Pt paste, and then fired at 900°C for 1 hour. With respect to current collector for LSCM based composite, different kinds of materials including Au mesh, Pt mesh, Pd/LSCM mixture, Pt paste etc., were tried and compared, aiming to find a suitable one. For Pd/LSCM mixture, it was screen-printed on top of cathode layer and was co-sintered with the latter to obtain a good bonding, similar to description in ref [22]. For the other current collectors, they were applied after firing cathode layer at high temperature.

The as-prepared single cell was attached to testing jig, as described in Chapter 2. Pt probes were used to connect the cell to electrochemical instruments. The testing chamber was heated to 300°C slowly to properly cure the ceramic cement so to seal the chamber, before heating up to operating temperature 900°C, at which 5% H<sub>2</sub>/Ar was flowed to the fuel compartment, to firstly reduce NiO to metallic Ni in the case of Ni/YSZ cathode. At steady state, the I-V curves and EIS were recorded. Afterwards, CO<sub>2</sub>-CO mixture (at a total flow rate of 30 ml/min) with different CO<sub>2</sub>/CO ratios was introduced while 5% H<sub>2</sub>/Ar was stepped to zero. The CO<sub>2</sub>/CO ratios investigated varied from 90/10 to 50/50 in the case of Ni/YSZ cathode, and to 30/70 in the case of LSCM based cathodes. Cathode performance was characterized in CO<sub>2</sub>/CO mixtures by polarization curves and EIS measurement, and factors that would affect the CO<sub>2</sub> electrochemical reduction processes, e.g., cathode material, operation potential and temperature were studied. The EIS, with frequency ranging from 10<sup>5</sup> to 0.1 or 0.015 Hz at AC voltage amplitude of 10mV, were recorded at OCV and under different voltages applied to the cell. The applied voltages were 0.2V, 0.5V, 0.8V, and 1.0V referred to the OCV value respectively herein (stated otherwise), meaning that if the OCV was -0.9V, the operating potential would be -1.1V (absolute voltage) when 0.2V was applied to the cell.

After measurements at 900°C, the cell was tested in the temperature range of 850-750°C at an interval of 50°C in CO<sub>2</sub>/CO 70/30 atmosphere. When all the electrochemical characterizations were finished, 5% H<sub>2</sub>/Ar gas was switched back on during cooling furnace to room temperature. During the whole tests, air was flowed to the air/oxygen side at a constant flow rate of 100 ml/min.

Simulations of EIS were carried out using Equivalent circuit approach to better understand the cathode properties on CO<sub>2</sub> electrolysis. The SEM and EDX were employed to look into the electrode microstructures after electrochemical measurements, and XRD was performed to identify material composition after electrochemical characterization.

#### 4.2 Ni-YSZ cermet cathode performance towards CO<sub>2</sub> electrolysis

Fig. 4.1 shows the SEM images of the cell with Ni/YSZ cathode after being tested at different atmospheres and temperatures. The Ni/YSZ and LSM/ScSZ electrode are ca. 30  $\mu\text{m}$  in thickness, and both electrodes show evenly porous structure. It can be seen that both Ni/YSZ cathode (Fig. 4.1(a)) and LSM/ScSZ anode (Fig. 4.1(b)) bind very well to YSZ electrolyte after cell measurements, without any detectable delamination.

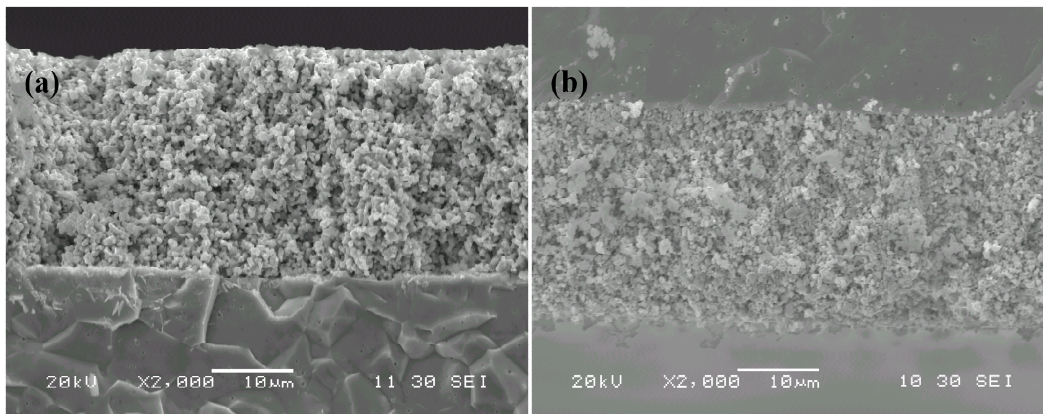


**Fig. 4.1** SEM micrographs of Cross-section view of (a) Ni/YSZ-electrolyte interface and (b) LSM/ScSZ- electrolyte interface

Typical I-V curves of the Ni/YSZ cathode cell working in both the electrolysis (negative current densities) and fuel cell (positive current densities) modes at 900°C are displayed in Fig. 4.2. The open circuit voltage (OCV) values, obtained from I-V curves at different atmospheres are summarized in Table 4.1. The practical OCV value is -0.92V in wet 5% H<sub>2</sub>/Ar atmosphere, -(0.7-0.9)V in different CO<sub>2</sub>/CO mixtures studied presently, quite close to the theoretical values predicted by Nernst equation.

It can be observed from Fig. 4.2 that all the I-V curves tested in different fuels go smoothly from electrolysis manner to fuel cell manner. And, there is nearly no hysteresis from electrolysis to fuel cell mode and backwards, especially under CO<sub>2</sub>/CO atmosphere, suggesting the cell works well in a reversible manner. Moreover, the I-V curves of the cell in different CO<sub>2</sub>/CO mixtures show clearly linear trends in both the electrolysis and fuel cell modes, while the I-V curve in wet H<sub>2</sub> gas has an appreciable increase in cell resistance in the potential range of -(1.2-2.0) V in electrolysis mode,

distorting the I-V curve to the non-linear behaviour, probably due to the inadequate steam supplied, which will be discussed in detail in Chapter 7.

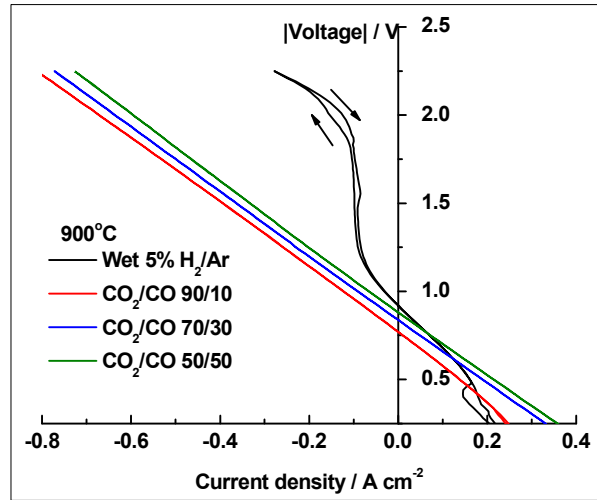


**Fig. 4.2** I-V curves of the Ni/YSZ cathode cell operated at 900°C at different atmospheres (the I-V curves start from OCV to -2.25 V, then come down to -0.25V through OCV, and finally go back to OCV to complete a scanning cycle)

**Table 4.1** Summary of the OCV values of the Ni/YSZ cathode cell operated at 900°C

	Theoretical OCV value (V)*	Practical OCV value (V)
Wet 5% H <sub>2</sub> /Argon	-0.94	-0.918
CO <sub>2</sub> /CO 90/10	-0.785	-0.769
CO <sub>2</sub> /CO 70/30	-0.853	-0.837
CO <sub>2</sub> /CO 50/50	-0.896	-0.881
CO <sub>2</sub> /CO 30/70	-0.939	---

\* Calculation according to Nernst equation: In the calculation of the theoretical OCV values, an assumption that the dissociation of CO<sub>2</sub> is the mainly reaction that takes place on the Ni/YSZ cathode was made. The reaction equilibrium coefficient refers to HSC 5.1 software.

--- Not tested in this case

The Nyquist plot of the impedance of the Ni/YSZ cathode working in CO<sub>2</sub>/CO 70/30 at different voltages at 900°C is illustrated in Fig. 4.3. One can see that an inductive portion, which could be assigned to losses from the test wires and the instrument, appears at high frequency with the resistance of the intercept, namely, ohmic resistance  $R_s$ , coming mainly from the thick YSZ electrolyte. There are two distinct arcs in Fig. 4.3, similar with the report on CO<sub>2</sub> reduction using Ni/YSZ electrode in the same atmosphere [23] and contrast to those found by Matsuzaki and Yasuda for CO oxidation on Ni/YSZ electrode [24], probably due to differences in microstructures resulting from different fabrication conditions.

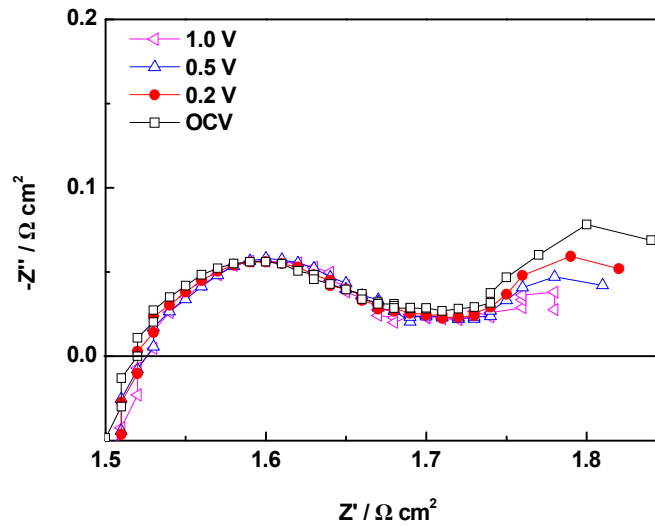


**Fig. 4.3** Nyquist plots of impedance from the Ni/YSZ cathode operated in CO<sub>2</sub>/CO 70/30 atmospheres at different cell voltage at 900°C in SOEC operation (The OCV value for this one is -0.837V, and the cell voltages are -1.037V, -1.337V, and -1.837V when 0.2V, 0.5V and 1.0V is applied)

In Fig. 4.3, the  $R_s$  does not change much with voltage, nor does the impedance arc at high frequency range. The low frequency arc, however, decreases slightly with increasing voltage, which is rational as the I-V curve (Fig. 4.2) in corresponding atmosphere was weakly current dependent and no evidence for major diffusion limitations were observed. It is assumed that the high frequency arc reflects impedance from charge transfer processes for CO<sub>2</sub> dissociation, with the low frequency arc coming from impedance from mass transfer processes, including dissociative adsorption of CO<sub>2</sub>

and intermediate active species from CO<sub>2</sub> dissociation on the electrode surface and subsequent diffusion of the species absorbed on the surface to the sites of the charge-transfer reaction [20, 24], consequently, the decreased low frequency arc means that the surface kinetics are probably improved with the progress of CO<sub>2</sub> reduction at higher voltages.

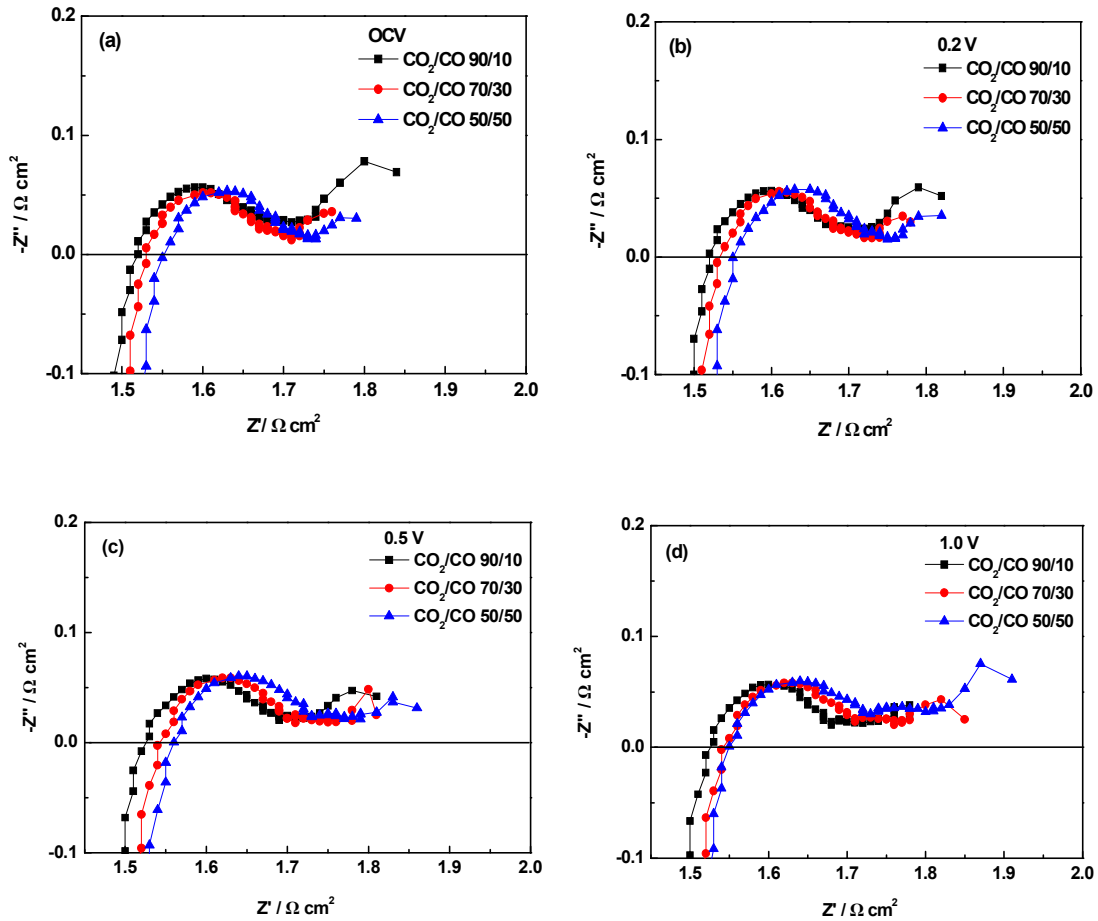


**Fig. 4.4** Nyquist plots of the impedance of the Ni/YSZ cathode under (a) OCV, (b) 0.2V, (c) 0.5V and (d) 1.0V at different atmospheres at 900°C (Black: CO<sub>2</sub>/CO 90/10, red: CO<sub>2</sub>/CO 70/30, and blue: CO<sub>2</sub>/CO 50/50. The cell voltages are the same as explained in Fig. 4.3 and the frequency of the impedance ranges from 10<sup>5</sup>Hz to 0.1Hz. The measurements were taken from OCV condition to more negative voltage conditions)

The impedance responses of the Ni/YSZ cathode in different CO<sub>2</sub>/CO ratios, as well as at different voltages, are compared in Fig. 4.4. Over a range of loading, the R<sub>s</sub> increases

with CO content in fuels; on the other hand, the  $R_p$  reduces with increasing voltage in CO<sub>2</sub>/CO 90/10 mixture, with  $R_p$  being 0.32, 0.3, 0.28, 0.25  $\Omega \text{ cm}^2$  at OCV, 0.2, 0.5, 1.0V respectively, whereas  $R_p$  increases with voltage in the gas mixture at CO concentration higher than 30%, for instance, the  $R_p$  are 0.24, 0.27, 0.30, 0.36  $\Omega \text{ cm}^2$  at OCV, 0.2, 0.5, 1.0V respectively in CO<sub>2</sub>/CO 50/50 mixture. Additionally, the cell shows smaller  $R_p$  (0.24  $\Omega \text{ cm}^2$ ) in CO<sub>2</sub>/CO 50/50 compared to that in CO<sub>2</sub>/CO 90/10 at OCV (Fig. 4.4(a)), however it displays larger  $R_p$  (0.36  $\Omega \text{ cm}^2$ ) in CO<sub>2</sub>/CO 50/50 upon applying 1.0V to the cell (Fig. 4.4(d)). Regarding the limitations of Ni-cermets addressed before, it could be supposed that the increment in  $R_p$  with increasing CO concentration is possibly due to carbon formation through Boudouard reaction. The coke formed on the surface of Ni catalyst would block pores and reduce the active sites for CO<sub>2</sub> reduction reaction, as a result, increase the  $R_p$ .

In Fig. 4.4, with increasing CO content, the high frequency arc from impedance spectra is almost unchanged but the low frequency arc decreases for the cell working at different voltages, except that at 1.0V in the atmosphere with CO content higher than 30 vol.%. In regard to the exceptional case mentioned above, the low frequency arc becomes larger with increasing voltage and CO concentration instead, probably resulting from carbon deposition on Ni surface, as discussed previously. Some researchers thought that another origin for C formation was from deeper electrolysis of CO<sub>2</sub> under high load [3, 25], hence enlarged the low frequency arc with increasing voltage. Although the coking has been reported to be catalytically favourable on Ni surface in CO<sub>2</sub>/CO or hydrocarbon fuels, we should bear in mind that there could be a variety of possibilities involved [26]. For instance, the deposited carbon could be oxidized through the reverse Boudouard reaction when the cell gets back to OCV, and the presence of steam could remove carbon via Equation (3.1). In the present study, the carbon has been detected on Ni/YSZ cathode after testing (not presented), but it is difficult to certain of the conditions under which the carbon formed as it was detected ex-situ.

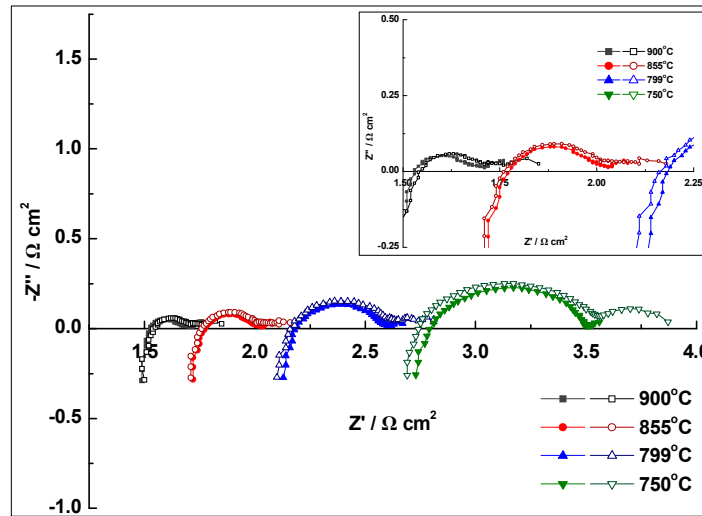


**Fig. 4.5** Impedance spectra of Ni/YSZ cathode operating at OCV (solid symbols) and at 1.0 V (open symbols) at different temperatures in CO<sub>2</sub>/CO 70/30 mixture

The impedance spectra of Ni/YSZ cermet cathode operating at different temperatures in CO<sub>2</sub>/CO 70/30 mixture are presented in Fig. 4.5 at OCV (solid symbols) and at 1.0V (open symbols). As operation temperature decreases, both R<sub>s</sub> and R<sub>p</sub> increase considerably, thereby the cathode performance declines significantly. In addition, the R<sub>s</sub> drops slightly when applying 1.0V to the cell, in comparison with R<sub>s</sub> at OCV at all temperatures, whereas R<sub>p</sub> increases evidently when working at high voltage, probably as a consequence of carbon formation. Noticeably, the impedance spectrum of Ni/YSZ cathode in CO<sub>2</sub>/CO 70/30 mixture shows two well developed arcs upon loading at 750°C, a bigger one at high frequency attributed to charge transfer processes as it was almost potential independent (Fig. 4.3 and 4.4) and a smaller one at low frequency (ranges from 10 to 0.1Hz), rather than a small tail observed at OCV and at higher temperatures (the close-up interpolated in Fig. 4.5), relating to surface kinetics. In Ni/YSZ material set, Ni acts as an electronic conductor and the catalyst for cathode reaction while YSZ serves as an ionic conductor, accordingly, the charge transfer associated processes play a dominant role in the whole CO<sub>2</sub> electrochemical reduction processes, especially at low temperatures, for that the oxygen ion mobility on YSZ material decreased markedly with lowering temperature [27].

### 4.3 LSCM-YSZ composite

#### 4.3.1 Choice of current collector for LSCM/YSZ cathode

Before evaluating the performance of LSCM based cathodes, different kinds of materials for current collectors were applied.

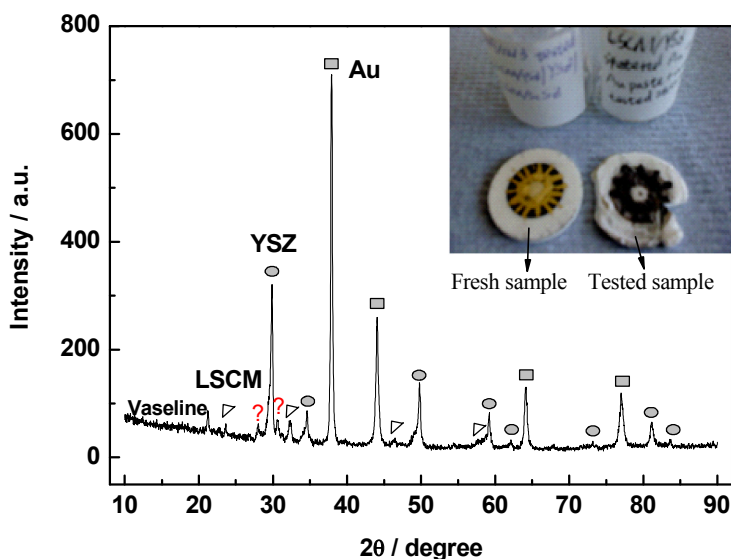


**Fig. 4.6** XRD pattern of LSCM/YSZ-Au after electrochemical testing in various CO<sub>2</sub>-CO mixtures (the colour comparison of Au paste on cathode before and after cell testing is inserted on top right. The Au paste were painted manually, so its thickness was ca. 30-50 $\mu$ m)

Au paste was firstly tried as cathode current collector as Au is an inert catalyst for most electrochemical reactions [28]. However, Au might be problematic in application as high temperature CO<sub>2</sub> electrolysis, because that there was discoloration happened to Au paste, i.e. the colour of Au changed from yellow to black after tests in CO<sub>2</sub>-CO mixtures as shown in Fig. 4.6. To figure out the possible reason for this phenomenon, XRD measurement of cathode was carried out after cell testing, also shown in Fig. 4.6. There are two unidentified diffraction peaks appeared around 30° besides those expected for LSCM, YSZ and Au phases. The possible origin of the above unidentified peaks is that Au alloy with elements from sealing parts in test jig since Au was reported to alloy with

Mg, Mn etc. at high temperature [29]. Although the assignments of the extra peaks in XRD pattern could not be made so far, it is suspicious that the discolouration of Au might pose questions for LSCM based cathode performance in CO<sub>2</sub>/CO fuels.

Other current collectors including Pt paste, Pd/LSCM mixture, Au mesh, Pd paste etc. were tried as well, and the cathode performance of using them as current collector for LSCM/YSZ cathode working at 900°C in CO<sub>2</sub>/CO 70/30 fuel are compared in Fig. 4.7. It is obvious that using mesh, either Au mesh or Pt mesh as cathode current collector, is not wise due to the significantly large R<sub>s</sub> obtained in Fig. 4.7. LSCM perovskite is a p-type conductor and its conductivity in reducing atmosphere declined remarkably [14, 15], thus a fairly high conducting connection between cathode and electrochemical instrument is needed for cathode current collection. It can be observed in Fig. 4.7 that Pd/LSCM mixtures and Pt paste show reasonable R<sub>s</sub> values as expected for 2mm thick YSZ electrolyte, thus they might be suitable cathode current collectors.

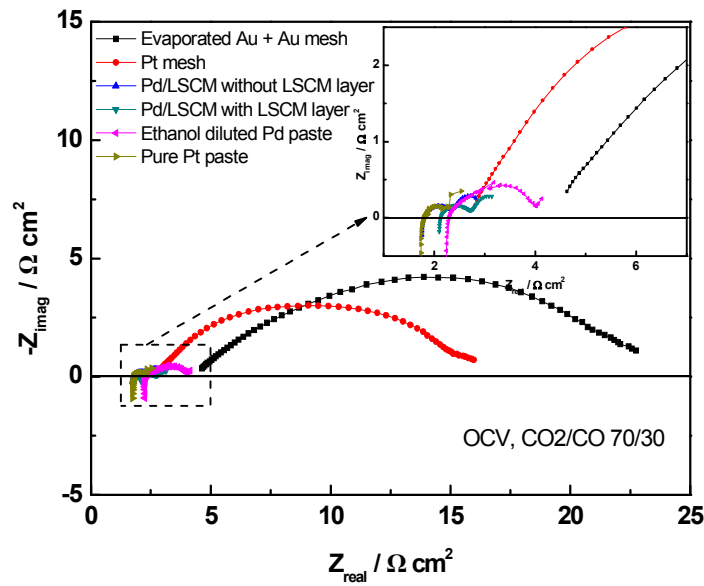


**Fig. 4.7** Choice of cathode current collector suitable for LSCM based cathode

Noting that Pt current collector in solid oxide cells has always been a concern for its possible catalytic property [28-31]. However, from the catalysis point of view, the catalytic effect of metal depends significantly on its microstructure and particle sizes [32]. In our experiments, the catalytic contributions from Pt paste current collector was

regarded as insignificant because the type we used sintered well and formed much larger grains than electrodes and pores in electrode structure, thereby Pt may not diffuse into bulk electrode layer to affect the electrode performance catalytically, as a confirmation of which, the SEM images of electrode/current collector interfaces in Fig. 4.8 show large grained Pt stayed outside smaller grained electrode layer. This has also been applied to using Pd/LSCM as current collector [22], in which case the large grained Pd particles formed a skeleton and smaller sized LSCM distributed homogeneously on its surface, with Pd picking up current and LSCM binding well to the electrode functional layer. It has been believed that such a structure allowed Pd act more likely as only current collector, and if this was the case, Pt might not contributed a lot to electrode activity, in that the two had similar structures in SEM tests. Furthermore, in Fig. 4.7 we observe that there is no big difference between the performance for the cell with Pt paste and Pd/LSCM cathode current collector. Consequently, in the following experiment, Pd/LSCM mixture or Pt paste was used as current collector for LSCM based cathode materials in CO<sub>2</sub> electrolysis.

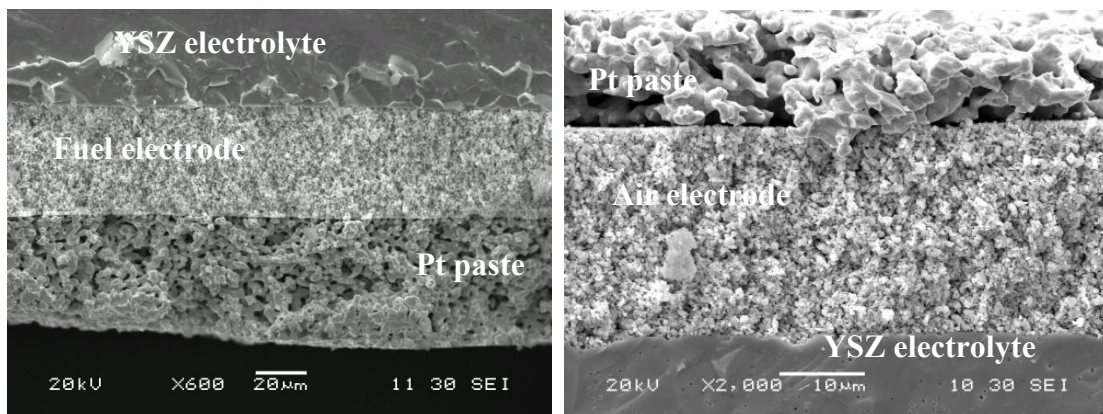


**Fig. 4.8** SEM cross-section views of cathode current collector/cathode interface (left-hand side) and anode current collector/anode interface (right-hand side)

### 4.3.2 Performance from LSCM/YSZ composite cathode for CO<sub>2</sub> electrolysis

Fig. 4.9 shows the I-V curves of the LSCM/YSZ cathode cell working at 900°C in CO<sub>2</sub>/CO mixtures using Pd/LSCM mixture as cathode current collector. The OCV values obtained in different atmospheres are listed in Table 4.2. Again, the practical OCV values are close to the Nernst potentials, falling in the range of -(0.7-0.9)V in

CO<sub>2</sub>/CO atmospheres and -0.92V in H<sub>2</sub> containing atmosphere. Similarly to Ni/YSZ cathode cell (Fig. 4.2), the I-V curves of the LSCM/YSZ cathode cell show that the cell resistance is weakly current dependent in CO<sub>2</sub>/CO mixtures, but the I-V curve in wet 5% H<sub>2</sub>/Ar shows remarkable increase in resistance when cell potential is -(1.3-2.0) V. This phenomenon, again, can be ascribed to the steam starvation which will be discussed more when we consider different amounts of steam supply.

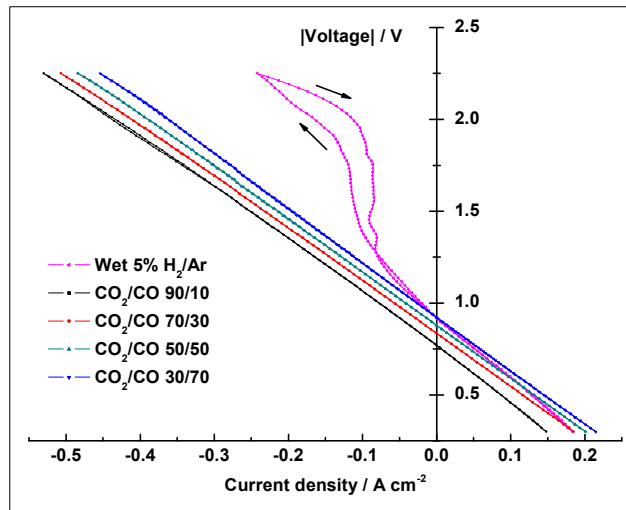


**Fig. 4.9** I-V curves of the cell with LSCM/YSZ cathode operated at 900°C at different atmospheres

**Table 4.2** Summary of the OCV values of the cell with LSCM/YSZ cathode operated at 900°C under different atmospheres

	Theoretical OCV value (V)*	Practical OCV value (V)
Wet 5% H <sub>2</sub> /Argon	-0.94	-0.917
CO <sub>2</sub> /CO 90/10	-0.785	-0.771
CO <sub>2</sub> /CO 70/30	-0.853	-0.836
CO <sub>2</sub> /CO 50/50	-0.896	-0.879
CO <sub>2</sub> /CO 30/70	-0.939	-0.923

\* Calculation according to Nernst equation and similar to the calculations on Ni/YSZ cathode cell in part 4.2.

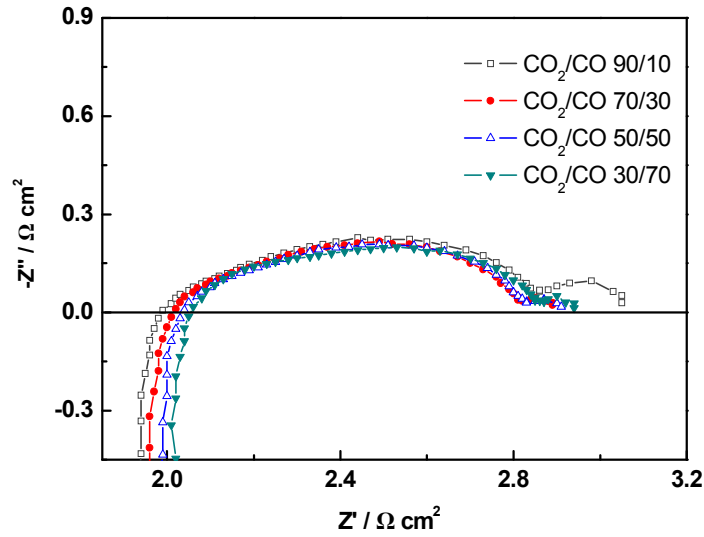


**Fig. 4.10** Impedance spectra of the single cell with LSCM/YSZ cathode under OCV and different atmospheres at 900°C (frequency ranges from  $10^5$  down to 0.015Hz)

The impedance spectra of the LSCM/YSZ cathode at OCV at 900°C in different atmospheres are shown in Fig. 4.10. The ohmic resistance,  $R_s$ , 1.99  $\Omega\text{cm}^2$ , 2.02  $\Omega\text{cm}^2$ , and 2.04  $\Omega\text{cm}^2$  for 10%, 30%, and 50% CO in fuel gas respectively, increases with CO concentration, which, assuming that the lateral resistance of the electrode has a small contribution to  $R_s$ , is rational as LSCM is a p-type conductor, and its conductivity declines with the drop of oxygen partial pressure [14, 15]. As to the  $R_p$ , the cathode shows the highest  $R_p$ , around 1.1  $\Omega\text{cm}^2$ , in CO<sub>2</sub>/CO 90/10 gas mixture. This value is doubled compared to that from Ni/YSZ cermets working under the identical conditions, indicating insufficient activity of LSCM/YSZ towards CO<sub>2</sub> reduction though optimizations could to be done for cathode performance improvement. The  $R_p$  decreases when the CO fraction is higher than 10%, but  $R_p$  does not decrease further when CO fraction rises up to 70%. Similar with the effect of CO content on  $R_p$ , the  $R_p$  decreases with increasing working potential (not shown), reflecting accelerated cathode kinetics at high CO concentrations and high loadings. In contrast with the Ni/YSZ cathode cell, there are at least three overlapped arcs in the impedance responses of LSCM/YSZ cathode in Fig. 4.10, a small depressed arc at the high frequency range, a large one at the middle frequency zone, and a small tail at the low frequency end, which

implies different rate-limiting steps might take place on LSCM/YSZ composite compared to those on Ni/YSZ cathode. Generally speaking, the mixed electronic and ionic conductivity of LSCM is beneficial for CO<sub>2</sub> electrochemical reduction processes, in comparison with Ni/YSZ cathode, which showed bigger high frequency arcs under the same operating conditions especially at low temperatures, yet the drop in electronic conductivity in reducing atmosphere and the insufficient catalytic activity of LSCM/YSZ composite limit its performance for CO<sub>2</sub> dissociation.

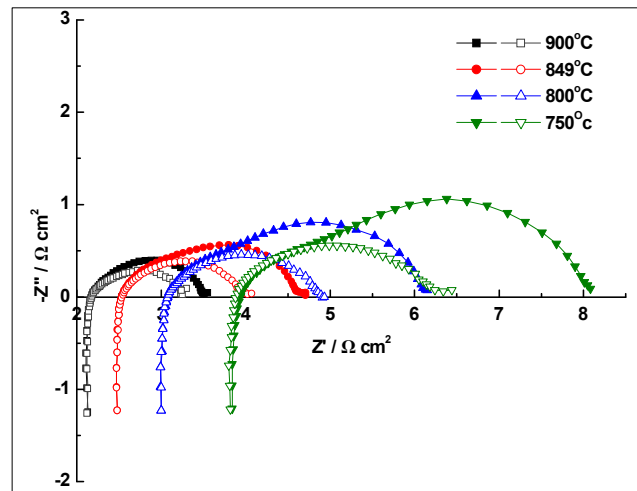


**Fig. 4.11** Impedance spectra of LSCM/YSZ cathode working at OCV (solid symbols) and at 1.0 V (open symbols) in CO<sub>2</sub>/CO 70/30 atmosphere at different temperatures (frequency ranges from 10<sup>5</sup> down to 0.1Hz)

The LSCM/YSZ cathode performance at different temperatures was characterized in CO<sub>2</sub>/CO 70/30 mixture for CO<sub>2</sub> electrolysis, as displayed in Fig. 4.11. The cell resistance from impedance spectra is plotted in Fig. 4.12. As expected, both the R<sub>s</sub> and R<sub>p</sub> increase when operation temperature declines, thereby, the cathode performance reduces distinctly. The R<sub>p</sub> from LSCM/YSZ cathode at 750°C at OCV is ~ 4.2 Ω cm<sup>2</sup>, three times larger than that at 900°C. Besides, the R<sub>p</sub> decreases appreciably against applying 1.0V (open symbols in Fig. 4.11), compared to the situation at OCV (solid symbols in Fig. 4.11), particularly at lowered temperatures, for instance, the R<sub>p</sub> at 1.0V at 750°C is ~2.6 Ω cm<sup>2</sup>. The above results are also presented in Fig. 4.12, which shows

that the gap between R<sub>p</sub> value at OCV and at 1.0V becomes larger at reduced temperatures.

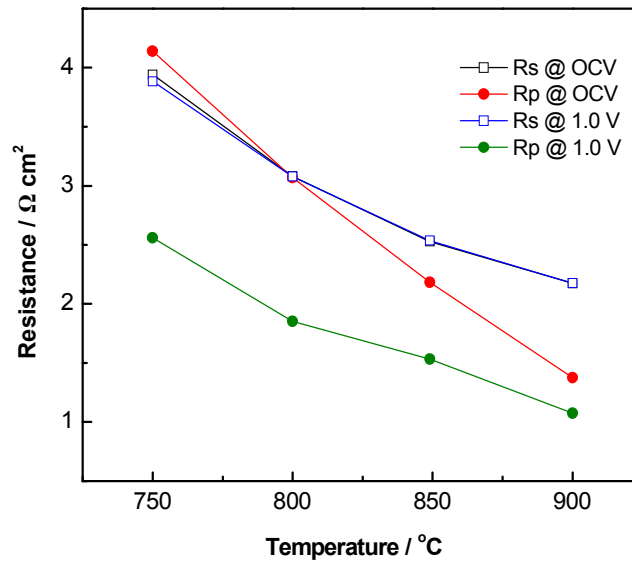


**Fig. 4.12** Cathode resistance from LSCM/YSZ composite working at different temperatures in CO<sub>2</sub>/CO 70/30 mixture

Corresponding to the remarkably reduced R<sub>p</sub> at 1.0V, a severely depressed low frequency arc and a constant high frequency arc can be observed in Fig. 4.11, with comparison to impedance arcs from LSCM/YSZ cathode working at OCV, which announces facilitated CO<sub>2</sub> electrochemical reduction processes and also possibly an indicator of improved catalytic properties of LSCM towards CO<sub>2</sub> dissociation under loading. The above phenomenon from LSCM/YSZ cathode is on the contrary from Ni/YSZ cermets cathode which presented enlarged low frequency arcs upon loading 1.0 V and might be subjected to coke formation working with CO<sub>2</sub>-CO mixtures. As LSCM-based material does not suffer from carbon formation (Fig. 3.12 and 3.13), it can be considered as alternative cathode in high temperature CO<sub>2</sub> electrolysis by an electrolyser, if the cathode activity could be promoted to at least comparable with Ni/YSZ cermet cathode. Efforts will be concentrated on modification of LSCM-based cathode performance for high temperature CO<sub>2</sub> electrolysis.

#### 4.4 LSCM-GDC composite cathode

CO<sub>2</sub> reduction on GDC, instead of YSZ, was investigated as LSCM/GDC cathode in CO<sub>2</sub> electrolysis, seeking to obtain better catalytic activity as GDC possesses higher conductivity than YSZ and GDC also demonstrated catalytic property for CO<sub>2</sub> reduction reaction [20, 33]. The I-V curves of the cell with LSCM/GDC as fuel electrode working in a range of CO<sub>2</sub>/CO mixtures are exhibited in Fig. 4.13. The OCV values under each condition are listed in Table 4.3. The polarization curve of LSCM/GDC composite cell in wet H<sub>2</sub>-containing atmosphere presents large resistance in -(1.2-2.0) V voltage range, which seems independent of cathode material for electrolysis in atmosphere short of steam supply as similar polarization behaviour were observed with Ni/YSZ cermets and LSCM/YSZ composite cell previously. In CO<sub>2</sub>/CO mixtures, the I-V curves are likely to be linear except that in CO<sub>2</sub>/CO 90/10 mixture, which obviously shows signs from diffusion limitations in fuel cell operation due to the poor availability of reactants (CO). It can be observed in Fig. 4.13 that the cell resistance around OCV in CO<sub>2</sub>/CO 90/10 atmosphere is higher than those with lower CO<sub>2</sub> concentration, suggesting higher activation energy is required for the onset of CO<sub>2</sub> reduction with higher amount of CO<sub>2</sub> in fuel.

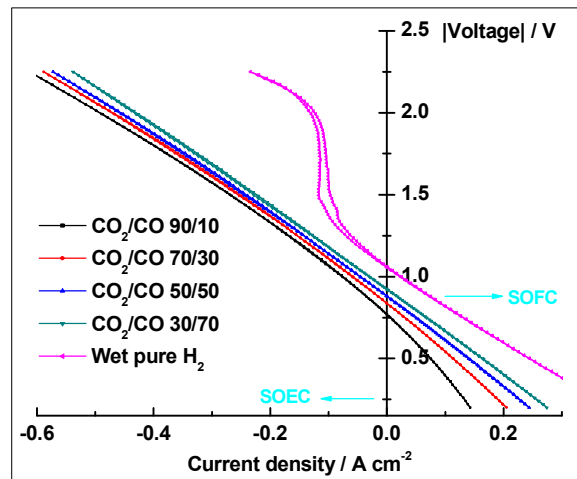


**Fig. 4.13** I-V curves of the cell with LSCM/GDC cathode operated at different atmospheres at 900°C

**Table 4.3** Summary of the OCV values of the cell with LSCM/GDC cathode operated at 900°C under different atmospheres

	Theoretical OCV value (V)	Practical OCV value (V)
Wet 5% H <sub>2</sub> /Argon	-0.94	-0.92
CO <sub>2</sub> /CO 90/10	-0.785	-0.769
CO <sub>2</sub> /CO 70/30	-0.853	-0.838
CO <sub>2</sub> /CO 50/50	-0.896	-0.881
CO <sub>2</sub> /CO 30/70	-0.939	-0.924

Fig. 4.14 shows the impedance spectra from the LSCM/GDC cathode operating in different CO<sub>2</sub>/CO mixtures at 900°C under OCV. Noticeably from the Nyquist plot of impedance in Fig. 4.14, linear responses (with a 45 degree inclination to real axis) at high frequencies at positive imaginary part and slightly depressed semi-circular arcs at low frequencies can be seen, which seems a characteristic of LSCM/GDC cathode towards CO<sub>2</sub> electrolysis. This impedance dispersion appears to be a Gerischer like impedance graphically, according to Boukamp [34], indicating a semi-infinite diffusion for charge transfer processes followed by chemical surface adsorption/desorption equilibration and/or surface diffusion processes for CO<sub>2</sub> reduction. Matsuzaki and Yasuda have also reported similar impedance behavior for CO oxidation in CO<sub>2</sub>-CO systems but on Ni/YSZ electrode, assigning the high frequency linear act to Warburg impedance [24]. Although the difference between Gerischer and Warburg impedance is really subtle based on that both show a linear response at high frequency range followed by a semi-circular arc at low frequency regime, it is generally acknowledged that the former tended to occur on the materials with mixed electronic and ionic conductivities. Previously, Gerischer impedance was reported on Tb-doped YSZ ceramics [34] and on porous La<sub>1-x</sub>Sr<sub>x</sub>CoO<sub>3-δ</sub> perovskite electrode for oxygen reduction reaction [35, 36], with both materials being mixed conductors, though the lab observations of Gerischer impedance are still scarce. A recent derived Gerischer like impedance behaviour was on pure Gd<sub>0.4</sub>Ce<sub>0.6</sub>O<sub>2-δ</sub> cathode for CO<sub>2</sub> reduction processes under similar conditions to the present study [20]. In LSCM/GDC composite, it is believed that the mixed conductivity of both LSCM and GDC might play an important role in the origins of Gerischer type responses for CO<sub>2</sub> dissociation.

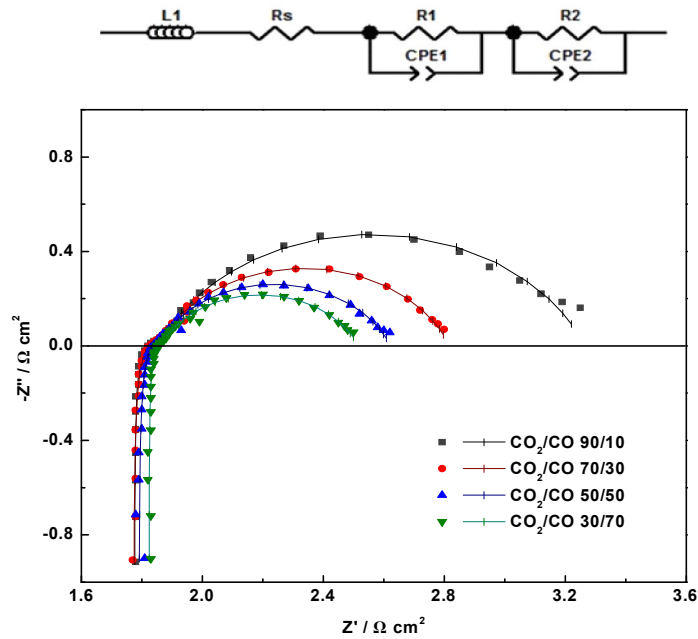


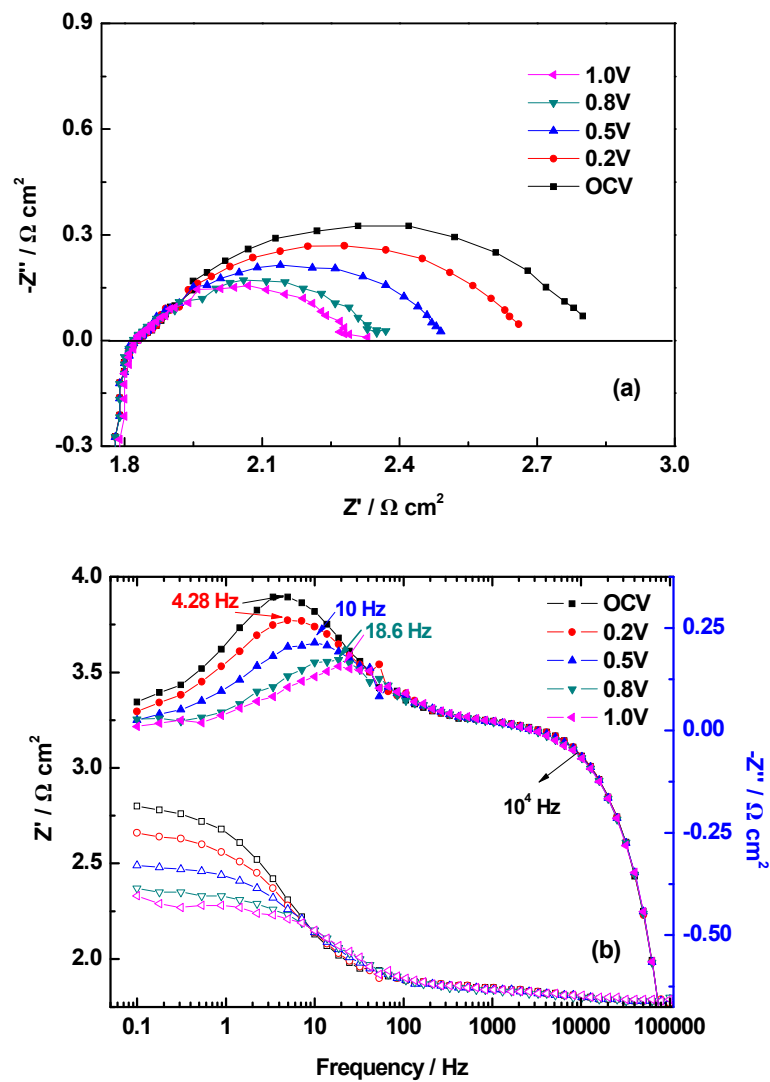
**Fig. 4.14** Impedance spectra of the cell with LSCM/GDC cathode operating in different atmospheres at OCV at 900°C (solid symbols) together with fitted results (straight lines) (the equivalent circuit used to fit the experimental data is on top of impedance spectra)

The experimental data from impedance spectra were fitted using the equivalent circuit interpolated in Fig. 4.14, and clearly, the fittings agree very well with those obtained in our measurements. The resistance values from equivalent circuit fittings are presented in Table 4.4. Evidently, the  $R_s$  increases only slightly with increasing CO content, contrast to the observations on LSCM/YSZ composite cathode. Given the reduction of  $Ce^{4+}$  to  $Ce^{3+}$  in reducing atmosphere [37], the extra electronic conductivity resulted from  $Ce^{4+}$  reduction probably compensates the decline in electronic conductivity of LSCM materials in the atmosphere with higher CO content. In Table 4.4, the  $R_p$  (sum of  $R_1$  and  $R_2$ ) reduces considerably with increasing CO fraction, from 1.5  $\Omega\text{ cm}^2$  for CO<sub>2</sub>/CO 90/10 mixture to 1.05, 0.84, and 0.70  $\Omega\text{ cm}^2$  for CO<sub>2</sub>/CO 70/30, CO<sub>2</sub>/CO 50/50 and CO<sub>2</sub>/CO 30/70 atmosphere, respectively. Compared to pure Gd<sub>0.4</sub>Ce<sub>0.6</sub>O<sub>2- $\delta$</sub>  cathode in a CO<sub>2</sub> electrolyser [20], the  $R_p$  values from LSCM/GDC cathode are smaller in similar conditions even though the LSCM/GDC composite was sintered at higher temperature, implying that catalytic contributions from both LSCM and GDC material to the higher performance of LSCM/GDC composite towards CO<sub>2</sub> reduction.

**Table 4.4** Summary from Equivalent circuit fitting of the EIS of LSCM/GDC cathode cell operated under different atmospheres at OCV at 900°C

	CO <sub>2</sub> /CO ratio			
	90/10	70/30	50/50	30/70
Rs/Ωcm <sup>2</sup>	1.775	1.768	1.786	1.822
R1/Ωcm <sup>2</sup>	0.081	0.088	0.069	0.041
R2/Ωcm <sup>2</sup>	1.41	0.962	0.767	0.654
Rp/Ωcm <sup>2</sup>	1.491	1.050	0.836	0.695

Besides, it can be found in Fig. 4.14 that the low frequency arc becomes increasingly smaller with increasing CO concentration, meaning that the cathode kinetics are facilitated when more CO is presented, which has been reported by other researchers [20, 24]. Indeed, the appearance of CO<sub>2</sub> in the reactant stream would retard the cathode reaction in that CO<sub>2</sub> needs higher activation energy for dissociation (Fig. 4.13) and that the large CO<sub>2</sub> molecules have larger diffusion resistance resulting from the preferential adsorption of CO<sub>2</sub> on cathode surface, and as a confirmation of which, the R2, namely, resistance from low frequency arc, decreases with CO<sub>2</sub>/CO ratio in Table 4.4. Moreover, the R2 values are around 90% of Rp in Table 4.4, indicating their predominant contribution to Rp. As has been addressed, the low frequency arc from the impedance of LSCM/GDC cathode suggested the dissociative adsorption of active species on cathode surface and the subsequent surface diffusion of the active species [21], hence, it can be deduced that the adsorption/desorption equilibration and surface diffusion play a dominant role in CO<sub>2</sub> reduction by a high temperature electrolysis cell. Noting that the impedance arcs of Ni/YSZ (Fig. 4.3 and 4.4) and LSCM/YSZ cathode (Fig. 4.10 and 4.11) differ from those from LSCM/GDC cathode, both the charge transfer processes and surface exchange reactions may affect the performance of CO<sub>2</sub> reduction significantly for Ni/YSZ and LSCM/YSZ cathodes.



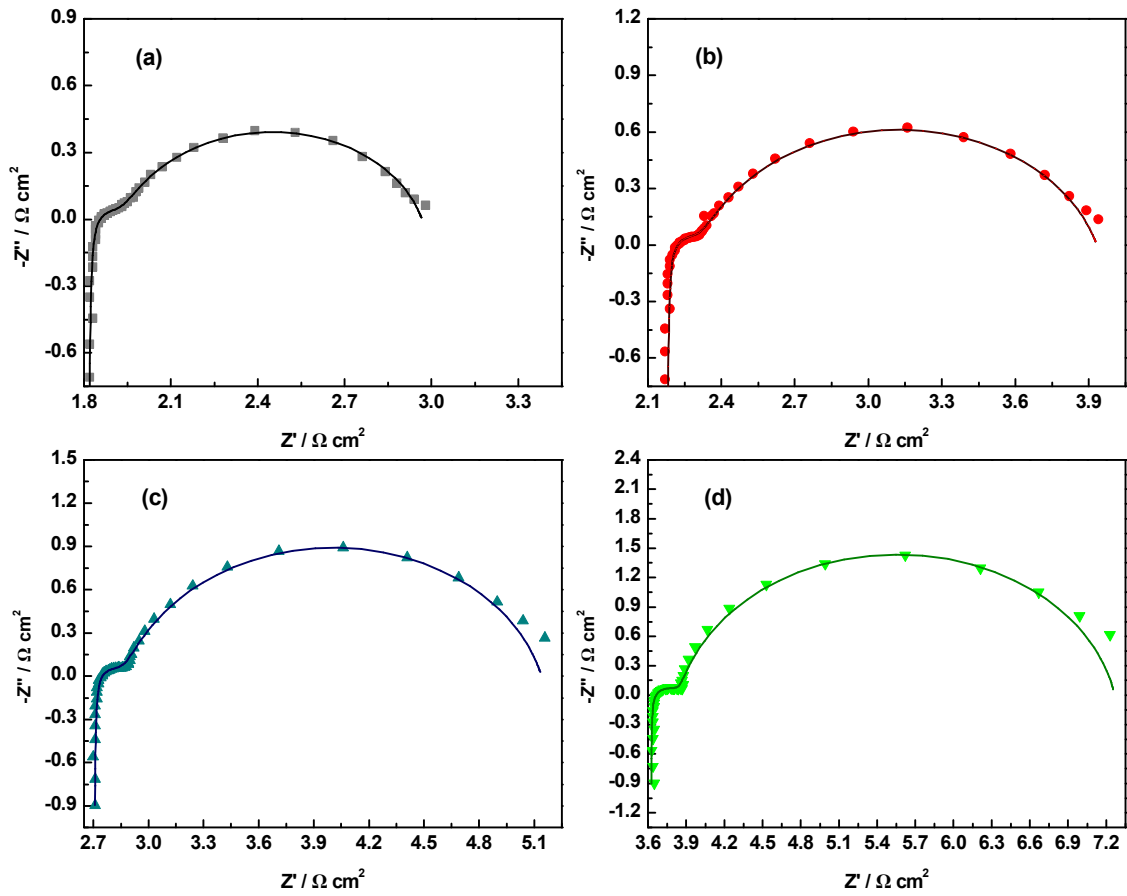
**Fig. 4.15** EIS of LSCM/GDC cathode working at 900°C at different voltages in CO<sub>2</sub>/CO 70/30 atmosphere: (a) Nyquist plots (b) Bode plots (summit frequencies were labeled in the Bode plots)

Fig. 4.15 displays the impedance spectra of LSCM/GDC cathode working at different operating potentials at 900°C in CO<sub>2</sub>/CO 70/30 atmosphere. The Gerischer-like impedance dispersion is found at all potentials tested. It can be seen from Fig. 4.15 that  $R_s$  changes little whilst,  $R_p$  decreases monotonously when operating voltage increases. The  $R_p$  values are ca. 1.0, 0.85, 0.67, and 0.46  $\Omega \text{ cm}^2$  at OCV, 0.2V, 0.5V, and 1.0V, respectively. Additionally, the low frequency arc diminishes with increasing loads in

Fig. 4.15(a), indicating faster cathode kinetics at higher working potentials, which is also supported by the increase in summit frequencies for low frequency arcs upon increasing voltage, as shown in the EIS Bode plots in Fig. 4.15 (b). In both Fig. 4.15 (a) and (b), only the low frequency arc is affected by the variation in operating potential, indicative of a fact that the surface kinetics plays a vital role in the whole process of CO<sub>2</sub> reduction on the LSCM/GDC composite used as an SOEC cathode.

The decline in low frequency arcs of LSCM/GDC cathode upon varying CO concentration (Fig. 4.14) and working potential (Fig. 4.15) reflects accelerated cathode kinetics at high CO contents and voltages, which reveals that the higher level of CO<sub>2</sub> in the fuels retards the CO<sub>2</sub> dissociation processes, especially the surface reaction processes. With decreasing CO<sub>2</sub>/CO ratio or with the progress of CO<sub>2</sub> reduction at higher loads, the CO content increases, and the retarding effect of CO<sub>2</sub> gas is mitigated, therefore, R<sub>p</sub> decreases. According to the report on pure Gd<sub>0.4</sub>Ce<sub>0.6</sub>O<sub>2-δ</sub> cathode for CO<sub>2</sub> reduction [20], the electrode utilization thickness increased with decreasing P<sub>O<sub>2</sub></sub>, leading to improved surface kinetics. Meanwhile, the vacancy diffusion coefficient and surface exchange rate of GDC electrode increased with decreasing P<sub>O<sub>2</sub></sub>. These all might contribute to the higher performance of LSCM/GDC cathode for CO<sub>2</sub> electrolysis at lower CO<sub>2</sub>/CO ratios and at higher applied voltages.

In Fig. 4.16, the impedance spectra of the LSCM/GDC cathode measured at OCV at different temperatures in CO<sub>2</sub>/CO 70/30 atmosphere are plotted, together with the simulated results using the equivalent-circuit shown in Fig. 4.14. Apparently, the measured results agree well with the simulated ones, indicating the reliability of the equivalent-circuit employed. In Fig. 4.16, as temperature decreases, the impedance behaviour at high frequency region develops from a linear response to a small semi-circular arc, distorting it from the Gerischer dispersion. In the mean time, with lowering operating temperature, both R<sub>s</sub> and R<sub>p</sub> increased considerably, therefore, the performance of LSCM/GDC cathode for CO<sub>2</sub> electrolysis declines markedly.



**Fig. 4.16** Experimental and simulated EIS of LSCM/GDC composite cathode operating at OCV in CO<sub>2</sub>/CO 70/30 mixture at (a) 900°C, (b) 850°C, (c) 800°C, and (d) 750°C (the solid symbols reflect measured results and the lines represent the simulated results using equivalent-circuit method)

**Table 4.5** Results from the equivalent-circuit analysis on the EIS of LSCM/GDC cathode at OCV at different temperatures in CO<sub>2</sub>/CO 70/30 atmosphere for CO<sub>2</sub> electrolysis using SOEC

Temperature (°C)	Rs (Ω cm <sup>2</sup> )	R1 (Ω cm <sup>2</sup> )	R2 (Ω cm <sup>2</sup> )	Rp (Ω cm <sup>2</sup> )
900	1.81	0.136	1.02	1.156
850	2.27	0.161	1.6	1.761
800	2.70	0.19	2.25	2.44
750	3.62	0.235	3.41	3.645

From the summary of the equivalent-circuit analysis on the EIS of LSCM/GDC cathode working at different temperatures in Table 4.5, one can see that the high frequency arc, R1, increases only at a small magnitude as temperature drops, from 0.136  $\Omega \text{ cm}^2$  at 900°C to 0.235  $\Omega \text{ cm}^2$  at 750°C; whereas the low frequency arc, R2 increased significantly as temperature falls, for instance, R2 exceeds 3.40  $\Omega \text{ cm}^2$  at 750°C, three times higher than that at 900°C, therefore, the low frequency arc, i.e. the surface adsorption/desorption equilibration and/or surface diffusion, plays a dominant role in the whole processes of electrochemical reduction of CO<sub>2</sub> in comparison with that of the high frequency arc which relates to the charge transfer processes, and the surface activity of LSCM/GDC cathode for CO<sub>2</sub> electrolysis becomes critical as operating temperature drops.

#### **4.5 Comparisons between Ni-cermet and LSCM based cathode**

##### **4.5.1 Microstructure comparisons**

So far, we have prepared and evaluated different cathodes for high temperature SOEC used for CO<sub>2</sub> electrolysis. Discrepancies were found between Ni/YSZ cermets, LSCM/YSZ composite and LSCM/GDC composite, in terms of cathode performance and cathode kinetics, as functions of potential, operation temperature, and reactant gas composition. To explain the differences among the above cathodes, SEM was undertaken for each cathode after electrochemical characterization. Fig. 4.2 is the cross-sectional view of each cathode/electrolyte interface and the magnified view of each cathode.

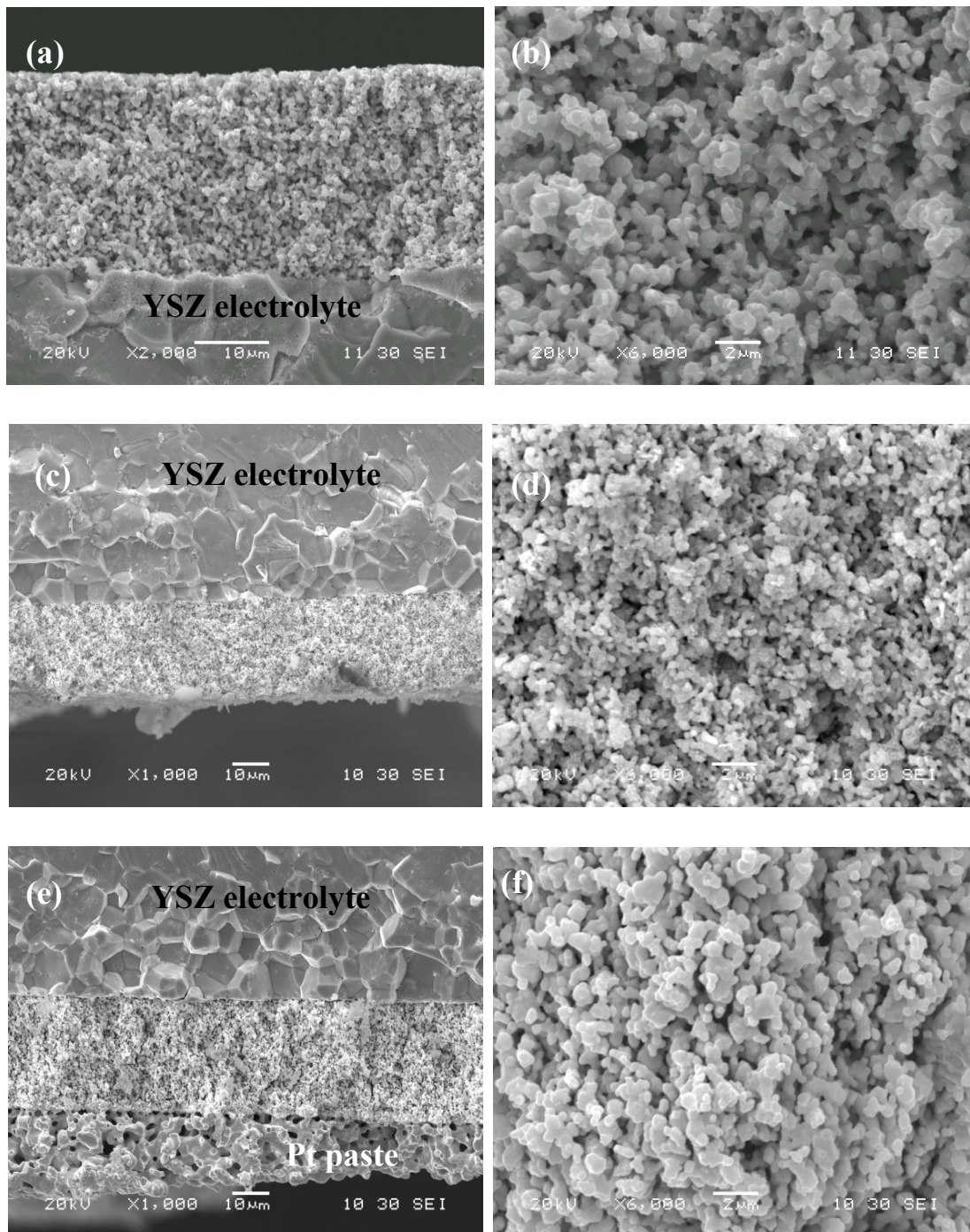


**Fig. 4.17** SEM cross-sectional view of (a) Ni/YSZ cathode/electrolyte interface, (b) Ni/YSZ cathode, (c) LSCM/YSZ cathode/electrolyte interface, (d) LSCM/YSZ cathode, (e) LSCM/GDC cathode/electrolyte interface and (f) LSCM/GDC cathode

From Fig. 4.17 (a), (c), and (e), fairly good adhesion of cathode to electrolyte layer can be seen, indicating the corresponding sintering temperature, 1350°C for Ni/YSZ, 1200°C for LSCM/YSZ composite and 1300°C for LSCM/GDC composite, were fine in this aspect. However, when it comes to cathode performance, there are more factors, for example, particle size and resulting surface area, pore sizes and porosity etc., besides interfacial connecting. In Fig. 4.17 (b), (d), and (f), apparently, all the cathodes possess porous structures, and the pore sizes are around 1-2µm. Originated from different firing temperature and diverse sinterability, the particle size varies, with particle sizes falling in the range of ~0.25-1µm for Ni/YSZ and LSCM/GDC electrode that were fired at higher temperature and of ~0.2-0.5µm for LSCM/YSZ composite sintered at relatively low temperature. From catalysis point of view, the diversity in particle size would result in different surface areas and reaction active sites, thus the activity of different materials, which might be related to distinctness in electrochemical performance from different cathode materials we have studied.

#### **4.5.2 Performance comparisons for CO<sub>2</sub> electrolysis by SOEC**

Displayed in Fig. 4.18 is the CO<sub>2</sub> electrolysis performance comparison from different cathodes including Ni/YSZ cermets, LSCM/YSZ composite and LSCM/GDC composite working in CO<sub>2</sub>/CO 70/30 environment at OCV at 900°C. It is obvious that Ni/YSZ cermets cathode performs superior in the identical conditions, exhibiting diminutive impedance arcs and much smaller R<sub>p</sub> value, compared to LSCM based cathode. With regarding to LSCM based composite cathodes, the LSCM/YSZ cathode shows smaller R<sub>p</sub> and depressed impedance arc when opposed to LSCM/GDC composite cathode.

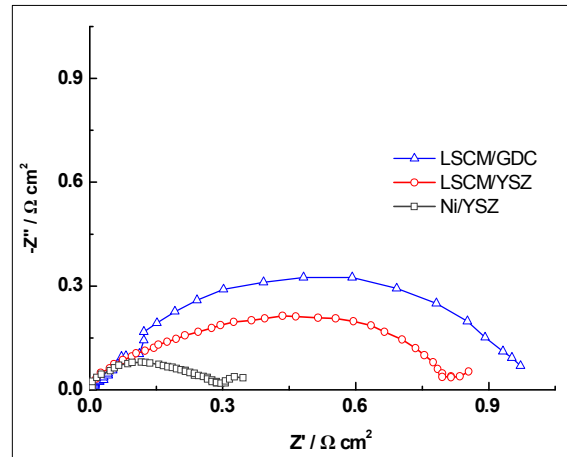


**Fig. 4.18** Impedance comparisons from Ni/YSZ cermets cathode, LSCM/YSZ and LSCM/GDC composite cathode working in CO<sub>2</sub>/CO 70/30 mixture at OCV at 900°C

Combined with observations from SEM images (Fig. 4.17), the Ni/YSZ cathode has excellent catalytic properties for CO<sub>2</sub> reduction by a solid electrolyser though it displayed indistinctive and larger particle sizes comparing with LSCM/GDC and LSCM/YSZ composites, respectively. Nevertheless, the unfavourable coke formation on Ni/YSZ in CO<sub>2</sub>/CO mixture is a critical limitation for efficient operation in CO<sub>2</sub> electrolysis. As for LSCM/YSZ composite cathode, it showed much smaller particle size, which would lead to enlarged surface area and as a result, expand the gas/electrolyte/electrode triple phase boundaries (TPBs). The above points account for the higher performance from LSCM/YSZ composite cathode at OCV at 900°C, compared to that from LSCM/GDC composite cathode operated in the identical conditions, with the latter possibly having diminished TPB areas and inadequate active reaction sites resulting from high temperature fabrication. Another possibility is the reactivity of ceria towards YSZ at elevated temperature as it has been reported that ceria could react with YSZ at 1300°C, forming a GDC-YSZ inter-diffusion layer with a decreased electric conductivity between electrolyte and electrode interface [38-40]. Although the inter-diffusion layer can hardly be detected in Fig. 4.17 (e), it is impossible to eliminate this effect on the poor performance of LSCM/GDC toward CO<sub>2</sub> electrolysis. Therefore, further efforts will be made involved lowering fabrication

temperature and modifying the LSCM/GDC cathode microstructure to ensure enlarged TPB area and sufficient active sites for CO<sub>2</sub> reduction reaction.

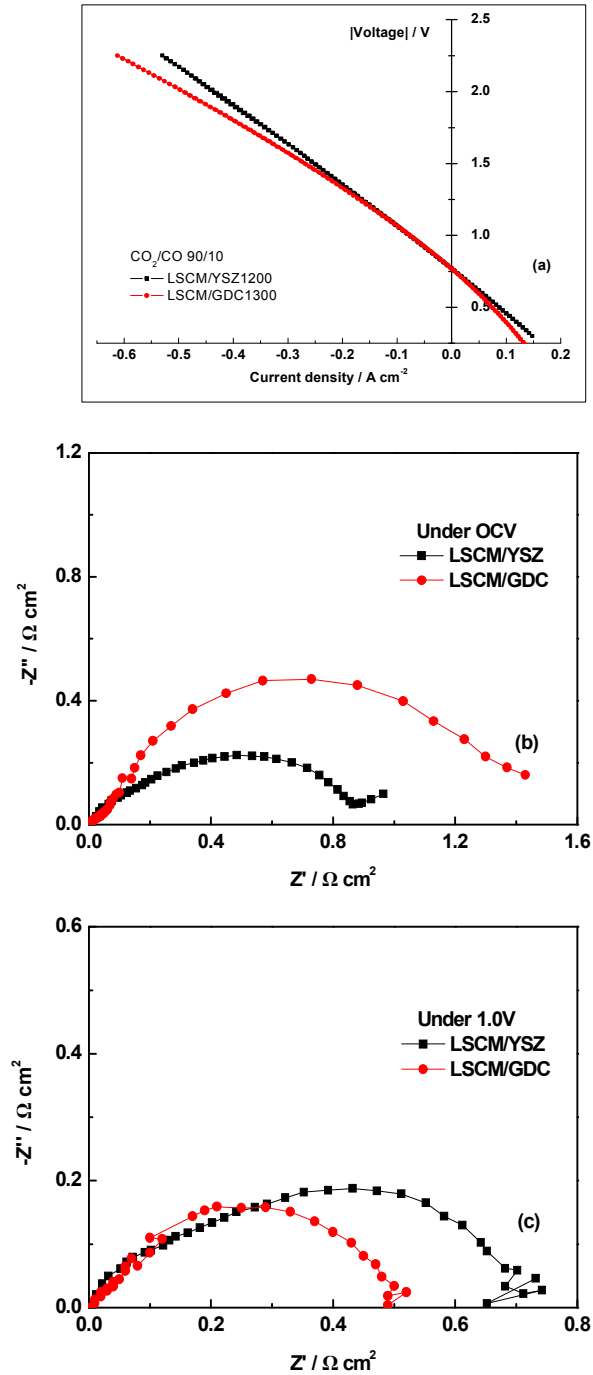


**Fig. 4.19** Performance comparisons between LSCM/YSZ composite and LSCM/GDC composite working in CO<sub>2</sub>/CO 90/10 fuel at 900°C (a) I-V curves, (b) impedance comparison at OCV and (c) impedance comparison at 1.0V

Very interestingly, when comparing the cathode performance from LSCM/YSZ and LSCM/GDC composite under loading, different conclusions from OCV circumstance are obtained. Expressed in Fig. 4.19(a) is the I-V curve comparison between the LSCM/YSZ and LSCM/GDC cathode cell working in CO<sub>2</sub>/CO 90/10 atmosphere at 900°C. Surprisingly, the I-V curve of the LSCM/GDC cathode cell has a milder gradient at loadings higher than -1.25V (absolute potential) in electrolysis operation though it shows a sharper slope at OCV, meaning LSCM/GDC cathode performs better than LSCM/YSZ composite for CO<sub>2</sub> electrolysis, quite meaningful as SOEC is an active rather than passive process. Combining with results presented in part 4.4, the accelerated surface kinetics and promoted catalytic activity from LSCM/GDC cathode with increase loads are the reasons underlying the higher performance from LSCM/GDC than from LSCM/YSZ cathode. The phenomena from the I-V curves are supported by impedance comparisons between LSCM/YSZ and LSCM/GDC composite cathode at OCV in Fig. 4.19(b) and at 1.0 V in Fig. 4.19(c).

In addition, LSCM/GDC also performs better than LSCM/YSZ composite cathode at lowered temperature (results not shown here, but can refer to results from part 4.3 and part 4.4), profiting from the higher conductivity of GDC over YSZ at lowered operation temperature. These all demonstrate the promise of using LSCM/GDC as cathode material CO<sub>2</sub> electrolysis by SOEC.

#### 4.5.3 Cathode activation energy for CO<sub>2</sub> reduction via a SOEC

Fig. 4.20 exhibits the cathode resistances at OCV from LSCM/YSZ composite (Fig. 4.20(a)) and LSCM/GDC composite (Fig. 4.20(b)) as a function of the reciprocal temperature, i.e., the Arrhenius plots in CO<sub>2</sub>/CO 70/30 atmosphere. In Fig. 4.20, the Arrhenius plots show good linearity over the whole operation temperature range and the linear fit presents activation energy of ~55-58 kJ mol<sup>-1</sup> for area specific resistance (ASR, the sum of R<sub>s</sub> and R<sub>p</sub>) from LSCM based cathode, much smaller than the value (~100 kJ mol<sup>-1</sup>) obtained from pure Gd<sub>0.4</sub>Ce<sub>0.6</sub>O<sub>2-δ</sub> cathode in similar CO<sub>2</sub>-CO atmosphere [20].

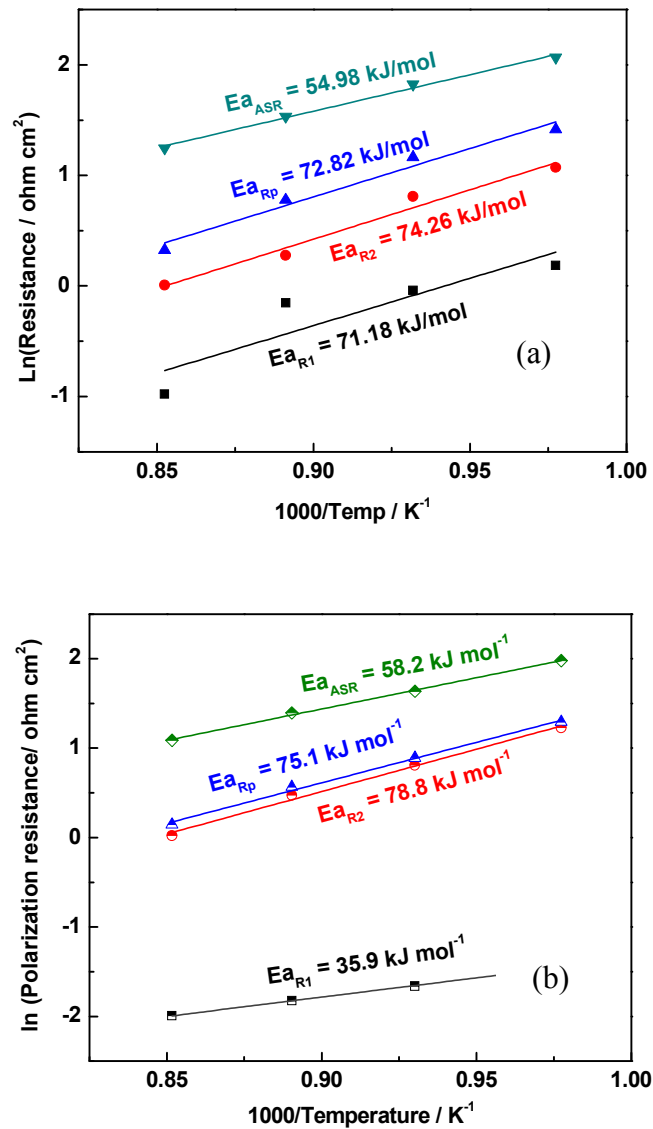


**Fig. 4.20** The Arrhenius plot of the cathode resistance from (a) LSCM/YSZ and (b) LSCM/GDC composite at OCV over a range of operating temperatures in CO<sub>2</sub>/CO 70/30 atmosphere

Further, the Arrhenius plots provide activation energy of ca. 73, 72, and 74 kJ mol<sup>-1</sup> for Rp, R1, and R2 respectively for LSCM/YSZ cathode. With respect to LSCM/GDC composite cathode, the Arrhenius plots give activation energy of ca. 75, 36, and 79 kJ mol<sup>-1</sup> for Rp, R1, and R2, respectively. Apparently, both the activation energy of R1 and R2 are close to that of Rp from LSCM/YSZ composite, whilst the activation energy of

R1 is much lower than that of Rp, with activation energy of R2 close to Rp, from LSCM/GDC cathode, which confirms that the low frequency arc, namely, surface kinetics plays a dominant limiting role on LSCM/GDC composite cathode whereas both charge transfer processes and surface kinetics are limiting steps on LSCM/YSZ composite cathode for CO<sub>2</sub> reduction by SOEC. The Arrhenius plot for Rp from the Ni/YSZ cathode (not shown here) gives activation energy of 45.4kJ mol<sup>-1</sup>, much smaller than the LSCM based composite. However, as discussed previously, the presence of carbon on Ni limited the application of Ni-cermets as practical cathode material for high temperature CO<sub>2</sub> electrolysis.

#### 4.6 Stability test on LSCM/GDC cathode in CO<sub>2</sub>-CO mixture

The durability of LSCM/GDC composite cathode in CO<sub>2</sub> electrolysis operation was investigated in CO<sub>2</sub>/CO 70/30 mixture at 900°C. During this stability test, a constant current density of -0.25A cm<sup>-2</sup> was performed, and the variations in potential vs. time were recorded as illustrated in Fig. 4.21.

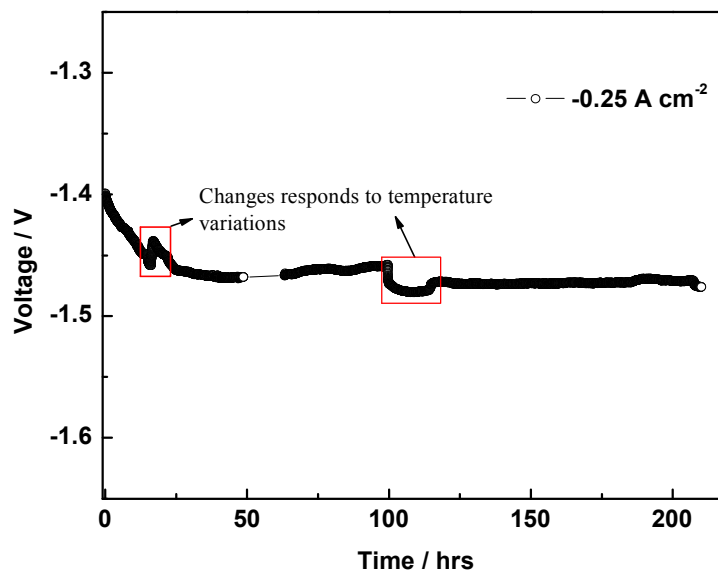


**Fig. 4.21** The cell voltage versus time under a constant current density of -0.25A cm<sup>-2</sup> in CO<sub>2</sub>/CO 70/30 atmosphere at 900°C

In Fig. 4.21, the cell voltage increases with the progress of operation in the first 30 hrs, then it starts to stay stable. No more significant changes in potential except those respond to temperature variations are observed, indicating LSCM/GDC is a durable cathode material in CO<sub>2</sub> electrolysis using a solid oxide electrolyser.

The cathode performance of LSCM/GDC composite was compared before and after the galvanostatic running in CO<sub>2</sub>/CO 70/30 atmosphere for 220 hrs. Fig. 4.22 displays the impedance comparisons of LSCM/GDC composite cathode working at OCV as well as at -0.25 A cm<sup>-2</sup>. The R<sub>p</sub> under OCV drops after the durability test, but the R<sub>s</sub> increased considerably after the stability measurement, probably due to the deterioration in contacts. There is no great change in R<sub>p</sub> of operation under -0.25 A cm<sup>-2</sup> during stability test for more than 200 hrs, again, suggesting the promise in LSCM/GDC composite as cathode material for SOEC used for CO<sub>2</sub> electrolysis.

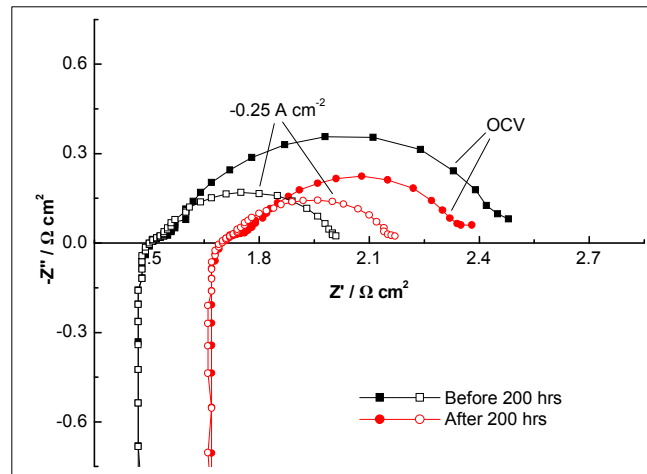


**Fig. 4.22** Impedance spectra from LSCM/GDC cathode cell before (black symbols) and after (red symbols) a galvanostatic operation (constant current of -0.25 A cm<sup>-2</sup>) of around 200hrs in CO<sub>2</sub>/CO 70/30 atmosphere at 900°C

#### 4.7 Summary

In this chapter, three candidate cathode materials, Ni/YSZ cermet, LSCM/YSZ composite and LSCM/GDC composite were employed for high temperature CO<sub>2</sub> electrolysis, in order to find a high performance cathode material in CO<sub>2</sub> electrolysis application.

The I-V curves from different cathode cells showed weakly dependence of potential on current density in CO<sub>2</sub>/CO ratios studied, which ranged from 90/10 to 30/70. The OCVs fell in the range of 0.7-0.9V at 900°C in CO<sub>2</sub>/CO atmospheres, close to the values indicated by Nernst equation.

Differences were observed among the impedance behaviour of the above three cathodes towards CO<sub>2</sub> electrolysis, implying different rate limiting processes on these cathodes. Ni-YSZ cathode exhibited much lower polarization resistance  $R_p$  thus excellent performance towards CO<sub>2</sub> reduction, but might suffer from coke formation, precluding its wide application in this field.

Regarding LSCM/YSZ composite cathode, it had higher  $R_p$  coming from insufficient activity towards both charge transfer and surface kinetics for CO<sub>2</sub> reduction, compared to Ni/YSZ cermet cathode. As to LSCM/GDC composite cathode, the characteristic was that it displayed Gerischer type impedance dispersion, with surface kinetics, i.e. the adsorption/desorption equilibration and surface diffusion playing a dominant role for CO<sub>2</sub> dissociation reaction.

LSCM/GDC displayed better performance under load, though it had worse performance than LSCM/YSZ composite at OCV due to high temperature fabrication. Additionally, LSCM/GDC composite cathode performed well in a ca.220 hrs stability test in CO<sub>2</sub>/CO 70/30 atmosphere, without significant degradation except that from contact.

The activation energy of ASR for LSCM based cathode was 55-58 kJ/mol. The LSCM/GDC composite is promising cathode material for SOEC used for CO<sub>2</sub> electrolysis yet a suitable fabrication approach should be adopted to promote its cathode activity.

## References

1. G. Tao, K. Sridhar, C. Chan, *Solid State Ionics*, **175**, 615 (2004)
2. G. Tao, K. Sridhar, C. Chan, *Solid State Ionics*, **175**, 621 (2004)
3. J. Hartvigsen, S. Elangovan, L. Frost, A. Nickens, C. Stoots, J. O' Brien, J. Stephen Herring, *ECS Transactions*, **12** (1), 625 (2008)
4. Z. Zhan, W. Kobsiriphat, J. Wilson, M. Pillai, I. Kim and S. Barnett, *Energy & Fuels*, **23**, 3089 (2009)
5. A. Hauch, S. Ebbesen, S. Jensen and M. Mogensen, *J. Mater. Chem.*, **18**, 2331 (2008)
6. S. Jensen, P. Larsen, M. Mogensen, *Int. J. Hydrogen Energy*, **32**, 3253 (2007)
7. S. Ebbesen, M. Mogensen, *J. Power Sources*, **193**, 349 (2009)
8. M. Ni, M. Leung, D. Leung, *Int. J. Hydrogen Energy*, **33**, 2337 (2008)
9. A. Brisse, J. Schefold, M. Zahid, *J. Hydrogen Energy*, **33**, 5375 (2008)
10. A. Hauch, S. Jensen, S. Ramousse, M. Mogensen, *J. Electrochem. Soc.*, **153**, A1741 (2006)
11. A. Hauch, S. Ebbesen, S. Jensen, M. Mogensen, *J. Electrochem. Soc.*, **155**, B1184 (2008)
12. K. Sasaki, J. Maier, *Solid State Ionics*, **134**, 303 (2000)
13. S. Park, J. M. Vohs & R. J. Gorte, *Nature*, **404**, 265 (2000)
14. S. Tao, J. Irvine, *Nature Mater.*, **2**, 320 (2003)
15. S. Tao, J. Irvine, *J. Electrochem. Soc.*, **151**, A252 (2004)
16. G. Kim, G. Corre, J. T. S. Irvine, J. M. Vohs, and R. J. Gorte, *Electrochem. Solid-State Lett.*, **11(2)**, B16 (2008)
17. X. Yang and J. T. S. Irvine, *J. Mater. Chem.*, **18**, 2349 (2008)
18. G. Tsekouras and J. T. S. Irvine, *J. Mater. Chem.*, **21**, 9367 (2011)
19. F. Bidrawn, G. Kim, G. Corre, J. Irvine, J. Vohs, R. Gorte, *Electrochem. Solid-State Lett.*, **11**, B167 (2008)
20. R. Green, C. Liu, S. Adler, *Solid State Ionics*, **179**, 647 (2008)
21. X. Yue and J. T. S. Irvine, *Electrochem. Solid-State Lett.*, **15**, B1 (2012)
22. S. Boulfrad, M. Cassidy, J. T. S. Irvine, *Adv. Fun. Mater.*, **5**, 861 (2010)
23. S. D. Ebbesen, M. Mogensen, *J. Power Sources*, **193**, 349 (2009)
24. Y. Matsuzaki and I. Yasuda, *J. Electrochem. Soc.*, **147** (5), 1630 (2000)

25. C. Stoots, J. O'Brien, Proceedings of ASME international Mechanical Engineering Congress and Exposition (IMECE), 2007, Seattle, Washington, USA
26. P. Holtappels, L. G. J. De Haart, U. Stimming, I. C. Vinke and M. Mogensen, *J. Appl. Electrochem.*, **29** (5), 561 (1999)
27. K. Sasaki, J. Maier, *Solid State Ionics*, **134**, 303 (2000)
28. S. P. Simner, M. D. Anderson, L. R. Pederson, and J. W. Stevenson, *J. Electrochem. Soc.*, **152** (9), A1851 (2005)
29. Y. Huang, R. I. Dass, Z. Xing, J. B. Goodenough, *Science*, **312**, 254 (2006)
30. G. Kim, et al, *Electrochem. Solid-State Lett.*, **12**, B48 (2009)
31. Supporting online material for ref 29
32. N. Sun, X. Wen, F. Wang, W. Wei and Y. Sun, *Energy Environ. Sci.*, **3**, 366 (2010)
33. B. C. H. Steele & A. Heinzl, *Nature*, **414**, 345 (2001)
34. B. A. Boukamp, H. J. M. Bouwmeester, *Solid State Ionics*, **157** (1-4), 29 (2003)
35. S. B. Adler, *Solid State Ionics*, **111** (1-2), 125 (1998)
36. M. Gonzalez-Cuenca, W. Zipprich, B. A. Boukamp, G. Pudmich and F. Tietz, *Fuel cells*, **1** (3-4), 256 (2001)
37. K. Huang, M. Feng, and J. B. Goodenough, *J. Am. Ceram. Soc.*, **81** (2), 357 (1998)
38. O. A. Marina, C. Bagger, S. Primdahl, M. Mogensen, *Solid State Ionics*, **123** (1-4), 199 (1999)
39. K. Eguchi, N. Akasaka, H. Mitsuyasu, Y. Nonaka, *Solid State Ionics*, **135** (1-4), 589 (2000)
40. A. Tsoga, A. Gupta, A. Naoumidis and P. Nikolopoulos, *Acta Mater.*, **48** (18), 4709 (2000)

## **Chapter 5: Modification of LSCM based cathode to enhance performance for high temperature CO<sub>2</sub> electrolysis**

### **Table of Contents**

Introduction .....	123
5.1 Cathode with a graded structure .....	124
5.1.1 Preparation of the graded LSCM/YSZ cathode cell .....	124
5.1.2 Performance of the graded LSCM/YSZ cathode cell .....	125
5.1.3 Microstructure of the LSCM/YSZ gradient cathode .....	128
5.2 LSCM/GDC composite cathode with additional catalyst.....	129
5.2.1 Fabrication and characterization of LSCM/GDC cathode with extra catalyst	129
5.2.2 Performance from LSCM/GDC composite impregnated with different catalyst .....	130
5.2.3 Performance from LSCM/GDC composite cathode with different levels of catalyst loading .....	136
5.2.4 Microstructure analysis on LSCM/GDC composite impregnated with extra catalyst .....	138
5.3 LSCM based cathode with impregnated architecture.....	140
5.3.1 Single cell fabrication and characterization.....	140
5.3.1.1 Fabrication and characterization of LSCM impregnated YSZ cathode cell .....	140
5.3.1.2 Preparation and characterization of GDC impregnated LSCM cathode cell .....	141
5.3.2 LSCM impregnated YSZ cathode.....	143
5.3.3 GDC impregnated LSCM cathode.....	149

5.3.3.1 Microstructure of the GDC impregnated LSCM cathode .....	149
5.3.3.2 Performance of the GDC impregnated LSCM cathode for CO <sub>2</sub> electrolysis .....	151
5.3.3.3 Effect of introducing H <sub>2</sub> on the performance of the GDC impregnated LSCM cathode for CO <sub>2</sub> electrolysis.....	158
5.4 Pd and GDC co-impregnated LSCM cathode .....	162
5.4.1 Manufacture and characterization of Pd and GDC co-impregnated LSCM cathode cell .....	162
5.4.2 Performance from Pd and GDC co-impregnated cathode in various CO <sub>2</sub> -CO atmospheres .....	163
5.4.3 Microstructure analysis of the Pd-GDC co-impregnated cathode material .....	167
5.4.4 Stability of the Pd and GDC co-impregnated LSCM cathode for CO <sub>2</sub> electrolysis .....	168
5.5 Conclusions .....	169
References .....	170

## **Chapter 5: Modification of LSCM based cathode to enhance performance for high temperature CO<sub>2</sub> electrolysis**

### **Introduction**

Previously, it has been found that LSCM based composite is an alternative cathode material over Ni/YSZ cermets for high temperature CO<sub>2</sub> electrolysis, however, the requirement of high temperature sintering via ceramic mixing and subsequent screen-printing fabrication resulted in grain growth which led to insufficient cathode activity. Efforts are to be made to modify the LSCM based cathode microstructure for enhancement in performance for CO<sub>2</sub> electrolysis by SOEC.

Wet impregnation is a well known approach for the preparation of heterogeneous catalysts in the field of catalysis [1], and it has also been applied as an alternative method for the fabrication of high performance and nano-structured electrodes in SOFCs in recent years [2-11]. By placing the precursor solution which penetrated into the established electrode backbone and converted to catalytically active nanoparticles in later treatments, the electrode properties were found to be remarkably promoted due to the enlarged electrode reaction area and electro-catalytic activity. The advantage of wet impregnation over conventional ceramic mixing method is that it avoids the high temperature sintering considering that precursors are introduced into pre-fired electrode skeleton and are usually fired at 400-800°C. On the other hand, very good electrode/electrolyte interface can be maintained since the electrode backbone, usually a YSZ porous layer, is sintered separately and prior to the infiltration steps, through which detrimental solid reactions between different electrode components could be inhibited. The frequently applied materials in wet impregnation are oxide catalysts, such as doped ceria [4, 6, 9-10, 12], and metal catalysts including precious metals [3-4, 6, 8, 10-11], e.g. Pt, Pd, Rh, etc. Transition metals, such as Ni [3, 10, 13-14], Fe [3, 6], Cu [4, 8], are also frequently used catalysts for enhancement in electrode activity in SOFCs regarding that they possess good catalytic properties towards a lot of oxidation reactions.

Another performed technique in aim of promoting electrode performance in SOFCs is the introduction of graded microstructure [15-17]. That is to introduce a thin functional layer which provides the main reaction active sites near the electrolyte and a thicker

conduction layer further from the electrolyte primarily for current collecting purpose. Compared to the electrode made through ceramic mixing by average weight, a graded microstructure would give rise to larger TPB areas and faster electronic conduction paths as the electrode compositions are optimized in each layer. Nonetheless, this method still requires high temperature sintering, thus can only enhance the electrode performance to some extent, if the electrode compositions are optimized.

In this chapter, we set out to modify the LSCM based cathode performance for high temperature CO<sub>2</sub> electrolysis, by means of adopting graded cathodes and fabricating cathodes via low temperature wet impregnation. Adding extra metal catalyst, for instance, Pd, Pt, and Ni will be carried out to investigate their influences on the cathode properties and cathode kinetics for LSCM based materials. Ceria, which has been demonstrated as a promising cathode component, will be introduced to LSCM based cathode, similar to the above mentioned metal catalyst. Cathode activity will be assessed and compared, in order to find a high performance material for use as SOEC cathode for CO<sub>2</sub> electrolysis. The microstructure of various cathodes will be studied to analyze their contribution to the diverse performances observed.

## 5.1 Cathode with a graded structure

### 5.1.1 Preparation of the graded LSCM/YSZ cathode cell

Three-electrode geometry was used in the preparation of the graded cathode cell for which detailed procedures are as following. (La<sub>0.75</sub>Sr<sub>0.25</sub>)<sub>0.97</sub>(Cr<sub>0.5</sub>Mn<sub>0.5</sub>)O<sub>3-δ</sub> (LSCM, EMPA) and YSZ (PI-KEM) powders in weight ratios of 60/40 and 30/70 were mixed and ball-milled to prepare into screen-printing inks, denoted as LSCM/YSZ 60/40 and LSCM/YSZ 30/70 herein, respectively. The as-prepared LSCM/YSZ 30/70 ink was screen printed on the surface of YSZ pellet, and dried in oven at 80°C. Then the LSCM/YSZ 60/40 ink was printed on top of LSCM/YSZ 30/70 layer, followed by co-sintering of these two layers at 1200°C for 2 hrs. The introduced gradient LSCM/YSZ cathode structure is sketched schematically in Fig. 5.1.

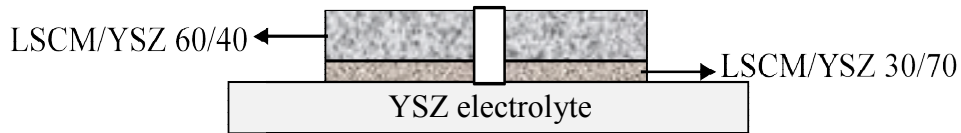


**Fig. 5.1** Schematic graph of graded cathode structure

LSM/ScSZ was printed and fired at 1100°C on the other side of YSZ pellet, as counter electrode and reference electrode, which is identical for all the cathode cells studied. Pt paste was painted and fired at 900°C for 1h as current collectors, prior to electrochemical characterizations for which I-V polarization curves and impedance spectra of the as-prepared cathode cell were measured in diverse CO<sub>2</sub>/CO mixtures at 900°C. The microstructure of the gradient cathode was examined by SEM after electrochemical tests.

### **5.1.2 Performance of the graded LSCM/YSZ cathode cell**

Fig. 5.2 shows the I-V curve of the cell with gradient LSCM/YSZ fuel electrode working in CO<sub>2</sub>/CO 70/30 environment at 900°C, and the I-V curve of the cell with the LSCM/YSZ composite prepared via ceramic mixing and high temperature sintering, as was dealt with in Chapter 4, is illustrated here as well for comparison. As electrolyte supported single cell configuration was used in sample fabrication, the ohmic losses  $R_s$  from YSZ electrolyte contributes overwhelmingly to the total cell losses. Therefore, no significant differences are observed from the polarization curves of the above two cathode cells in Fig. 5.2, except that the gradient cathode cell displays smaller cell resistance at high loadings under electrolysis operation.

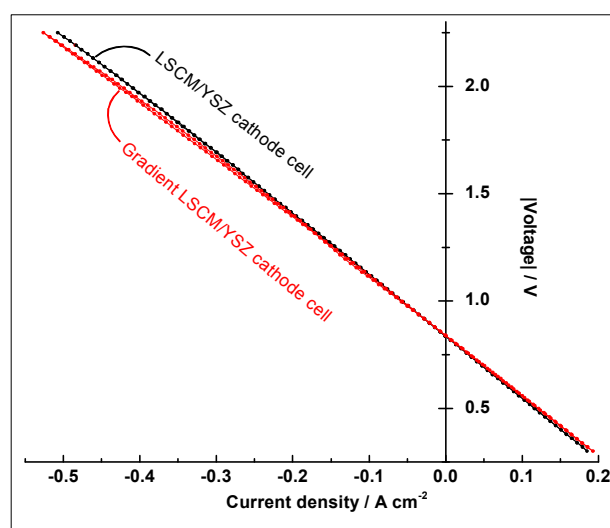


**Fig. 5.2** I-V curves of the cells based on LSCM/YSZ composite working at 900°C in CO<sub>2</sub>/CO 70/30 atmosphere

The impedance data clearly show the discrepancy in performance for cathode made by different methods. Shown in Fig. 5.3 are the impedance comparisons between the normal LSCM/YSZ cathode and the gradient LSCM/YSZ cathode, with both cathodes working at different levels of loading in CO<sub>2</sub>/CO 70/30 mixture at 900°C. The  $R_s$  was corrected as  $R_s$  mainly came from the ca.2 mm thick YSZ electrolyte therefore  $R_s$  from lateral electrodes were neglected for both cathode cells. It can be observed in Fig. 5.3 that the polarization resistance  $R_p$  from the gradient LSCM/YSZ cathode is smaller than that from the averaged composite cathode under OCV condition. With the gradient cathode microstructure, the cathode impedance arcs are apparently suppressed, implying that the graded structure is beneficial for the enhancement in cathode performance and CO<sub>2</sub> electrochemical reduction kinetics. The above phenomena get more pronounced in electrolysis operation conditions, e.g. at 0.5V (refers to OCV value herein) and at 1.0V in Fig. 5.3. At 1.0V, the  $R_p$  values are 0.47 and 0.74  $\Omega \text{ cm}^2$ , respectively for the gradient and normal LSCM/YSZ cathodes. Noting that the shape and outline of the impedance arcs are hardly changed, though the size of impedance arcs from the gradient cathode are remarkably reduced, which may be indicative that the rate limiting processes for cathode reaction, i. e. the CO<sub>2</sub> electrochemical reduction, are consistent

for the gradient LSCM/YSZ cathode and the one prepared via ceramic mixing by average weight and high temperature sintering.

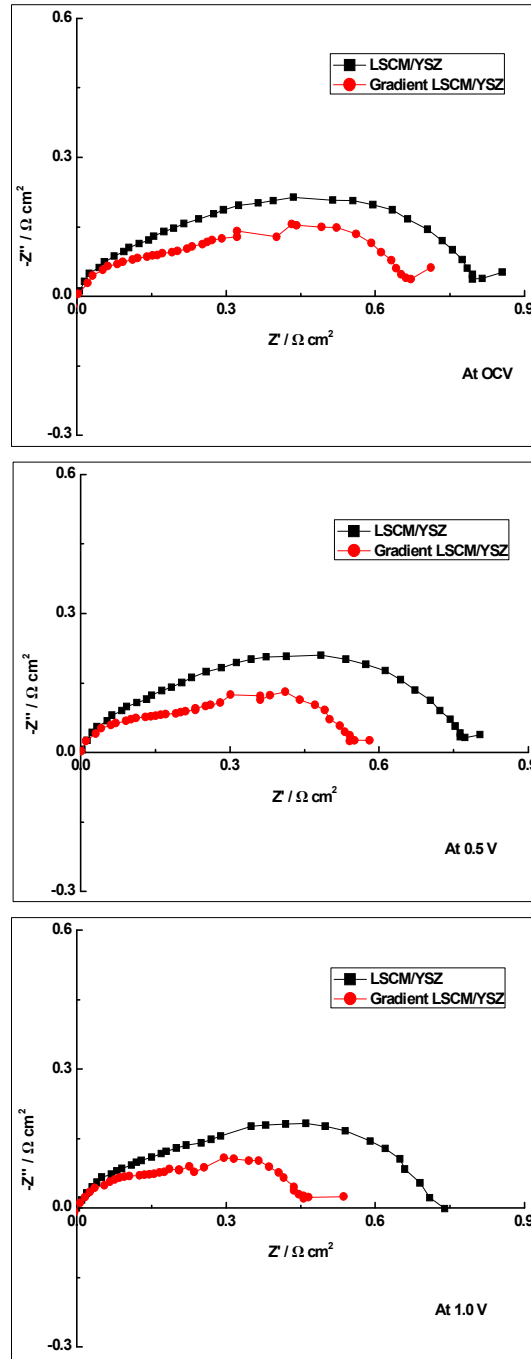


**Fig. 5.3** Performance comparisons of LSCM/YSZ cathode and graded LSCM/YSZ cathode working at OCV (the top graph), 0.5V (the middle graph) and 1.0V (the bottom graph) in CO<sub>2</sub>/CO 70/30 mixture at 900°C

### 5.1.3 Microstructure of the LSCM/YSZ gradient cathode

The microstructure of the LSCM/YSZ gradient cathode was surveyed by SEM after electrochemical tests, as displayed in Fig. 5.4. From the SEM cross-sectional view, the LSCM/YSZ gradient cathode consists of two layers, the inner LSCM/YSZ 30/70 layer that is close to the electrolyte and the outer LSCM/YSZ 60/40 layer. The thicknesses of the inner and outer layer are around 10 $\mu$ m and 20 $\mu$ m, respectively. The gradient cathode contacts very well with the YSZ electrolyte.

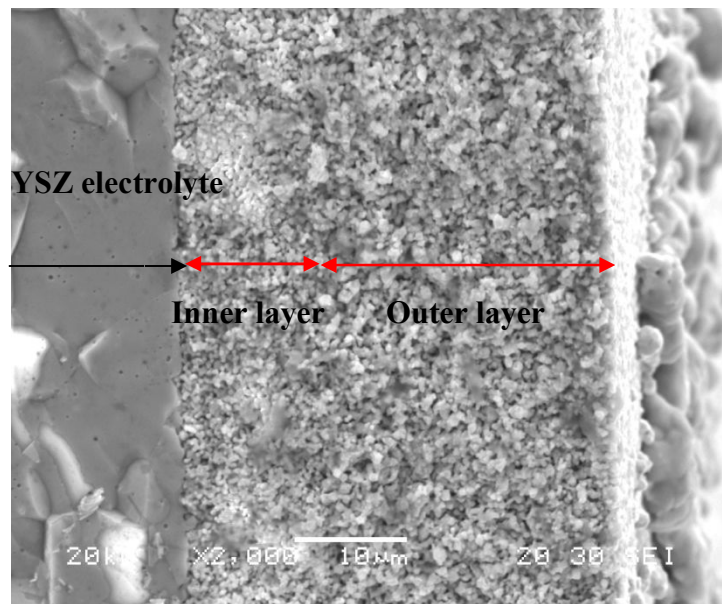


**Fig. 5.4** SEM graph of the gradient LSCM/YSZ cathode after testing in CO<sub>2</sub>/CO mixtures

LSCM is the catalyst and YSZ provided most oxide ion conducting paths in the present cathode material. Compared to LSCM/YSZ 50/50 composite cathode, the increased concentration of YSZ in inner layer of the graded structure is favourable for the diffusion of dissociated oxide ion into YSZ electrolyte, and the higher amount of LSCM in outer layer of the gradient cathode is advantageous for CO<sub>2</sub> dissociation as well as electronic conduction. According to literature review, gradient composite would introduce gradient distribution of particle sizes, pores and concentrations, which is believed to be beneficial for expand TPB area and mass transfer [16, 17]. As a result,

the raised amount of YSZ phase in the inner layer and of LSCM component in the outer layer might lead to enlarged TPB area and thus promoted cathode performance for LSCM/YSZ cathode. Besides, the high level of YSZ phase in the inner layer is helpful for improving cathode/electrolyte contacting, thereby, the cathode/electrolyte interfacial resistance in the gradient structure is probably decreased. Combined with the electrochemical results in Fig. 5.2 and Fig. 5.3, it is believed that the graded structure provides more active sites and conducting paths for the cathode reaction, which interprets the higher performance of the gradient LSCM/YSZ cathode over the LSCM/YSZ 50/50 composite cathode.

The gradient structure was not applied to LSCM/GDC composite cathode, which was demonstrated as an alternative cathode material, due to the concerns of possible solid phase reaction between GDC and YSZ and of increasing interfacial resistance upon the increasing GDC content in the layer close to YSZ electrolyte [18, 19].

## **5.2 LSCM/GDC composite cathode with additional catalyst**

### **5.2.1 Fabrication and characterization of LSCM/GDC cathode with extra catalyst**

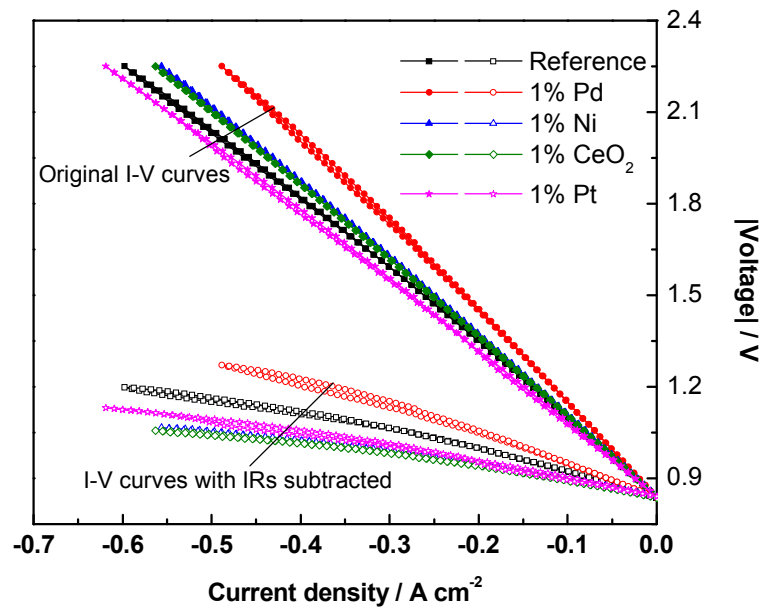
Single cells were fabricated as described before, with LSCM/GDC (1200°C) composite as cathode and LSM/ScSZ (1100°C) as anode. After this, extra catalyst, including Pd, Ni, CeO<sub>2</sub> and Pt, was introduced by wet impregnation, the schematic of which was shown in Fig. 2.4. A blank cell, which had no extra catalyst in cathode, was also prepared for comparison.

For wet impregnation, the aqueous metal nitrate solution was prepared and placed on top of LSCM/GDC composite cathode using a syringe, at a certain catalyst loading amount, usually 0.5-1 wt% of LSCM/GDC cathode. The nitrate solution then penetrated into cathode pores by capillary force, followed by firing at 500°C for 50 min to decompose nitrate. In the case of Pd extra catalyst, ethanol based nitrate solution with 1wt% of loading and water based solution with different amounts of loading were performed, to study the effect of solvent and loading amount on cathode performance. The cathode cell with 1wt% catalyst was denoted as 1% Pd, 1% Ni, 1% CeO<sub>2</sub> and 1% Pt, respectively, and the cathode cell without any extra catalyst was denoted as Reference.

Pt paste was painted on both cathode and anode side and fired at 900°C as current collectors before electrochemical testing. At operation temperature, humidified 5% H<sub>2</sub>/Ar was firstly flowed through cathode chamber to reduce metal oxide to metallic state for extra catalyst aided LSCM/GDC cathode cell, before switching to CO<sub>2</sub>/CO mixture gas. With respect to electrochemical characterization, I-V curves and impedance spectra were measured to compare the influence from different catalysts on the LSCM/GDC cathode performance. SEM and EDX inspection were carried out to characterize the microstructure of impregnated LSCM/GDC cathode after electrochemical tests. In the extra catalyst aided LSCM/GDC cathode, high resolution field emission scanning electron microscope (FE-SEM) was conducted for better study of the cathode microstructure.

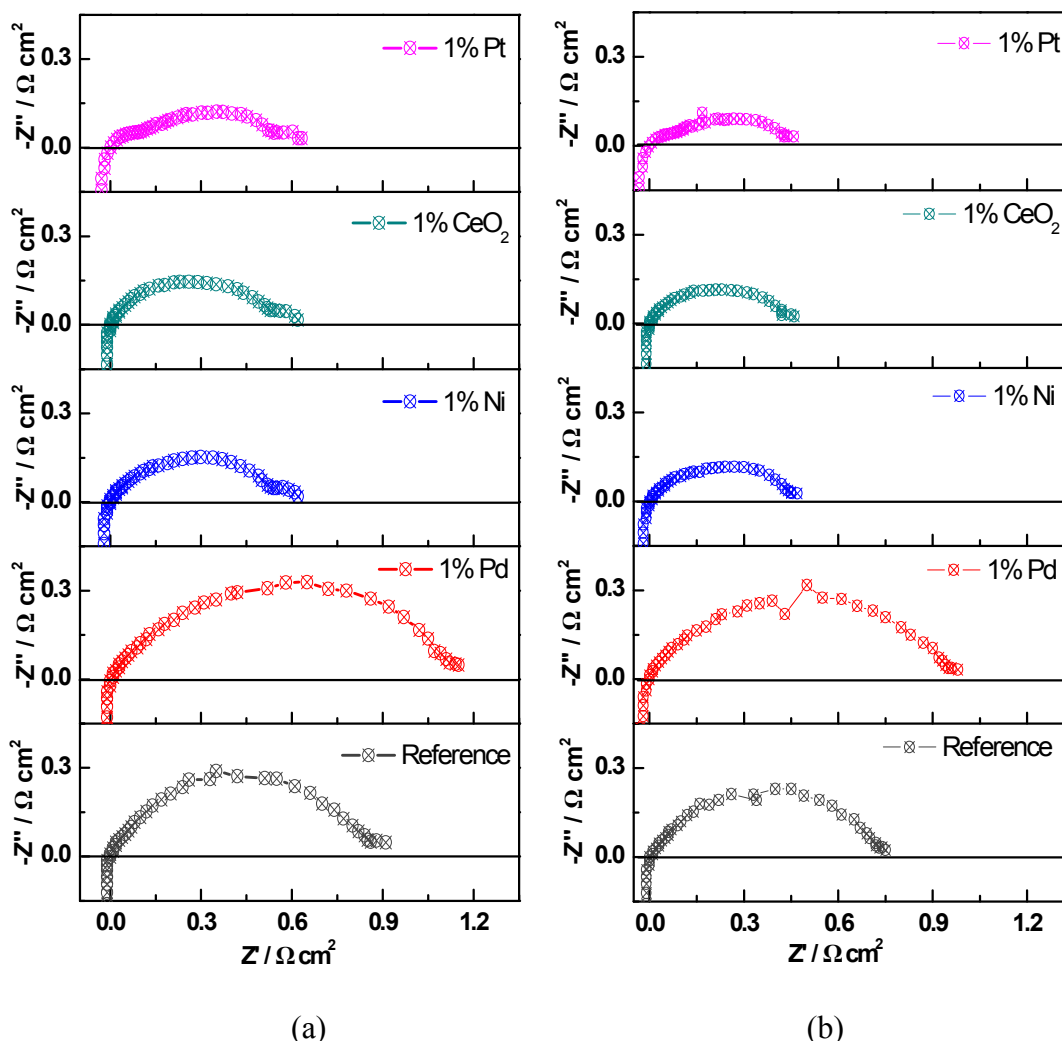
### **5.2.2 Performance from LSCM/GDC composite impregnated with different catalyst**

Fig. 5.5 shows the polarization curves of the cells with different extra catalysts infiltrated into LSCM/GDC cathode. The measurement was carried out in CO<sub>2</sub>/CO 70/30 atmosphere at 900°C, and the amount of catalysts were approximately 1wt%. From the original I-V curves, it can be observed that the introduction of additional catalyst seems to affect the cathode performance negatively except the case of Pt catalyst. Considering that the R<sub>s</sub> from the thick YSZ electrolyte contributed to cell performance to a significant extent which would cover the influence of extra catalyst, on the other hand, the amount of catalyst added into LSCM/GDC cathode was so low that it was believed to be less likely to affect the electrode conductivity [6], I-V curves with IRs subtracted were thus plotted, on the assumption that R<sub>s</sub> from electrolyte was independent of operating current as that concentration diffusion seemed not to be the limiting processes. The I-V curves with IRs deducted are also displayed in Fig. 5.5.



**Fig. 5.5** I-V curves of LSCM/GDC cathode cell with different extra catalyst in CO<sub>2</sub>/CO 70/30 atmosphere at 900°C

From the re-plotted I-V curves, one can see that the cell performance is clearly improved by the introduction of 1wt% Ni, 1 wt% CeO<sub>2</sub> and 1wt% Pt into LSCM/GDC composite cathode, compared to the blank cell, suggesting that the cathode catalytic property towards CO<sub>2</sub> reduction reaction is enhanced. In contrast, the cell with 1 wt% Pd in LSCM/GDC cathode shows no such effect. The influences from extra catalysts become more distinct under electrolysis operation conditions.



**Fig. 5.6** Performance comparison among different catalyst impregnated LSCM/GDC composite cathode working at (a) OCV (frequency  $10^5$ -0.015Hz) and (b) 0.5V (frequency  $10^5$ -0.1Hz) in CO<sub>2</sub>/CO 70/30 mixture at 900°C

Fig. 5.6 shows the impedance comparisons among different catalyst impregnated LSCM/GDC cathode working in CO<sub>2</sub>/CO 70/30 mixture at 900°C. By adding 1wt% Ni, CeO<sub>2</sub> and Pt respectively, the LSCM/GDC cathode performance is greatly promoted either at OCV (Fig. 5.6(a)) or at 0.5V (Fig. 5.6(b)), reflected by the diminished impedance arcs, compared with the impedance arcs of the reference cathode. The changes of the impedance arcs in Fig. 5.6 (a) and (b) indicate that the cathode catalytic activity for CO<sub>2</sub> reduction is clearly promoted by adding 1 wt% Ni, CeO<sub>2</sub> and Pt to LSCM/GDC composite. However, these changes are not observed in the impedance

spectra of 1 wt% Pd impregnated LSCM/GDC composite cathode, and instead, the low frequency arc increases at both OCV and 0.5V for 1 wt% Pd infiltrated LSCM/GDC cathode, hence, the cathode kinetics, especially the surface kinetics, seems to be retarded by introducing 1wt% Pd catalyst into LSCM/GDC composite cathode working for CO<sub>2</sub> dissociation. Further, the Gerischer like impedance dispersion, displayed by the reference cathode, changes to non-Gerischer impedance upon introducing 1 wt% Ni, CeO<sub>2</sub>, and Pt into LSCM/GDC composite cathode. In the case of adding Pt catalyst, the impedance develops to three distinguishable arcs, different from what have been observed from the impedance spectra of LSCM/GDC cathode with 1 wt% CeO<sub>2</sub> and 1 wt% Ni extra catalyst.

The R<sub>p</sub> values (extracted from impedance spectra in Fig. 5.6) from the LSCM/GDC composite cathode with different catalyst for CO<sub>2</sub> electrochemical reduction are compared at OCV and at 0.5V in Fig. 5.7. At OCV, the R<sub>p</sub> value for the Reference cathode is 0.91 Ω cm<sup>2</sup>, and the R<sub>p</sub> for 1% Ni, 1% CeO<sub>2</sub> and 1% Pt aided cathode is 0.62, 0.62 and 0.63 Ω cm<sup>2</sup>, respectively. At 0.5V, similar results can be observed as the R<sub>p</sub> value is 0.75, 0.47, 0.46, and 0.46 Ω cm<sup>2</sup> for the reference cathode, 1% Ni, 1% CeO<sub>2</sub>, and 1% Pt cathode, respectively. The R<sub>p</sub> value for 1% Pd cathode, 1.15 Ω cm<sup>2</sup> at OCV and 0.98 Ω cm<sup>2</sup> at 0.5V in CO<sub>2</sub>/CO 70/30 atmosphere at 900°C, is larger than the value from the reference cathode in the same conditions. The phenomena reflected in Fig. 5.6 and Fig. 5.7 is in accordance with those from the re-plotted I-V curves in Fig. 5.5.

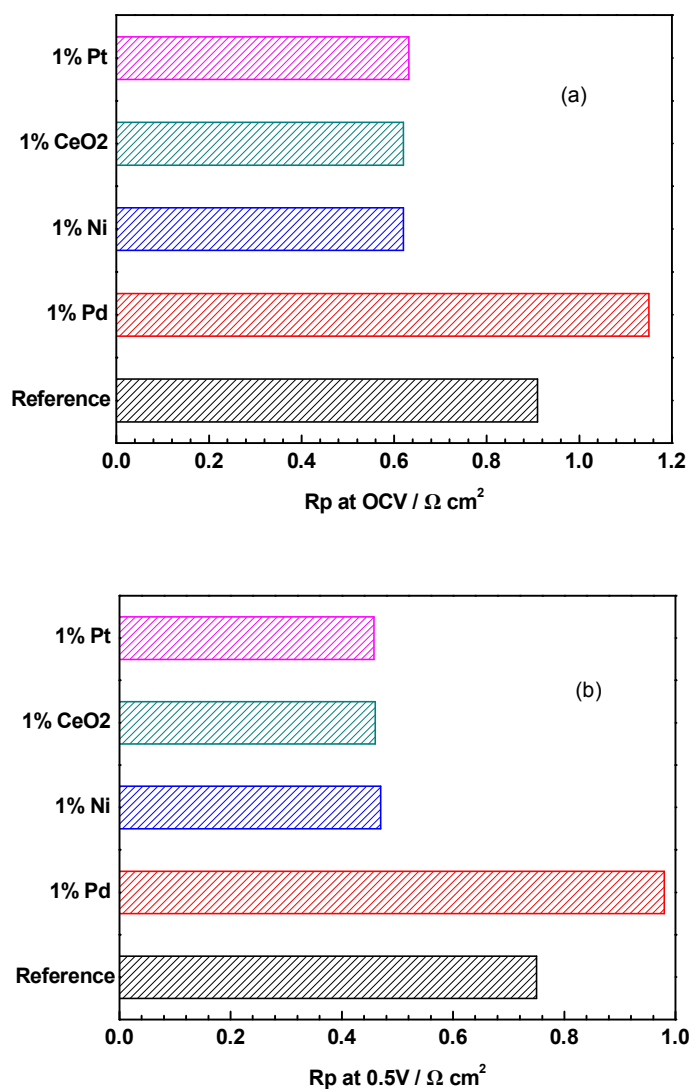


**Fig. 5.7** Bar chart of  $R_p$  from different catalyst impregnated LSCM/GDC composite cathode working at (a) OCV and (b) 0.5V

In the above, the investigated cathodes with extra catalyst were made using aqueous nitrate solution infiltrated into the LSCM/GDC composite, and it was found that the addition of 1wt% Pd into LSCM/GDC composite did not improve the cathode performance which does not agree with the observations from other researcher [7, 10-11]. Nevertheless, when using ethanol rather distilled water as solvent in preparing Pd nitrate precursor solution for impregnating LSCM/GDC composite cathode, different result was detected, as shown in Fig. 5.8. Operated in CO<sub>2</sub>/CO 70/30 mixture at 900°C at OCV, the LSCM/GDC cathode performance towards CO<sub>2</sub> reduction is apparently

reinforced by the introduction of 1 wt% Pd metal catalyst, as indicated by the suppression in the size of impedance arcs in Fig. 5.8, compared to that of the LSCM/GDC composite cathode without Pd.

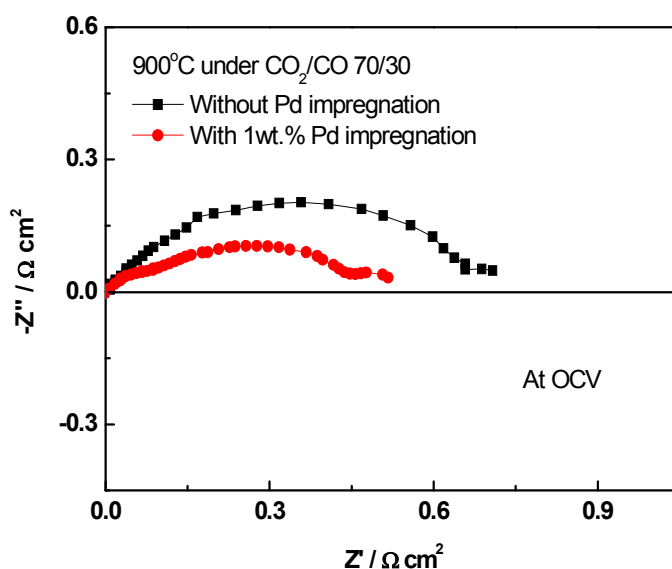


**Fig. 5. 8** Performance comparison between LSCM/GDC composite cathode with and without Pd catalyst added by wet impregnation using ethanol rather than water as solvent for the preparation of precursor nitrate solution (measurement conditions are OCV, 900°C and with CO<sub>2</sub>-CO 70-30 mixture gas)

It seems that the solvent used to prepare the Pd precursor solution plays an important role in determining the Pd distribution and consequently its catalytic property towards CO<sub>2</sub> reduction. Y. Zhang et al found that the Co/SiO<sub>2</sub> catalyst prepared from dehydrated ethanol exhibited a higher activity for F-T synthesis than the catalyst prepared from aqueous nitrate solution, due to the enhanced interaction between catalyst and support inducing highly dispersed cobalt and more active sites using ethanol solvent in the preparation of nitrate solution for incipient impregnation [20]. Similarly, highly dispersed Pd might be introduced via impregnating ethanol Pd precursor nitrate solution, avoiding possible large Pd clusters formed by impregnating aqueous Pd precursor nitrate solution into LSCM/GDC composite, and the highly dispersed Pd particles provide more catalytically active sites than the Pd clusters, attributing to the enhanced cathode activity.

### 5.2.3 Performance from LSCM/GDC composite cathode with different levels of catalyst loading

The LSCM/GDC composite cathodes with different levels of Pd loading were prepared to study the influence of catalyst amount on the cathode performance and the CO<sub>2</sub> reduction kinetics. Impedance results of the LSCM/GDC composite cathode with different amounts of Pd working in CO<sub>2</sub>/CO 70/30 atmosphere at 900°C for CO<sub>2</sub> electrochemical reduction are demonstrated in Fig. 5.9. One can see from the Nyquist plot in Fig. 5.9(a) that the addition of 0.5wt% Pd positively affects the LSCM/GDC composite cathode, with R<sub>p</sub> decreasing to 0.56 Ω cm<sup>2</sup> from 0.91 Ω cm<sup>2</sup> for the cathode without Pd, whereas the addition of 1wt% Pd seems to worsen the LSCM/GDC composite cathode performance for CO<sub>2</sub> electrolysis. Further rise of the Pd loading amount, 1.75wt% here, leads to an R<sub>p</sub> 0.7 Ω cm<sup>2</sup>, increased compared with that of 0.5wt% Pd aided cathode, but it is still lower than the R<sub>p</sub> from the cathode without Pd and the one with 1wt% Pd loading. Moreover, it can be seen from Fig. 5.9(a) that the addition of Pd catalyst to LSCM/GDC composite cathode basically suppresses the size of the low frequency arc, indicating that the rate determining steps associated with the low frequency arc, most likely the surface kinetics as discussed in section 4.4, are facilitated except the case in which 1 wt% Pd is added.

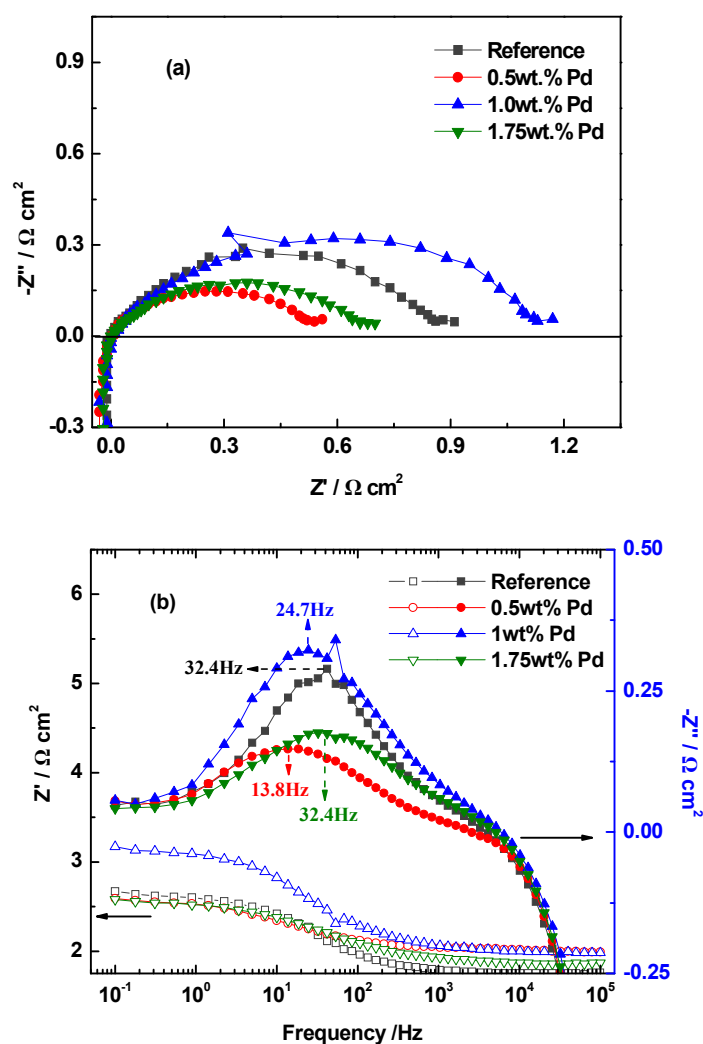


**Fig. 5. 9** Impedance behaviour of the LSCM/GDC cathode with different level of Pd catalyst added via aqueous impregnation (a) Nyquist plot; (b) Bode plot; the cathode operation conditions are: at OCV in CO<sub>2</sub>/CO 70/30 atmosphere at 900°C.

From the Bode plot in Fig. 5.9(b), different characteristic frequencies associated with the low frequency arc are obtained regarding the different amount of Pd incorporated LSCM/GDC composite cathode for CO<sub>2</sub> electrochemical reduction. The characteristic frequency decreases with increasing Pd loading level, compared with that of the cathode without Pd. In the previous section, it was found that using ethanol, instead of distilled water as solvent in preparing Pd precursor nitrate solution yields an enhanced cathode activity for 1wt% Pd impregnated LSCM/GDC cathode. The decreased polarity of

solvent might give rise to highly dispersed Pd particles and thus promote cathode performance. Considering this and combined with the observations in the Nyquist plot, it is supposed that Pd particle aggregation, if happened, is less likely in the case of 0.5wt% as loading amount. The exact reasons for the diverse effects from Pd loading are not known and will be looked into.

#### 5.2.4 Microstructure analysis on LSCM/GDC composite impregnated with extra catalyst

The SEM images of the fractured LSCM/GDC composite cathode with different extra catalysts incorporated by wet impregnation are presented in Fig. 5.10, with the images of the cathode without extra catalyst for the purpose of comparison. Also, the surface view of the LSCM/GDC composite cathode with and without 1% Pd introduced by Pd precursor nitrate ethanol solution are displayed through the micrographs measured by SEM.

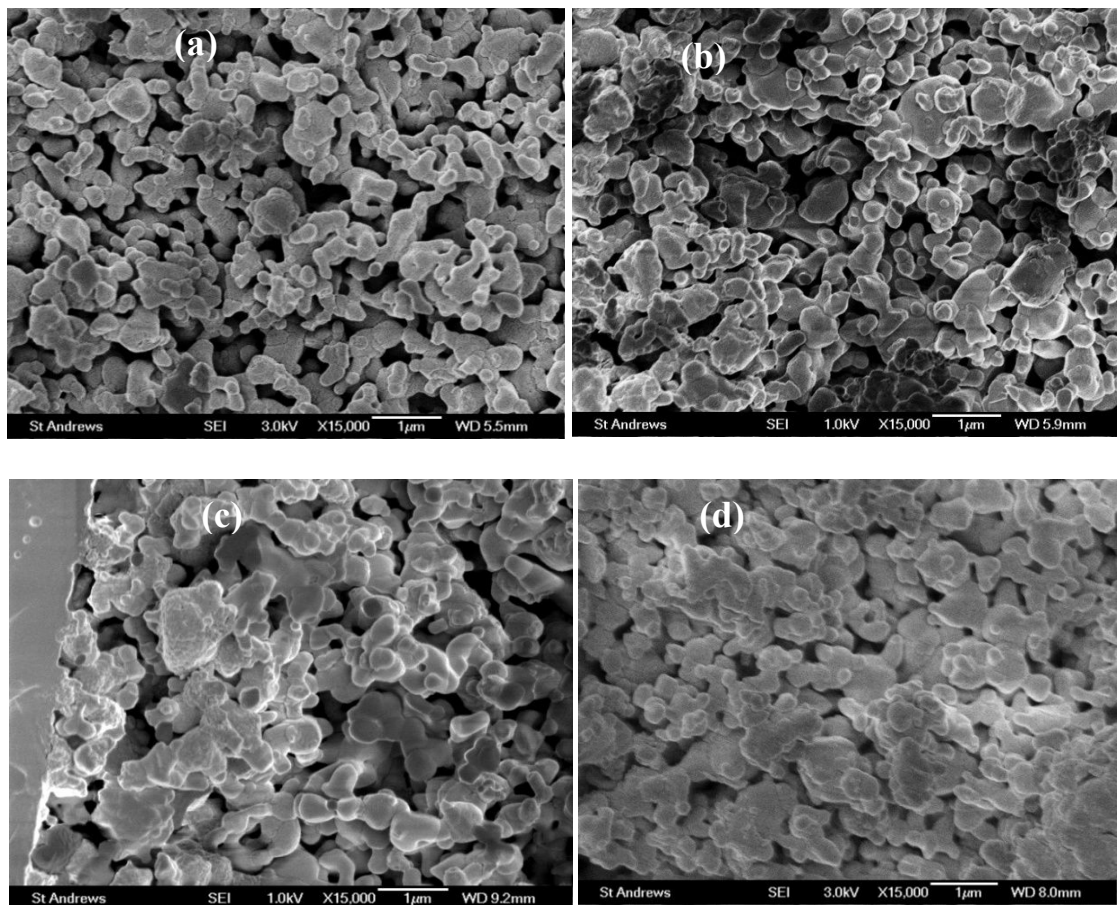


(Figure continued on the following page)

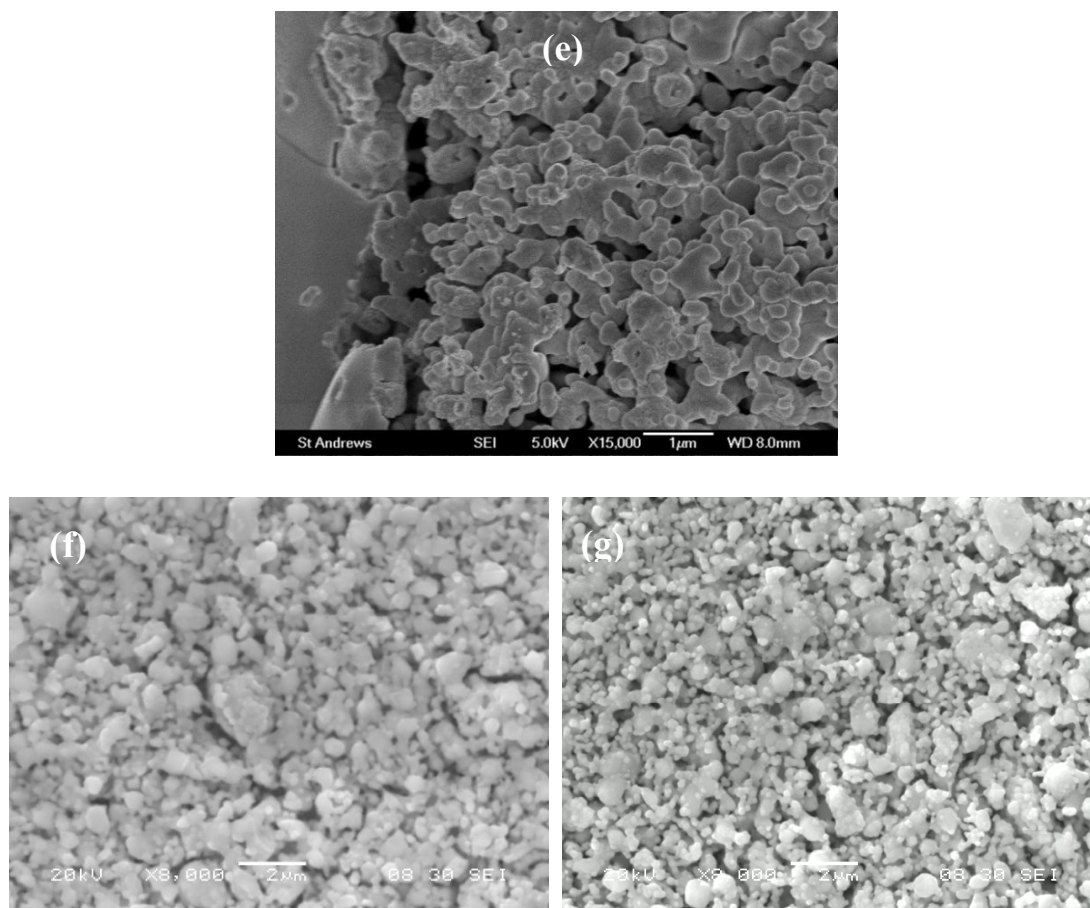


**Fig. 5. 10** FE-SEM images of cross-sectional view of the LSCM/GDC composite cathode with 0.5% Pd (a), 1% Ni (b), 1% CeO<sub>2</sub> (c), 1wt% Pt (d) and the LSCM/GDC composite cathode without extra catalyst (e), as well as SEM images of the surface view of the LSCM/GDC composite cathode (f) and of that with 1w% Pd incorporation via wet impregnation of ethanol nitrate solution (g)

Compared to the SEM image of the LSCM/GDC composite cathode, one can observe from Fig. 5.10 (a)-(d) that the introduced Pd, Ni, CeO<sub>2</sub> and Pt extra catalyst are located on the surface of the LSCM/GDC composite. The particle sizes of the added catalyst via aqueous impregnation are in the range of 100-300 nm. The distribution of the extra catalyst can be seen clearly in the surface view of 1wt% Pd impregnated LSCM/GDC cathode as shown in Fig. 5.10 (g), in which highly dispersed Pd particles are scattered on the surface of LSCM/GDC support. It is believed that the highly dispersed nano-structured catalyst provides extra active sites for the CO<sub>2</sub> dissociation on the

LSCM/GDC cathode, that is to say the TPBs on the cathode are extended. These are the reasons responsible for the enhanced performance observed on the LSCM/GDC composite cathode with dopant level of extra catalyst, such as Pd, Ni, CeO<sub>2</sub>, and Pt.

However, it has been found that the adhesion of LSCM/GDC composite cathode to the YSZ electrolyte disk deteriorates (not shown) with lowering sintering temperature from 1300°C (performed for the LSCM/GDC composite cathode in Chapter 4) to 1200°C, though decreasing fabrication temperature and adding extra catalyst in the meantime effectively promoted, to a certain extent, the LSCM/GDC cathode performance. This also was a significant concern for catalyst aided LSCM/GDC cathode, which would pose performance degradation over long-term operation.

### **5.3 LSCM based cathode with impregnated architecture**

#### **5.3.1 Single cell fabrication and characterization**

##### **5.3.1.1 Fabrication and characterization of LSCM impregnated YSZ cathode cell**

The initial steps involved the preparation of YSZ screen printing ink and LSCM nitrate solution. YSZ ink was prepared in a similar procedure as for making other screen printing inks which was described in Chapter 2, and the only difference was that glassy carbon and graphite were added as pore formers to prepare porous YSZ skeleton. The amount of pore formers was 30 wt%, lower than which did not give a sufficiently porous YSZ layer for subsequent infiltration of LSCM solution and higher than which made the YSZ ink too thick to be printed on the surface of YSZ pellet. The ratio between glassy carbon and graphite was 20: 80 by weight. The as-prepared YSZ ink was screen-printed on one surface of the YSZ pellet, and fired at 1350°C for 1h which would leave a thin porous YSZ layer as skeleton for LSCM impregnation.

For the fabrication of LSCM (in the formula of  $(La_{0.75}Sr_{0.25})_{0.97}(Cr_{0.5}Mn_{0.5})O_3$ ) nitrate solution (1.5M), La(NO<sub>3</sub>)<sub>3</sub>·6H<sub>2</sub>O (99.9%, Alfa Aesar), Sr(NO<sub>3</sub>)<sub>2</sub> (98%, STREM CHEMICALS), Cr(NO<sub>3</sub>)<sub>3</sub>·9H<sub>2</sub>O (99%, Alfa Aesar), and Mn(NO<sub>3</sub>)<sub>2</sub>·xH<sub>2</sub>O (99.98%, Alfa Aesar, x≈4) nitrates, in stoichiometric ratios, were dissolved into distilled water under stirring. LSCM nitrate solution was introduced into the above prepared YSZ porous layer by vacuum impregnation at 0.22bar, and then the sample was fired at 500°C to

decompose nitrates. The LSCM loading amount was obtained by weighing the sample before and after impregnation and firing, which were repeated until the required LSCM loading amount, that was LSCM:YSZ 50:50 by weight, was reached. Subsequently, the sample was sintered at 1100°C for 2 hrs. XRD was performed to examine the phase structure of the as-synthesized cathode.

After the fabrication of LSCM impregnated YSZ cathode, LSM/ScSZ anode was screen-printed on the other side of YSZ pellet and fired at 1100°C. The as-prepared single cell was in three-electrode geometry. Pt paste was painted and fired at 900°C as current collector. For electrochemical characterization at 900°C, humidified 5% H<sub>2</sub>/Ar was introduced into cathode chamber to reduce LSCM phase prior to the recording of I-V curves and impedance spectra of LSCM impregnated YSZ cathode cell in CO<sub>2</sub>/CO mixtures. SEM inspection was carried out to check the cathode microstructure after electrochemical characterization. SEM images of a freshly made cathode were measured as well for comparison.

### **5.3.1.2 Preparation and characterization of GDC impregnated LSCM cathode cell**

LSCM screen-printing ink was prepared similar to the preparation of YSZ ink, and 30 wt% pore formers were also adopted in manufacturing LSCM ink. GDC (in the formula of Gd<sub>0.1</sub>Ce<sub>0.9</sub>O<sub>1.95</sub>) nitrate solution (2M) was prepared for which Gd(NO<sub>3</sub>)<sub>3</sub>·6H<sub>2</sub>O (ALDRICH) and Ce(NO<sub>3</sub>)<sub>3</sub>·6H<sub>2</sub>O (Fisher Scientific) nitrates in stoichiometric ratio were dissolved into distilled water.

Regarding single cell fabrication, again, three-electrode geometry was employed. A YSZ pellet was pressed and fired as described in previous chapters. Then on the one side of YSZ pellet, a very thin YSZ porous layer was deposited using YSZ screen-printing ink. After drying the thin YSZ layer in oven at 80°C, LSCM ink was screen-printed on the top of YSZ thin layer, followed by co-sintering these two layers at 1300°C. The introduction of the thin YSZ porous layer between YSZ pellet and LSCM porous layer was to improve the interfacial adhesion. The following step was adding GDC aqueous nitrate solution into LSCM/YSZ porous layer in vacuum pressure condition (0.22bar) and heat treatment at 500°C to decompose nitrate. This step was repeated until the total GDC loading amount achieved 50 wt% with respect to the

weight of LSCM/YSZ. Finally, the sample was calcined at 1100°C in air. On the other side of YSZ pellet, LSM/ScSZ anode was prepared as described before. A single cell with GDC impregnated into YSZ porous layer as cathode was fabricated in the same way to make comparison with the GDC impregnated LSCM cathode cell, and in this case, the thickness of the YSZ porous layer was made identical to the thickness of LSCM/YSZ porous layer. The image of freshly made single cells is shown in Fig. 5.11.

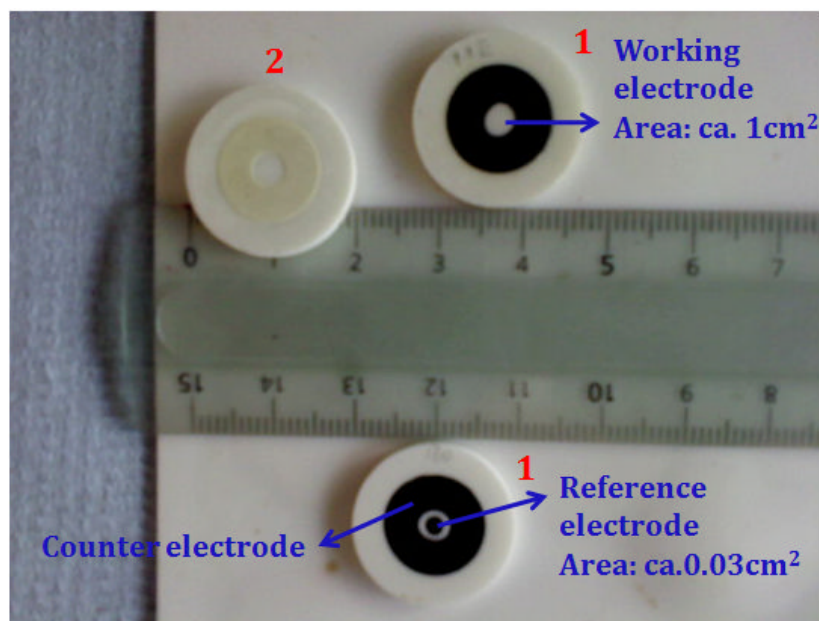


**Fig. 5.11** Image of freshly made GDC impregnated LSCM cathode cell (No. 1) and GDC impregnated YSZ cathode cell (No. 2)

Pt wires and Pt paste were used as electrical contact to external instrument for electrochemical test. I-V curves and impedance spectra of the GDC impregnated LSCM cathode were recorded in various CO<sub>2</sub>-CO mixtures over the temperature range of 900-750°C at an interval of 50°C. Comparisons were conducted on the performance of the GDC impregnated LSCM cathode with previously fabricated cathode for high temperature CO<sub>2</sub> electrolysis. The effect of introducing H<sub>2</sub> (5% H<sub>2</sub>/Ar was used) on the CO<sub>2</sub> reduction process was also investigated in CO<sub>2</sub>-CO 70-30 atmosphere. SEM and EDX were employed to study the microstructure of the GDC impregnated LSCM cathode after electrochemical tests.

### 5.3.2 LSCM impregnated YSZ cathode

The XRD result of the LSCM impregnated YSZ cathode from a freshly made single cell is displayed in Fig. 5.12. Diffraction peaks which are expected for LSCM and YSZ can be detected clearly in Fig. 5.12; however, Bragg peaks other than those from LSCM and YSZ can be seen from the zoomed XRD pattern of the framed zone in the top image in Fig. 5.12. Since the possibility of chemical reaction between LSCM and YSZ at 1100°C is little [21], the impurity peaks observed in Fig. 5.12 indicate that sintering temperature, such as 1100°C that was adopted in our fabrication, is not high enough to form the pure phased LSCM.

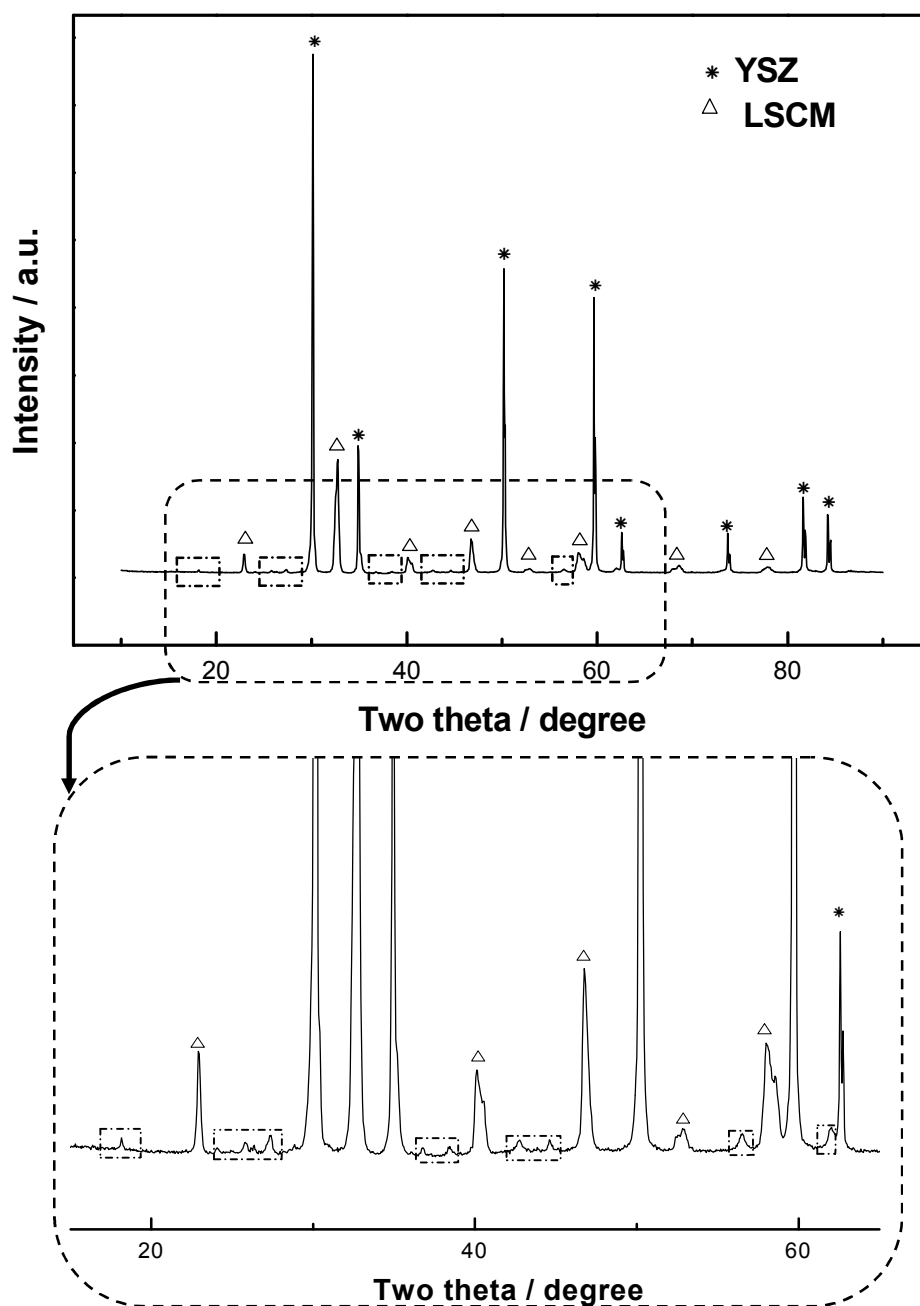


**Fig. 5.12** XRD pattern of the LSCM impregnated YSZ cathode from a freshly prepared single cell (the bottom graph is the close-up of the framed zone in the top graph)

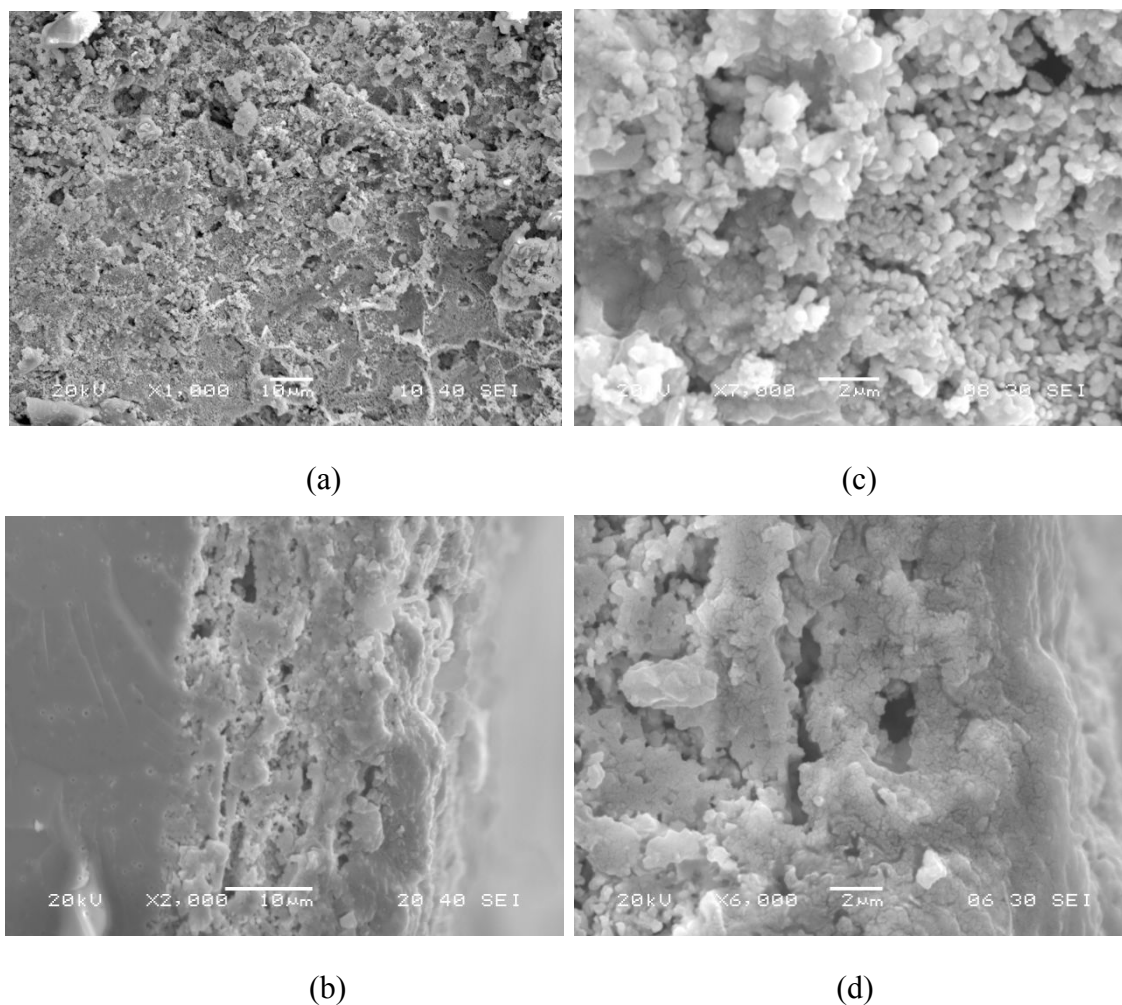


**Fig. 5.13** Surface view ((a) and (c)) and cross-sectional view ((b) and (d)) of a fresh LSCM impregnated YSZ cathode examined by SEM

The SEM micrographs of an untested LSCM infiltrated YSZ cathode are shown in Fig. 5.13. A uniform distribution of LSCM over porous YSZ can be observed from the surface view in Fig. 5.13 (a) and (c). By looking at it from cross-sectional view (Fig. 5.13 (b) and (d)), the LSCM introduced by aqueous impregnation seems to form a dense film over the porous YSZ phase. Similar observations were reported by other researchers for LSCM–YSZ composite with 45 wt% LSCM incorporated into porous YSZ by infiltration and it was reported that the LSCM coating on YSZ broke up into particles in reducing atmosphere which made it satisfactory electro-catalyst in electrode reaction [6, 22]. Distinguishable LSCM nano-particles were also detected by SEM (the

results are not shown here) in our study after running the LSCM impregnated YSZ cathode in 5% H<sub>2</sub>/Ar and testing it in CO<sub>2</sub>/CO atmospheres.

Fig. 5.14 exhibits the I-V curve from the LSCM impregnated YSZ cathode cell working at 900°C in CO<sub>2</sub>-CO 70-30 fuel gas. Apparently, there is hysteresis at high potential range on the polarization curve in electrolysis mode (negative current), which is different from the fairly linear I-V curves observed on LSCM/YSZ composite cathode (prepared via screen-printing) cell and LSCM/YSZ graded cathode cell as shown in Fig. 5.2. As extra peaks besides those expected for LSCM and YSZ were found on LSCM impregnated YSZ cathode in XRD results (Fig. 5.12), the hysteresis presented in Fig. 5.14 is probably caused by the phase changes in LSCM in reducing atmosphere. The OCV value is 0.84V in CO<sub>2</sub>-CO 70-30 mixture at 900°C for the LSCM impregnated YSZ cathode cell, and it is quite close to the theoretical value indicated by Nernst equation.

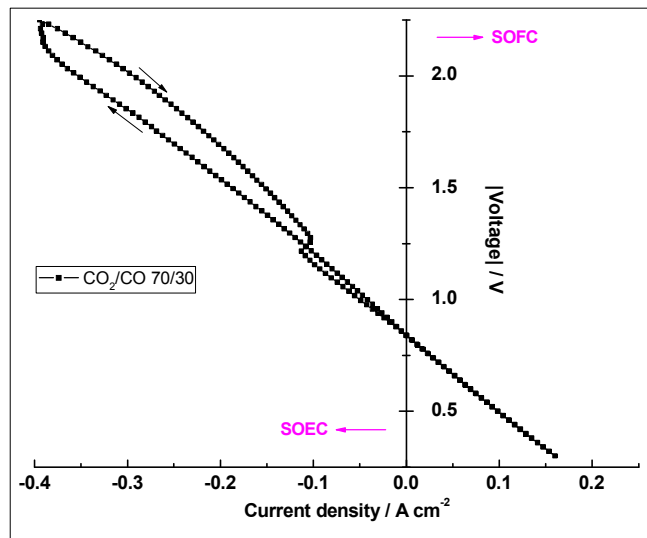


**Fig. 5.14** I-V curve of LSCM impregnated YSZ cathode cell working in CO<sub>2</sub>/CO 70/30 atmosphere at 900°C

The impedance responses from the LSCM infiltrated YSZ cathode operated at different voltages in CO<sub>2</sub>-CO 70-30 atmosphere at 900°C are presented in Fig. 5.15. The R<sub>s</sub> increases slightly and then decreases with increasing potential, which does not agree

with the expectation from LSCM/YSZ composite cathode as revealed in Fig. 4.10. This phenomenon may result from the impurities observed on LSCM impregnated YSZ cathode by XRD which vary the cathode conductivity in reducing atmosphere.

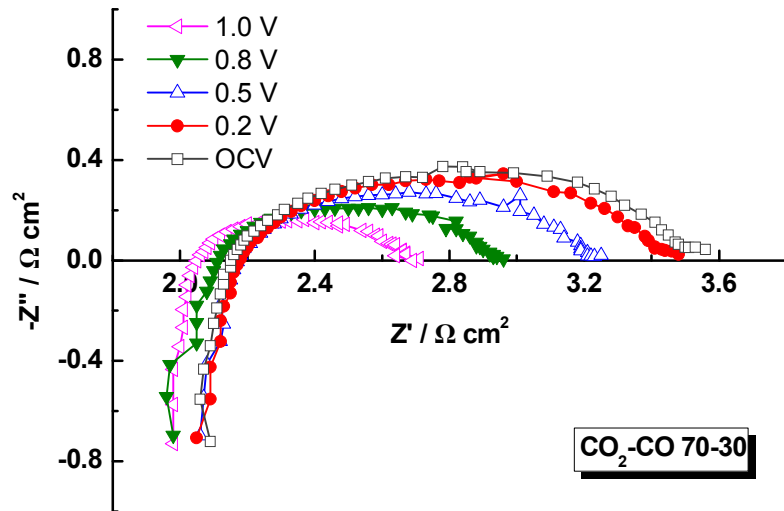


**Fig. 5.15** Impedance spectra from LSCM impregnated YSZ cathode operated at different potentials for CO<sub>2</sub> electrolysis at 900°C in CO<sub>2</sub>-CO 70-30 mixture

In Fig. 5.15, the  $R_p$  declines with increasing working potential, and at 1.0V (voltage referred to OCV), the  $R_p$  is only half of the value from OCV. The  $R_p$  values from the LSCM impregnated YSZ cathode working in CO<sub>2</sub>-CO 70-30 gas at 900°C were plotted as a function of operating potential, as shown in Fig. 5.16. The  $R_p$  values from screen-printed LSCM/YSZ (fired at 1200°C) composite and LSCM/GDC composite cathode (fired at 1300°C), as investigated in Chapter 4, are also plotted in the identical conditions in Fig. 5.16 for comparison. Obviously, the  $R_p$  from the LSCM impregnated YSZ cathode is larger than those from screen-printed LSCM/YSZ and LSCM/GDC composite cathode, surprising as higher electro-catalytic properties from LSCM introduced by impregnation method were expected. The enlargement in  $R_p$  of the LSCM impregnated YSZ cathode for high temperature CO<sub>2</sub> electrolysis may be related to appearance of impurities in LSCM when fired at 1100°C during fabrication. In addition, regarding the totally different cathode fabrication procedure, compared to the

screen-printed LSCM/YSZ composite, the poor performance from the LSCM impregnated YSZ cathode indicates that the cathode fabrication conditions, particularly the cathode microstructure, need to be optimized. In Fig. 5.16, the LSCM/GDC composite shows superior performance especially in electrolysis operation conditions, which demonstrates that LSCM-GDC components are a promising material set for CO<sub>2</sub> electrolysis by SOEC.

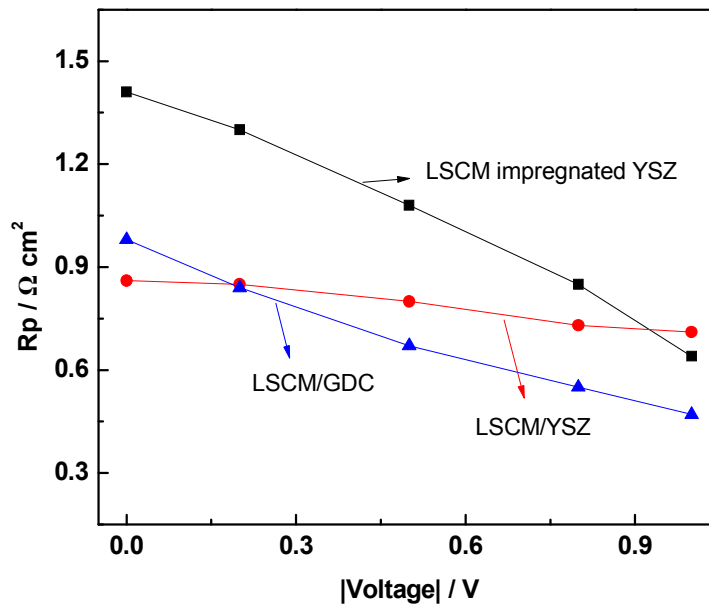


**Fig. 5.16** Rp comparison of different cathodes in CO<sub>2</sub>-CO 70-30 at 900°C at different voltages (Values refer to OCV which is ~ -0.84V)

### 5.3.3 GDC impregnated LSCM cathode

#### 5.3.3.1 Microstructure of the GDC impregnated LSCM cathode

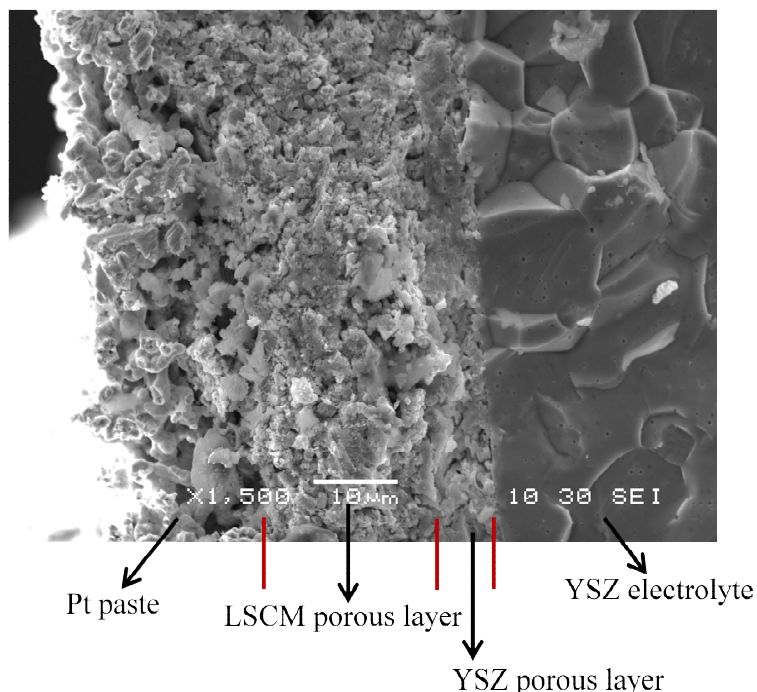


**Fig. 5.17** SEM image of GDC impregnated LSCM cathode after electrochemical characterization

The SEM micrograph of the GDC impregnated LSCM cathode is displayed in Fig. 5.17. It can be seen that the cathode binds very well to YSZ electrolyte by the introduction of a thin YSZ porous layer, which is roughly 5 μm in thickness, indicating that a good cathode/electrolyte interface is maintained for the impregnated cathode, in comparison to the screen-printed LSCM/GDC composite cathode that was studied before. Visibly, the LSCM layer is more porous and thicker than the YSZ porous layer, therefore, it is the main skeleton for GDC loading. The thickness of the LSCM porous layer is ca. 20-30 μm. The SEM micrograph and corresponding EDX spectra of elements in the GDC impregnated LSCM cathode are shown in Fig. 5.18. It can be seen that the introduced GDC by vacuum impregnation distributes uniformly along the LSCM-YSZ porous layer. Furthermore, Pt can only be found at the outer layer of the cathode, suggesting that it only acts as current collector.

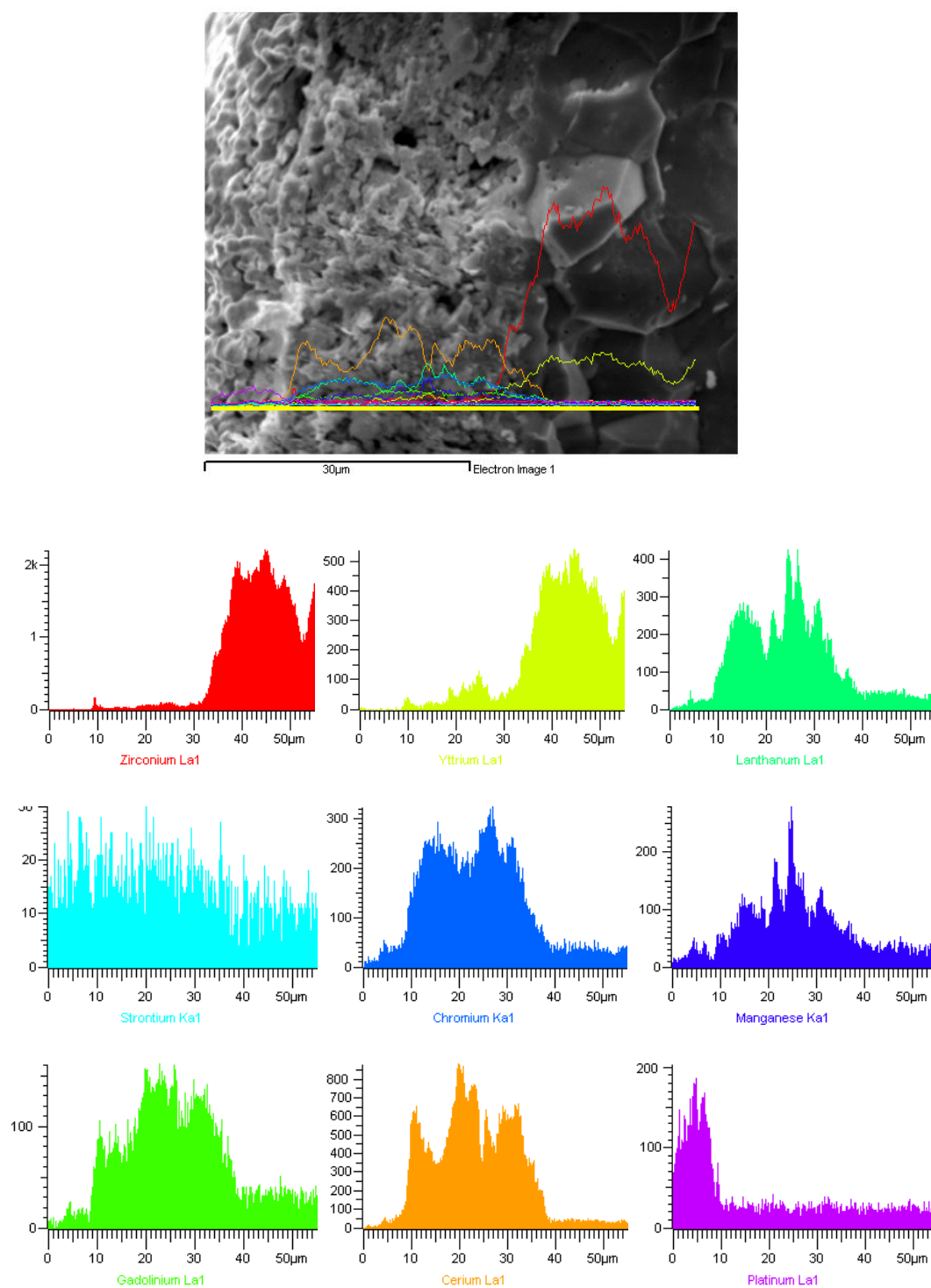


**Fig. 5.18** SEM micrograph and corresponding EDX spectra of elements in GDC impregnated LSCM/YSZ cathode after electrochemical tests in various CO<sub>2</sub>-CO mixtures under different conditions

### 5.3.3.2 Performance of the GDC impregnated LSCM cathode for CO<sub>2</sub> electrolysis

Fig. 5.19 presents the CO<sub>2</sub> electrolysis performance of the GDC impregnated LSCM cathode cell operated in CO<sub>2</sub>-CO mixtures at 900°C. The polarization curves in Fig. 5.19(a) shows no hysteresis in a scanning cycle from OCV to high potential and backwards. From Fig. 5.19(a), it can be detected that the cathode resistance declines with increasing potential, and at OCV, the cathode resistance decreases upon increasing CO concentration. In Fig. 5.19(b), the R<sub>p</sub> of the GDC impregnated LSCM cathode decreases distinctively upon the rising of working potential in CO<sub>2</sub>-CO 70-30 mixture, and this is consistent with the result the I-V curve revealed. Furthermore, the impedance arcs dwindle as operating potential increases in Fig. 5.19(b), reflecting accelerated electrochemical processes of CO<sub>2</sub> dissociation on the GDC impregnated LSCM cathode at elevated potentials, which is similar to the phenomenon observed on screen-printed LSCM/GDC cathode (see section 4.4), therefore, can be interpreted similarly by the reinforced catalytic property such as oxide ion mobility due to the reduction of Ce<sup>4+</sup> in reducing atmosphere.

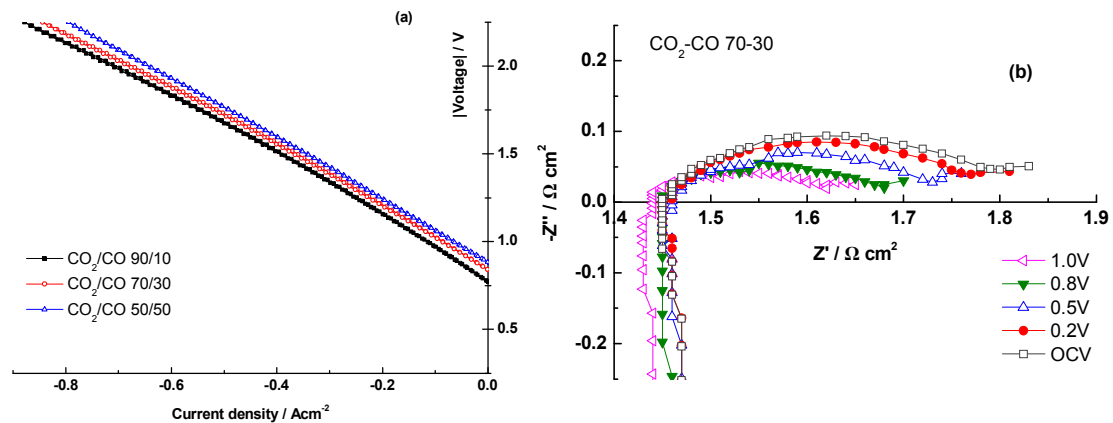


**Fig. 5.19** Performance of GDC impregnated LSCM cathode cell operated in CO<sub>2</sub>/CO mixtures at 900°C ((a) polarization curves for CO<sub>2</sub> electrolysis and (b) electrochemical impedance spectra of GDC impregnated LSCM cathode working in CO<sub>2</sub>-CO 70-30 gas with impedance frequency ranging from 10<sup>5</sup> to 0.1 Hz)

The Impedance spectra of the GDC impregnated LSCM cathode cell working in different CO<sub>2</sub>-CO fuel under OCV at 900°C are compared in Fig. 5.20. From the

Nyquist plot, one can see that the  $R_s$  keeps constant with the change of CO concentration, whereas the  $R_p$  reduces distinctively with increasing CO percentage in CO<sub>2</sub>-CO mixture, which was indicated above on the I-V curves in Fig. 5.19(a) and the interpretations are similar with the variation of  $R_p$  against working potential. Furthermore, from the Nyquist plot, two separable arcs, the magnitude of which decrease apparently with increasing CO content, can be seen at OCV at 900°C on the GDC impregnated LSCM cathode for CO<sub>2</sub> electrolysis, which is in contrast with the Gerischer characterized impedance dispersion of the screen-printed LSCM/GDC composite cathode in identical conditions [23, 24]. The completely different impedance behaviour implies dissimilar rate-limiting processes for CO<sub>2</sub> dissociation taking place on the above two cathodes. The Bode plot displays that the summit frequency for high frequency and low frequency arc locates at 15~20 Hz and 0.08~0.14 Hz, respectively, and that the summit frequency for the high frequency arc increases slightly whilst the one for the low frequency arc decreases a bit as CO concentration rises.

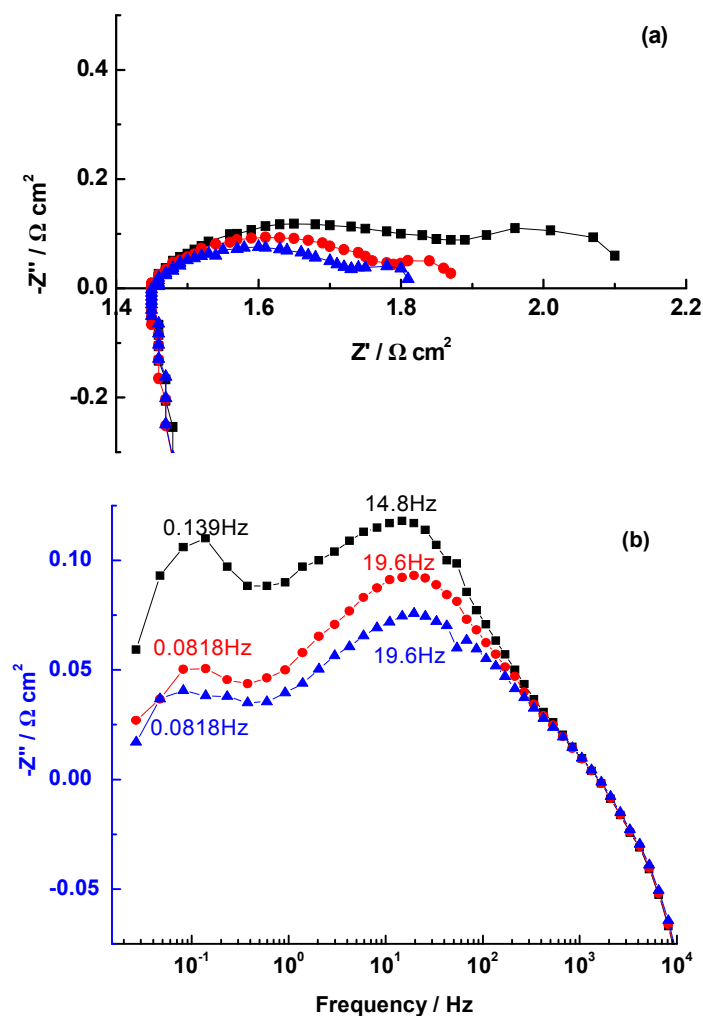


**Fig. 5.20** Impedance analysis of GDC impregnated LSCM cathode for CO<sub>2</sub> electrolysis at 900°C at OCV in various CO<sub>2</sub>-CO mixtures. (a) Nyquist plot and (b) Bode plot with scanning frequencies ranging from 10<sup>5</sup> to 0.015Hz and the summit frequencies are inserted in Bode plot. Black symbols indicate results in CO<sub>2</sub>-CO 90-10 gas, with red symbols in CO<sub>2</sub>-CO 70-30 and blue symbols in CO<sub>2</sub>-CO 50-50 atmosphere.

The impedance analysis of the GDC impregnated LSCM cathode operated at OCV in CO<sub>2</sub>-CO 70-30 mixture during cooling from 900 to 750°C at an interval of 50°C is illustrated in Fig. 5.21. When operation temperature is lowered, the impedance arc at high frequency and the one at low frequency regime become overlapped. In addition, the low frequency arc appears to increase more significantly than the high frequency one with lowering temperature, for instance, at temperature lower than 800°C, the low frequency arc seems to dominate the cathode resistance, rather than the high frequency

arc as was the case at 900°C. The variation trends of impedance arcs against temperature shown in Fig. 5.21 are similar as those of screen-printed LSCM/GDC composite cathode, though the nature of their impedance behaviours might be remarkably different.

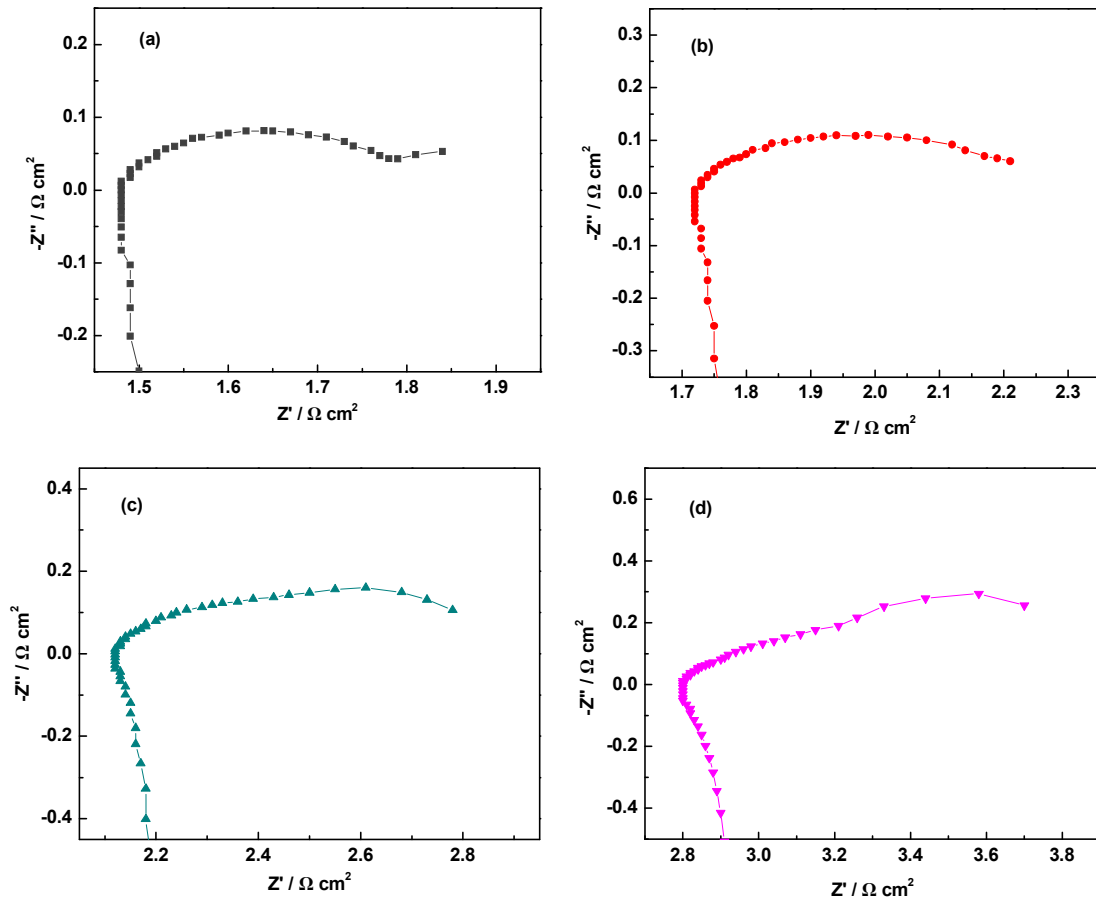


**Fig. 5.21** The impedance spectra of GDC impregnated LSCM cathode in CO<sub>2</sub>-CO 70-30 condition at OCV at (a) 900°C, (b) 850°C, (c) 800°C and (d) 750°C.

For the screen-printed LSCM/GDC composite cathode working in CO<sub>2</sub>-CO 70-30 atmosphere at 900°C, the summit frequency for the low frequency arc is around 4~19Hz depending on operation potential (Fig. 4.15 in section 4.4), and the low frequency arc was found to be associated with the dissociative adsorption of active species on cathode surface and the subsequent surface diffusion of the active species to TPB area. Relating this to the data from Fig. 5.20 and Fig. 5.21, the magnitude of both arcs varies with CO<sub>2</sub> concentration and operation temperature, therefore, it is assumed that the impedance

arcs in Fig. 5.20 and Fig. 5.21 are probably related to the adsorption/desorption equilibration and surface diffusion.

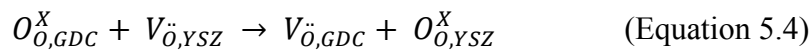
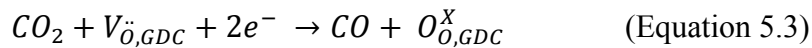
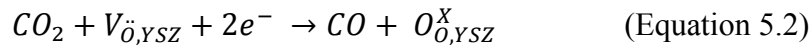
**Table 5.1** Reviews of Rp values from the LSCM/GDC SOEC cathode for CO<sub>2</sub> electrolysis working at 900°C in CO<sub>2</sub>/CO system with LSCM/GDC composite prepared by different approaches

Polarization resistance Rp at OCV ( $\Omega\text{cm}^2$ )				
CO <sub>2</sub> /CO ratio	LSCM/GDC (Screen-printing, 1300)	LSCM/GDC () (Screen-printing, 1200)	LSCM/GDC-1% Ni (Wet impregnation)	GDC impregnated LSCM (Vacuum impregnation)
90/10	1.49	1.14	0.88	0.65
70/30	1.05	0.91	0.62	0.42
50/50	0.84	0.80	0.53	0.35

The review of Rp from the LSCM/GDC composite prepared by different procedures for usage as SOEC cathode is shown in Table 5.1. The SOEC was operated at 900°C at OCV for high temperature CO<sub>2</sub> electrolysis. For the screen-printed LSCM/GDC composite cathode, the Rp declines slightly when lowering the sintering temperature from 1300°C to 1200°C due to the mitigation in particle growth and agglomeration which would reduce catalyst activity consequently, and the Rp decreases further upon introducing extra metallic catalyst to LSCM/GDC composite. In Table 5.1, the smallest Rp is presented on the LSCM/GDC composite cathode manufactured via wet impregnation, i.e. the GDC infiltrated LSCM cathode.

The Rp values from the GDC impregnated LSCM cathode are 0.65, 0.42, and 0.35  $\Omega\text{cm}^2$  for CO<sub>2</sub> electrochemical reduction in CO<sub>2</sub>/CO 90/10, 70/30 and 50/50 fuels at OCV at 900°C, respectively. These values are smaller than half of those on screen-printed LSCM/GDC composite without additional catalyst, and this trend becomes more profound with increasing CO concentration, in other words, with the operation surroundings getting more reducing. LSCM is p-type conductor and shows

predominantly electronic conductivity, therefore, the addition of oxygen ion conducting phase such as YSZ and/or GDC would tremendously promote the electrode ionic conductivity, and enhance cathode performance which could also be demonstrated by the overall reaction of CO<sub>2</sub> electrochemical reduction expressed by Equation 5.1 where  $V_{\ddot{O}}$ ,  $e^-$ , and  $O_O^X$  stand for an oxygen vacancy provided by electrolyte, an free electron from cathode, and an oxygen ion in the YSZ electrolyte lattice, respectively [25]. In LSCM/YSZ and LSCM/GDC composite cathodes, the CO<sub>2</sub> electrochemical reduction could be realised through Equation 5.2 and 5.3 where  $V_{\ddot{O},YSZ}$ ,  $V_{\ddot{O},GDC}$  and  $O_{O,YSZ}^X$ ,  $O_{O,GDC}^X$  represent oxygen vacancies supplied by YSZ/GDC phase and oxygen ions in YSZ/GDC lattice in composite cathode, respectively. Indicated by Equation 5.1-5.3, the active reaction area for CO<sub>2</sub> reduction is significantly extended by adding high oxygen ion conducting phase to LSCM, and this is particularly the case when the introduced phase is in nano-sized particles as for the GDC impregnated LSCM Cathode studied here. Along with the processes expressed by Equation 5.2 and 5.3, the elementary step reflected by Equation 5.4 would take place concerning oxygen diffusion from cathode to YSZ electrolyte.



For the GDC infiltrated LSCM cathode, the Rp becomes increasingly smaller with increasing CO fraction in atmosphere, compared to the screen-printed LSCM/GDC cathode and Ni aided LSCM/GDC composite cathode, attributed to the diverse microstructures from different fabrication approaches. In the GDC impregnated LSCM cathode, the GDC phase is highly dispersed on the surface of LSCM backbone and the increase in the vacancy diffusion coefficient and surface exchange rate from GDC with increasing CO concentration, proposed by Green and Adler [26], is more significant in the nano-sized GDC than the analogy in the screen printed cathode, thereby, boosting the cathode performance for CO<sub>2</sub> electrochemical reduction to a further extent.

GDC is a well-known mixed electronic and ionic conductor, and it possesses good catalytic properties towards oxidation reaction in SOFC operation, and CO<sub>2</sub> electrolysis via SOEC as well. Here thus comes the question that the nano-sized GDC rather the LSCM phase is responsible for the excellent performance from the GDC impregnated LSCM cathode. To clarify this, a comparison is performed between the GDC infiltrated LSCM cathode and the GDC impregnated YSZ cathode, as exhibited in Fig. 5.22. Both cathodes present two distinguishable impedance arcs, while the arcs of the GDC infiltrated LSCM cathode are smaller than those of the GDC impregnated YSZ cathode, suggesting the electro-catalytic contribution from the LSCM component in cathode material. The contrast between the impedance responses from the above two cathodes is much distinct with regard to the low frequency arc on the impedance spectra. Regarding LSCM, the substitution of Sr into the A-site of perovskite leads to a charge-compensating transition of Cr<sup>3+</sup>/Mn<sup>3+</sup> to Cr<sup>4+</sup>/Mn<sup>4+</sup>, and in the case of low oxygen partial pressure (at high CO content here), the compensation is achieved by the formation of oxygen vacancies [21]. As a result, it can be concluded that both the GDC and LSCM component contribute to the prominent performance of the GDC infiltrated LSCM cathode towards high temperature CO<sub>2</sub> electrolysis via SOEC.

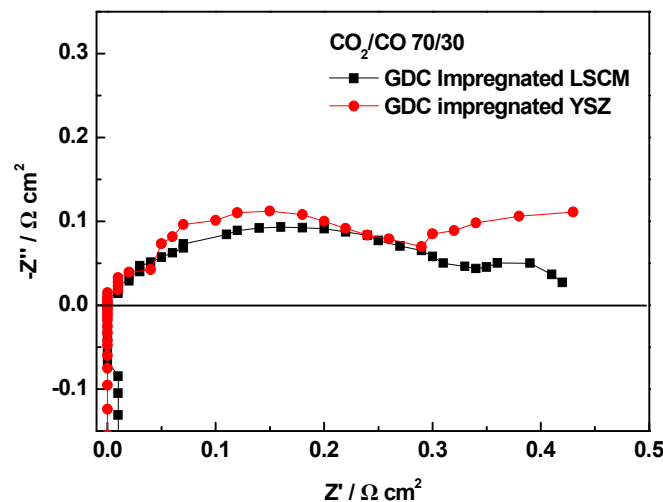


**Fig. 5.22** Impedance comparison between the GDC impregnated LSCM and GDC impregnated YSZ cathode with both working at OCV at 900°C in CO<sub>2</sub>-CO 70-30 gas

The impressively small  $R_p$  values exhibited on the GDC impregnated LSCM cathode indicates that vacuum impregnation offers an effective means to improve the cathode performance for CO<sub>2</sub> electrolysis. Moreover, the inferior cathode/electrolyte interfaces encountered on screen-printed LSCM/GDC composite cathodes when sintered at low temperature are avoided by adopting a thin porous YSZ layer between YSZ electrolyte and bulk cathode. In short, both the cathode activity and cathode/electrolyte interface are significantly reinforced, by introducing a thin porous YSZ buffer layer between cathode and electrolyte and infiltrating GDC precursor nitrate solution into porous LSCM/YSZ layer later on. Last, it is worth mentioning that the solid reaction between GDC and YSZ is less likely when the cathode is made in such way.

### 5.3.3.3 Effect of introducing H<sub>2</sub> on the performance of the GDC impregnated LSCM cathode for CO<sub>2</sub> electrolysis

It has been put forwarded by several researchers that the reverse water gas shift reaction (expressed by Equation 5.5), which is a kinetically fast, equilibrium reaction at high temperature, would affect the reaction kinetics for steam-CO<sub>2</sub> co-electrolysis to a certain extent, and it was believed that most CO production was from the reverse gas shift reaction, rather the electrochemical reduction of CO<sub>2</sub> [27, 28].



The influence of H<sub>2</sub> on the CO<sub>2</sub> reduction reaction through SOEC was investigated by introducing 5% H<sub>2</sub>/Ar into fuel electrode chamber along with CO<sub>2</sub>/CO gas. Fig. 5.23 shows the I-V curves of the GDC infiltrated LSCM cathode cell under operation with and without H<sub>2</sub> in CO<sub>2</sub>/CO 70/30 mixture at 900°C (Fig. 5.23(a)) as well as 750°C (Fig. 5.23(b)).

At 900°C, it is difficult to discriminate the I-V curves of the GDC infused LSCM cathode cell working in the gas with and without H<sub>2</sub>, however, taking a careful look, there are two zones where the cell displays diverse resistances between the atmosphere with and without H<sub>2</sub>. Around OCV area and at the potential up to 1.8V, the introduction of H<sub>2</sub> facilitates the electrochemical reduction of CO<sub>2</sub>, whereas it seems affect the CO<sub>2</sub> dissociation performance adversely at extremely high potential. At 750°C, it is quite clear that the presence of 5%H<sub>2</sub>/Ar is profitable for CO<sub>2</sub> dissociation by high

temperature SOEC, for that the cell resistance in the H<sub>2</sub>-containing atmosphere becomes smaller than that in the atmosphere without H<sub>2</sub> at all potential range. The results from the comparison of the polarization curves for the GDC infiltrated LSCM cathode cell operated under the conditions with and without the appearance of 5%H<sub>2</sub>/Ar are supported by the impedance studies discussed in the following parts.

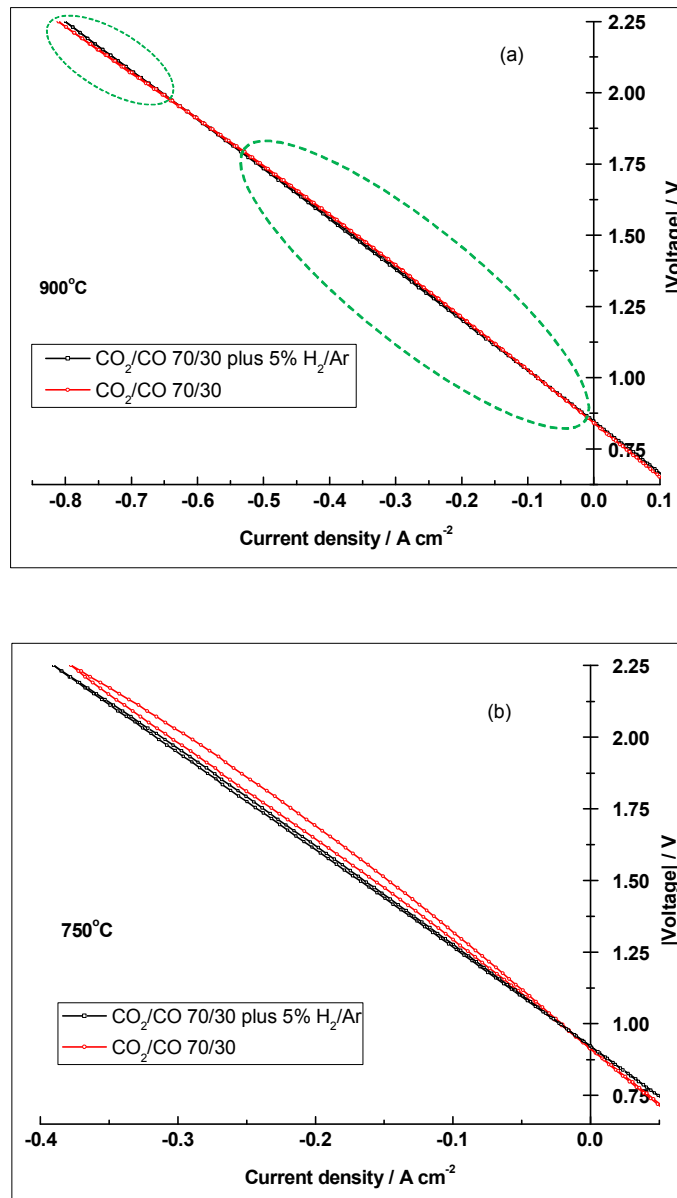


**Fig. 5.23** The effect of H<sub>2</sub> on the I-V curves of GDC impregnated LSCM cathode cell for CO<sub>2</sub> electrolysis in CO<sub>2</sub>-CO 70-30 atmosphere at (a) 900°C and (b) 750°C

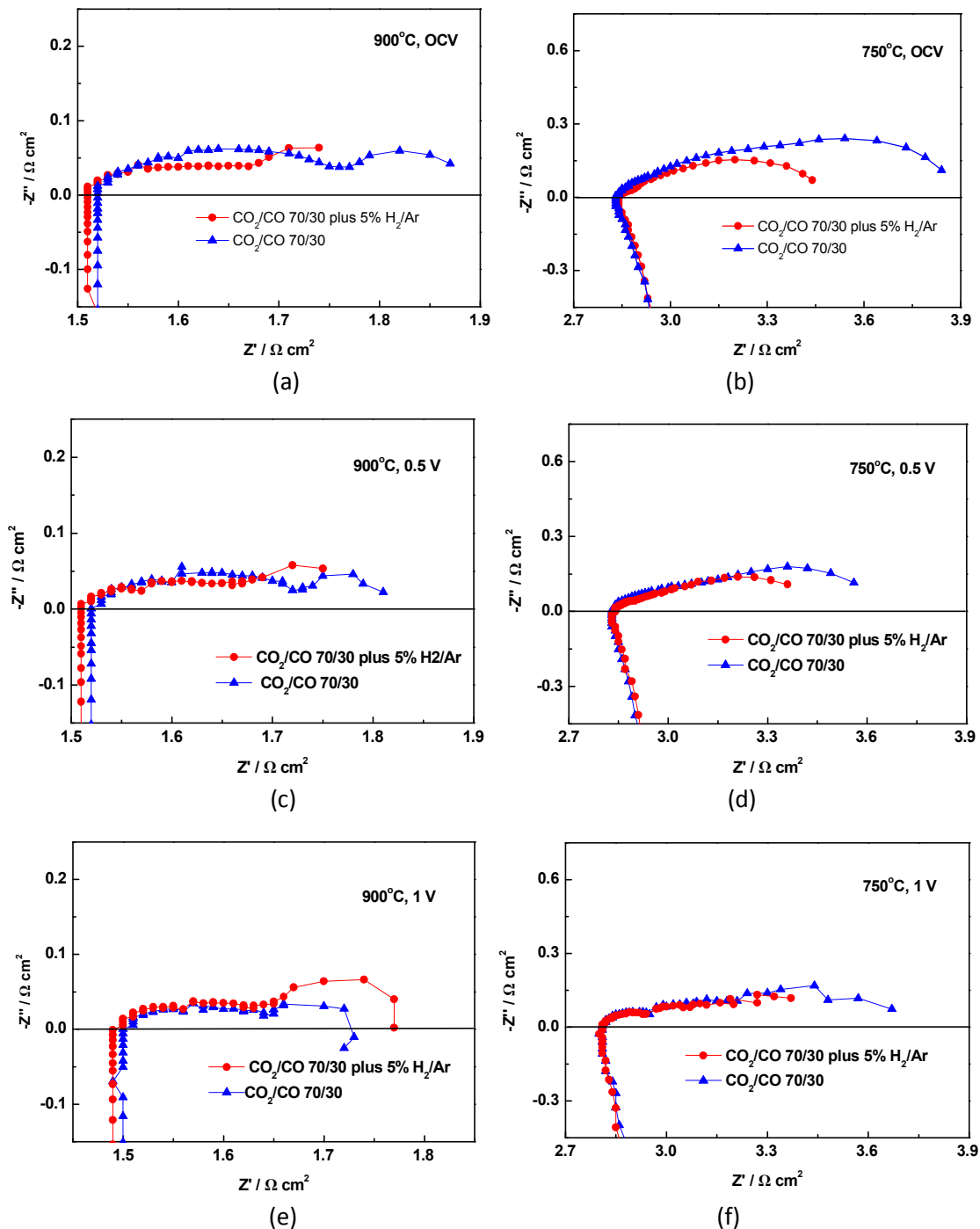


**Fig. 5.24** Impedance analysis of the GDC impregnated LSCM cathode cell for CO<sub>2</sub> electrochemical reduction operated at 900 (a, c, and e) and 750°C (b, d, and f) at different potentials upon introducing 5% H<sub>2</sub>/Ar into CO<sub>2</sub>-CO 70-30 mixture

The impedance behaviour of the GDC impregnated LSCM cathode cell operated at 900 and 750°C at different potentials upon introducing 5% H<sub>2</sub>/Ar into CO<sub>2</sub>-CO 70-30

mixture for CO<sub>2</sub> reduction is exhibited in Fig. 5.24. It is revealed by Fig. 5.24 (a), (c), and (e) that the effect of H<sub>2</sub> on CO<sub>2</sub> electrochemical reduction process differs at different voltages at 900°C. At OCV and 0.5V, the R<sub>p</sub> values decline markedly on the occurrence of H<sub>2</sub>, and the primary reduction in R<sub>p</sub> is reflected by the decrease in the magnitude of the high frequency arc. The observations at high potentials at 900°C are on the contrary. For instance, at 1.0V, the R<sub>p</sub> increases when introducing 5% H<sub>2</sub>/Ar into the GDC impregnated LSCM cathode. Additionally, the high frequency arc keeps constant whilst the low frequency arc enlarges upon introducing 5% H<sub>2</sub>/Ar, compared to the impedance response from the cathode working in atmosphere without H<sub>2</sub>.

Concerning the effect of introducing H<sub>2</sub> on CO<sub>2</sub> electrochemical reduction process on the GDC impregnated LSCM cathode at 750°C, one can see from the impedance results in Fig. 5.24 (b), (d) and (f) that the introduction of 5% H<sub>2</sub>/Ar remarkably accelerates the CO<sub>2</sub> dissociation at all operation potentials. The principle reduction in impedance at 750°C is that the low frequency arc decreases greatly against introducing 5% H<sub>2</sub>/Ar. This can be interpreted by the decrease in the content of CO<sub>2</sub> with the participation of reverse gas shift reaction, and consequently the facilitated surface reaction resulting from the mitigated retarding effect from CO<sub>2</sub> adsorption/desorption. The impedance results reflected by Fig. 5.24 also confirms the assumption that the impedance arcs in impedance spectra of the GDC infiltrated LSCM cathode are likely associated with the surface adsorption/desorption equilibration and surface diffusion.

The discrepancies of the impact from the existence of 5% H<sub>2</sub>/Ar on the performance of CO<sub>2</sub> electrochemical reduction via SOEC at different temperatures indicates that the cathode reaction is quite complicated concerning the participation of the kinetically fast gas shift/reverse gas shift reaction. M. Mogensen et al found that the introduction of pure H<sub>2</sub> to CO<sub>2</sub>/CO mixture activated the Ni/YSZ cathode performance during durability test at 850°C, but the exact reason for that was not mentioned [29]. Other work concerning the impact of H<sub>2</sub> on CO<sub>2</sub> electrochemical reduction at different operation conditions has not been reported. More efforts need to be dedicated to it for better understanding of the reaction mechanism of CO<sub>2</sub> reduction via high temperature electrolysis.

## 5.4 Pd and GDC co-impregnated LSCM cathode

### 5.4.1 Manufacture and characterization of Pd and GDC co-impregnated LSCM cathode cell

The manufacture and characterization of the Pd and GDC co-impregnated LSCM cathode SOEC are similar to those of the GDC infused LSCM cathode cell. Yet, the brief procedures are described as following. A thin YSZ porous layer was coated on one side of the previously made 2mm thick YSZ pellet, and then a porous LSCM layer was screen-printed on top of porous YSZ layer, followed by the co-sintering of these two layers at 1300°C. It is worth mentioning that the solid/vehicles ratio for LSCM ink preparation was changed from 70/30 (used in previous section) to 60/40 for ease in printing the LSCM slurry. GDC component was introduced in the form of aqueous nitrate solution via vacuum impregnation and heat treatment at 500°C to decompose nitrate coated on the LSCM /YSZ porous structure. The impregnation and heat treatment were repeated to get sufficient GDC loading. The calcination of GDC component at 1100°C was conducted then and LSM/ScSZ composite was screen-printed and fired on the other side of YSZ pellet. Pd extra catalyst was incorporated into the GDC infiltrated LSCM cathode by aqueous impregnation at ambient pressure. Addition of 0.5 and 1.0 wt% Pd were investigated. The GDC infused LSCM cathode cell without Pd catalyst was made as comparison. Pt paste was painted and fired at 900°C as current collectors.

Concerning electrochemical characterization, impedance spectra of the as-prepared cathodes working in various CO<sub>2</sub>-CO mixtures were recorded with frequency ranging from 10<sup>5</sup> to 0.1Hz at amplitude of 20mV. A stability test of the 0.5wt% Pd-GDC co-impregnated LSCM cathode working with CO<sub>2</sub>-CO 50-50 mixture for CO<sub>2</sub> electrolysis was carried out by measuring the voltage vs. time at a constant current density of -0.15 Acm<sup>-2</sup>, and the impedance responses before and after the stability test were measured. The microstructure inspection was performed after electrochemical measurement.

#### **5.4.2 Performance from Pd and GDC co-impregnated cathode in various CO<sub>2</sub>-CO atmospheres**

The performance of the Pd and GDC co-impregnated LSCM cathode for CO<sub>2</sub> electrolysis in CO<sub>2</sub>-CO 70-30 at 900°C is displayed in Fig. 5.25, in comparison to the cathode without Pd catalyst. As expected, the addition of Pd extra catalyst notably intensifies the GDC infiltrated LSCM cathode property to a further extent, in terms of smaller R<sub>p</sub> and much more depressed impedance arcs. The smallest R<sub>p</sub>, i.e. the highest performance, occurs on the cathode with 0.5 wt% Pd catalyst, and increasing Pd catalyst loading to 1 wt% is not helpful for further improvement in cathode activity. Noting in the Nyquist plot in Fig. 5.25(a), different impedance response is observed on the GDC impregnated LSCM cathode, compared to the cathode studied in section 5.3 though they were fabricated and measured in the same procedures. This might be due to the microstructural difference coming from the variation in the solid/vehicle ratio in preparing LSCM ink for ease of screen printing as mentioned in part 5.4.1. However, the R<sub>p</sub> values are almost the same for the above two cathodes.

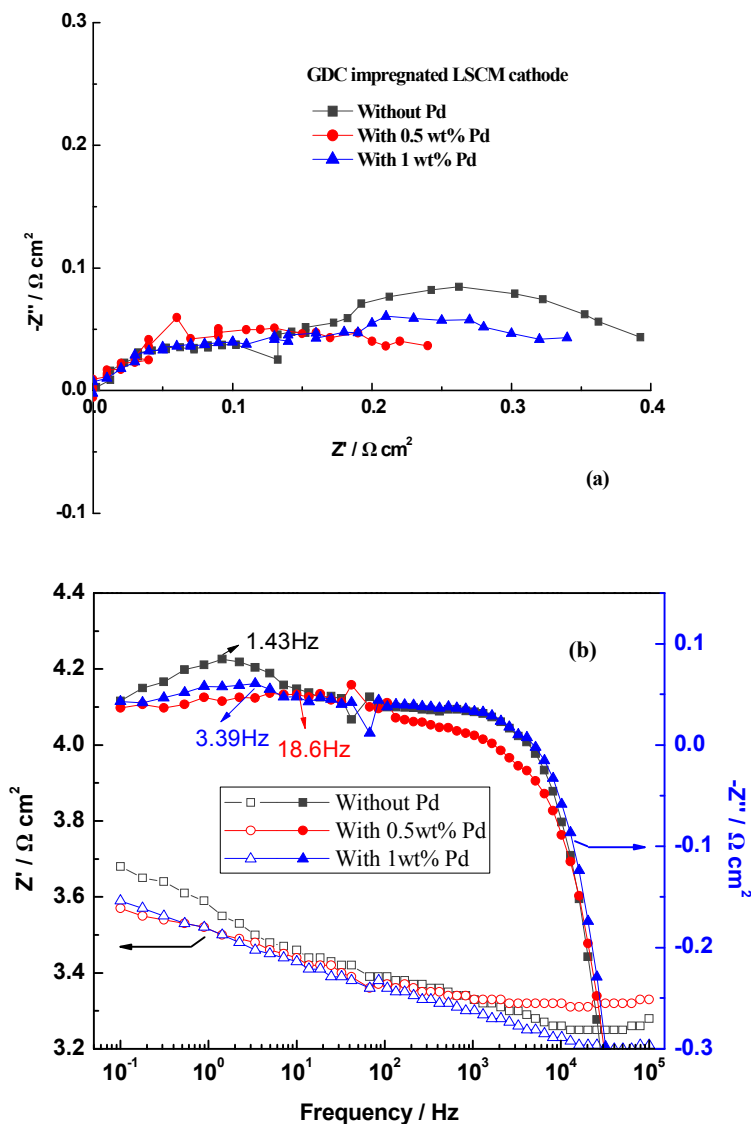


**Fig. 5.25** Impedance spectra of the GDC impregnated LSCM cathode with and without Pd working in CO<sub>2</sub>/CO 70/30 at OCV at 900°C with (a) Nyquist plot (IRs from the 2 mm thick YSZ electrolyte for these cathodes cell was subtracted) and (b) Bode plot

Compared to the GDC impregnated LSCM cathode, the addition of Pd catalyst substantially decreases the low frequency arc, that is to say the relevant processes, likely the surface exchange and diffusion of reactant species, is facilitated with the introduction of Pd catalyst. Y. Ye and S. Jiang et al investigated the Pd impregnated LSCM/YSZ composite anode in methane fuelled SOFCs, and found that the electrode polarization resistance associated with the low frequency arc was essentially decreased upon adding Pd catalyst [11]. The enhancing effect of Pd on the surface exchange and

diffusion and the CH<sub>4</sub> decomposition was proposed to be related to the co-existence of Pd and Pd/PdO<sub>x</sub> on the LSCM/YSZ electrode surface, and the presence of water was found to favour the formation of Pd/PdO<sub>x</sub>, which would accelerate the oxygen species diffusion in the LSCM/YSZ composite and thus promoting the methane oxidation and decomposition reaction. Similarly, the formation of Pd/PdO<sub>x</sub> is possibly facilitated by the appearance of CO<sub>2</sub> in the fuel gas, and accordingly, leads to the boosted catalytic properties for Pd-GDC doped LSCM cathode in CO<sub>2</sub> electrolysis.

Regarding the 1.0 wt% Pd and GDC co-infiltrated LSCM cathode, the low frequency arc enlarges compared to the 0.5wt% Pd doped counterpart, in that the Pd/PdO<sub>x</sub>, formed as a result of the interaction between LSCM/GDC and Pd, is a semiconductor which would affect the electrode conductivity. Correspondingly, the Bode plots in Fig. 5.25(b) presents the characteristic frequency of 18.6 and 3.39 Hz for 0.5 wt% and 1 wt% Pd assisted GDC infused LSCM cathode, respectively, whereby the characteristic frequency for the cathode without Pd is 1.43 Hz. The higher summit frequencies observed on the Pd aided GDC impregnated LSCM cathode can be attributed to the accelerated processes correlated with the low frequency arc.

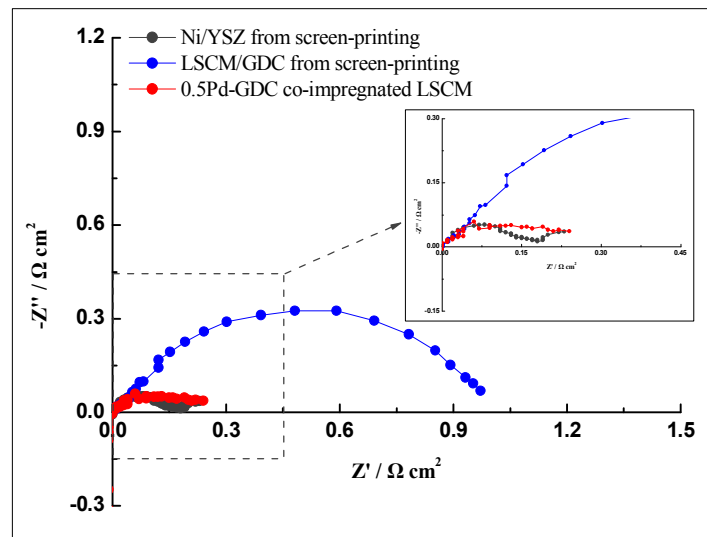


**Fig. 5.26** Impedance comparison (after IRs correction) from different cathodes operated in CO<sub>2</sub>/CO 70/30 gas at OCV at 900°C

Comparison is conducted among the Ni/YSZ cermet cathode, the screen-printed LSCM/GDC composite cathode, and the 0.5 wt% Pd-GDC co-impregnated LSCM cathode, and is demonstrated in Fig. 5.26. It can be seen that the impedance responses from LSCM/GDC cathode manufactured by aqueous impregnation, screen-printed LSCM/GDC composite cathode and Ni/YSZ cathode are sharply different though being tested in the identical operation conditions, indicating that different rate-determined processes for CO<sub>2</sub> electrochemical reduction, originated from diverse microstructures induced by variation in fabrication approaches as well as dissimilar electro-catalytic properties from different materials, take place on the three cathodes.

In Fig. 5.26, the 0.5wt% Pd-GDC co-impregnated LSCM cathode shows much smaller arcs and  $R_p$ , due to the enhanced electrochemical and catalytic properties from nano-structured GDC component and extra Pd, in comparison with the screen-printed LSCM/GDC composite cathode. In fact, the 0.5 wt% Pd and GDC doped LSCM cathode exhibits comparable  $R_p$  value with that of the conventional Ni/YSZ cermet cathode, as shown in Table 5.2 in which  $R_p$  from different cathodes working under the same conditions are summarized. And unlike Ni/YSZ, both LSCM and GDC are considered excellent carbon resistant materials [4, 8-9, 21], therefore, the Pd-GDC co-impregnated LSCM material can be regarded as a promising alternative cathode in the application of high temperature CO<sub>2</sub> electrolysis.

**Table 5.2** Summary of  $R_p$  from different cathodes working at OCV in diverse CO<sub>2</sub>/CO mixtures at 900°C

$R_p$ at 900°C( $\Omega$ cm <sup>2</sup> )			
CO <sub>2</sub> /CO ratio	Ni/YSZ (Screen printing)	GDC impregnated LSCM	0.5Pd-GDC co-impregnated LSCM
90/10	0.33	0.65	0.34
70/30	0.23	0.42	0.24
50/50	0.24	0.35	0.22

### 5.4.3 Microstructure analysis of the Pd-GDC co-impregnated cathode material

The microstructure of the Pd–GDC co-impregnated LSCM cathode was examined at room temperature by SEM after electrochemical tests. Fig. 5.27 shows the SEM image of the 1 wt% Pd and GDC co-infiltrated LSCM cathode. It can be found that, for the Pd and GDC doped LSCM cathode, it is the LSCM phase, and/or the YSZ phase in the regions close to the dense YSZ electrolyte, acts as the skeleton for cathode and the support for GDC and Pd loading. The highly dispersed GDC and Pd introduced by aqueous impregnation are located on the surface of porous LSCM and YSZ phases, and visibly, the GDC and Pd nanoparticles are much smaller than the LSCM phase.

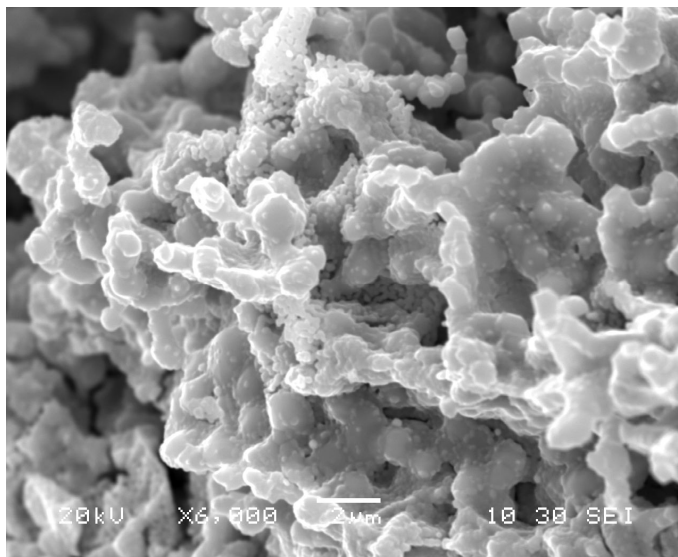


**Fig. 5.27** SEM cross-sectional view of 1 wt% Pd-GDC co-impregnated LSCM cathode after testing in various CO<sub>2</sub>/CO atmospheres

The cathode microstructure in Fig. 5.27 is in stark contrast to those of screen-printed Ni/YSZ and LSCM/GDC cathode displayed in Fig. 4.17 in section 4.5.2. Compared to the screen-printed LSCM/GDC cathode, it is believed that the superior performance of the GDC doped LSCM cathode is greatly benefited by its microstructure. The pattern of particles distribution and the significantly decrease in particle size of the GDC phase from the GDC infiltrated LSCM cathode would give birth to more active sites and extended TPB areas for the cathode reaction for CO<sub>2</sub> electrolysis, and as a result, enhanced performance. Further, with the aid of Pd precious metal catalyst, the cathode

catalytic property is tremendously promoted, so that the Pd and GDC co-impregnated cathode shows excellent performance for CO<sub>2</sub> dissociation through SOEC.

#### 5.4.4 Stability of the Pd and GDC co-impregnated LSCM cathode for CO<sub>2</sub> electrolysis

The durability of the Pd and GDC co-infiltrated LSCM cathode SOEC was studied in galvanostatic mode for the application of high temperature CO<sub>2</sub> electrolysis. Fig. 5.28 exhibits the voltage variation as a function of time from the 0.5 wt% Pd and GDC doped LSCM cathode SOEC operated at a constant current density of  $-0.15 \text{ A cm}^{-2}$  in CO<sub>2</sub>-CO 50-50 atmosphere at 900°C. The voltage of the studied cathode cell does not change much during the roughly 22hrs testing, suggesting excellent stability from the 0.5 wt% Pd and GDC co-impregnated cathode in CO<sub>2</sub> electrolysis operation environment. The initial voltage fluctuation observed in Fig. 5.28 is due to the switch of fuel from steam-H<sub>2</sub> to CO<sub>2</sub>-CO mixture, which will be discussed in a later Chapter.

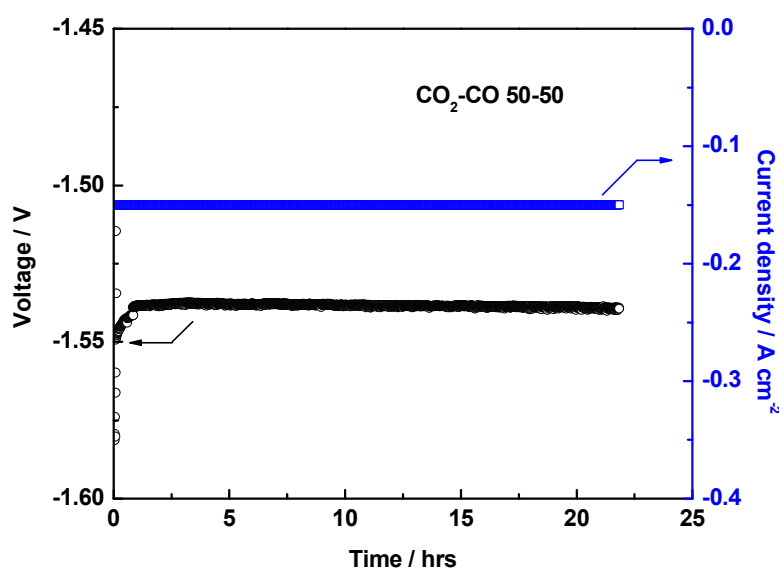


**Fig. 5.28** Voltage vs. time of the 0.5 wt% Pd-GDC co-impregnated LSCM cathode cell working at  $-0.15 \text{ A cm}^{-2}$  in CO<sub>2</sub>-CO 50-50 environment at 900°C for CO<sub>2</sub> electrolysis

The impedance spectra of the 0.5 wt% Pd and GDC co-impregnated LSCM cathode were recorded before and after the stability test in CO<sub>2</sub>-CO 50-50 fuel at 900°C, and are shown in Fig. 5.29. Apparently, no difference can be seen between the impedance

response of the cathode before and that of the cathode after the stability measurement, the impedance spectra are almost overlapped. This is in line with the results shown in Fig. 5.28, indicating that there is no performance degradation for the 0.5 wt% Pd and GDC co-infiltrated LSCM cathode during the ca. 22 hrs' operation in CO<sub>2</sub>-CO 50-50 environment, and that this cathode material has potential in the application of high temperature CO<sub>2</sub> electrolysis via SOEC.

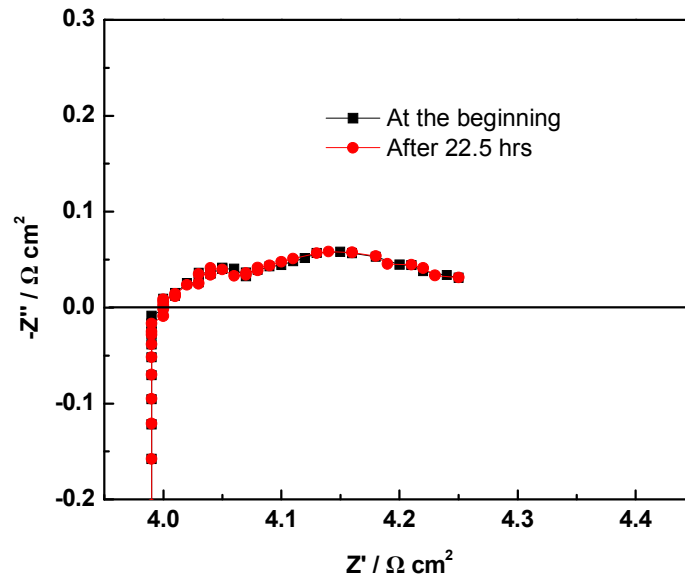


**Fig. 5.29** Impedance comparison before and after the stability test of the 0.5wt% Pd-GDC co-impregnated LSCM cathode working in CO<sub>2</sub>-CO 50-50 for CO<sub>2</sub> electrolysis at 900°C

## 5.5 Conclusions

To improve the performance of the LSCM based cathode material for high temperature CO<sub>2</sub> electrolysis by SOEC, a variety of means were carried out in order to modify the cathode microstructure, and hence cathode performance. Several conclusions can be arrived at as follows.

Adopting the gradient cathode structure effectively promoted the LSCM/YSZ composite activity for CO<sub>2</sub> electrochemical reduction via SOEC, in comparison to the

average LSCM/YSZ 50/50 (by weight) composite cathode operated in the same conditions.

By decreasing sintering temperature and introducing extra catalyst, such as Ni, CeO<sub>2</sub> and Pt, the catalytic activity of the LSCM/GDC composite was enhanced in the application of CO<sub>2</sub> dissociation by SOEC, however, the cathode/electrolyte interface was worsened at lower firing temperature. For the Pd catalyst, the solvent used to prepare Pd precursor nitrate solution and the Pd loading amount affected its impact on the LSCM/GDC cathode performance for CO<sub>2</sub> reduction.

The cathode prepared by infiltrated LSCM nitrate solution into a porous YSZ skeleton showed no improvement in performance for CO<sub>2</sub> reduction reaction, probably due to the occurrence of impurities in LSCM phase when sintered at 1100°C and the un-optimized cathode microstructure.

Incorporating the GDC component into porous LSCM backbone via vacuum impregnation gave rise to a success in modification of cathode microstructure, and the cathode performance towards the electrochemical reduction of CO<sub>2</sub> was enormously enhanced without risk the cathode/electrolyte interface as a thin porous YSZ layer was added between YSZ electrolyte and bulk cathode. The R<sub>p</sub> for the 0.5wt% Pd and GDC co-impregnated LSCM cathode is 0.24 Ω cm<sup>2</sup> at OCV at 900°C in CO<sub>2</sub>-CO 70-30 mixture, comparable with the Ni/YSZ cermet cathode operated in the identical conditions, indicating the potential usage of this cathode in CO<sub>2</sub> electrolysis via high temperature SOEC.

## References

1. F. B. Noronha, M. Schmal, E. F. Sousa-Aguiar, *Natural Gas Conversion VIII*, p.103-109 (2007)
2. S. Jiang, *Mater. Sci. and Eng. A*, **418**, 199 (2006)
3. J. Rossmesl, W. G. Bessler, *Solid State Ionics*, **178**, 1694 (2008)
4. R. J. Gorte, S. Park, J. M. Vohs, and C. Wang, *Adv.Mater.*, **12**, 1465 (2000)
5. S. McIntosh, J. M. Vohs, and R. J. Gorte, *Electrochem. Solid-State Lett.*, **6 (11)**, A240 (2003)

6. G. Kim, S. Lee, J. Y. Shin, G. Corre, J. T. S. Irvine, J. M. Vohs, and R. J. Gorte, *Electrochem. Solid-State Lett.*, **12 (3)**, B48 (2009)
7. A. Babaei, S. Jiang, and J. Li, *J. Electrochem. Soc.*, **156 (9)**, B1022 (2009)
8. X. C. Lu, J. H. Zhu, *Solid State Ionics*, **178**, 1467 (2007)
9. S. Jiang, X. Chen, S. H. Chan, and J. T. Kwok, *J. Electrochem. Soc.*, **153 (5)**, A850 (2006)
10. J. Kim, V. V. Nair, J. M. Vohs, and R. J. Gorte, *Scripta Mat.*, **65(2)**, 90 (2011)
11. Y. Ye, T. He, Y. Li, E. H. Tang, T. L. Reitz, and S. Jiang, *J. Electrochem. Soc.*, **155 (8)**, B811 (2008)
12. K. Chen, N. Ai, and S. Jiang, *J. Electrochem. Soc.*, **157 (11)**, P89 (2010)
13. H. Uchida, N. Osada, and M. Watanabe, *Electrochem. Solid-State Lett.*, **7 (12)**, A500 (2004)
14. N. Sun, X. Wen, F. Wang, W. Wei, and Y. Sun, *Energy Environ. Sci.*, **3**, 366 (2010)
15. N. T. Hart, N. P. Brandon, M. J. Day, N. Lapeña-Rey, *J. Power Sources*, **106**, 42 (2002)
16. A. C. Müller, D. Herbstritt, E. Ivers-Tiffée, *Solid State Ionics*, **152-153**, 537 (2002)
17. N. P. Bansal, P. Singh, *Advances in Solid Oxide Fuel Cells V*, Volume 30 (4), p. 75-81 (2009)
18. K. Eguchi, N. Akasaka, H. Mitsuyasu, Y. Nonaka, *Solid State Ionics*, **135**, 589 (2000)
19. A. Tsoga, A. Gupta, A. Naoumidis and P. Nikolopoulos, *Acta Mater.*, **48**, 4709 (2000)
20. Y. Zhang, Y. Liu, G. Yang, S. Sun, N. Tsubaki, *Appl. Catal. A: General*, **321**, 79 (2007)
21. S. Tao and J. T. S. Irvine, *J. Electrochem. Soc.*, **151 (2)**, A252 (2004)
22. G. Kim, G. Corre, J. T. S. Irvine, J. M. Vohs, and R. J. Gorte, *Electrochem. Solid-State Lett.*, **11 (2)**, B16 (2008)
23. X. Yue and J. T. S. Irvine, *Electrochem. Solid-State Lett.*, **15 (3)**, B31 (2012)
24. X. Yue and J. T. S. Irvine, *J. Electrochem. Soc.*, **159 (8)**, F442 (2012)
25. G. Tao, K. R. Sridhar, C. L. Chan, *Solid State Ionics*, **175**, 615 (2004)
26. R. D. Green, C. Liu, S. B. Adler, *Solid State Ionics*, **179**, 647 (2008)

27. C. Stoots, J. O'Brien, Proceedings of ASME international Mechanical Engineering Congress and Exposition (IMECE), Seattle, Washington, USA( 2007)
28. Q. Fu, C. Mabilat, M. Zahid, A. Brisse and L. Gautier, *Energy Environ. Sci.*, **3**, 1382 (2010)
29. S. D. Ebbesen, M. Mogensen, *J. Power Sources*, **193**, 349 (2009)

## **Chapter 6: Efficiency analysis on CO<sub>2</sub> electrolysis by SOEC and CO<sub>2</sub> electrolysis without protective gas**

### **Table of Contents**

Introduction .....	174
6.1 Gas chromatography analysis and Faraday efficiency calculation.....	175
6.2 Faradaic efficiency analysis for CO <sub>2</sub> electrolysis on different cathode materials for SOEC .....	177
6.2.1 CO <sub>2</sub> electrolysis efficiency on screen-printed LSCM/GDC cathode with extra Pt catalyst .....	177
6.2.2 CO <sub>2</sub> electrolysis efficiency on the GDC impregnated LSCM cathode for SOEC .....	183
6.2.3 CO <sub>2</sub> electrolysis efficiency on the Pd-GDC co-impregnated LSCM cathode for SOEC .....	188
6.3 CO <sub>2</sub> electrolysis without protective gas and corresponding efficiency evaluation	190
6.3.1 Performance and efficiency of CO <sub>2</sub> electrolysis with CO <sub>2</sub> -N <sub>2</sub> fed into SOEC cathode .....	190
6.3.2 Impact of 5%H <sub>2</sub> /Ar on the SOEC cathode performance and efficiency of CO <sub>2</sub> electrolysis in CO <sub>2</sub> -N <sub>2</sub> feed.....	197
6.4 Summary.....	201
References .....	202

## Chapter 6: Efficiency analysis on CO<sub>2</sub> electrolysis by SOEC and CO<sub>2</sub> electrolysis without protective gas

### Introduction

Like SOFC, SOEC system involves energy in and out. External electricity is loaded and, heat is provided to SOEC to drive the cathode reaction, which is endothermic in nature. With increasing applied potential, joule heat from cell resistance gradually reaches the heat the cathode reaction consumed. At this point, the applied potential is termed as thermal neutral voltage. For CO<sub>2</sub> electrolysis, the thermal neutral voltage is -1.46V at 900°C according to the following equation [1].

$$E_{NEV} = \frac{\Delta H}{2F}$$

Where  $\Delta H$  is the enthalpy of the CO<sub>2</sub> reduction reaction,  $F$  is Faraday constant, and  $E_{NEV}$  is thermal neutral voltage.

The CO<sub>2</sub> electrolysis by high temperature SOEC can be assessed by thermal efficiency and electric efficiency [2-5]. The former indicates the heat usage and the latter suggests the effective electricity utilization. The electric efficiency, also termed as Faraday efficiency (or electricity-to-CO efficiency similar to electricity-to-H<sub>2</sub> efficiency adopted in H<sub>2</sub> production via SOEC), evaluates the effective current used for CO<sub>2</sub> splitting. In this chapter, electric efficiency analysis on CO<sub>2</sub> electrolysis by SOEC will be carried out, considering the factors of cathode materials, working potential, fuel composition and operating temperature.

In chapter 4-5, CO<sub>2</sub> electrolysis was studied in CO<sub>2</sub>-CO mixture; the CO in the mixture diluted the reactant concentration for CO<sub>2</sub> electrolysis and would inevitably decrease the CO<sub>2</sub> electrolysis efficiency. The LSCM/GDC materials have been reported to possess carbon resistance [6-8]. Therefore, performance of CO<sub>2</sub> electrolysis in feed gas without protective CO gas will be measured on the LSCM/GDC composite cathode prepared with different approaches. The Faradaic efficiency for CO<sub>2</sub> electrolysis in feed without protective gas will be evaluated as well.

### 6.1 Gas chromatography analysis and Faraday efficiency calculation

Similar as in previous chapters, CO<sub>2</sub>/CO mixtures, in a total flow rate of 30 ml/min, were supplied as gas for high temperature CO<sub>2</sub> electrolysis cells. The studied CO concentration ranged from 10 to 50 vol%. In some case, e.g. the GDC impregnated LSCM cathode cell, 5%H<sub>2</sub>/Ar at a flow rate of 10 ml/min was introduced to investigate its effect on CO<sub>2</sub> electrolysis behaviour. The SOEC cathode outlet gas was flowed through a paraffin bubbler to get rid of most steam before analysis.

Gas chromatography (GC) was employed to analyze the cathode outlet gas compositions. At a certain external load, the cathode downstream gas was connected to an Agilent 3000 Micro gas chromatograph (instrument series number: US10713003), which was equipped with an injection port. There were two modules, A and B in the operation of instrument, the detailed information of which were described in Table 6.1. Inert Ar and He were respectively used as carrier gas for module A and B. Both modules used 1.0μl backflush injector for sample injection, with Mol-sieve 5A and PLOTU, adopted as columns in module A and B respectively. Different gases were detected by thermal conductivity detectors (TCD) and distinguished according to their fingerprint retention time in the chromatography. The concentrations, i.e. the volume percentages of each gas in the mixture were proportional to the GC peak areas, which were calibrated regularly using mass flow controllers.

**Table 6.1** The detailed information of the GC operation modules

Module	Inlet	Column (Film/Inner diameter/Length)	Detector	Carrier Gas
A	Backflush	Molsieve: 12.00μm/320.00μm/10m Pre col: PLOTU: 30.00μm/320.00μm/3m	TCD	Ar
B	Backflush	PLOTU: 30.00μm/320.00μm/8m Pre col: PLOTQ: 10.00μm/320.00μm/1m	TCD	He

In the current gas system, H<sub>2</sub>, N<sub>2</sub>, O<sub>2</sub> and CO were detected and exit from the 5A molsieve column, and CO<sub>2</sub> was exit from the PLOTU column. The retention time for these gas component are in the sequence of CO<sub>2</sub> < H<sub>2</sub> < O<sub>2</sub> < N<sub>2</sub> < CO. At a certain current, the CO production rate was calculated using gas flow rate and the percentage differences between CO concentration at loading and that at OCV. The calculation of CO<sub>2</sub> reduction rate was similar.

With regard to electricity efficiency, also as Faradaic efficiency, Faraday's law (expressed in Equation 6.1) was used for calculation.

$$Q = I t = n z F \quad (\text{Equation 6.1})$$

Where: Q is the total electric charge passed through the electrolysis cell;

I is the constant current passed through the electrolysis cell;

t is the total time the constant current was applied;

n is the number of moles for a certain substance;

z is the valency of ion involved, z equals to 2 considering CO<sub>2</sub>→CO+1/2O<sub>2</sub>;

F is the Faraday constant, equals to 96,485 C mol<sup>-1</sup>.

The Faradaic yield of CO in CO<sub>2</sub> electrolysis could be obtained by transferring Equation 6.1 into:

$$n/t = I/(z F) \quad (\text{Equation 6.2})$$

At a certain current, the Faradaic efficiency for, e.g. CO yield thus could be described as:

$$\eta = \frac{\text{Actual CO production rate from GC analysis}}{\text{Theoretical CO production rate calculated by Equation 6.2}} \quad (\text{Equation 6.3})$$

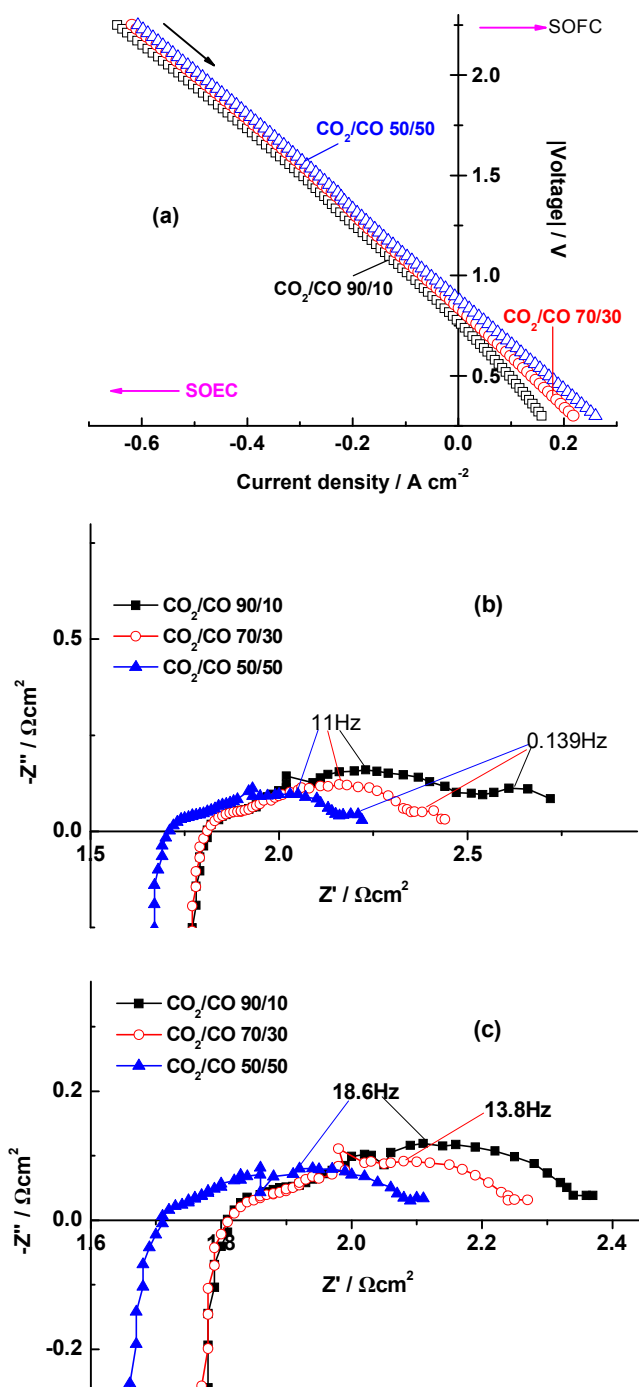
The actual CO production rate was calculated from the total flow rate and the variation of volume percentage in the condition between a certain load and OCV. At external load, the cell potential was kept constant for a while, during which GC analysis was employed to estimate the capability of CO production. 4 gas samples were collected at

each potential, and the last one was used for calculation. The amount of CO generated and CO<sub>2</sub> reduced was calculated with GC peak analysis and total flow rate. The Faraday yield was calculated using the current at the loading potential, according to Faraday's law. The electric efficiency, i.e. Faradaic efficiency of CO production was evaluated in different conditions, for instance, various CO<sub>2</sub>/CO ratios, operation temperatures, and cathode materials. In some cases, 5% H<sub>2</sub>/Ar was introduced to study its impact on the CO<sub>2</sub> electrochemical reduction process as well as on the Faradaic efficiency of CO<sub>2</sub> electrolysis.

## **6.2 Faradaic efficiency analysis for CO<sub>2</sub> electrolysis on different cathode materials for SOEC**

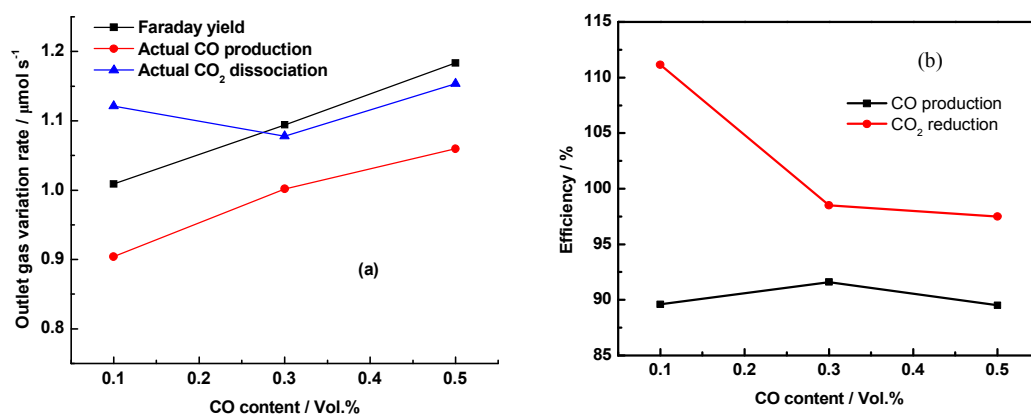
### **6.2.1 CO<sub>2</sub> electrolysis efficiency on screen-printed LSCM/GDC cathode with extra Pt catalyst**

Fig. 6.1 shows the CO<sub>2</sub> electrolysis performance from an SOEC with screen-printed LSCM/GDC cathode, 2mm YSZ electrolyte and LSM/ScSZ anode measured in CO<sub>2</sub>/CO mixtures at 900°C. 1wt% Pt was introduced into LSCM/GDC composite by wet impregnation to boost the cathode activity. I-V curves of this SOEC were recorded both in electrolysis and fuel cell mode, starting from SOEC to SOFC. In Fig. 6.1(a), the I-V curves seem to be fairly linear in CO<sub>2</sub>/CO mixtures, with minor curvature against varying potential. The OCV values are -0.77, -0.84, -0.882V for the CO<sub>2</sub>/CO mixture containing 10, 30, 50 vol. % CO, respectively. These measured OCV values are close to those predicted by Nernst equation.



**Fig. 6.1** Performance from an SOEC with 1 wt% Pt aided LSCM/GDC cathode, 2mm thick YSZ electrolyte and LSM/ScSZ anode operated in CO<sub>2</sub>/CO mixtures at 900°C. (a) I-V curves; (b) Nyquist plot at OCV (frequency range: 10<sup>5</sup>-0.015Hz); and (c) Nyquist plot at 0.5V (voltage referred to OCV value; Frequency range: 10<sup>5</sup>-0.1Hz)

The impedance data are displayed in Fig. 6.1 (b) and (c). At OCV, the impedance spectra of the cathode working in different environments exhibit three arcs, one at high frequency (magnitude of 10<sup>3</sup> Hz) regime, and two at low frequency range with characteristic frequency located at 11 and 0.139Hz, respectively. With increasing CO concentration, the R<sub>p</sub> reduces for the Pt aided LSCM/GDC cathode, indicating improved cathode properties and fast cathode kinetics at more reducing atmosphere. Similar trends are observed when external potential, such as 0.5V (referred to OCV value, hereinafter and stated otherwise), is applied to SOEC. Besides, as can be seen from Fig. 6.1(c), the summit frequency for low frequency arc shifts to around 18.6Hz, a higher value than that at OCV, which is also an indication of accelerated cathode electrochemical processes at elevated working potential and this also explains the smaller R<sub>p</sub> achieved at loads than at OCV.



**Fig. 6.2** Outlet gas component variation rate (a) and electrolysis efficiencies (b) as a function of CO concentration in CO<sub>2</sub>-CO mixture at potential load of 0.5V on the 1 wt% Pt assisted LSCM/GDC composite cathode SOEC working at 900°C

The GC analysis results and efficiency evaluation in different CO content from 1% Pt dispersed LSCM/GDC cathode SOEC are shown in Fig. 6.2. It can be seen that CO is produced successfully, and with decreasing CO<sub>2</sub> reactant, the amount of CO product from CO<sub>2</sub> dissociation increases. In CO<sub>2</sub>/CO 90/10 mixture, the CO yield is 0.9μmol/s, and it rises to 1.06μmol/s when CO<sub>2</sub>/CO 50/50 is the fuel for electrolysis. The actual CO yield is a bit lower than the corresponding Faraday yield, which leads to Faraday

efficiencies in the range of 90-92% in term of CO production in the tested conditions. The amount of CO<sub>2</sub> dissociated in the identical conditions is also displayed in Fig. 6.2. The actual quantity of CO<sub>2</sub> reduced is higher than the amount of generated CO. In fact, the dissociated CO<sub>2</sub> amount reaches 1.12 μmol/s, giving a Faraday efficiency of 111% in term of CO<sub>2</sub> dissociation using CO<sub>2</sub>/CO 90/10 as feed gas. At higher CO levels, the CO<sub>2</sub> dissociation quantity gets to closer to the theoretical value; therefore, the Faraday efficiency in term of CO<sub>2</sub> reduction is around 100%.

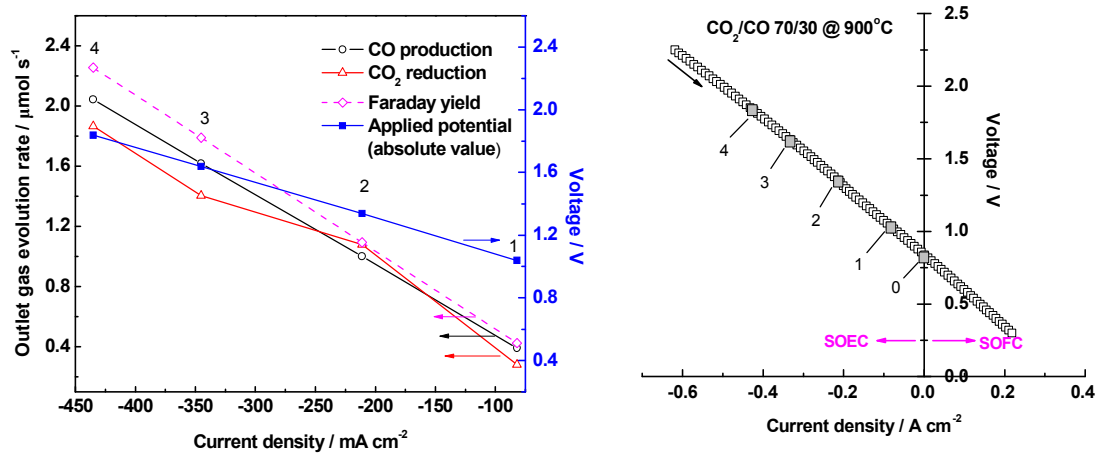


**Fig. 6.3** Outlet gas evolution rate (left graph) and working potential (right graph) vs the current passing through SOEC in CO<sub>2</sub>/CO 70/30 mixture at 900°C. The cathode is 1 wt% Pt impregnated LSCM/GDC composite; the solid points on the I-V curves (right graph) correspond to current/potential under which GC analysis was performed

The CO production and CO<sub>2</sub> dissociation rates, as well as Faraday yield from Pt impregnated LSCM/GDC cathode cell measured as a function of current passing through SOEC are illustrated in Fig. 6.3. The feed gas is CO<sub>2</sub>/CO 70/30 for these tests. Both CO yield and CO<sub>2</sub> reduction quantity increase on increasing the current passing through SOEC. At lower external loads, such as 0.5V (absolute potential is -1.34V indicated by point 2), the CO yield is 1.0 μmol/s and the CO<sub>2</sub> reduction is 1.08 μmol/s, producing Faraday efficiencies of 91.6% in term of CO generation and 98.5% in term of CO<sub>2</sub> reduction. When the applied voltage reaches 1.0V (absolute potential -1.84V), the

CO yield and CO<sub>2</sub> reduction rate is 2.04, 1.87 μmol/s, respectively, leading to Faraday efficiencies of 90.7% in term of CO yield and 82.7% in term of CO<sub>2</sub> reduction.

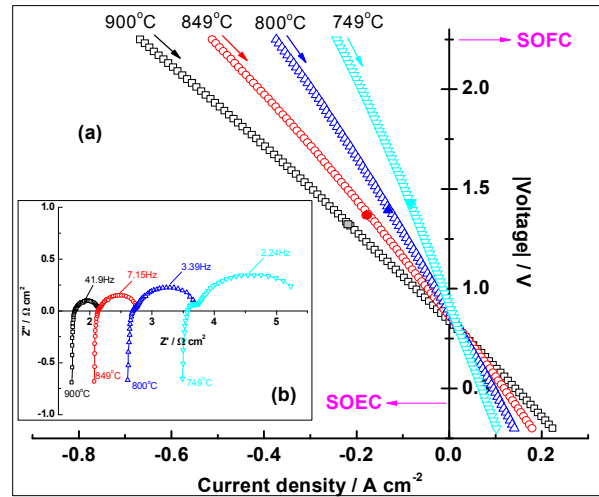


**Fig. 6.4** a. I-V curves from the 1 wt% Pt assisted LSCM/GDC cathode SOEC operated in CO<sub>2</sub>/CO 70/30 environment during cooling from 900 to 750°C at an interval 50°C; b. Impedance data in the conditions (at 0.5V) indicated by the solid point on I-V curves

The electrochemical performance of 1% Pt assisted LSCM/GDC cathode SOEC during cooling SOEC from 900 to 750°C at an interval of 50°C is displayed in Fig. 6.4. The I-V curves were obtained in CO<sub>2</sub>/CO 70/30 feed, and at each temperature, impedance data at applied voltage of 0.5V (corresponding to the solid points on I-V curves) were collected. The OCV value for the cathode cell working in CO<sub>2</sub>/CO 70/30 is -0.84, -0.87, -0.89 and -0.92V at 900, 849, 800 and 749°C, respectively. With decreasing temperature, the cell resistance increases remarkably, revealed by the sharper slope from I-V curves as well as enlarged arcs from impedance spectra at lowered temperatures. The R<sub>p</sub> is 1.65 Ωcm<sup>2</sup> at 750°C, four times larger than that at 900°C. Furthermore, the characteristic frequency for the low frequency arc in impedance spectra decreases distinctly, from 41.9Hz at 900°C to 2.24Hz at 750°C, which means that the relative steps are retarded accordingly with decreasing temperature.

Fig. 6.5 shows the results of CO yield and CO<sub>2</sub> reduction rates vs. current at operation temperature ranging from 900°C to 750°C at an interval of around 50°C. The applied

potential is 0.5V referred to OCV value, and are -1.338V, 1.366V, 1.389V, and -1.415V at 900, 850, 800 and 750°C respectively. The theoretical values for CO generation, i.e. Faradaic yields, are also plotted in Fig. 6.5. Both CO yield and CO<sub>2</sub> reduction rate decline with lowering temperature, consistent with the electrochemical results indicated in Fig. 6.4, so does the faraday yields which reflect a linear relationship with current density. With regard to Faraday efficiency, the CO production efficiency falls in the range of 86-92%, increased slightly with current density which is dependent on operation temperature. For CO<sub>2</sub> reduction efficiency, it increases with current density/temperature, except at 850°C. The fluctuation of CO<sub>2</sub> reduction efficiency at 850°C is possibly from experiment errors within the gas chromatograph and CO<sub>2</sub> mass flow controller. The latter should be calibrated regularly as well as GC.

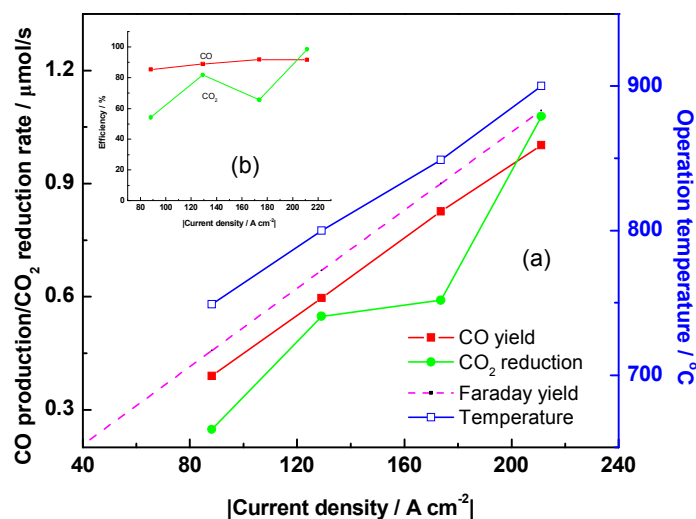


**Fig. 6.5** CO production/CO<sub>2</sub> reduction rate (a) and efficiency (b) vs. current density (at voltage of 0.5V referred to OCV) in CO<sub>2</sub>/CO 70/30 at temperature range of 900-750°C for the 1wt% Pt aided LSCM/GDC cathode SOEC (The OCV value is -0.838, -0.866, -0.889, and -0.915V at 900, 850, 800 and 750°C respectively, and the applied potentials at these temperatures are -1.338V, -1.366V, -1.389V, and -1.415V respectively)

## 6.2.2 CO<sub>2</sub> electrolysis efficiency on the GDC impregnated LSCM cathode for SOEC

CO formation and CO<sub>2</sub> reduction were monitored for the GDC impregnated LSCM cathode in SOEC. The microstructure and electrochemical performance of this cathode for CO<sub>2</sub> electrolysis were discussed in section 5.3.3. Here focus is on the exit gas from the cathode chamber. The outlet gas composition at different voltages in CO<sub>2</sub>/CO 70/30 fuel for CO<sub>2</sub> electrolysis at 900°C from the GDC impregnated LSCM cathode cell is presented in Fig. 6.6. With increasing potential, the CO<sub>2</sub> concentration declines and CO concentration rises simultaneously, so that the concentrations of the two gradually get close with the increase of potential. Further, H<sub>2</sub> is also detected probably as a result of the reduction of moist from the surroundings and its content also increases with potential, however, at a very low level, suggesting that the reduction of CO<sub>2</sub> is the dominant process, and most of current is used for this reaction.

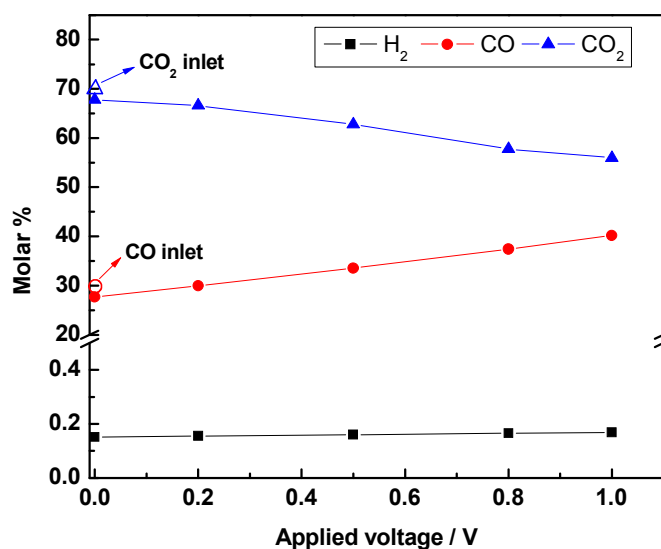


**Fig. 6.6** Outlet gas composition at different potentials in CO<sub>2</sub>/CO 70/30 fuel gas for CO<sub>2</sub> electrolysis at 900°C on the GDC impregnated LSCM cathode (the voltage value is referring to OCV which is around -0.842V)

Shown in Fig. 6.7 is the CO formation rate, CO<sub>2</sub> dissociation rate and corresponding theoretical value as a function of applied voltage in CO<sub>2</sub>/CO 70/30 mixture from the

GDC infiltrated LSCM cathode SOEC at 900°C. The theoretical value, i.e. Faradaic yield/reduction increases with applied voltage, which is in accord with the I-V curve from this cathode SOEC in Fig. 5.20(a). Similar tendency is observed on the CO generation rate as well as CO<sub>2</sub> splitting rate. The efficiencies in term of CO formation and CO<sub>2</sub> reduction at these applied voltages are listed in Table 6.2. Evidently, increasing applied voltage raises both the CO formation and CO<sub>2</sub> splitting efficiency. The reasons for discrepancies in CO yield and CO<sub>2</sub> reduction are not clear at the moment. However, H<sub>2</sub>, though in an insignificant yield, adds more complexity to the electrochemical processes happening at the cathode.

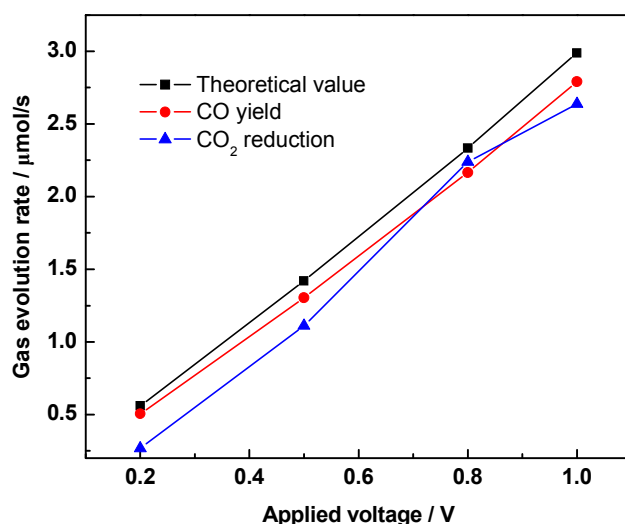


**Fig. 6.7** Gas evolution rate at different voltages using CO<sub>2</sub>/CO 70/30 as fuel gas from the GDC infiltrated LSCM cathode SOEC operated at 900°C

**Table 6. 2** Efficiency of CO production and CO<sub>2</sub> dissociation in CO<sub>2</sub>/CO 70/30 mixture at different voltages from the GDC infiltrated LSCM cathode SOEC working at 900°C

	Efficiency (%)			
	0.2V	0.5V	0.8V	1.0V
CO	90.2	91.8	92.8	93.4
CO <sub>2</sub>	47.9	78.3	95.9	88.3

The impact of introducing 5% H<sub>2</sub>/Ar on the CO production and CO<sub>2</sub> electrolysis efficiencies was investigated at 900°C and 750°C, respectively, in CO<sub>2</sub>/CO 70/30 mixture from the GDC impregnated LSCM cathode SOEC, the results are exhibited in Fig. 6.8-6.9 and the corresponding electrochemical results were dealt with previously in Fig. 5.24 -5.25 in section 5.3.3.3. In this experiment, 10ml/min 5% H<sub>2</sub>/Ar was added to the 30ml/min CO<sub>2</sub>/CO mixture and the results are compared to those from CO<sub>2</sub>/CO mixture without 5% H<sub>2</sub>/Ar at different temperatures.

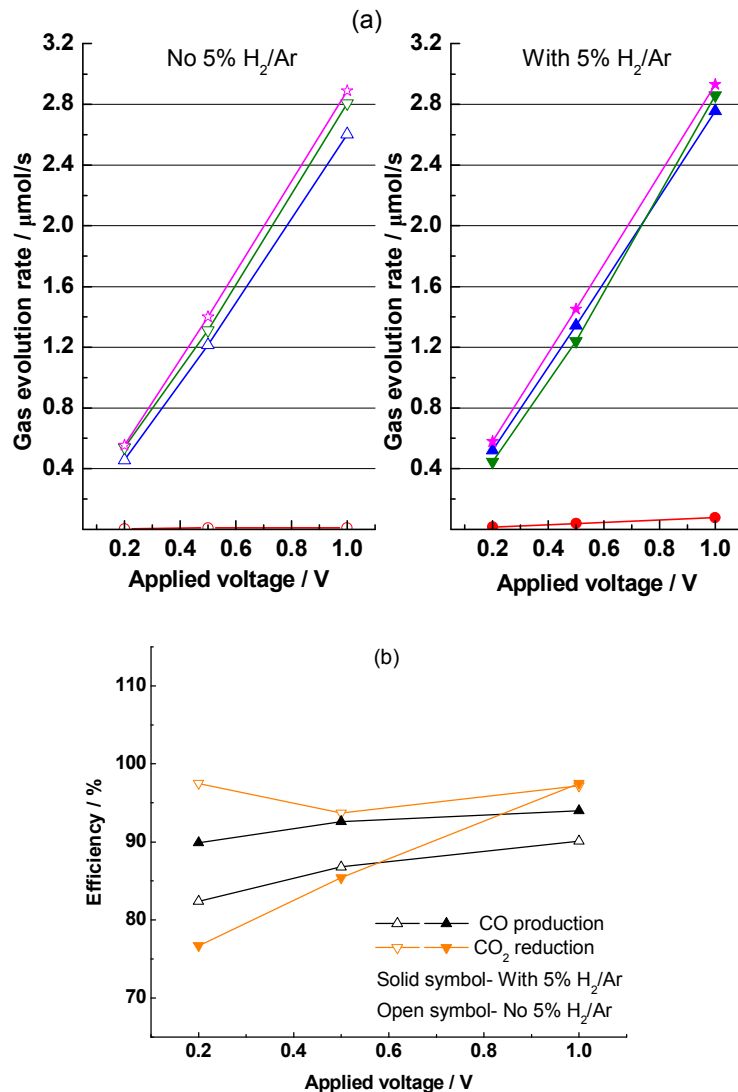


**Fig. 6.8** Effect of introducing 5% H<sub>2</sub>/Ar on gas evolution (a) and Faradaic efficiencies (b) for CO<sub>2</sub> electrolysis in CO<sub>2</sub>-CO 70-30 atmosphere at 900°C. Circle: H<sub>2</sub> production; up-triangle: CO production; down-triangle: CO<sub>2</sub> reduction; and star: theoretical values. The tested OCV is -0.84V for feed without 5% H<sub>2</sub>/Ar and -0.847V for that with 5% H<sub>2</sub>/Ar.

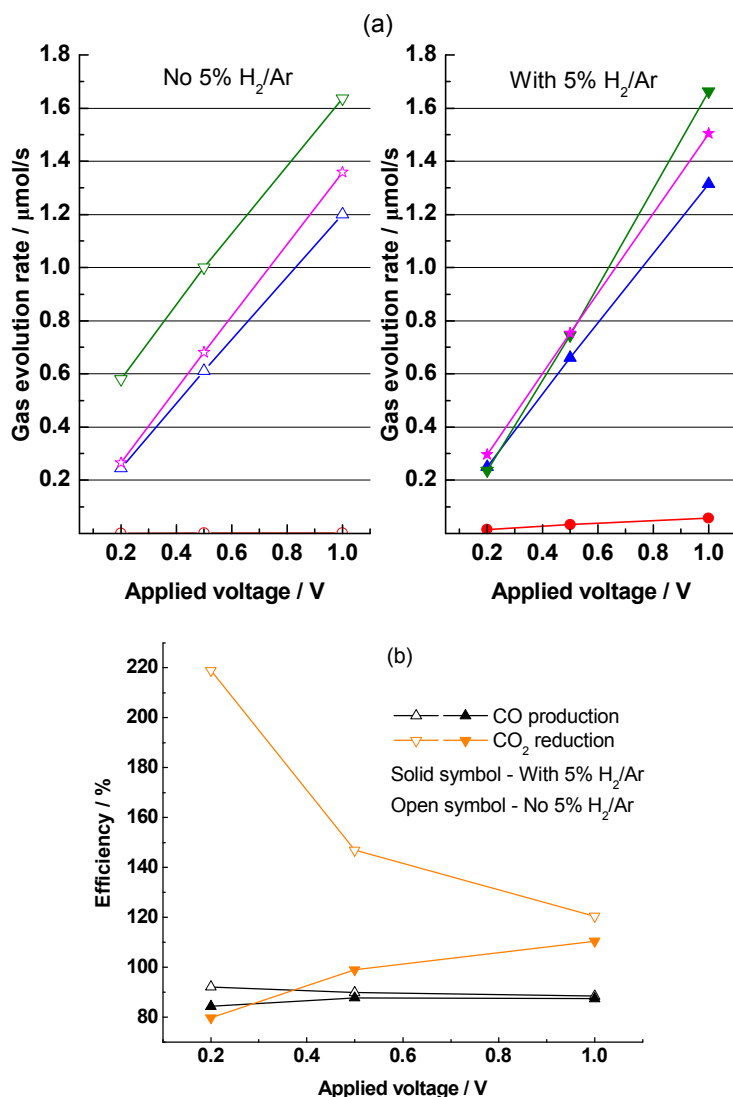


**Fig. 6.9** Effect of introducing 5%H<sub>2</sub>/Ar on gas evolution (a) and Faradaic efficiencies (b) for CO<sub>2</sub> electrolysis in CO<sub>2</sub>-CO 70-30 environment at 750°C. Circle: H<sub>2</sub> production; up-triangle: CO production; down-triangle: CO<sub>2</sub> reduction; and star: theoretical values. The OCV at 750°C is -0.914V for feed without 5%H<sub>2</sub>/Ar and -0.922V for that with 5% H<sub>2</sub>/Ar.

At 900°C (Fig. 6.8), the CO formation increases upon adding 5% H<sub>2</sub>/Ar into feed gas at the same voltage, so the efficiencies regarding CO production are higher than those from the atmosphere without 5% H<sub>2</sub>/Ar. The CO<sub>2</sub> reduction amount, on the contrary, decreases at applied voltage up to 0.5V with the introduction of 5% H<sub>2</sub>/Ar, and it increases a bit when voltage is higher, compared to those with the absence of 5% H<sub>2</sub>/Ar.

The CO<sub>2</sub> electrolysis efficiency with respect to CO<sub>2</sub> reduction first decreases then increase with the applied voltage, in comparison to the corresponding value in the environment without 5% H<sub>2</sub>/Ar. Recalling the electrochemical results at 900°C, the introduction of 5% H<sub>2</sub>/Ar facilitated the cathode kinetics at voltages below 1.0V, and it showed adverse effect at higher voltages. In combination, it is supposed that the gas shift/reverse gas shift reaction happens together with the CO<sub>2</sub> reduction reaction.

At 750°C (Fig. 6.9), the trends of CO production and CO<sub>2</sub> dissociation with the variation of applied voltage against introduction of 5% H<sub>2</sub>/Ar are similar to those at 900°C. That is, compared to the values in the mixture without 5%H<sub>2</sub>/Ar, the CO production increases with applied voltage and the CO<sub>2</sub> dissociation decreases until applied voltage reaches 0.5V and then increases when applied voltage gets higher upon the presence of 5%H<sub>2</sub>/Ar in feed gas. What is different from the phenomena at 900°C is that, at 750°C, both the efficiency concerning CO yield and CO<sub>2</sub> splitting are lower in the mixture containing 5%H<sub>2</sub>/Ar than that in the feed without H<sub>2</sub>. Considering the performance enhancement induced by the addition of 5%H<sub>2</sub> at all potentials at 750°C from the electrochemical results in section 5.3.3.3, it is assumed that the water gas shift reaction occurs, which decreases the amount of CO yield as well as CO<sub>2</sub> reduction, along with the dissociation of CO<sub>2</sub>. However, more evidence needs to be found for the confirmation of this assumption.

Noting that H<sub>2</sub> production increases with applied voltage in all cases, and in the surroundings without 5%H<sub>2</sub>/Ar, the amount of it is negligibly low, in a factor of 10<sup>-3</sup> μmol/s at 900°C and 10<sup>-4</sup> μmol/s at 750°C. In the feed containing 5% H<sub>2</sub>/Ar, the amount of produced H<sub>2</sub> is in the factor of 10<sup>-2</sup> μmol/s at 900°C and 750°C, still very low compared with CO production and CO<sub>2</sub> reduction rates. The detected H<sub>2</sub> is probably from the splitting of moist in the surroundings. Besides, the CO generation efficiency value falls in the range of 82-95% in the measured potentials and temperatures, indicating that the dominant process is still the CO<sub>2</sub> reduction reaction.

### 6.2.3 CO<sub>2</sub> electrolysis efficiency on the Pd-GDC co-impregnated LSCM cathode for SOEC

The SOEC with 0.5wt% Pd and GDC co-impregnated LSCM cathode, 2mm YSZ electrolyte and LSM/ScSZ anode was fabricated and measured. Fig. 6.10 illustrates the electrochemical performance, specifically, the I-V curves of this SOEC operated in different CO<sub>2</sub>/CO mixtures at 900°C. The cell performance declines with increasing CO<sub>2</sub> concentration at OCV, but it improves with increasing potential. This observation agrees with the impedance results (not shown here). The I-V curves do not show any sign from diffusion limitations in all the fuels studied. The OCV value is -0.781, -0.848, and -0.891V in the feed containing 90, 70 and 50% CO<sub>2</sub>, respectively. These values are higher than those from other cathode cells in identical testing conditions (covered in Chapter 5), indicating the superiority from the 0.5% Pd and GDC co-impregnated LSCM cathode for CO<sub>2</sub> electrolysis. In fact, this cathode was reported to be comparable with the conventional Ni/YSZ cermet cathode for application in high temperature CO<sub>2</sub> electrolysis via SOEC (see section 5.4).

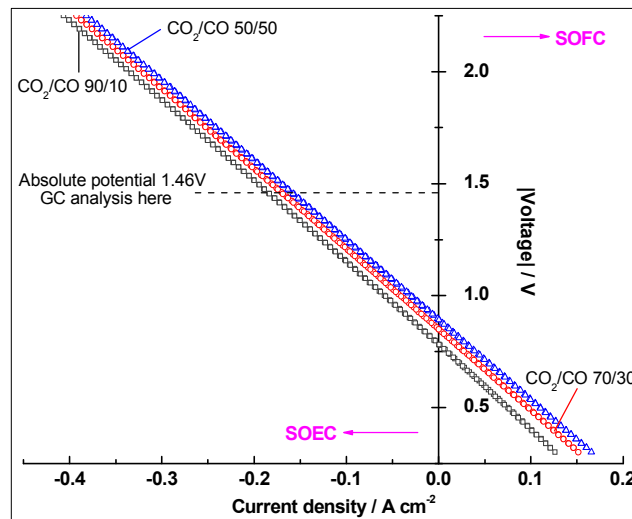


**Fig. 6.10** I-V curves from the 0.5wt% Pd and GDC co-infiltrated LSCM cathode SOEC working in different CO<sub>2</sub>/CO environments at 900°C

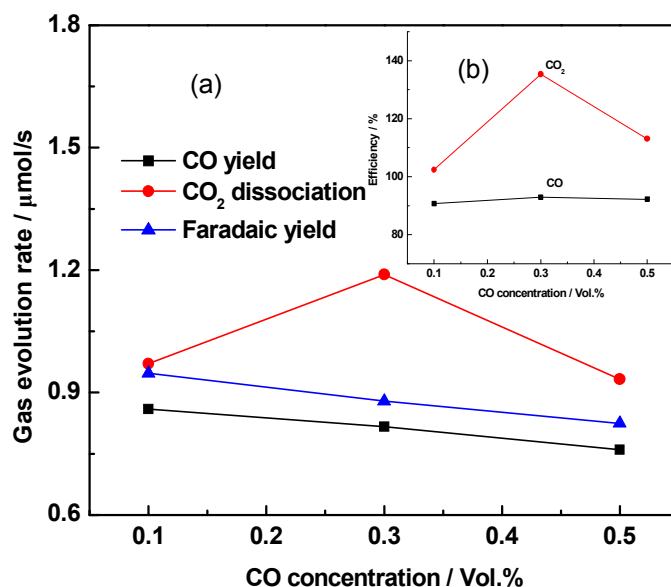


**Fig. 6.11** Gas evolution (a) and CO<sub>2</sub> electrolysis efficiencies (b) at 1.46V (absolute potential also as thermal neutral voltage for CO<sub>2</sub> electrolysis at 900°C) with a function of CO concentration on the 0.5%Pd-GDC co-impregnated LSCM cathode SOEC working at 900°C

The capability of CO production as well as CO<sub>2</sub> reduction as a function of CO concentration is displayed in Fig. 6.11. The tested potential is -1.46V (absolute potential), i.e. the thermal neutral voltage, at which the Joule heat is equal to the heat the CO<sub>2</sub> reduction reaction consumed at 900°C. In Fig. 6.11, the CO production rate diminishes slightly, from 0.86 μmol/s to 0.76 μmol/s, with rising CO concentration from 10% to 50%. Since current density declines with increasing CO fraction at -1.46V, the Faradaic yield decreases correspondingly, thus, the Faradaic efficiency concerning CO production (around 92%) is roughly unchanged against variation in CO content. The CO<sub>2</sub> reduction rate and efficiency, on the contrast, seem to be dependent on the CO<sub>2</sub> concentration, both reaching a peak value when CO<sub>2</sub> fraction takes up to 70%. The CO<sub>2</sub> reduction in CO<sub>2</sub>/CO 90/10 mixture is 0.97 μmol/s, and its corresponding efficiency is 102%, agrees well with the theoretical value.

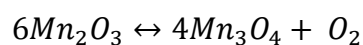
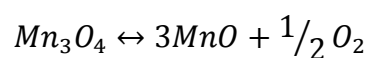
The disagreement in the CO yield and CO<sub>2</sub> reduction amount is observed almost in all tests, which might indicate that other processes, e.g. the deep reduction of CO<sub>2</sub> to C may

also take place [9]. The specific reasons for the observed disagreement are not known, nevertheless, the experimental errors in GC peak analysis is one of them and cannot be ruled out.

### 6.3 CO<sub>2</sub> electrolysis without protective gas and corresponding efficiency evaluation

#### 6.3.1 Performance and efficiency of CO<sub>2</sub> electrolysis with CO<sub>2</sub>-N<sub>2</sub> fed into SOEC cathode

Previously, the CO<sub>2</sub> electrolysis we have done were carried out using CO<sub>2</sub>-CO mixture as fuel gas, which, inevitably, would decrease the CO<sub>2</sub> electrolysis efficiency because of the dilute fuels utilised. Here in this section, performance of CO<sub>2</sub> electrolysis in fuels without protective CO gas is assessed on the SOEC with GDC impregnated LSCM as cathode (some with extra Pd catalyst), 2mm YSZ pellet as electrolyte and LSM/ScSZ as anode material. Presented in Fig. 6.12 are the I-V curves of the above SOEC working in CO<sub>2</sub>-N<sub>2</sub> mixtures as well as in CO<sub>2</sub>-CO 50-50 mixture at 900°C. For this SOEC, the studied CO<sub>2</sub>/N<sub>2</sub> ratios are 10/90, 30/70, and 50/50 in a total feed flow rate of 30ml/min. Unlike the fairly linear I-V curve observed in CO<sub>2</sub>-CO mixture, curvature occurs on the I-V curves in CO<sub>2</sub>-N<sub>2</sub> environments, specifically in the voltage range from OCV to around -0.8V (absolute value). The OCV value is -0.128V in CO<sub>2</sub>-N<sub>2</sub> mixtures, and -0.891V in CO<sub>2</sub>-CO 50-50 mixture. The low OCV in CO<sub>2</sub>-N<sub>2</sub> mixtures indicates that the activation energy required for the offset of CO<sub>2</sub> split reaction is much higher, compared to that in CO<sub>2</sub>-CO mixture, and this also explains the remarkably large cell resistance observed at low potentials due to diffusion limitations. The process in this potential range (from OCV to ca. -0.8V) is possibly the electrolysis of impure O<sub>2</sub>, the existence of which has been confirmed by experimental OCV value. However, the P<sub>O<sub>2</sub></sub> at OCV in CO<sub>2</sub>-N<sub>2</sub> mixtures at cathode side is 1.3\*10<sup>-3</sup> atm, from the back calculation of Nernst equation (Equation 1.5). This high P<sub>O<sub>2</sub></sub> value indicates other sources of O<sub>2</sub>, for instance, the reduction of CO<sub>2</sub> which might take place at a low amount. Other possibility includes O<sub>2</sub> from the buffer reaction



in defect chemistry in LSCM phase in the potential arrange around OCV. The MnO-Mn<sub>3</sub>O<sub>4</sub> buffer fixes a P<sub>O<sub>2</sub></sub> of ~10<sup>-9</sup>atm theoretically at 900°C [10], and the Mn<sub>3</sub>O<sub>4</sub>-Mn<sub>2</sub>O<sub>3</sub> buffer gave an equilibrium potential of ~60mV at 1100K [11]. With the progress of impure O<sub>2</sub> electrolysis, P<sub>O<sub>2</sub></sub> at cathode side decreases, which drives an increase in potential to OCV value. When applied potential is high enough to overcome the energy barrier for CO<sub>2</sub> reduction reaction, the reduction of CO<sub>2</sub> becomes significant, and the cell resistance in CO<sub>2</sub>-N<sub>2</sub> feed begins to decrease.

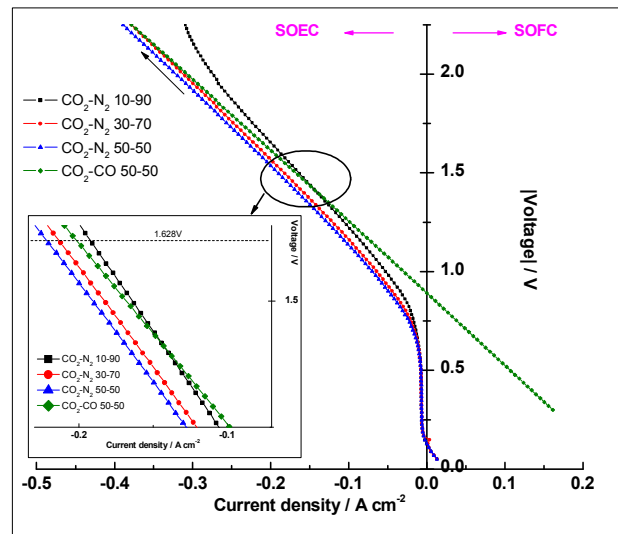


**Fig. 6.12** I-V curves of the GDC impregnated LSCM cathode SOEC working in CO<sub>2</sub>-N<sub>2</sub> mixtures as well as in CO<sub>2</sub>-CO 50-50 mixture at 900°C

From Fig. 6.12, one can see that the cell exhibits higher performance in CO<sub>2</sub>-CO gas than in CO<sub>2</sub>-N<sub>2</sub> fuels, however, at 1.5V (absolute potential -1.628V), the cell resistance in different fuels is in the sequence of CO<sub>2</sub>-N<sub>2</sub> 50-50 < CO<sub>2</sub>-N<sub>2</sub> 30-70 < CO<sub>2</sub>-CO 50-50 < CO<sub>2</sub>-N<sub>2</sub> 10-90. The larger cell resistance in CO<sub>2</sub>-N<sub>2</sub> 10-90 at high potentials originates from limited gas transport, specifically, insufficient CO<sub>2</sub> supply, compared to other CO<sub>2</sub>-N<sub>2</sub> mixtures. Indeed, limiting current density appears on the I-V curve for the cell working in CO<sub>2</sub>-N<sub>2</sub> 10-90 environment and this limiting current density causes larger concentration overpotential than those in other CO<sub>2</sub>-N<sub>2</sub> mixtures, from which the limiting currents are absent on the I-V curves.

The impedance spectra of CO<sub>2</sub> electrolysis in feed without CO on the GDC impregnated LSCM cathode at different potentials in various CO<sub>2</sub>-N<sub>2</sub> mixtures are compared in Fig. 6.13. At OCV, the impedance in CO<sub>2</sub>-CO 50-50 mixture is compared with those in CO<sub>2</sub>-N<sub>2</sub> fuels, apparently, the latter is much larger, ascribed to the large molecular size and chemical stability of CO<sub>2</sub> which requires much higher input energy for the onset of CO<sub>2</sub> reduction reaction. A markedly smaller R<sub>s</sub> is observed with CO<sub>2</sub>-CO mixture, compared to that with CO<sub>2</sub>-N<sub>2</sub> mixture, which is because the presence of CO in cathode chamber leads to an enhanced conductivity in GDC component. This has also been seen from the I-V curves in Fig. 6.12. Besides, the LSCM/GDC based cathode activity were found to be boosted in reducing atmospheres [8, 12], which also contributes to the higher CO<sub>2</sub> electrolysis performance in CO containing atmosphere. The R<sub>p</sub> value in CO<sub>2</sub>-CO 50-50 fuel is 0.32 Ωcm<sup>2</sup> at OCV, while the R<sub>p</sub> values in CO<sub>2</sub>-N<sub>2</sub> fuel at OCV are higher than 3.0 Ωcm<sup>2</sup>, more than 10 times larger.

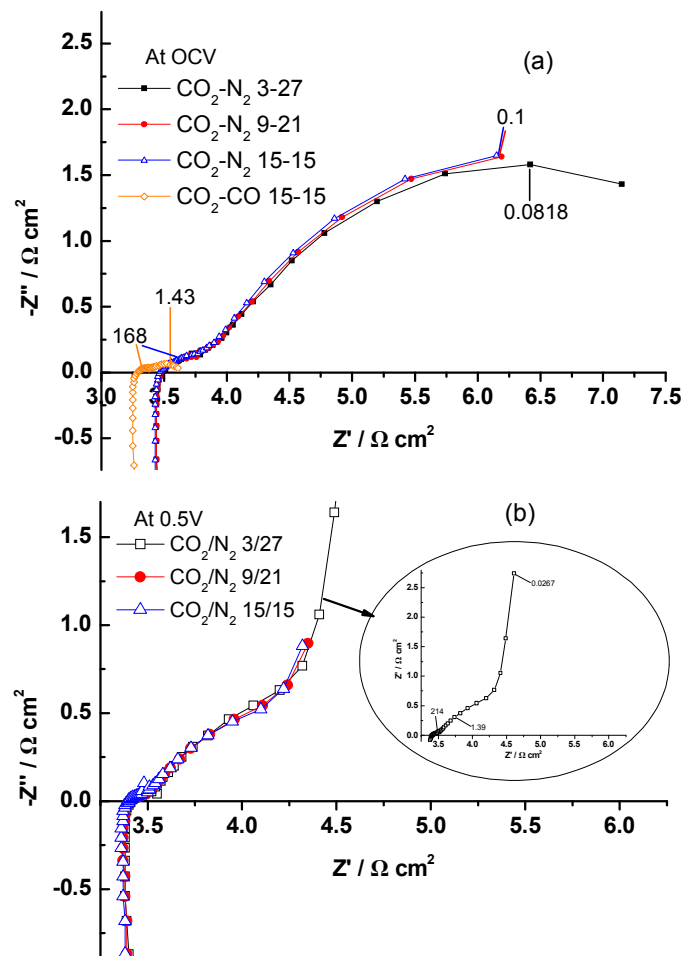


(Figure continued on the following page)

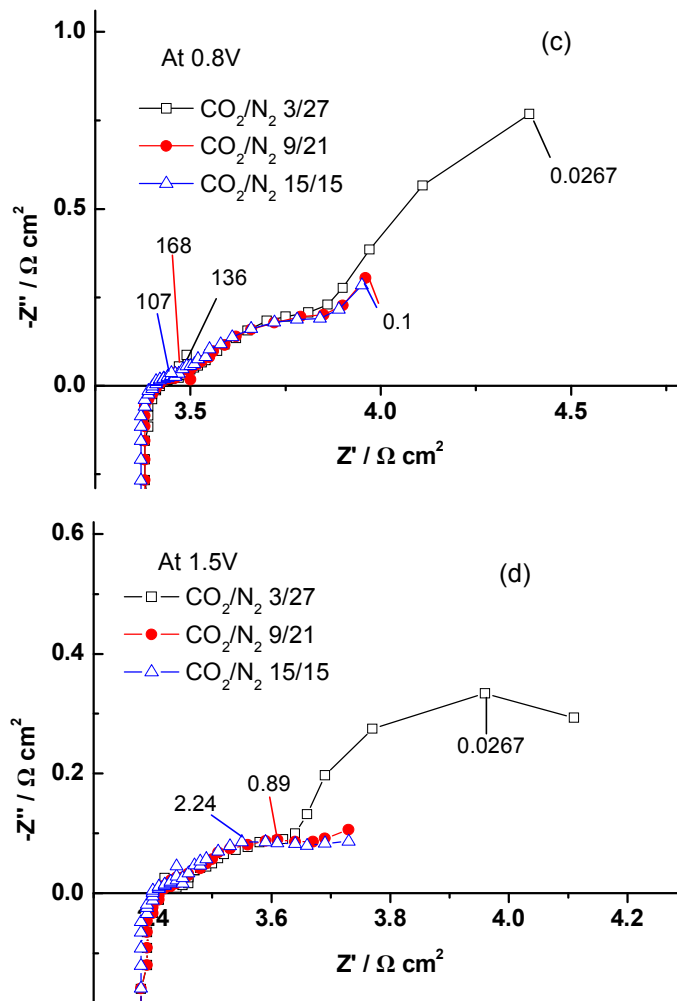


**Fig. 6.13** Impedance data from the GDC impregnated LSCM SOEC cathode at OCV (a), 0.5V (b), 0.8V (c) and 1.5V (d) at 900°C in various CO<sub>2</sub>-containing atmospheres

Concerning the cathode resistance in different CO<sub>2</sub>-N<sub>2</sub> fuels, it can be observed that the impedance is almost the same value in various CO<sub>2</sub>-N<sub>2</sub> mixtures at OCV. Nevertheless, when potential increases gradually, the cathode impedance increases with decreasing CO<sub>2</sub> content. This phenomenon is quite evident at 1.5V (absolute potential -1.628V), which is higher than the thermal neutral voltage (-1.46V). The explanation is, with more energy input, CO starts to be produced, which in return, enhances the cathode electrochemical activity and favours the further reduction of CO<sub>2</sub>. When applied potential surpasses the thermal neutral value, Joule heat from cell resistance can give

extra energy for CO<sub>2</sub> reduction reaction, at this circumstance, more CO<sub>2</sub> present in fuel gas will give rise to more CO, consequently, higher performance.

In Fig. 6.13(a-d), the cathode impedance decreases when potential is higher than 0.5V in CO<sub>2</sub>-N<sub>2</sub> 30-70 and CO<sub>2</sub>-N<sub>2</sub> 50-50 fuels, whereas, it enlarges further till potential is higher than 0.8V and declines then for the cathode working in CO<sub>2</sub>-N<sub>2</sub> 10-90. These observations agree well with what is indicated from I-V curves in Fig. 6.12. Compared to the values in CO<sub>2</sub>-N<sub>2</sub> 30-70 and CO<sub>2</sub>-N<sub>2</sub> 50-50 fuels, the cathode impedance is much larger in CO<sub>2</sub>-N<sub>2</sub> 10-90 mixture, especially the low frequency responses, suggesting that the cathode suffers from gas diffusion/surface diffusion difficulty in this condition. Moreover, although not measured here, the cathode impedance in CO<sub>2</sub>-N<sub>2</sub> 10-90 would increase again at potentials higher than 2.0V due to CO<sub>2</sub> shortage, and this has been confirmed by the I-V curve in CO<sub>2</sub>-N<sub>2</sub> 10-90 mixture. The R<sub>p</sub> for the GDC impregnated LSCM cathode working in CO<sub>2</sub>-N<sub>2</sub> 10-90 environment is around 0.8 Ωcm<sup>2</sup> at applied voltage of 1.5V, and it decreases to around 0.4 Ωcm<sup>2</sup> for this cathode working in CO<sub>2</sub>-N<sub>2</sub> 50-50 feed in the same conditions. These values reflect the great potential of utilising the GDC impregnated LSCM cathode for high temperature CO<sub>2</sub> electrolysis without protective gas, and it can be predicted that the cathode performance would be further improved with the introduction of metal catalyst, such as Pd, and with more CO<sub>2</sub> provided in fuel gas.

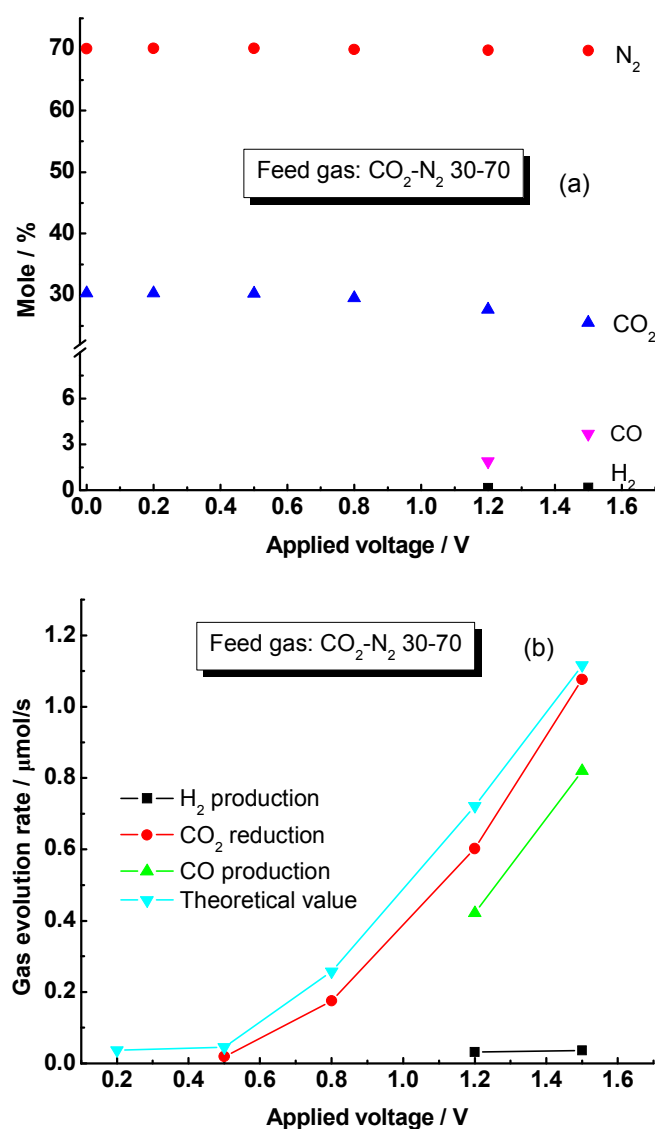


**Fig. 6.14** Cathode outlet gas composition (a) and gas evolution (b) at different potentials from GDC impregnated LSCM cathode SOEC working in CO<sub>2</sub>-N<sub>2</sub> 30-70 feed at 900°C

Fig. 6.14 shows the GC analysis results, i.e. the cathode outlet gas composition and gas evolution at different potentials from the GDC infiltrated LSCM cathode SOEC being operated in CO<sub>2</sub>-N<sub>2</sub> 30-70 environment at 900°C. As expected, the N<sub>2</sub> content is independent of applied voltages, suggesting its function of only as saturate gas. The reduction of CO<sub>2</sub> is observable when potential goes higher than 0.5V (referred to OCV hereinafter), and it increases with rising potential, in accord with the tendency of the theoretical value predicted by Faraday's law. The CO production is detected at

potentials higher than 0.8V, and at 0.8V, the CO amount is so tiny that it is under the GC detection limit. The CO production also increases with applied potential. Besides, at potentials higher than 0.8V, H<sub>2</sub> is also detected though there is no H<sub>2</sub> in feed, but its amount is at a negligible level (0.03-0.04 μmol/s), as a result, the CO<sub>2</sub> reduction is still considered as the dominant process taking place on the measured SOEC.

The Faradaic efficiencies with respect to CO<sub>2</sub> reduction and CO production are summarized in Table 6.3, and it is achieved that the efficiency regarding CO<sub>2</sub> splitting increases with applied potential, so does the efficiency concerning CO generation. The quantity of CO<sub>2</sub> dissociation at 1.5V in CO<sub>2</sub>-N<sub>2</sub> 30-70 environment is 1.08 μmol/s (Fig. 6.14(b)), and the corresponding efficiency is 96.4%.

**Table 6. 3** The Faradaic efficiency of CO<sub>2</sub> reduction and CO yield at different voltages in CO<sub>2</sub>-N<sub>2</sub> 30-70 environment from the GDC impregnated LSCM cathode SOEC working at 900°C

Voltage (V)	Faradaic efficiency (%)	
	CO <sub>2</sub>	CO
0 (i.e. OCV)	-	-
0.2	-	-
0.5	43	-
0.8	68	-
1.2	83.5	58.5
1.5	96.4	73.5

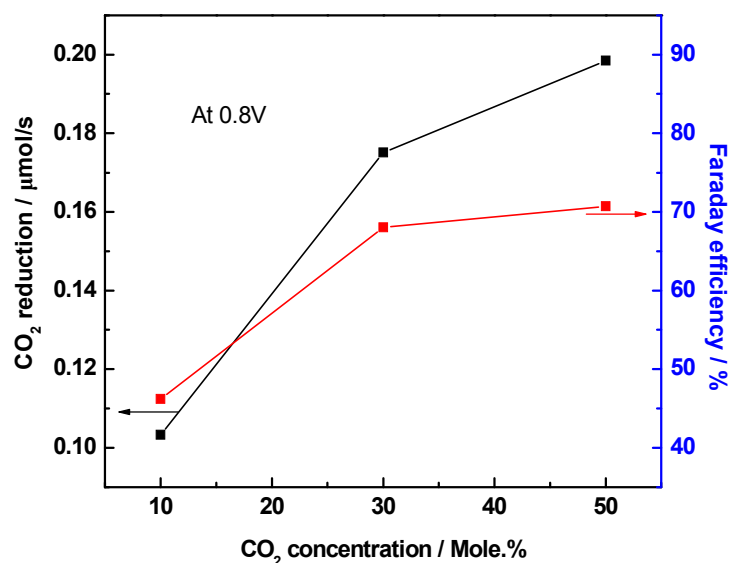


**Fig. 6.15** CO<sub>2</sub> reduction rate and Faradaic efficiency regarding CO<sub>2</sub> splitting in different CO<sub>2</sub>-N<sub>2</sub> feed at 0.8V from the GDC impregnated LSCM cathode SOEC at 900°C

The CO<sub>2</sub> reduction quantity and Faradaic efficiency for CO<sub>2</sub> dissociation at 0.8V (absolute potential -0.928V) as a function of CO<sub>2</sub> concentration is revealed in Fig. 6.15. At the same potential, the CO<sub>2</sub> reduction amount increases with rising CO<sub>2</sub> content in feed, and the Faradaic efficiency over CO<sub>2</sub> dissociation increases with CO<sub>2</sub> concentration accordingly. This is favourable for CO<sub>2</sub> electrolysis, especially in atmospheres without protective gas, in that the CO<sub>2</sub> electrolysis efficiency will be enhanced without sacrificing CO<sub>2</sub> supply.

### 6.3.2 Impact of 5%H<sub>2</sub>/Ar on the SOEC cathode performance and efficiency of CO<sub>2</sub> electrolysis in CO<sub>2</sub>-N<sub>2</sub> feed

The impact of introducing 5%H<sub>2</sub>/Ar on the cathode performance and efficiency for CO<sub>2</sub> electrolysis was investigated in CO<sub>2</sub>-N<sub>2</sub> environment on the Pd-GDC co-impregnated LSCM cathode SOEC, to see at what scale the performance difference in these atmospheres is.

Fig. 6.16 exhibits the performance comparisons from the 1%Pd-GDC co-impregnated LSCM cathode SOEC working at 900°C in CO<sub>2</sub>-N<sub>2</sub> 70-30 (total gas flow rate is

30ml/min) feed with and without 5%H<sub>2</sub>/Ar (at a flow rate of 10ml/min). The performance of this cathode SOEC working in CO<sub>2</sub>-CO 70-30 atmosphere is also shown for comparison. The I-V curves show that the CO<sub>2</sub> electrolysis in CO<sub>2</sub>-N<sub>2</sub> mixture without reducing gas undergoes large resistance around OCV, caused by high activation energy required, as discussed in previous part, and upon introducing 5%H<sub>2</sub>/Ar, the cell resistance reduces significantly. Apparently, the introduction of 5%H<sub>2</sub>/Ar into CO<sub>2</sub>-N<sub>2</sub> fuel gas also greatly promotes the OCV value of the tested SOEC, essentially utilising chemical energy to supplant electrical energy required for reduction. The OCV values are -0.706 and -0.123V in the CO<sub>2</sub>-N<sub>2</sub> fuel with and without 5%H<sub>2</sub>/Ar, respectively. The highest OCV value is achieved from the SOEC operated in CO<sub>2</sub>-CO mixture in Fig. 6.16 (a), indicating that the cell resistance is the smallest when working in this feed. However, when potential is raised gradually, the cell resistance in CO<sub>2</sub>-N<sub>2</sub> 70-30 gets close to that in the feed with 5%H<sub>2</sub>/Ar, so that the performance improvement from 5%H<sub>2</sub>/Ar on CO<sub>2</sub> electrolysis in CO<sub>2</sub>-N<sub>2</sub> mixture is only significant at potentials around OCV value.

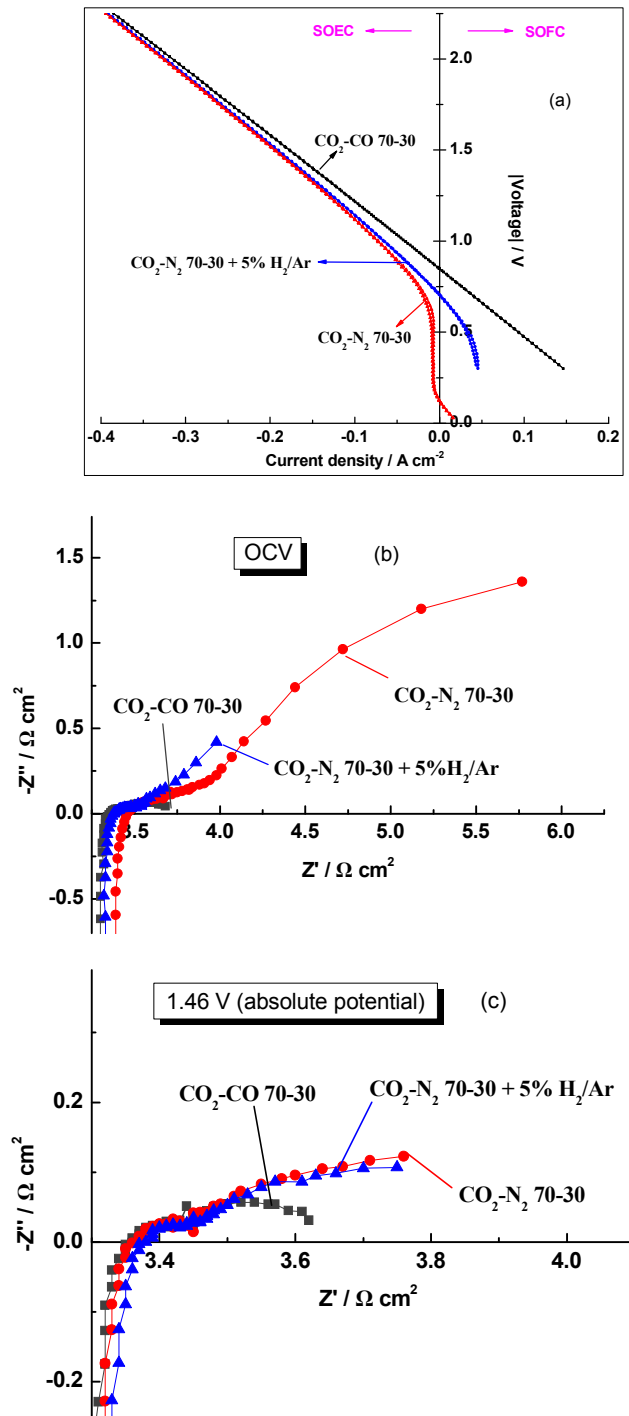


**Fig. 6.16** Performance of the 1%Pd-GDC co-impregnated LSCM cathode SOEC working in CO<sub>2</sub>-CO 70-30 feed and in CO<sub>2</sub>-N<sub>2</sub> 70-30 mixture with and without 5% H<sub>2</sub>/Ar (a) I-V curves; (b) and (c) impedance data

The results that have been observed from the I-V curves in Fig. 6.16(a) are confirmed by the impedance responses at OCV and at -1.46V (absolute voltage) in CO<sub>2</sub>-N<sub>2</sub> mixture with and without 5%H<sub>2</sub>/Ar as well as in CO<sub>2</sub>-CO 70-30 environment, as displayed in Fig. 6.16 (b) and (c). At OCV, the impedance for the tested cathode in CO<sub>2</sub>-N<sub>2</sub> 70-30 feed is remarkably reduced by the introduction of 5%H<sub>2</sub>/Ar and/or by the replacement of N<sub>2</sub> with CO, especially the impedance associated with the low frequency responses, which are probably related to the surface adsorption/desorption equilibration and surface diffusion of intermediate species to TPBs [11]. Whereas at -1.46V, the resistance values are close for the cathode working in CO<sub>2</sub>-N<sub>2</sub> mixture with and without 5%H<sub>2</sub>/Ar, suggesting that the effect from H<sub>2</sub> on the CO<sub>2</sub> reduction reaction is insignificant due to the low fraction of H<sub>2</sub> (around 1.25%) in the feed gas. Noticeably, the cathode R<sub>p</sub> in CO<sub>2</sub>-N<sub>2</sub> 70-30 is dramatically larger than that in CO<sub>2</sub>-CO 70-30 gas at OCV, but the contrast becomes mild when potential rises. At -1.46V, the R<sub>p</sub> for cathode working in CO<sub>2</sub>-N<sub>2</sub> fuel is ca. 0.4-0.5Ωcm<sup>2</sup>, and the counterpart R<sub>p</sub> in CO<sub>2</sub>-CO mixture is ca. 0.3 Ωcm<sup>2</sup>.

**Table 6. 4** The CO<sub>2</sub> electrolysis performance from the Pd-GDC co-impregnated LSCM cathode SOEC (denoted by the amount of Pd in corresponding cathode in the table) operated at 900°C with different feeds

(a) CO<sub>2</sub>-N<sub>2</sub> 70-30 mixture

	R <sub>p</sub> (Ωcm <sup>2</sup> )		Gas evolution at -1.46V (μmol/s)		
	At OCV	At 1.46V	CO <sub>2</sub> reduction	CO yield	Theoretical value
0.5%Pd	1.48	0.36	0.35	0.60	0.97
1% Pd	2.32	0.40	0.86	0.63	0.95

(b) CO<sub>2</sub>-N<sub>2</sub> 70-30 mixture with 5%H<sub>2</sub>/Ar

	R <sub>p</sub> (Ωcm <sup>2</sup> )		Gas evolution at -1.46V (μmol/s)		
	At OCV	At 1.46V	CO <sub>2</sub> reduction	CO yield	Theoretical value
0.5%Pd	0.50	0.34	1.21	0.82	0.96
1% Pd	0.60	0.38	1.32	0.94	0.94

The CO<sub>2</sub> electrolysis performance in the atmosphere without protective gas was also measured on the SOEC comprised of a 0.5 wt% Pd and GDC co-impregnated LSCM cathode, which was found to be comparable with the state-of-the-art Ni/YSZ cermet with regard to performance for CO<sub>2</sub> electrolysis in CO<sub>2</sub>-CO surroundings. The results from the 0.5% Pd-GDC co-impregnated LSCM cathode SOEC working in CO<sub>2</sub>-N<sub>2</sub> 70-30 mixture (with and without adding 5%H<sub>2</sub>/Ar) at 900°C are summarized in Table 6.4, with comparison to those from the 1% Pd-GDC co-impregnated LSCM cathode SOEC (also shown in Fig. 6.16) operated in identical conditions. With aid of 0.5wt% Pd extra catalyst, the GDC impregnated LSCM cathode exhibits higher performance both in the CO<sub>2</sub>-N<sub>2</sub> feed with and without introducing 5%H<sub>2</sub>/Ar, demonstrating its promise in the application of CO<sub>2</sub> electrolysis via SOEC. Moreover, one can see from Table 6.4 (a) and (b) that, both the CO<sub>2</sub> reduction level and CO production increase upon introducing 5%H<sub>2</sub>/Ar (containing 1.25% H<sub>2</sub>) into the CO<sub>2</sub>-N<sub>2</sub> feed, which suggests that the gas shift/reverse gas shift reaction occurs besides the CO<sub>2</sub> dissociation. However, how the gas shift/reverse gas shift affect the equilibration of CO<sub>2</sub> dissociation reaction is hard to assess in the current measurements.

#### 6.4 Summary

Electrical efficiency, i.e. Faradaic efficiency regarding CO production and CO<sub>2</sub> reduction were evaluated on the LSCM/GDC composite cathode fabricated with different procedures, and effect from fuel composition, applied potential, and operation temperature on Faradaic efficiency were studied. Generally speaking, the CO production quantity increased with increasing CO concentration in feed and with rising potential and temperature, and was close to the Faraday yield in most cases.

Introducing 5%H<sub>2</sub>/Ar into CO<sub>2</sub>-CO mixture caused CO production amount to increase and CO<sub>2</sub> reduction level first decreased then increased, with increasing applied potential. The difference in CO<sub>2</sub> electrolysis performance for the GDC impregnated LSCM cathode SOEC in feed with and without 5%H<sub>2</sub>/Ar implied the participation of gas shift/reverse gas shift reaction into the CO<sub>2</sub> electrochemical reduction process.

CO<sub>2</sub> electrolysis in CO<sub>2</sub>-N<sub>2</sub> mixture feed were researched on the GDC impregnated LSCM cathode SOEC (with small doping of Pd catalyst in cathode in some cases). In

the feed without protective CO, the GDC impregnated LSCM cathode SOEC displayed very low OCV value and large resistance at potentials close to OCV, due to the high activation overpotential it suffered. However, the cell resistance in CO<sub>2</sub>-N<sub>2</sub> mixture was close to that in CO<sub>2</sub>-CO mixture at applied potential of -1.46V (absolute value). CO was produced at potentials higher than 0.8V (referred to OCV value), and CO yield increased with increasing potential. The 0.5%Pd and GDC co-impregnated LSCM cathode showed R<sub>p</sub> of ca. 0.3-0.4 Ωcm<sup>2</sup> in CO<sub>2</sub>-N<sub>2</sub> 70-30 mixture at 900°C, indicating its promise in the application of CO<sub>2</sub> electrolysis by high temperature SOEC.

### References

1. S. H. Jensen, P. H. Larsen, M. Mogensen, *Int. J. Hydrogen Energy*, **32**, 3253 (2007)
2. T. Yamamoto, D. A. Tryk, A. Fujishima, H. Ohata, *Electrochem. Acta*, **47**, 3327 (2007)
3. O. A. Marina, L. R. Pederson, M. C. Williams, G. W. Coffey, K. D. Meinhardt, C. D. Nguyen, and E. C. Ehomsen, *J. Electrochem. Soc.*, **154** (5), B452 (2007)
4. T. Ishihara and T. Kanno, *ISI J International*, **50** (9), 1291 (2010)
5. X. Yang, PhD thesis, Cathode development for solid oxide electrolysis cells for high temperature hydrogen production, pp.120
6. S. Tao, J. T. S. Irvine, and S. M. Plint, *J. Phys. Chem. B*, **110**, 21771 (2006)
7. R. D. Green, C. Liu, S. B. Adler, *Solid State Ionics*, **179**, 647 (2008)
8. X. Yue and J. T. S. Irvine, *J. Electrochem. Soc.*, **159** (8), F442 (2012)
9. C. Stoots, J. O'Brien, J. Hartvigsen, *Proceedings of International Mechanical Engineering Congress and Exposition (IMECE)*, Seattle, Washington, USA (2007)
10. S. M. Plint, PhD thesis, Compositional design and fabrication of a perovskite anode for the intergrated planar solid oxide fuel cell, pp. 132
11. K. T. Jacob, A. Kumar, G. Rajitha and Y. Waseda, *High Temp. Mater. Proc.*, **30**, 459 (2011)
12. X. Yue and J. T. S. Irvine, *Electrochem. Solid-State Lett.*, **15** (3), B31 (2012)

## **Chapter 7: High temperature steam electrolysis and steam-carbon dioxide co-electrolysis**

### **Table of Contents**

Introduction .....	204
7.1 Steam delivery and single cell characterization.....	205
7.2 Steam electrolysis on LSCM/GDC cathode SOEC.....	207
7.2.1 Steam electrolysis on screen-printed LSCM/GDC cathode SOEC .....	207
7.2.2 Steam electrolysis on the GDC impregnated LSCM cathode SOEC .....	213
7.2.3 Comparisons between high temperature steam electrolysis and CO <sub>2</sub> electrolysis .....	218
7.3 Steam and CO <sub>2</sub> co-electrolysis on LSCM/GDC cathode cell .....	219
7.3.1 Co-electrolysis study on screen-printed LSCM/GDC cathode SOEC.....	219
7.3.2 Co-electrolysis study on the GDC impregnated LSCM cathode SOEC.....	223
7.3.3 Co-electrolysis in different ratio of H <sub>2</sub> O-H <sub>2</sub> -CO <sub>2</sub> -CO mixture .....	226
7.3.4 Co-electrolysis stability test in H <sub>2</sub> O-H <sub>2</sub> -CO <sub>2</sub> -CO mixtures.....	228
7.4 Conclusions .....	230
References .....	231

## Chapter 7: High temperature steam electrolysis and steam-carbon dioxide co-electrolysis

### Introduction

Hydrogen production from water electrolysis through SOEC has been receiving increasing interest world wide due to the great potential of H<sub>2</sub> economy, which will solve the problems posed by the current energy system based on fossil fuel combustion, such as, global warming, price, and depletion [1-3]. SOEC enables a superior means for hydrogen generation over ordinary alkaline electrolysis, in that it is all solid state device hence has a long lifetime by avoiding liquid electrolyte corrosion and evaporation issues subjected to alkaline electrolysis, and that it could utilize the intermittent renewable sources as energy input so that realize a high overall efficiency [4-5]. Moreover, as SOEC usually works in the temperature range of 700-1000°C, it favours the thermodynamics and electrochemical kinetic conditions for electrode reaction, and high quality heat from nuclear reactor can be utilized. Though promising, steam electrolysis via SOEC requires extensive efforts for R&D, regarding materials selections and system engineering.

Considering applying H<sub>2</sub> from steam electrolysis and CO from CO<sub>2</sub> electrolysis to synthetic fuel production, steam and carbon dioxide co-electrolysis offers a way to generate CO and H<sub>2</sub> (so-called syngas) at one goal [6]. In the co-electrolysis operation, not only the steam and CO<sub>2</sub> dissociation reaction, but also the gas shift/reverse gas shift reaction will take place, and it is believed that the latter (specifically the reverse gas shift reaction), which is a kinetically fast, equilibrium reaction at high temperatures, contributes to the most portion of CO production [7-8]. Apparently, co-electrolysis can be conducted on the identical system as steam/CO<sub>2</sub> electrolysis, but is a more complicated process because of the multiple reactions involved.

In previous chapters, LSCM/GDC cathode material set has been applied to CO<sub>2</sub> electrolysis by SOECs, and performed comparably with Ni/YSZ cermet when fabricated by impregnating nanosized GDC into porous LSCM backbone and by the aid of 0.5wt% extra Pd catalyst. This material has also been applied to steam electrolysis with low steam concentration (3%). Briefly, sigmoidal I-V curves were found on this and other

cathode materials studied in Chapter 4, which is in contrast with fairly linear I-V curves from CO<sub>2</sub> electrolysis on the same SOEC, leaving its answer to be figured out. In this chapter, steam electrolysis behaviour will be investigated in different level of steam supply. Performance from different cathodes in the application of steam electrolysis will be evaluated, and comparison between steam electrolysis and CO<sub>2</sub> electrolysis will be employed on the same cathode. Besides, co-electrolysis will be performed on LSCM/GDC cathodes prepared in different approaches and in diverse fuel compositions. Finally, a lifetime test will be carried out on the Pd-GDC co-impregnated LSCM cathode SOEC to assess the material viability for co-electrolysis.

### 7.1 Steam delivery and single cell characterization

Single cells with different cathode were prepared as described in Chapter 5. Basically, 2mm YSZ pellets were pressed and fired, with LSM/ScSZ screen-printed on one side of YSZ pellet as anode and different cathode material prepared on the other side of YSZ pellet. Three-electrode geometry was employed likewise.

The as-prepared single cell was mounted on the test apparatus, and was sealed to the cathode chamber using ceramic cement (Aremco 552), prior to being heated up to operating temperature. At 900°C, steam carried by 5% H<sub>2</sub>/Ar gas at a flow rate ranging from 10 to 30 ml/min was introduced to the cathode. The required amount of steam was generated by heating a saturator (BekkTech, BT-512) at a certain temperature, as shown in Table 7.1. With respect to the anode, air was flushed through at a constant flow rate (100 ml/min) during the whole test. After testing for steam electrolysis, fuel gas was switched to CO<sub>2</sub>-CO mixture (total flow rate was 30 ml/min) for carbon dioxide electrolysis. For steam-carbon dioxide co-electrolysis measurements, steam carried by 5%H<sub>2</sub>/Ar and CO<sub>2</sub>-CO mixture gas at a total flow rate of 30ml/min were co-fed into the cathode chamber. In some cases for co-electrolysis study, steam was carried by CO<sub>2</sub>-CO mixture gas, and in such circumstances, the dissolution of CO<sub>2</sub> into water, which decreases with increasing temperature, was neglected in that the amount of dissolved CO<sub>2</sub> is small [9].

**Table 7.1** List of saturator temperature and corresponding steam concentration

Saturator temperature /°C	Nominal steam concentration [10] / %
24	3.0
33	5.0
46	10.1
60	19.9
69	29.9
76	40.2
82	51.3
90	70.1

Electrochemical characterization was conducted similarly as in previous chapters. Polarization curves of different cathode SOEC were measured, starting from open circuit voltage (OCV) to electrolysis mode, then to fuel cell mode and finally back to OCV to finish a scanning cycle. The electrochemical impedance spectroscopy (EIS) was recorded using a ZAHNER IM6 Electrochemical Workstation. Impedance spectra, with AC voltage amplitude of 10 mV and frequency ranging from  $10^5$  Hz to 0.1 or 0.015 Hz, were recorded under OCV, as well as under a certain external loading. The applied voltages were 0.2V, 0.5V, 0.8V, and 1.0V etc., referring to OCV value (herein after, stated otherwise), respectively, meaning that if the OCV was -0.9V, the operating voltage would be -1.1V (absolute potential) when 0.2V was applied to the cell.

The GC peak analysis was performed to examine the cathode outlet gas composition, in order to evaluate the steam/CO<sub>2</sub> and/or co-electrolysis efficiency. For these measurements, the cathode outlet gas was flowed through a paraffin bubbler first to get rid of steam and then connected to a micro-GC with an injection port. Four samples were taken under each condition and the result from the last one was used for analysis. At a certain loads, the variation in concentration from that at OCV was obtained from GC analysis, using this value and the flow rate, the practical steam/CO<sub>2</sub> split quantity was calculated. The theoretical value according to Faraday's law was used to calculate the faradaic efficiency.

## 7.2 Steam electrolysis on LSCM/GDC cathode SOEC

### 7.2.1 Steam electrolysis on screen-printed LSCM/GDC cathode SOEC

Fig. 7.1 shows the polarization (I-V) curves of the screen-printed LSCM/GDC cathode SOEC working at 900°C under atmosphere containing steam ranging from 3% to 20% with 5% H<sub>2</sub>/Ar (20 ml/min) as carrier gas. The voltage variations against current density were recorded both in electrolysis manner (negative current) and fuel cell manner (positive current). The I-V curves tend to have sigmoidal shape and there are abrupt increases in the slope of the polarization curves in electrolysis operation in all the atmospheres studied here. The sigmoidal I-V curve was reported before in 3% steam-containing atmosphere, and the increase in the gradient of polarization curve, namely, the enlargement in cell resistance was thought to be related to the possible decomposition of LSCM phase at high potentials, which may not be a sound explanation [11]. In Fig. 7.1, the onset voltage of the above slope-increasing phenomenon increases with steam concentration, and the potential range in which very steep slope shows up becomes smaller. The onset potentials are -1.20V, -1.44V, -1.62V, and -2.12V (absolute potentials) for nominal 3%, 5%, 10%, and 20% steam-containing atmosphere, respectively. Consequently, the increase in cell resistance on I-V curves can be ascribed to difficulty in gas diffusion resulting from inadequate steam supply. Yet, at the onset voltage mentioned above, according to Faraday's law, the required steam at corresponding current is 1.11%, 2.57%, 3.79%, and 6.1% , respectively, which are significantly less than the steam supplied in feed. Thus, it might be that not only insufficient steam supply but also restricted diffusion are the reasons that cause the non-linear I-V curves.

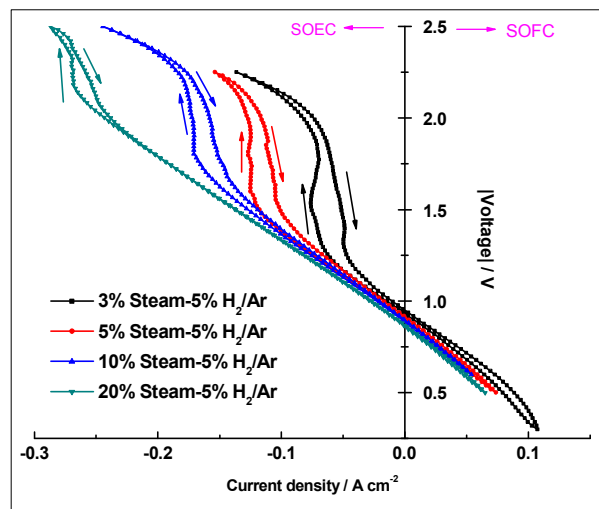


**Fig. 7.1** Polarization curves from the screen-printed LSCM/GDC cathode SOEC running at 900°C being exposed to atmospheres with different steam content (flow rate 20ml/min)

**Table 7.2** Theoretical and experimental OCV values of the screen-printed LSCM/GDC cathode SOEC working in various H<sub>2</sub>O-5%H<sub>2</sub>/Ar atmospheres at 900°C

	Nominal steam amount in 5% H <sub>2</sub> /Ar			
	3%	5%	10%	20%
OCV(th) / V	-0.935	-0.908	-0.872	-0.834
OCV(ex) / V	-0.938	-0.908	-0.887	-0.864

The OCV(th) and OCV (ex) stand for the theoretical OCV predicted by Nernst equation and experimental OCV value, respectively.

The OCV values from I-V curves in Fig. 7.1 are summarized in Table 7.2. The theoretical OCV values predicted by Nernst potential are compared with the experimental ones. At lower steam content, e.g. 3% and 5%, the practical OCV values agree very well with the theoretical ones, implying the cell was well sealed. However, when it goes to higher steam amounts, the practical OCV values are higher than the theoretical ones, indicating lower steam supplied than expected. As steam was

generated by evaporating water at a certain saturator temperature, and the more steam required, the higher temperature the saturator worked at, it is doubted that the saturator being used was not efficient enough to get the nominal steam content, as in the cases of 10% and 20% in Table 7.2. And if this was the case, the actual steam concentrations were 7.66%, 12.3% other than the nominal 10% and 20%, according to the back calculation of Nernst equation with the practical OCV values at higher steam content.

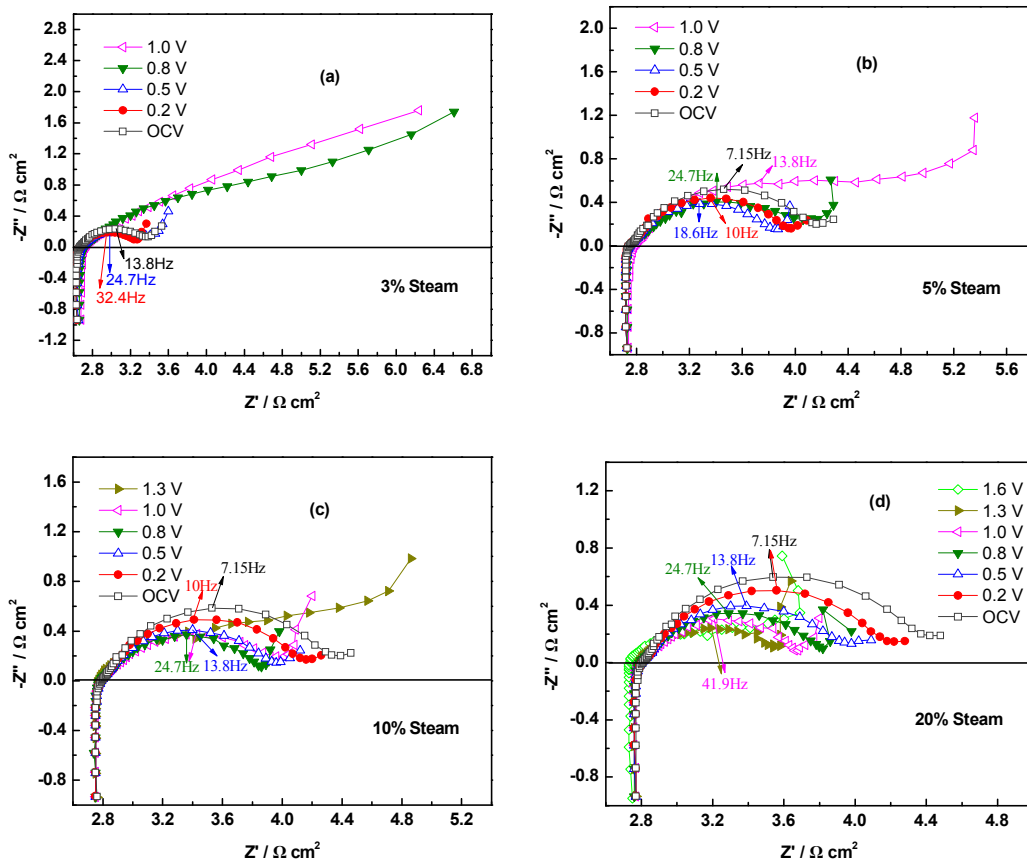


**Fig. 7.2** Complex impedance spectra of the screen-printed LSCM/GDC cathode for steam electrolysis at nominal steam concentration of (a) 3% (b) 5% (c) 10% and (d) 20% at different potentials at 900°C (summit frequencies were labelled in impedance spectra)

Fig. 7.2 displays the complex impedance spectra of LSCM/GDC cathode working at SOEC mode at different potentials and atmospheres with different level of steam. With the variation of potential and steam concentration, the ohmic resistance  $R_s$ , mainly from the thick YSZ electrolyte, changes only slightly. However, the polarization resistance

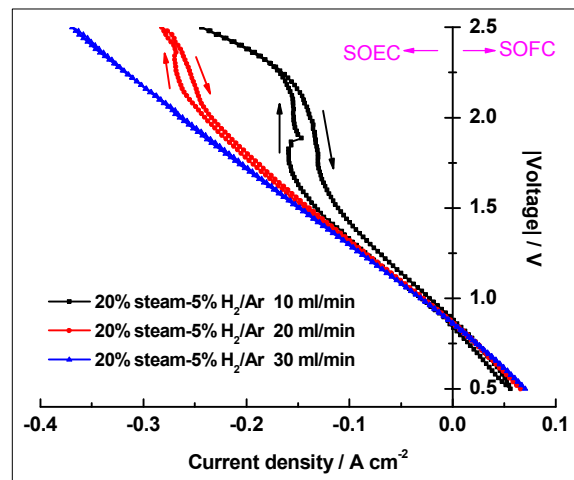
$R_p$  is strongly correlated with working potential and steam content. In Fig. 7.2 (a-d),  $R_p$  decreases with applied potential but increases markedly when applied voltage is higher than a certain value, which is 0.5V in 3% steam-containing atmosphere. The dramatic increase in  $R_p$  happens only at voltage higher than 0.8 V, 1.0V, and 1.3V for the atmosphere containing 5%, 10% and 20% steam, respectively. These observations are in accordance with what the I-V curves demonstrated in Fig. 7.1.

In Fig. 7.2 (a-d), a small high frequency arc and a very large arc at low frequency region are present in the impedance spectra, similar to the impedance behaviour reported on Ni-Fe bimetallic catalyst in steam/N<sub>2</sub> fuel for steam electrolysis [12]. The large low frequency arc is indicative of a dominant process such as, the gas diffusion or the surface diffusion of adsorbed or intermediate species from steam dissociation to three phase boundary (TPB), is taking place on the screen-printed LSCM/GDC cathode. As discussed previously, the steam required (according to Faraday's law) at the onset voltage of non-linear I-V curves is less than the steam amount in the feed, as a result, gas diffusion could be ruled out, with the surface diffusion of absorbed or activated species to catalytically active sites remains the rate limiting step for steam splitting reaction.

In Fig. 7.2 (a-d), the low frequency arc increases distinctively with applied potential when the working voltages fall in the range where sharp increases in the gradient of I-V curve appear in Fig. 7.1. On the other hand, the low frequency arcs at 1.0V, where abrupt increases in cell resistance all showed up on I-V curves in 3-20% steam containing fuel, declines with increasing steam concentration. This again reflects that the non-linear I-V curves are more related to the insufficient steam supply and limited surface diffusion, rather LSCM reduction. And our previous stability test of LSCM/GDC cathode in CO<sub>2</sub>/CO 70/30 atmosphere at 900°C showed that this material was quite stable in high temperature reducing atmosphere [13].

In the above experiment, the cathode gas was kept at a flow rate of 20 ml/min. The effect of flow rate on steam electrolysis performance from the screen-printed LSCM/GDC cathode SOEC was also investigated, as illustrated in Fig. 7.3, with steam concentration fixed at 20%. It can be seen that at gas flow rate lower than 30 ml/min, a large diffusion resistance from inadequate steam supply become the limiting factor at

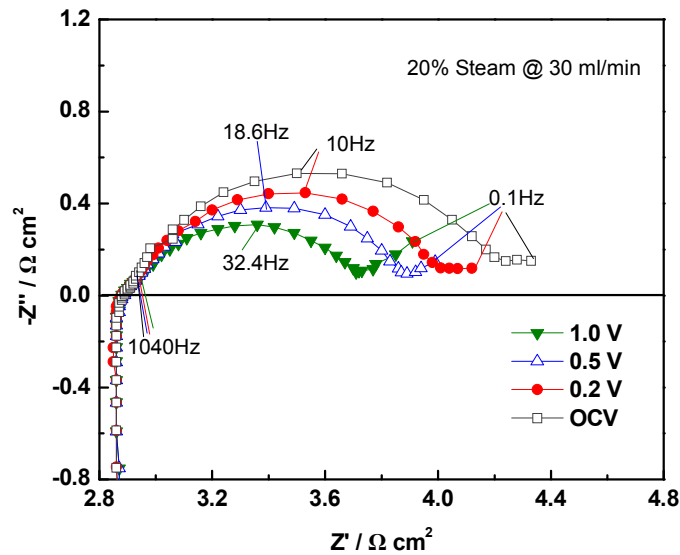
higher voltages, similar to the phenomenon in Fig. 7.1, therefore, the I-V curves at gas flow rate of 10 and 20 ml/min show non-linear responses, and the I-V curve at flow rate of 30 ml/min is fairly linear, showing little evidence from diffusion limitation. These results again reveal the distinct increase in cell resistance for steam electrolysis and this is not related to the reduction of LSCM perovskite phase. The above results from I-V curves are supported by impedance spectra (not shown here) of the screen-printed LSCM/GDC cathode at different feed gas flow rate.



**Fig. 7.3** Effect of flow rate on the performance of the screen-printed LSCM/GDC cathode SOEC operated in 20% steam-5% H<sub>2</sub>/Ar environment at 900°C

From Fig. 7.1 and Fig. 7.3, it can be detected that the cell resistance drops when the applied voltage exceeds -2.25V (absolute potential) at flow rate lower than 30 ml/min, possibly due to the resulting electronic conductivity of YSZ electrolyte in the case of steam starvation. Schefold et al. found that electronic conduction of YSZ was typically induced when the steam supply was interrupted, and when this happened, cell voltage would rise to a saturated value to prevent voltage from reaching the YSZ decomposition potential [14]. With regard to high temperature steam electrolysis, electronic conduction in YSZ is believed quite relevant when steam transport becomes limiting. Besides, with the progress of steam dissociation, the P<sub>O<sub>2</sub></sub> at cathode chamber will decrease, which is favourable for YSZ reduction, hence varying the electrochemical and physical properties of cathode/electrolyte interface. As shown in Fig. 7.1 and Fig. 7.3, cell

voltage rises quickly and then seems to level off in inadequate steam feed. An alternative explanation is that the factors limiting steam availability at the electrode/electrolyte interface are overcome at these higher potentials with facilitation of surface diffusion of species to active sites. This is consistent with indication that the electrochemical responses tend towards coalescence at higher potentials. Surface reduction of YSZ or the other oxides present may well facilitate such processes. In practical SOEC operation, applied potential should remain reasonably low and sufficient steam should be provided meanwhile to avoid electronic conduction in YSZ for long term durability.



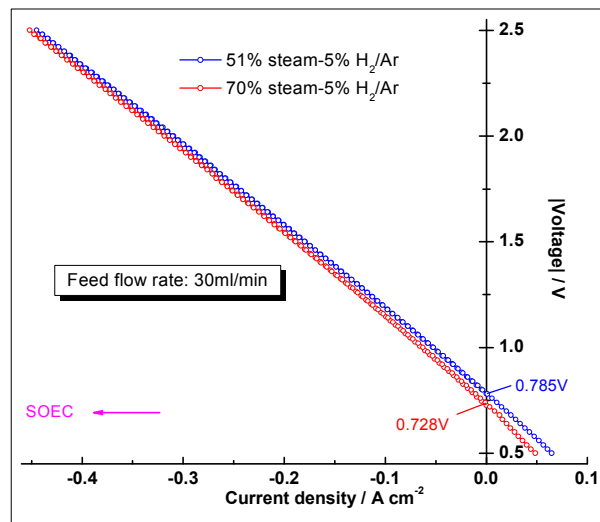
**Fig. 7.4** Impedance spectra of the screen-printed LSCM/GDC cathode working at different potential in 20% steam-5% H<sub>2</sub>/Ar atmosphere at flow rate of 30ml/min (OCV value is -0.863V)

Fig. 7.4 displays the complex impedance spectra of the screen-printed LSCM/GDC cathode operating at different potentials in 20% steam-5%H<sub>2</sub>/Ar surroundings at 900°C. The impedance spectra of this cathode present a large low frequency arc, which reduces in magnitude accordingly with increasing voltage, and a small tail at very low frequency. At feed flow rate of 30ml/min, one can see that R<sub>s</sub> stays constant, whereas R<sub>p</sub> decreases monotonously at more negative working potential. The R<sub>p</sub> value reaches 1.6 Ωcm<sup>2</sup> at OCV from the screen-printed LSCM/GDC cathode working in 20% steam-5%H<sub>2</sub>/Ar

mixture at 900°C, and it reduces to around 1.1  $\Omega\text{cm}^2$  when applied voltage increases to 1.0V (absolute potential is around -1.86V). These values are quite large compared to those reported in **Reference [15]**, implying space for cathode performance improvement for the application in high temperature steam electrolysis.

### 7.2.2 Steam electrolysis on the GDC impregnated LSCM cathode SOEC

Fig. 7.5 shows the I-V curves of the GDC impregnated LSCM cathode SOEC working with ca. 51% and 70% steam carried by 5% $\text{H}_2/\text{Ar}$  gas at 900°C. It can be learned that the cell resistance decreases with working potential, and no signs from gas diffusion limitations at high potentials are observed. The OCV value is -0.785V and -0.728V for the feed containing 51% and 70% steam, respectively. These values are a little higher than the theoretical OCV values, -0.756V and -0.715V for nominal 51% and 70% steam containing fuels respectively, predicted by Nernst equation, suggesting that the actual steam content is 37.0% and 64.5% respectively according to discussions in previous section.



**Fig. 7.5** I-V curves from the GDC impregnated LSCM cathode SOEC working at ca. 51% and 70% steam-containing atmospheres at 900°C

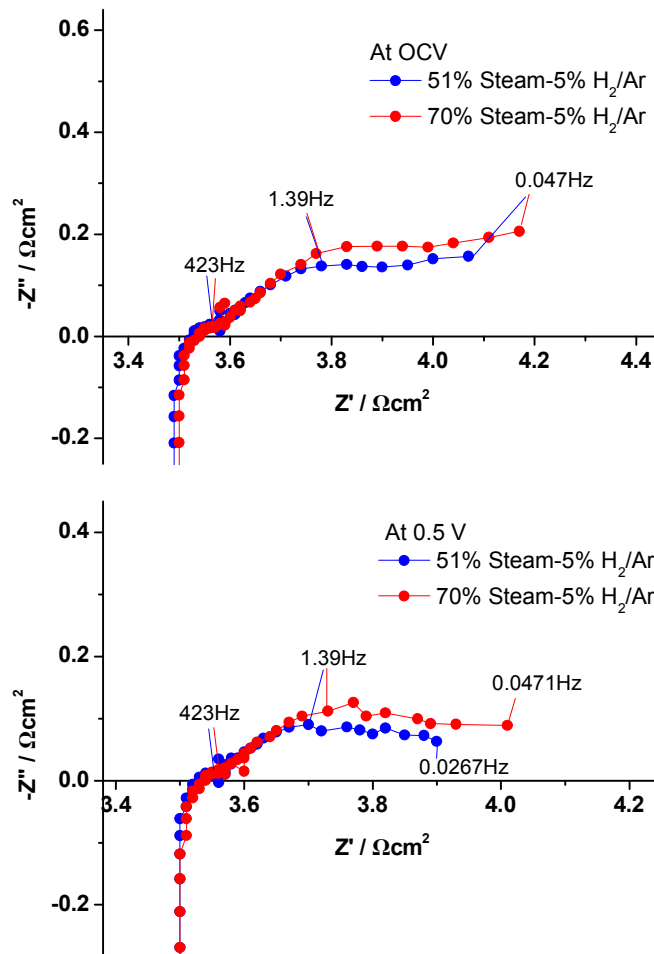


**Fig. 7.6** Impedance results from the GDC impregnated LSCM cathode used for steam electrolysis in 51% and 70% steam containing fuels working at OCV and 0.5V at 900°C

The impedance data of the GDC impregnated LSCM cathode for steam electrolysis in 51% and 70% steam containing surroundings at 900°C are presented in Fig. 7.6. A small impedance arc at high frequency range ( $10^2$ - $10^3$ Hz) and a large one at low frequency regime ( $10^{-2}$ - $10^2$ Hz) can be seen from the impedance spectra for steam electrolysis on the GDC impregnated LSCM SOEC cathode when higher amount of steam is provided. Similar responses were found from the impedance spectra of steam electrolysis on screen-printed LSCM/GDC cathode and CO<sub>2</sub> electrolysis in different cathode (Chapter 4-5), which indicates that charge transfer processes are less profound on the rate-limiting steps in SOEC operation. This has also been reported in **Reference [16]** in which the charge transfer coefficient in SOEC were smaller than those in SOFC

direction on Ni/YSZ fuel electrode. The impedance in 70% steam containing fuel is larger than that in 51% steam feed, similar with the observations on CO<sub>2</sub> electrolysis, probably caused of the difficulty in high concentration H<sub>2</sub>O/CO<sub>2</sub> diffusion. In Fig. 7.6, the cathode R<sub>p</sub> reduces when working at applied voltage of 0.5V, compared to the R<sub>p</sub> at OCV, which is in agreement with the results from the polarization curves. At OCV, the R<sub>p</sub> is around 0.7 Ωcm<sup>2</sup> from the GDC infiltrated LSCM cathode in 70% steam feed at 900°C, and the R<sub>p</sub> decreases to ca. 0.5 Ωcm<sup>2</sup> upon increasing applied voltage to 0.5V (referred to OCV value). The GC analysis reveals a Faraday efficiency of 100.4% for H<sub>2</sub> production at 0.5V (absolute potential is -1.228V) on the GDC impregnated LSCM cathode SOEC using 70% steam-5%H<sub>2</sub>/Ar as feed gas. These values are quite promising and are believed to arise from the modified cathode microstructure of nanosized GDC dispersed LSCM material (section 5.3.3), in comparison with the screen-printed LSCM/GDC cathode, indicating the potential of the GDC impregnated LSCM cathode material utilization in steam electrolysis.

Steam electrolysis using pure H<sub>2</sub> as carrier gas for steam delivery was studied and compared on the 0.5wt% Pd and GDC co-impregnated LSCM cathode SOEC at 900°C with 51% steam feed. Fig. 7.7 displays the performance comparisons between the SOEC working in 5%H<sub>2</sub>/Ar and pure H<sub>2</sub> carried steam fuel. Basically, the difference between the steam fuels carried by 5%H<sub>2</sub>/Ar and by pure H<sub>2</sub> is that the oxygen partial pressure (P<sub>O<sub>2</sub></sub>) in cathode chamber is higher in steam-5%H<sub>2</sub>/Ar environment than in steam-H<sub>2</sub> surroundings, which causes diverse properties in LSCM/GDC material set towards cathode reaction in these two different conditions. It is expected that in the more reducing H<sub>2</sub>O-H<sub>2</sub> atmosphere, the cathode activity of the LSCM/GDC material, particularly, the GDC component, will be enhanced. As can be seen from the polarization curves in Fig. 7.7, the steam electrolysis performance from the above SOEC working in H<sub>2</sub>-H<sub>2</sub>O environment is higher than that in 5%H<sub>2</sub>/Ar-H<sub>2</sub>O environment, which is presented by higher OCV and smaller cell resistance from the SOEC measured in H<sub>2</sub>-H<sub>2</sub>O fuels. The OCV value is -0.795V in 5%H<sub>2</sub>/Ar-51%H<sub>2</sub>O mixture and -0.943V in H<sub>2</sub>-51%H<sub>2</sub>O mixture.

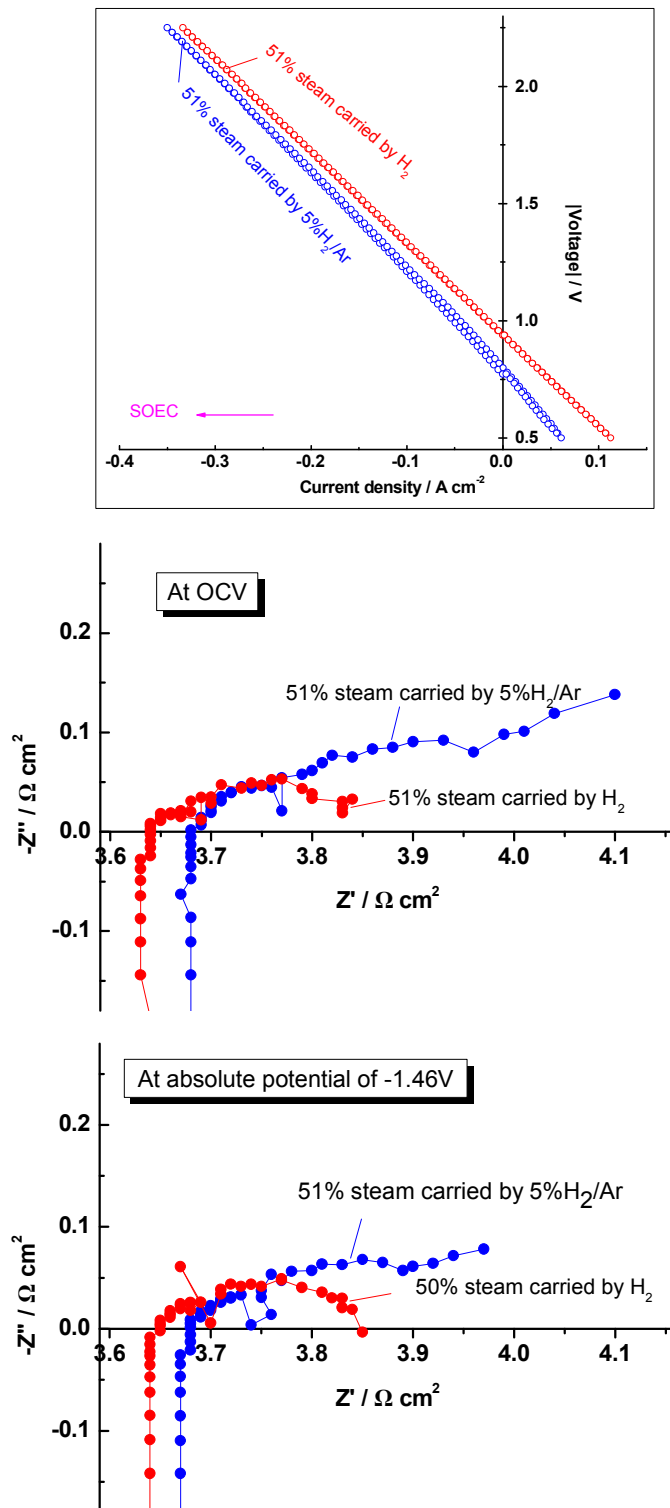


**Fig. 7.7** Performance comparisons for steam electrolysis using different carrier gas (flow rate is 15ml/min) for 51% steam fuel on the 0.5% Pd-GDC co-impregnated LSCM cathode SOEC at 900°C

The impedance data in Fig. 7.7 confirms the result from polarization curves. That is, using H<sub>2</sub> as replacement of 5%H<sub>2</sub>/Ar as steam carrier gas, the cathode performance from the 0.5%Pd-GDC co-infiltrated LSCM material is markedly enhanced, with respect to steam splitting process. From the impedance spectra, it can be observed that both R<sub>s</sub> and R<sub>p</sub> from the 0.5%Pd-GDC co-impregnated cathode decline in 51%H<sub>2</sub>O-H<sub>2</sub> atmosphere, compared to the values in 51%H<sub>2</sub>O-5%H<sub>2</sub>/Ar condition, probably ascribed to the enhanced electric conductivity and catalytic properties from GDC component in cathode in more reducing atmosphere. At 900°C, the R<sub>p</sub> is around 0.2 Ωcm<sup>2</sup> at both OCV and -1.46V from the 0.5%Pd-GDC co-impregnated LSCM cathode when operated in 51%H<sub>2</sub>O-H<sub>2</sub> mixture, and the R<sub>p</sub> doubles from the same cathode when operated in 51%H<sub>2</sub>O-5%H<sub>2</sub>/Ar mixture. These values indicate great potential of utilising the 0.5%Pd-GDC co-impregnated LSCM cathode material towards high temperature steam electrolysis.

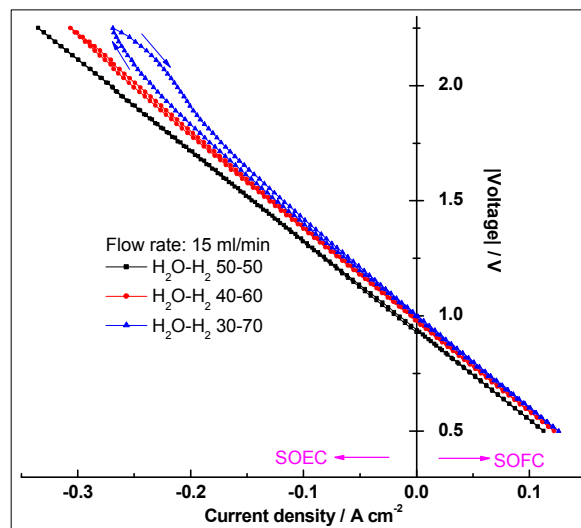


**Fig. 7.8** Steam electrolysis performance from the 0.5wt%Pd-GDC co-impregnated LSCM cathode SOEC working at 900°C in different level of steam feed carried by H<sub>2</sub>

Different level of steam supplied to SOEC cathode was conducted using H<sub>2</sub> as carrier gas for steam delivery. The performance of steam electrolysis in steam content ranges

from 30% to 51% from the 0.5Pd-GDC co-infiltrated LSCM cathode SOEC at 900°C is shown in Fig. 7.8. The OCV value increases with decreasing steam content. Clearly, steam electrolysis performance reduces with decreasing steam concentration, due to insufficient fuel supply and the resulting difficulty in surface diffusion (this is confirmed by the enlarged low frequency arc in lower steam concentration from impedance spectra which are not shown here). This is quite observable from the I-V curves for the SOEC working in 30% steam containing atmosphere, as the cell suffers from gas diffusion limitations at high potentials, which is not significant in 51% steam containing environment.

### **7.2.3 Comparisons between high temperature steam electrolysis and CO<sub>2</sub> electrolysis**

The CO<sub>2</sub> electrolysis performance in CO<sub>2</sub>-CO 50-50 mixture is compared to that of steam electrolysis with 51% steam feed on the 0.5% Pd-GDC co-infiltrated LSCM cathode SOEC working at 900°C, as shown in Fig. 7.9. The R<sub>s</sub> increases evidently upon switching feed gas from CO<sub>2</sub>-CO mixture to steam-H<sub>2</sub> mixture at OCV, the reasons for which might be related to an interaction between LSCM material and steam, and more evidence needs to be provided in future work. The R<sub>p</sub>, nevertheless, decreases in 51% steam-H<sub>2</sub> atmosphere, compared to that in CO<sub>2</sub>-CO mixture. This observation is in agreement with other researchers' reports [16, 17]. Similar trends are observed at applied potential of -1.46V (absolute value). At OCV, the R<sub>p</sub> is 0.32 Ωcm<sup>2</sup> in CO<sub>2</sub>-CO mixture and 0.2 Ωcm<sup>2</sup> in 51% steam-H<sub>2</sub> atmosphere, and the R<sub>p</sub> is 0.42 Ωcm<sup>2</sup>, the highest in 51% steam feed carried by 5%H<sub>2</sub>/Ar.

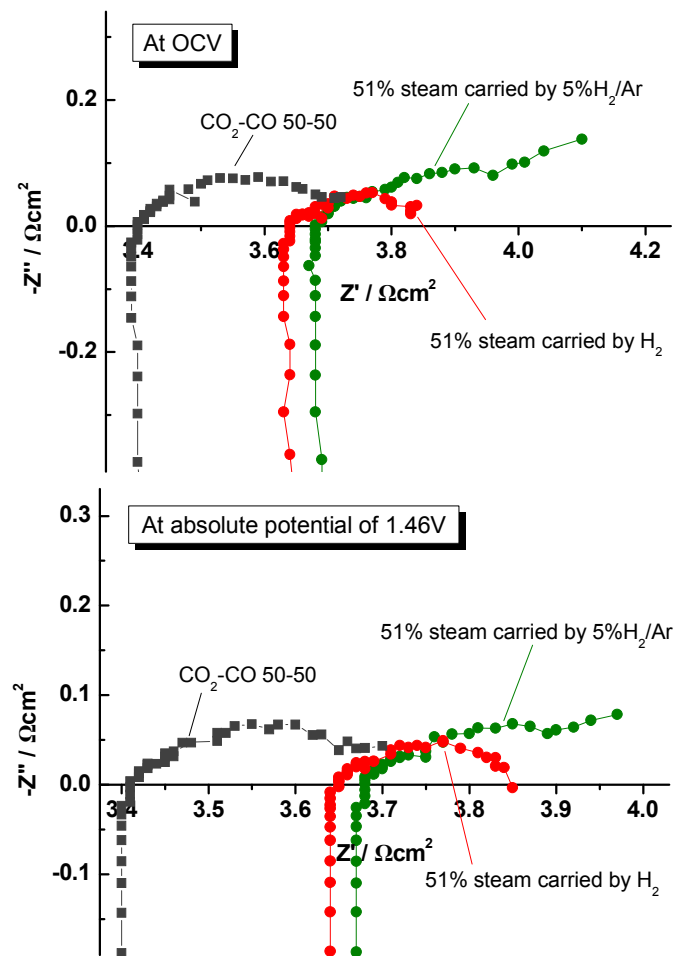


**Fig. 7.9** Comparisons between steam electrolysis and CO<sub>2</sub> electrolysis on the 0.5wt%Pd and GDC co-impregnated LSCM cathode SOEC operated at 900°C

### 7.3 Steam and CO<sub>2</sub> co-electrolysis on LSCM/GDC cathode cell

#### 7.3.1 Co-electrolysis study on screen-printed LSCM/GDC cathode SOEC

Fig. 7.10(a) presents the I-V curve of screen-printed LSCM/GDC cathode SOEC exposed to H<sub>2</sub>O-5% H<sub>2</sub>/Ar-CO<sub>2</sub>-CO (30 ml/min) mixtures at 900°C. The I-V curves of the cell in CO<sub>2</sub>/CO 70/30 mixture (30 ml/min) and H<sub>2</sub>O-5% H<sub>2</sub>/Ar mixture (30 ml/min) are also given in Fig. 7.10(a). It can be observed that the I-V curves of co-electrolysis and CO<sub>2</sub> or steam electrolysis are only separated at high potentials, with that for CO<sub>2</sub> electrolysis exhibiting highest and that of steam electrolysis the lowest current density at the same voltage, which is contrast with reports on other electrodes, that found co-

electrolysis was easier than purely CO<sub>2</sub> electrolysis due to the participation of reverse gas shift reaction along with CO<sub>2</sub> and steam dissociation reaction in co-electrolysis operation [17, 18]. Since here the I-V curve of co-electrolysis was measured with 20% steam-5% H<sub>2</sub>/Ar mixture at a flow rate of 10 ml/min and CO<sub>2</sub>/CO 70/30 mixture at a flow rate of 20 ml/min being co-fed to LSCM/GDC cathode, the insufficiency in steam delivery or the difficulty in steam transport is probably the origin for the difference in I-V curves of co-electrolysis and steam or carbon dioxide electrolysis, as discussed in section 7.2.1, and the steam diffusion resistance was the rate limiting step for steam electrolysis, especially when steam feed flow rate was as low as 10 ml/min.

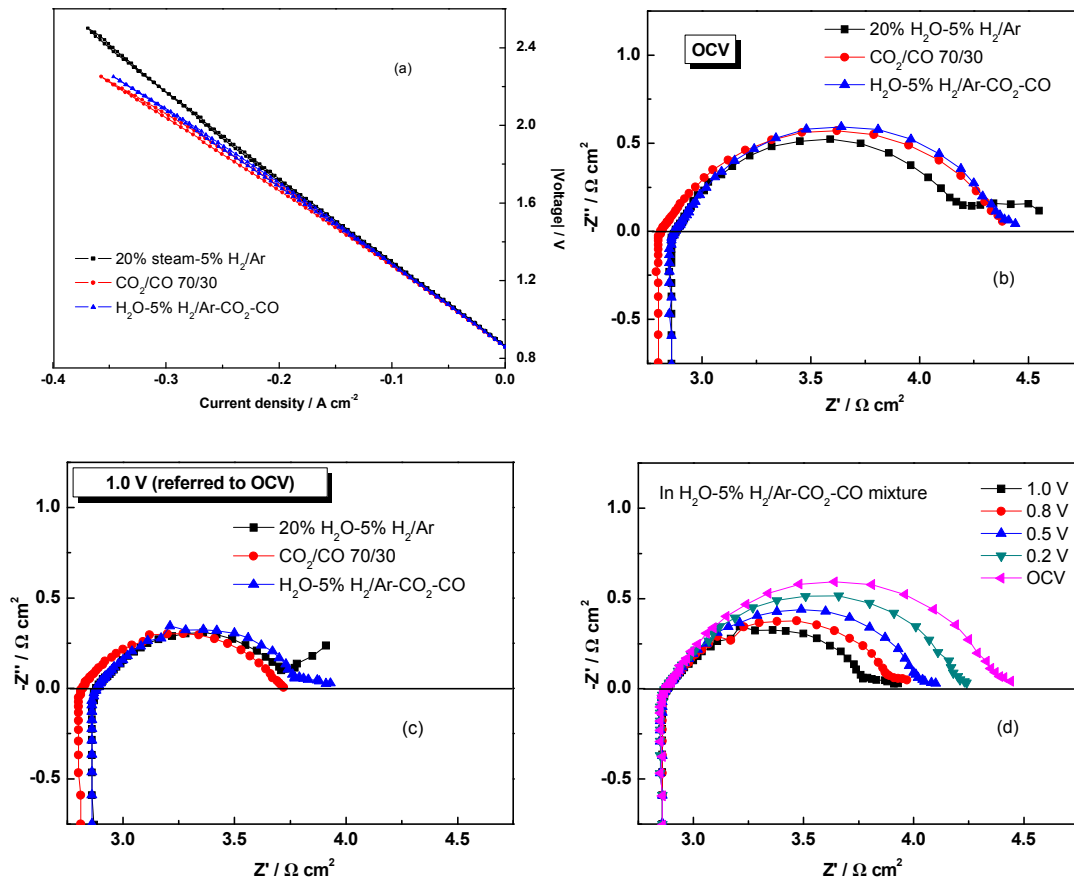


**Fig. 7.10** Performance of screen-printed LSCM/GDC cathode SOEC towards H<sub>2</sub>O-CO<sub>2</sub> co-electrolysis, steam electrolysis and CO<sub>2</sub> electrolysis at 900°C (a) I-V curves; (b) Impedance comparison at OCV; (c) impedance comparison at 1.0V and (d) impedance spectra for co-electrolysis at different potentials

The impedance spectra of LSCM/GDC cathode for H<sub>2</sub>O-CO<sub>2</sub> co-electrolysis, steam electrolysis, and CO<sub>2</sub> electrolysis are compared in Fig. 7.10 (b-c). At OCV, the impedance spectra of co-electrolysis and steam electrolysis are overlapped. However, at applied voltage of 1.0V, clear difference is observed between co-electrolysis, steam electrolysis, and CO<sub>2</sub> electrolysis at low frequency, as a large extra arc appears in low frequency range for steam electrolysis and a small extra arc shows up for co-electrolysis, while no extra arc at low frequency for CO<sub>2</sub> electrolysis. The R<sub>p</sub> for steam electrolysis at applied voltage of 1.0 V is highest, which can be attributed to difficulty in steam transport and which is also the possible reason for a larger R<sub>p</sub> from co-electrolysis compared to that of CO<sub>2</sub> electrolysis. The results from impedance spectra are consistent with what we have obtained from the comparison on the I-V curves of co-electrolysis, steam electrolysis and CO<sub>2</sub> electrolysis in Fig. 7.10(a). With low fraction of steam supplied in the feed for co-electrolysis, the impedance spectra from co-electrolysis at different potentials, as shown in Fig. 7.10(d), are similar to those from CO<sub>2</sub> electrolysis in CO<sub>2</sub>-CO 70-30 mixture (shown in Fig. 4.15), indicating the insignificant role of steam electrolysis and gas shift/reverse gas shift reaction in the process of co-electrolysis at these cathodes.

Fig. 7.11 shows the gas evolution rate at different potentials for CO<sub>2</sub> electrolysis as well as for H<sub>2</sub>O-CO<sub>2</sub> co-electrolysis on screen-printed LSCM/GDC cathode SOEC at 900°C. For CO<sub>2</sub> electrolysis in Fig. 7.11(a), the H<sub>2</sub> detected, possibly from moist in surroundings, does not change with voltage and is negligible, compared with CO production, which increases with potential and is close to theoretical value (shown in Table 7.3). As for co-electrolysis in Fig. 7.11(b), both H<sub>2</sub> and CO production rates increase with applied voltage, and the CO production rates are slightly lower than theoretical values (Table 7.3), probably because some part of current was used for steam splitting though at a very small amount. These observations are reasonable as the reverse gas shift/gas shift reaction seems insignificant when steam supply is inadequate, as discussed previously. Further work will be carried out with higher steam concentration to avoid steam transportation being the limiting step for co-electrolysis process.

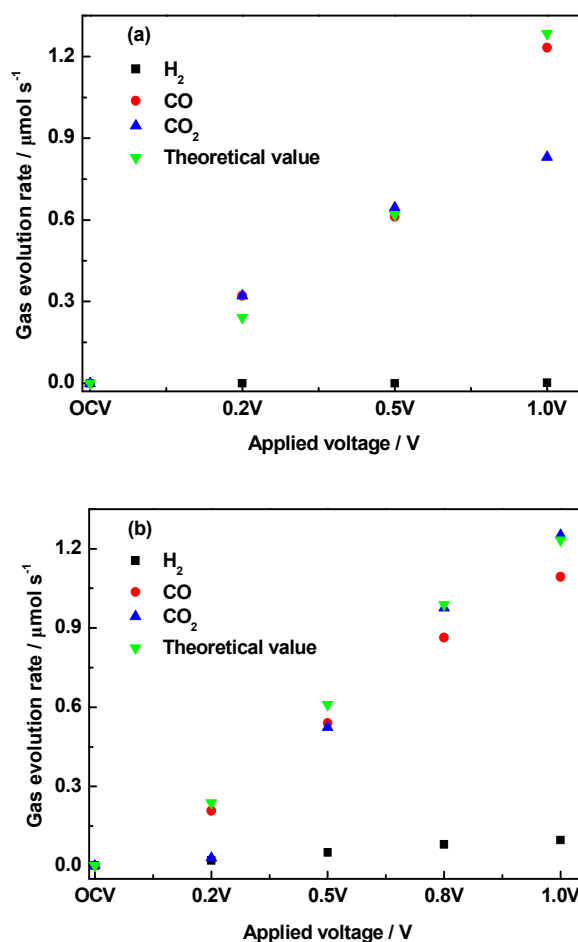


**Fig. 7.11** Gas evolution/utilisation rate vs. applied voltage under (a) CO<sub>2</sub> electrolysis and (b) co-electrolysis at 900°C

**Table 7.3** Faraday efficiency of CO production on screen-printed LSCM/GDC cathode cell working in CO<sub>2</sub>-CO and H<sub>2</sub>O -5% H<sub>2</sub>/Ar-CO<sub>2</sub>-CO atmospheres at 900°C

	Applied voltage (V) <sup>a</sup>		
	0.2	0.5	1.0
<b>CO<sub>2</sub>-CO 70-30</b>			
Faraday efficiency of CO production (%)	133	98.7	96
	Applied voltage (V) <sup>a</sup>		
	0.2	0.5	1.0
<b>H<sub>2</sub>O -5% H<sub>2</sub>/Ar-CO<sub>2</sub>-CO<sup>b</sup></b>			
Faraday efficiency of CO production (%)	87.3	88.6	87.3

---<sup>a</sup> The applied voltage values are referred to OCV (-0.860V);

---<sup>b</sup> The reduction of CO<sub>2</sub> was assumed to be the main reaction as steam supply was inadequate and gas shift /reverse gas shift reaction might not be significant.

### 7.3.2 Co-electrolysis study on the GDC impregnated LSCM cathode SOEC

In this section, steam and carbon dioxide co-electrolysis, conducted on the GDC impregnated LSCM cathode (in some cases, Pd was introduced as extra catalyst) SOEC, will be investigated in feed gas with diverse H<sub>2</sub>O-CO<sub>2</sub> compositions. The related steam electrolysis and CO<sub>2</sub> electrolysis will be compared with co-electrolysis, in terms of performance and cathode kinetics.

Fig. 7.12 displays the performance of steam electrolysis, CO<sub>2</sub> electrolysis and co-electrolysis from the GDC impregnated LSCM cathode SOEC at 900°C. For steam electrolysis and CO<sub>2</sub> electrolysis, the fuel gas, 51% steam carried by 5%H<sub>2</sub>/Ar for the former and CO<sub>2</sub>-CO 70-30 mixture for the latter, was introduced to cathode at a flow rate of 30ml/min in total. Regarding co-electrolysis, 51% steam carried by 5%H<sub>2</sub>/Ar at a flow rate of 20ml/min and CO<sub>2</sub>-CO 70-30 mixture at a flow rate of 20ml/min were joined at a point before being flowed into the cathode chamber. From the impedance comparison in Fig. 7.12(a), it can be seen that the steam electrolysis presents the largest (0.45 Ωcm<sup>2</sup>), co-electrolysis the middle (0.34 Ωcm<sup>2</sup>) and CO<sub>2</sub> electrolysis the lowest Rp (0.24 Ωcm<sup>2</sup>) at OCV. The impedance arc, specifically, the low frequency arc of the co-electrolysis process is depressed compared to that of the steam electrolysis, meaning that the correlated processes is favourable in H<sub>2</sub>O-5%H<sub>2</sub>/Ar-CO<sub>2</sub>-CO mixture.

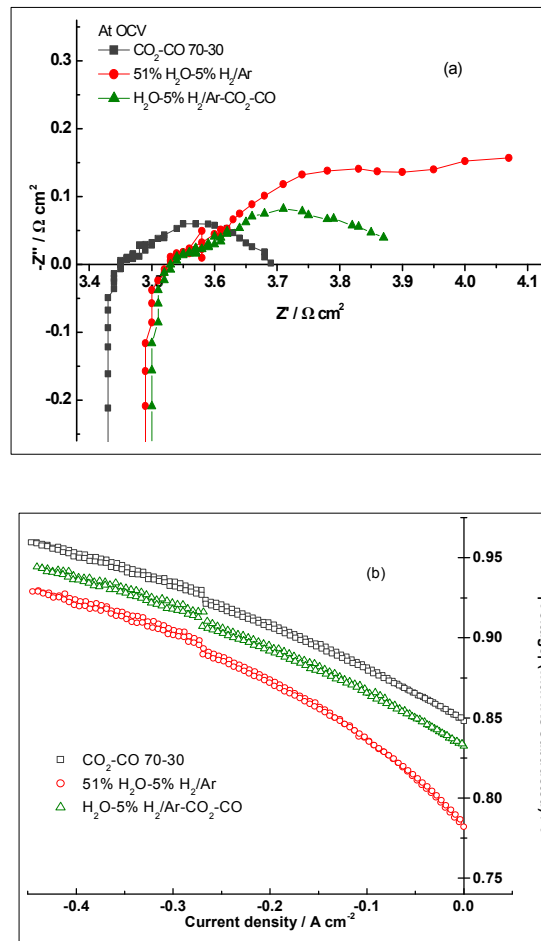


**Fig. 7.12** Performance comparisons among steam electrolysis,  $\text{CO}_2$  electrolysis and  $\text{H}_2\text{O-CO}_2$  co-electrolysis from the GDC impregnated LSCM cathode SOEC working at  $900^\circ\text{C}$  (a) Impedance comparison at OCV and (b) polarization curves in diverse mixture gas (the IRs is subtracted from potential)

The I-V curves of steam electrolysis,  $\text{CO}_2$  electrolysis and co-electrolysis are compared in Fig. 7.12(b). The ohmic loss, i.e. IRs which constitutes the main loss in SOEC with a 2mm YSZ electrolyte, is subtracted from potential to clear the differences between co-electrolysis and steam/ $\text{CO}_2$  electrolysis. The OCV value is -0.849, -0.785, and -0.832V for  $\text{CO}_2$  electrolysis, steam electrolysis and co-electrolysis, respectively. The different OCV value of co-electrolysis from either  $\text{CO}_2$  electrolysis or steam electrolysis implies the participation of gas shift/reverse gas shift reaction along with  $\text{CO}_2$ /steam splitting reaction. From the polarization curves in Fig. 7.12(b),  $\text{CO}_2$  electrolysis and co-

electrolysis processes seem to be easier than steam electrolysis, which is consistent with the impedance results. This phenomenon is controversial with other reports [17], probably caused by the using  $\text{H}_2\text{O}-5\%\text{H}_2/\text{Ar}$  fuel which resulted in increased  $\text{P}_{\text{O}_2}$  in cathode side compared to  $\text{H}_2\text{O}-\text{H}_2$  fuel for steam electrolysis.

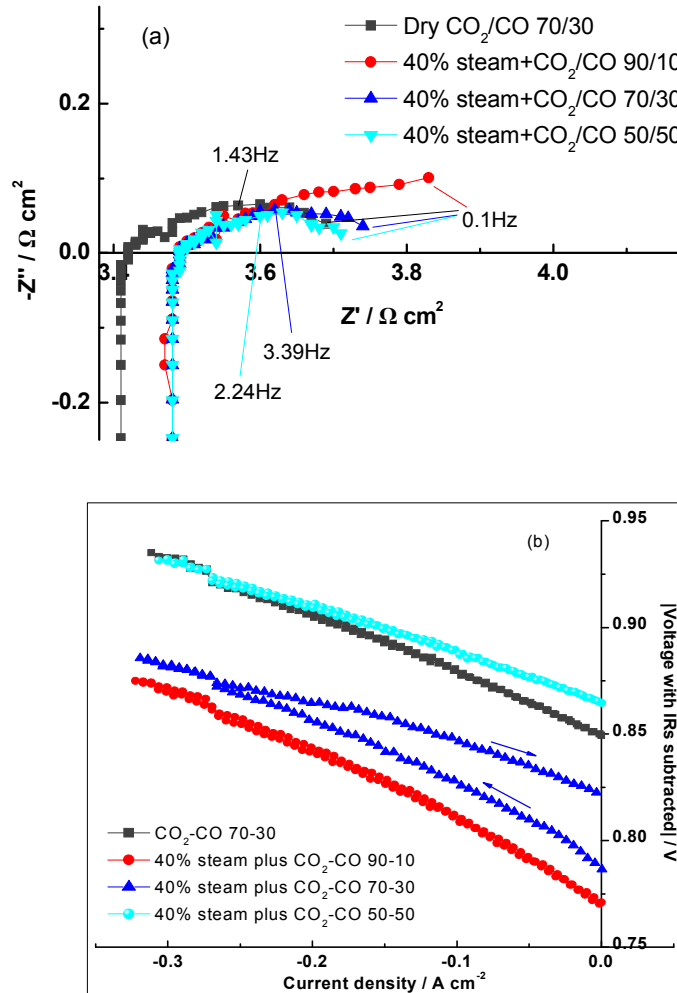


**Fig. 7.13** Co-electrolysis performance from the 0.5%Pd-GDC co-impregnated LSCM cathode SOEC working at  $900^\circ\text{C}$  with steam and different ratios of  $\text{CO}_2\text{-CO}$  mixture as feed gas (a) Impedance spectra at OCV and (b) I-V curves with IRs subtracted

Co-electrolysis in feed containing 40% steam and different ratios of  $\text{CO}_2\text{-CO}$  mixture was measured on the 0.5wt% Pd and GDC co-impregnated LSCM cathode SOEC at  $900^\circ\text{C}$ . The obtained results are exhibited in Fig. 7.13. Data for  $\text{CO}_2$  electrolysis in  $\text{CO}_2\text{-CO}$  70-30 mixture is also given for comparison. Different from previous experiment,

here, steam was carried by CO<sub>2</sub>-CO mixture being sent to cathode chamber, and the flow rate of CO<sub>2</sub>-CO gas was 30ml/min. The CO<sub>2</sub>-CO mixture used in feed gas for H<sub>2</sub>O-CO<sub>2</sub> co-electrolysis is CO<sub>2</sub>-CO 90-10, CO<sub>2</sub>-CO 70-30, and CO<sub>2</sub>-CO 50-50, same as those used for CO<sub>2</sub> electrolysis. The cathode performance towards co-electrolysis increases with decreasing CO<sub>2</sub> concentration in feed gas, similar with the observation from CO<sub>2</sub> electrolysis. The co-electrolysis in 40% steam plus CO<sub>2</sub>-CO 70-30 mixture shows nearly the same response with that of CO<sub>2</sub> electrolysis in CO<sub>2</sub>-CO 70-30 mixture, namely, close R<sub>p</sub> values (around 0.25Ωcm<sup>2</sup>) and similar impedance behaviour. It seems that the addition of 40% steam only affects the cathode conductivity as R<sub>s</sub> increases a bit for co-electrolysis in H<sub>2</sub>O-CO<sub>2</sub>-CO mixtures. The I-V curves in Fig. 7.13(b) reveals similar results with the impedance spectra. The I-V curves overlap between the way separate from OCV to high potentials and that backwards, except that in 40% steam plus CO<sub>2</sub>-CO 70-30 mixture which possibly is due to signal oscillations.

### 7.3.3 Co-electrolysis in different ratio of H<sub>2</sub>O-H<sub>2</sub>-CO<sub>2</sub>-CO mixture

Fig. 7.14 illustrates the performance of co-electrolysis in H<sub>2</sub>O-H<sub>2</sub>-CO<sub>2</sub>-CO 25-25-25-25 (total flow rate is 30ml/min) mixture from the 0.5% Pd and GDC co-impregnated LSCM cathode SOEC at 900°C. Again, the performance from CO<sub>2</sub> electrolysis in CO<sub>2</sub>-CO 50-50 atmosphere and from steam electrolysis in mixture with 50% steam carried by 5%H<sub>2</sub>/Ar and by H<sub>2</sub> is also provided. One can see that the I-V curve of co-electrolysis and that of steam electrolysis in H<sub>2</sub>O-H<sub>2</sub> mixture show quite mild slope whereas relatively steep gradient is seen from the I-V curves of CO<sub>2</sub> electrolysis and especially, that of steam electrolysis in H<sub>2</sub>O-5%H<sub>2</sub>/Ar mixture. These observations are in accord with the impedance results, as the smallest R<sub>p</sub> shows up for steam electrolysis in H<sub>2</sub>O-H<sub>2</sub> environment, with R<sub>p</sub> from co-electrolysis in H<sub>2</sub>O-H<sub>2</sub>-CO<sub>2</sub>-CO 25-25-25-25 locating between the value for steam electrolysis and CO<sub>2</sub> electrolysis and more close to steam electrolysis, and the largest R<sub>p</sub> appears for steam electrolysis in H<sub>2</sub>O-5%H<sub>2</sub>/Ar atmosphere at OCV and at -1.46V (absolute potential). Similar result was reported on Ni/YSZ cathode cell in identical fuel compositions [18].

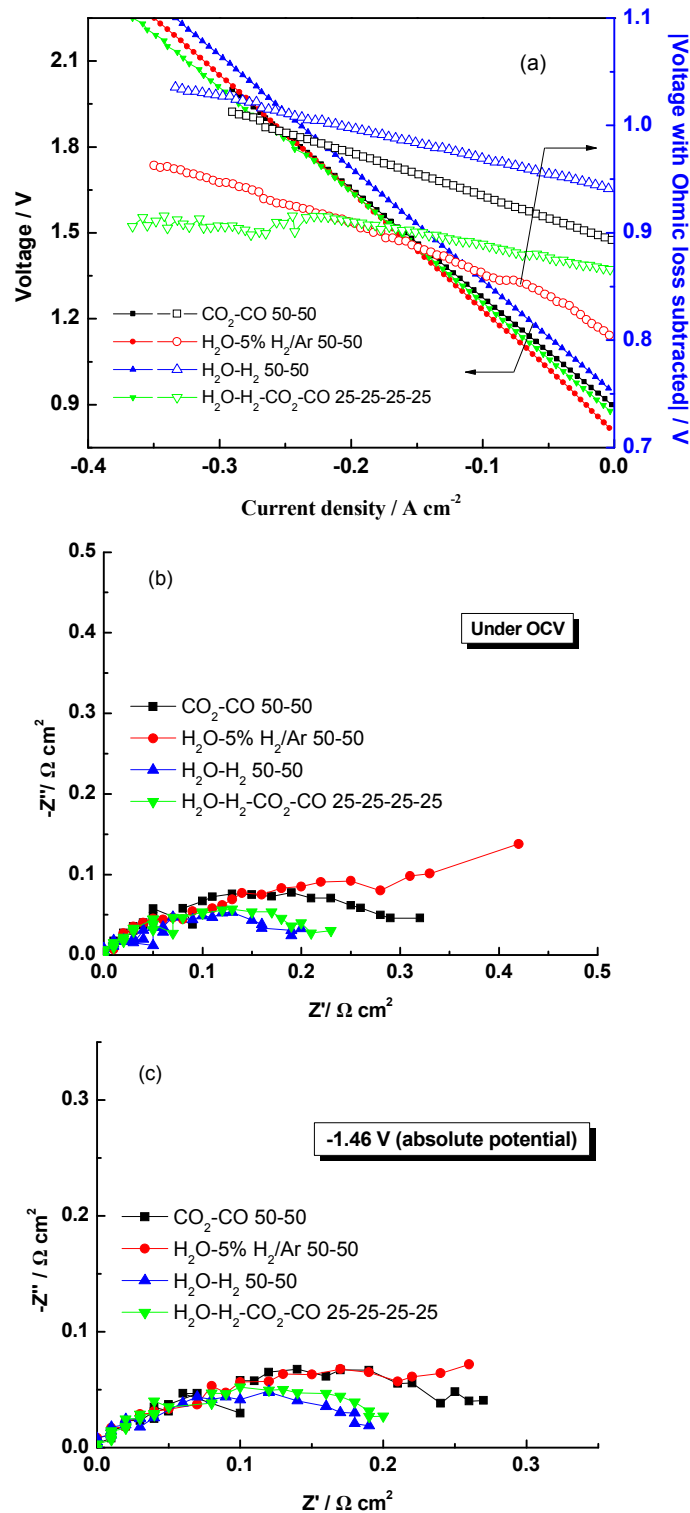


**Fig. 7.14** Electrolysis performance from the 0.5%Pd-GDC co-infiltrated LSCM cathode SOEC operated with different fuels at 900°C (a) I-V curves; (b-c) Impedance data. Fuels include CO<sub>2</sub>-CO 50-50 mixture, 51% steam carried by 5%H<sub>2</sub>/Ar and by H<sub>2</sub>, and H<sub>2</sub>O-H<sub>2</sub>-CO<sub>2</sub>-CO 25-25-25-25 mixture.

**Table 7.4** Summary of  $R_s$  and  $R_p$  from the 0.5% Pd-GDC co-impregnated LSCM cathode for electrolysis working at 900°C in different fuels

	CO <sub>2</sub> -CO 50-50	H <sub>2</sub> O-5%H <sub>2</sub> /Ar 50-50	H <sub>2</sub> O-H <sub>2</sub> 50-50	H <sub>2</sub> O-H <sub>2</sub> -CO <sub>2</sub> -CO 25-25-25-25
$R_s$ at OCV /Ω cm <sup>2</sup>	3.4	3.68	3.64	3.66
$R_s$ at -1.46 V /Ω cm <sup>2</sup>	3.41	3.68	3.65	3.67
$R_p$ at OCV /Ω cm <sup>2</sup>	0.32	0.42	0.2	0.23
$R_p$ at -1.46 V /Ω cm <sup>2</sup>	0.29	0.29	0.20	0.22

The  $R_s$  and  $R_p$  from the 0.5% Pd-GDC co-impregnated LSCM cathode for electrolysis working at 900°C in different fuels are extracted from the impedance spectra in Fig. 7.14, as summarized in Table 7.4. The  $R_s$  is independent of potential, but depends on the composition of fuels used. Briefly,  $R_s$  increases a bit when steam is introduced into feed. Furthermore,  $R_s$  is around 10-15 times larger than that of  $R_p$  in different conditions, implying that there is a large room for performance enhancement in high temperature electrolysis via SOEC. The  $R_p$  value is the largest for steam electrolysis in H<sub>2</sub>O-5%H<sub>2</sub>/Ar mixture, and the smallest in H<sub>2</sub>O-H<sub>2</sub> mixture. Besides, the  $R_p$  for CO<sub>2</sub> electrolysis and for H<sub>2</sub>O-CO<sub>2</sub> co-electrolysis are larger than that of steam electrolysis in H<sub>2</sub>O-H<sub>2</sub> mixture. The  $R_p$  reaches 0.2 Ω cm<sup>2</sup>, 0.23 Ω cm<sup>2</sup> and 0.3 Ω cm<sup>2</sup> for steam electrolysis, co-electrolysis, and CO<sub>2</sub> electrolysis respectively in the studied conditions as listed in Table 7.4, reflecting the great potential of utilization the 0.5% Pd and GDC co-impregnated LSCM as cathode material for high temperature electrolysis via SOEC.

#### 7.3.4 Co-electrolysis stability test in H<sub>2</sub>O-H<sub>2</sub>-CO<sub>2</sub>-CO mixtures

The stability test from the 0.5% Pd-GDC co-impregnated cathode SOEC was employed in H<sub>2</sub>O-H<sub>2</sub>-CO<sub>2</sub>-CO mixture and CO<sub>2</sub>-CO mixture at a constant current density of -0.15 A cm<sup>-2</sup>. Presented in Fig. 7.15 is the potential of the above cell with operation time at a

constant current density in electrolysis operation at 900°C. Pulses (increases in potential) are detected to appear regularly when operated in H<sub>2</sub>O-H<sub>2</sub>-CO<sub>2</sub>-CO 25-25-25-25 mixture, and as reducing steam content to 40% and 30%, the time gap between two pulses increases, i.e. the frequency of pulse decreases. The speculation for the above phenomena is, cold point probably emerges on the gas line which causes condensation of steam, in this case, the steam amount carried into the cathode chamber increases and the cell resistance enlarges. When decreasing the steam concentration, the condensation of steam happens less frequently. No pulse shows up when operating the cell in CO<sub>2</sub>-CO gas mixture, which confirms the above assumption.

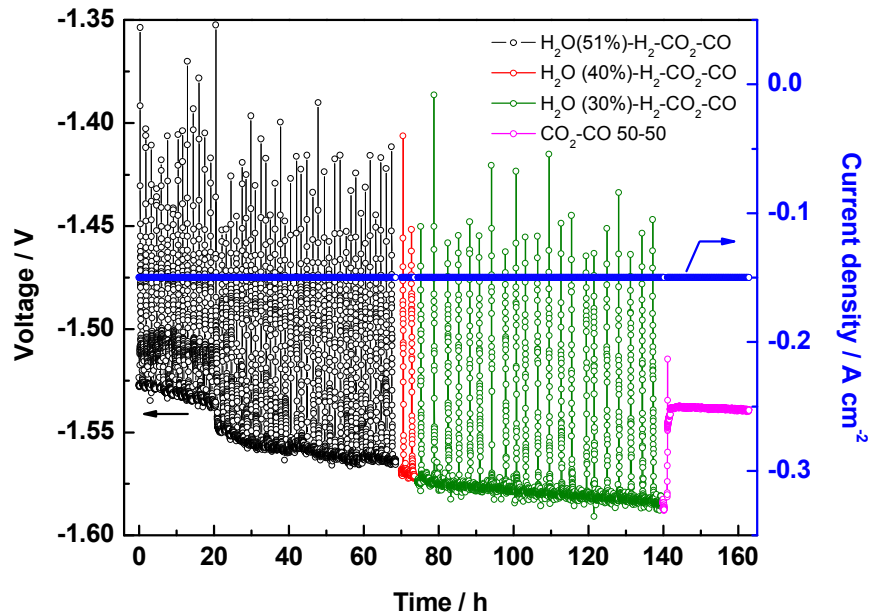


**Fig. 7.15** The durability measurement in electrolysis operation mode on the 0.5% Pd-GDC co-impregnated LSCM cathode SOEC working in various atmospheres at 900°C at a constant current density of  $-0.15 \text{ A cm}^{-2}$

Excluding the pulses, the cell potential does not change much in the co-electrolysis operation for ca. 140hrs, meaning the degradation is insignificant in such long time operation. This observation is more apparent when switching the fuel gas from H<sub>2</sub>O-H<sub>2</sub>-CO<sub>2</sub>-CO mixtures to CO<sub>2</sub>-CO 50-50 gas. The electrolysis operation in CO<sub>2</sub>-CO mixture at a constant current ( $-0.15 \text{ A cm}^{-2}$ ) is sustained for, at least, 22hrs, which was covered previously in section 5.4.4. No evident variation on potential is observed with operation

time. The impedance tests of cathode resistance before and after electrolysis in CO<sub>2</sub>-CO 50-50 mixture (Fig. 5.29) demonstrate that the 0.5% Pd and GDC co-impregnated LSCM cathode barely degrades during the electrolysis operation in CO<sub>2</sub>-CO 50-50 condition. Therefore, it is reliable to apply the 0.5%Pd-GDC co-impregnated LSCM cathode material in the field of high temperature electrolysis via SOEC.

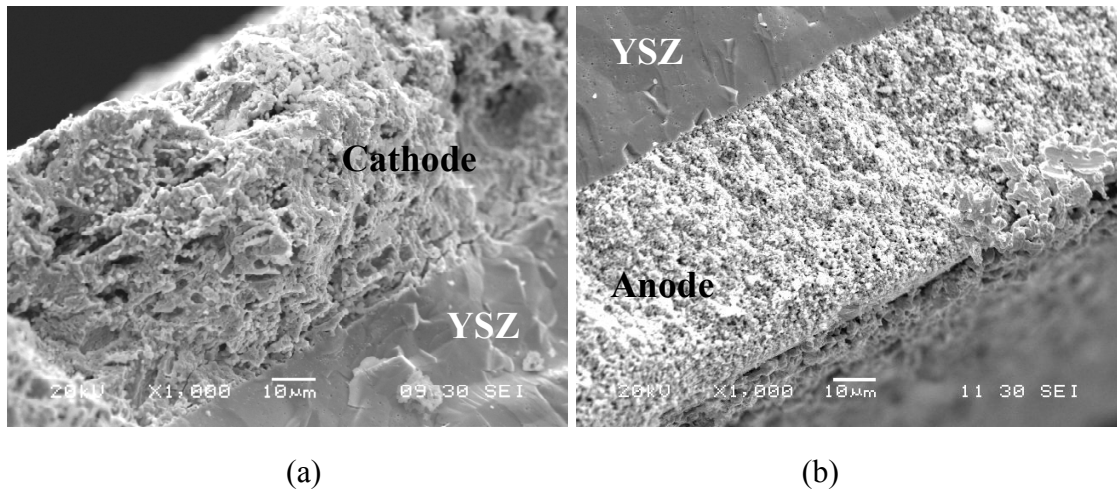


**Fig. 7.16** SEM micrographs of the 0.5% Pd-GDC co-impregnated LSCM cathode/electrolyte interface (a) and the LSM/ScSZ anode/electrolyte interface (b) after the durability measurement in various atmospheres

The microstructure of the 0.5%Pd-GDC co-impregnated LSCM cathode SOEC was examined after exposing to H<sub>2</sub>O-H<sub>2</sub>-CO<sub>2</sub>-CO and CO<sub>2</sub>-CO mixtures for as long as ca.160hrs, the result of which is displayed in Fig. 7.16. It can be seen that both the GDC impregnated LSCM/YSZ cathode and the LSM/ScSZ/YSZ anode adhere well to the thick YSZ electrolyte after durability test, and no delamination is detected between cathode/anode and electrolyte. This also indicates the viability of applying the GDC impregnated LSCM cathode material in high temperature SOECs.

## 7.4 Conclusions

In this chapter, performance evaluation for steam electrolysis and H<sub>2</sub>O-CO<sub>2</sub> co-electrolysis was carried out on LSCM/GDC cathode SOECs prepared from different procedures. Cathode kinetics was studied in different fuel compositions.

Screen-printed LSCM/GDC cathode SOEC was studied with different level of steam supply and with fuel supply at different flow rate, and it was found that the sigmoid I-V curve was related to insufficient steam supply and limited transport, rather the LSCM phase reduction at high potentials. At 20% steam fuel carried by 5%H<sub>2</sub>/Ar and at a flow rate higher than 20ml/min, the polarization curve showed a V-I relation more likely to be linear.

The R<sub>p</sub> reached app. 0.7 Ωcm<sup>2</sup> from the GDC impregnated LSCM cathode operated at 900°C at OCV in feed with steam concentration as high as 70%, indicating higher performance than that from the screen-printed LSCM/GDC cathode. The high performance from the GDC dispersed LSCM cathode over screen-printed LSCM/GDC cathode was believed to have benefited from the modified microstructure of the former. Steam electrolysis performance was enhanced further using H<sub>2</sub>, rather than 5%H<sub>2</sub>/Ar, as steam carrier gas, which could be explained by the promoted cathode properties caused by variation in P<sub>O<sub>2</sub></sub>. The more reducing atmosphere is favourable to promote the activity of the cathode material, in particular, that of the GDC component in LSCM/GDC material.

The 0.5wt% Pd and GDC co-impregnated LSCM cathode displayed outstanding performance for steam/CO<sub>2</sub> and co-electrolysis via SOEC, and it was also found to be reliable for electrolysis operation in H<sub>2</sub>O-H<sub>2</sub>-CO<sub>2</sub>-CO mixtures for at least 160hrs. These suggest the potential application of the Pd-GDC co-impregnated LSCM cathode material in high temperature SOECs.

## References

1. J. D. Holladay, J. Hu, D. L. King, Y. Wang, *Catal. Today*, **139**, 244-260 (2009)
2. M. Ni, M. K. H. Leung, D. Y. C. Leung, *Int. J. Hydrogen Energy*, **33**, 2337 (2008)
3. M. Liu, B. Yu, J. Xu, J. Chen, *J. Power Sources*, **177**, 493 (2008)
4. B. Yu, W. Zhang, J. Chen, J. Xu, S. Wang, *Sci. China Ser. B-Chem.*, **51**, 289 (2008)
5. A. Hauch, S. D. Ebbesen, S. H. Jensen and M. Mogensen, *J. Mater. Chem.*, **18**, 2331 (2008)
6. Z. Zhang, W. Kobsiriphat, J. R. Wilson, M. Pillai, I. Kim, and S. A. Barnett, *Energy & Fuels*, **23**, 3089 (2009)

7. Q. Fu, C. Mabilat, M. Zahid, A. Brisse and L. Gautier, *Energy Environ. Sci.*, **3**, 1382 (2010)
8. C. Stoots, J. O'Brien, J. Hartvigsen, *Proceedings of International Mechanical Engineering Congress and Exposition (IMECE)*, Seattle, Washington, USA (2007)
9. Carbon dioxide, from Wikipedia, available online:  
[http://en.wikipedia.org/wiki/Carbon\\_dioxide](http://en.wikipedia.org/wiki/Carbon_dioxide)
10. Table of water vapour pressures. Available online:  
[http://www.Kayelaby.npl.co.uk/chemistry/3\\_4/3\\_4\\_2.html](http://www.Kayelaby.npl.co.uk/chemistry/3_4/3_4_2.html)
11. X. Yang and J. T. S. Irvine, *J. Mater. Chem.*, **18**, 2349 (2008)
12. T. Ishihara, N. Jirathiwathanakul and H. Zhong, *Energy Environ. Sci.*, **3**, 665 (2010)
13. X. Yue and J. T. S. Irvine, *J. Electrochem. Soc.*, **159** (8), F442 (2012)
14. J. Schefold, A. Brisse, and M. Zahid, *J. Electrochem. Soc.*, **156**, B897 (2009)
15. A. Hauch, S. H. Jensen, S. Ramousse, and M. Mogensen, *J. Electrochem. Soc.*, **153** (9), A1741 (2006)
16. O. A. Marina, L. R. Pederson, M. C. Williams, G. W. Coffey, K. D. Meinhardt, C. D. Nguyen, and E. C. Ehomsen, *J. Electrochem. Soc.*, **154** (5), B452 (2007)
17. S. H. Jensen, P. H. Larsen, M. Mogensen, *Int. J. Hydrogen Energy*, **32**, 3253 (2007)
18. C. Grabes, S. D. Ebbesen, M. Mogensen, *Solid State Ionics*, (2010) doi: 10.1016/j.ssi.2010.06.014

## General conclusions

Ni-YSZ cermets cathode material underwent carbon deposition, especially at high concentration of CO at temperature range of 400-600°C when treated in CO<sub>2</sub>-CO mixtures. Carbon was also detected ex-situ from Ni-YSZ SOEC cathode after CO<sub>2</sub> electrolysis operations in CO<sub>2</sub>-CO mixture at 900°C. In contrast, no carbon was detected from (La<sub>0.75</sub>Sr<sub>0.25</sub>)<sub>0.97</sub>(Cr<sub>0.5</sub>Mn<sub>0.5</sub>)O<sub>3±δ</sub> (LSCM) based SOEC cathode.

Different behaviour was observed from Ni-YSZ cermets cathode, LSCM/YSZ and LSCM/Gd<sub>0.1</sub>Ce<sub>0.9</sub>O<sub>1.95</sub> (GDC) composite cathode in the identical operation conditions, implying different rate-limiting steps happened due to diverse cathode microstructure and material properties towards the CO<sub>2</sub> electrochemical reduction reaction.

In LSCM/GDC set of material, the cathode properties were enhanced in reducing atmosphere, which was advantageous for SOEC operation over the LSCM/YSZ material set. Both LSCM and GDC component contributed to SOEC cathode activity for CO<sub>2</sub> electrolysis.

Adopting a gradient cathode structure, the SOEC cathode property was boosted from the LSCM/YSZ composite applied in CO<sub>2</sub> electrolysis, compared to the one made by average mixing of both components.

Introducing dopant level of Pd, Ni, CeO<sub>2</sub> and Pt added extra catalytic activity to LSCM/GDC SOEC cathode for CO<sub>2</sub> splitting process. Remarkably reduced cathode polarization resistance was obtained on metal or CeO<sub>2</sub> impregnated LSCM/GDC cathode SOEC used for CO<sub>2</sub> electrolysis.

The GDC infiltrated LSCM cathode fabricated by wet vacuum impregnation approach offered the desirably modified microstructure, which had the finely dispersed GDC nanoparticles on porous LSCM skeleton, and this resulting microstructure was believed to be the origins of performance improvement from LSCM/GDC SOEC cathode for CO<sub>2</sub> electrolysis. With the aid of 0.5wt% Pd, the GDC impregnated LSCM SOEC cathode gave a performance that was competitive to that from Ni-YSZ cermets cathode at 900°C in CO<sub>2</sub>/CO feed.

The gas chromatography (GC) revealed current-to-CO efficiencies over 80% from LSCM/GDC cathode SOEC. Discrepancies were found between the CO<sub>2</sub> dissociation and CO production. The slight lower faradaic efficiency (less than 100%) for CO production might come from the errors within the GC equipment and the CO<sub>2</sub>/CO mass flow controllers.

With respect to CO<sub>2</sub> electrolysis with pure CO<sub>2</sub> feed using N<sub>2</sub> as saturate gas, activation polarization was predominant at low current densities. However, similar R<sub>p</sub> values were detected between the pure CO<sub>2</sub> electrolysis and that with CO<sub>2</sub>/CO mixture as feed from the GDC impregnated LSCM cathode at SOEC operation potentials. CO was detected from potential higher than about 0.9V. Both CO<sub>2</sub> dissociation rate and CO production rate increased with increasing current/potential.

The high performance SOEC cathode in CO<sub>2</sub> electrolysis showed outstanding performance in steam electrolysis and steam-carbon dioxide co-electrolysis as well, but for steam electrolysis, supplying with sufficient steam to cathode was important to avoid limited transport which resulted in the appearance of sigmoidal polarization curve. Compared to CO<sub>2</sub> electrolysis operated in the identical conditions, the steam electrolysis showed higher performance when using pure H<sub>2</sub> as steam carrier gas, and the performance of steam electrolysis in H<sub>2</sub>O-5%H<sub>2</sub>/Ar mixture was lower. The 0.5wt%Pd-GDC co-impregnated LSCM SOEC cathode was reliable for electrolysis operation in H<sub>2</sub>O-H<sub>2</sub>-CO<sub>2</sub>-CO mixtures for at least 160hrs, implying a promising cathode material in high temperature SOECs applications.

## Publications

1. **Xiangling Yue**, and John T S Irvine. Alternative cathode material for CO<sub>2</sub> reduction by high temperature solid oxide electrolysis cells. *J. Electrochem. Soc.*, **159** (8), F442-F448 (2012)
2. **Xiangling Yue** and John. T. S. Irvine, LSCM/GDC cathode for high temperature steam electrolysis and steam-carbon dioxide co-electrolysis, *Solid State Ionics*, **225**, 132-135 (2012)
3. **Xiangling Yue**, and John T S Irvine. Impedance studies on LSCM/GDC cathode for high temperature CO<sub>2</sub> electrolysis. *Electrochem. Solid-State Lett.*, **15** (3), B31-B34 (2012)
4. **Xiangling Yue**, and John T S Irvine. Impedance studies on LSCM/GDC cathode for high temperature CO<sub>2</sub> electrolysis. *ECS Transactions*, **41** (33), 87-95 (2012)